Fluctuating and light-induced dynamics in cuprate superconductors

Dissertation
zur Erlangung des Doktorgrades
an der Fakultät für Mathematik, Informatik und Naturwissenschaften
Fachbereich Physik
der Universität Hamburg

vorgelegt von

Guido Frederik Homann

Hamburg

2023

Abstract

We present a semiclassical method for the simulation of fluctuating and light-induced dynamics in cuprate superconductors, based on the Ginzburg-Landau theory of superconductivity. Our method explicitly captures the coupled dynamics of the superconducting order parameter and the electromagnetic field on a layered lattice, including dissipation and thermal fluctuations.

In the first part of this dissertation, we characterize the superconducting ground state of a bilayer cuprate at zero temperature and investigate its fluctuating dynamics at nonzero temperature. In particular, we extract the temperature dependence of the plasma resonances and the optical conductivity from our simulations. While thermal fluctuations reduce the phase coherence of the superconducting state at low temperature, they cause a phase transition to a resistive state at high temperature. The resistive state that we find is characterized by a strong suppression of the interbilayer tunneling of Cooper pairs and the emergence of vortex excitations. This constitutes a possible scenario of the pseudogap regime in underdoped cuprates. Furthermore, we observe a nontrivial temperature dependence of the upper Josephson plasma frequency. Analytical calculations indicate that the upper Josephson plasma frequency is stabilized by vortex-induced disorder, which partly compensates for the reduction of intrabilayer coupling due to thermal fluctuations.

In the second part of this dissertation, we discuss light-induced nonequilibrium phenomena at temperatures well below the transition temperature. Specifically, we consider the periodic driving of a cuprate superconductor by an electric field polarized along the crystalline c axis, implementing two different scenarios. In the first scenario, the electric field directly couples to the superconducting order parameter. In the second scenario, the electric field resonantly couples to an infrared-active phonon mode, resulting in a periodic modulation of the coupling between the superconducting layers. Driving a superconductor via the nonlinear coupling of the electric field to the order parameter gives rise to Higgs oscillations. We propose to induce a time-crystalline state in a mono- or bilayer cuprate by driving a sum resonance of the Higgs mode and the Josephson plasma mode or the upper Josephson plasma mode, respectively. The nonlinear coupling between the electric field and the Higgs mode also opens up the possibility to enhance the interlayer transport in monolayer cuprates. We demonstrate that the superconducting weight in the c-axis conductivity is enhanced when the frequency of the optical driving is slightly blue-detuned from the Higgs frequency. Furthermore, we show how the nonlinear coupling of a plasma mode to another collective mode can be used for parametric amplification of terahertz radiation. We present two specific protocols to realize this general proposal. The first protocol applies to monolayer cuprates and exploits the nonlinear coupling to the Higgs mode. The second protocol applies to bilayer cuprates and exploits the nonlinear coupling to an infrared-active phonon mode. In previous work, parametric driving of a cuprate superconductor via a suitable phonon mode was also proposed as a possible explanation for the experimental observation of light-enhanced transport in $YBa_2Cu_3O_{6+x}$. We confirm that the superconducting weight in the c-axis conductivity is enhanced when the driving frequency is blue-detuned from a Josephson plasma frequency, while it is diminished by red-detuned driving. In contrast, both our analytical and numerical calculations show that blue-detuned driving reduces the Meissner screening as plasma waves generated at the surface are transmitted into the superconductor. For red-detuned driving, on the other hand, we find a tendency to an enhanced Meissner screening.

Zusammenfassung

Wir präsentieren eine semiklassische Methode zur Simulation fluktuierender und lichtinduzierter Dynamik in Kuprat-Supraleitern, basierend auf der Ginzburg-Landau-Theorie der Supraleitung. Unsere Methode erfasst explizit die gekoppelte Dynamik des supraleitenden Ordnungsparameters und des elektromagnetischen Feldes auf einem Gitter mit Schichtstruktur, wobei Dissipation und thermische Fluktuationen berücksichtigt werden.

Im ersten Teil dieser Dissertation charakterisieren wir den supraleitenden Grundzustand eines Doppelschicht-Kuprats bei verschwindender Temperatur und untersuchen seine fluktuierende Dynamik bei endlicher Temperatur. Dabei extrahieren wir insbesondere die Temperaturabhängigkeit der Plasma-Resonanzen und der optischen Leitfähigkeit aus unseren Simulationen. Während thermische Fluktuationen bei niedriger Temperatur die Phasenkohärenz des supraleitenden Zustands verringern, verursachen sie bei hoher Temperatur einen Phasenübergang in einen widerstandsbehafteten Zustand. Dieser widerstandsbehaftete Zustand ist durch eine starke Unterdrückung des Tunnelns von Cooper-Paaren zwischen den Doppelschichten sowie das Auftreten von Vortex-Anregungen charakterisiert. Er stellt ein mögliches Szenario für die Pseudogap-Phase unterdotierter Kuprate dar. Darüber hinaus beobachten wir eine nichttriviale Temperaturabhängigkeit der oberen Josephson-Plasmafrequenz. Analytische Berechnungen deuten darauf hin, dass die obere Josephson-Plasmafrequenz durch Vortex-induzierte Unordnung stabilisiert wird. Dies kompensiert teilweise die Reduzierung der Kopplung zwischen den beiden Schichten einer Doppelschicht aufgrund thermischer Fluktuationen.

Im zweiten Teil dieser Dissertation diskutieren wir lichtinduzierte Nichtgleichgewichtsphänomene bei Temperaturen deutlich unterhalb der Sprungtemperatur. Konkret betrachten wir das periodische Treiben eines Kuprat-Supraleiters durch ein elektrisches Feld, das entlang der kristallinen c-Achse orientiert ist. Dabei implementieren wir zwei Szenarien. Im ersten Szenario koppelt das elektrische Feld direkt an den supraleitenden Ordnungsparameter. Im zweiten Szenario koppelt das elektrische Feld resonant an eine infrarot-aktive Phonon-Mode, woraus eine periodische Modulation der Kopplung zwischen den supraleitenden Schichten resultiert. Das Treiben eines Supraleiters über die nichtlineare Kopplung des elektrischen Feldes an den Ordnungsparameter führt zu Higgs-Oszillationen. Wir schlagen vor, einen zeitkristallinen Zustand in einem Einzel- oder Doppelschicht-Kuprat zu induzieren, indem eine Summenresonanz der Higgs-Mode sowie der Josephson-Plasmamode bzw. der oberen Josephson-Plasmamode angeregt wird. Die nichtlineare Kopplung zwischen dem elektrischen Feld und der Higgs-Mode eröffnet auch die Möglichkeit, in Einzelschicht-Kupraten den Ladungstransport zwischen den supraleitenden Schichten zu verbessern. Wir demonstrieren, dass das supraleitende Gewicht in der Leitfähigkeit entlang der c-Achse erhöht wird, wenn die Frequenz des optischen Treibens leicht blauverstimmt von der Higgs-Frequenz ist. Weiterhin zeigen wir, wie die nichtlineare Kopplung der Plasmamode an eine andere kollektive Mode für die parametrische Verstärkung von Terahertz-Strahlung genutzt werden kann. Wir präsentieren zwei spezifische Protokolle, um diesen allgemeinen Vorschlag zu realisieren. Das erste Protokoll ist auf Einzelschicht-Kuprate anwendbar und nutzt die nichtlineare Kopplung an die Higgs-Mode aus. Das zweite Protokoll ist auf Doppelschicht-Kuprate anwendbar und nutzt die nichtlineare Kopplung an eine infrarot-aktive Phononmode aus. In früheren Arbeiten wurde das parametrische Treiben eines Kuprat-Supraleiters über eine geeignete Phononmode auch als eine mögliche Erklärung für die experimentelle Beobachtung

lichtverstärkten Ladungstransports in $YBa_2Cu_3O_{6+x}$ vorgeschlagen. Wir bestätigen, dass das supraleitende Gewicht in der Leitfähigkeit entlang der c-Achse erhöht wird, wenn die Frequenz des Treibens blauverstimmt von einer Josephson-Plasmafrequenz ist, während es durch rotverstimmtes Treiben verringert wird. Dagegen zeigen sowohl unsere analytischen als auch unsere numerischen Berechnungen, dass blauverstimmtes Treiben den Meissner-Effekt reduziert, da an der Oberfläche generierte Plasmawellen ungehindert in den Supraleiter eindringen. Auf der anderen Seite finden wir eine Tendenz zu einem verstärkten Meissner-Effekt für rotverstimmtes Treiben.

Preface

This cumulative thesis bases on the publications [H1–H4] and the manuscript [H5]. The publications [H1–H4] are included in the Appendix. A summary of the scientific contributions is presented in Chapters 2 and 3. Throughout this thesis, we follow the SI units convention. In our numerical simulations, we use units that are directly related to SI units. Important physical constants and their values are listed in Table 1.

Table 1: Physical constants occurring in this thesis. The units and values used in the numerical simulations are also specified.

Elementary charge e	1
Speed of light c ($\text{Å}\,\text{as}^{-1}$)	2.99792
Reduced Planck constant $\hbar$ ($\text{meV}\,\text{as}$)	6.58212×10^5
Boltzmann constant k_{B} ($\text{meV}\,\text{K}^{-1}$)	8.61733×10^{-2}
Vacuum permittivity ϵ_0 ($e\,\text{mV}^{-1}\,\text{Å}^{-1}$)	5.52635×10^{-6}
Vacuum permeability μ_0 ($\text{mV}\,\text{as}^2\,e^{-1}\,\text{Å}^{-1}$)	2.01336×10^4

Author's publications

[H1] G. Homann, J. G. Cosme and L. Mathey, *Higgs time crystal in a high-T_c superconductor*, Physical Review Research **2**, 043214 (2020).

[H2] G. Homann, J. G. Cosme, J. Okamoto and L. Mathey, *Higgs mode mediated enhancement of interlayer transport in high-T_c cuprate superconductors*, Physical Review B **103**, 224503 (2021).

[H3] G. Homann, J. G. Cosme and L. Mathey, *Terahertz amplifiers based on gain reflectivity in cuprate superconductors*, Physical Review Research **4**, 013181 (2022).

[H4] G. Homann, J. G. Cosme and L. Mathey, *Parametric control of Meissner screening in light-driven superconductors*, New Journal of Physics **24**, 113007 (2022).

[H5] G. Homann, M. H. Michael, J. G. Cosme and L. Mathey, *Vortex-induced stabilization of the upper Josephson plasma frequency in a bilayer cuprate*, in preparation.

[H6] G. Homann, *Optically enhanced interlayer tunneling in high-temperature superconductors*, Master's thesis, University of Hamburg (2018).

The publications [H1–H4] and the manuscript [H5] base on a semiclassical simulation method, which was developed by myself in close collaboration with my supervisor Ludwig Mathey. Minor parts of the simulation code originate from my master's thesis [H6], which was also supervised by Ludwig Mathey. I was deeply involved in writing the manuscripts for Refs. [H1–H5]. The individual contributions to these works are listed below.

[H1] All analytical and numerical results were obtained by myself. The results were discussed among all authors, and all authors participated in writing the manuscript.

[H2] All analytical and numerical results were obtained by myself, except for two parts of the Supplemental Material. Jayson Cosme implemented a quadratic version of our lattice gauge model and performed simulations for comparison with the fully nonlinear model and the analytical prediction. Junichi Okamoto analyzed the dynamical stability of our model using the harmonic balance method. The results were discussed among all authors, and all authors participated in writing the manuscript.

[H3] All analytical and numerical results were obtained by myself. The results were discussed among all authors, and all authors participated in writing the manuscript.

[H4] All numerical results were obtained by myself. The analytical calculation of the Meissner screening in the driven state was performed partly by Ludwig Mathey and partly by myself. The results were discussed among all authors, and all authors participated in writing the manuscript.

[H5] All numerical results were obtained by myself. The analytical derivation of the stabilization of the upper Josephson plasma frequency was performed partly by Marios Michael and partly by myself. The results were discussed among all authors, and all authors participated in writing the manuscript.

Contents

Chapter 1

Introduction

In this chapter, we review the basics of superconductivity and the properties of cuprate superconductors, focusing on those aspects that are relevant for the remainder of this work. Extensive presentations of the topic can be found in many textbooks, such as [1–6].

1.1 Phenomenology of superconductivity

A superconductor is a material that exhibits perfect conductivity and perfect diamagnetism below a critical temperature T_c. As depicted in Fig. 1.1(a), the electrical resistivity of a superconductor drops to zero when it is cooled below T_c. This was first observed by Kamerlingh Onnes in 1911 when he cooled mercury below its critical temperature of $T_c \approx 4.2$ K [7]. Today, numerous materials are known to display zero resistivity within experimental sensitivity at low temperatures.

   The sudden disappearance of the resistivity is in stark contrast to metallic behavior. The resisitivity of a metal decreases gradually with temperature as the effect of electron-phonon scattering lessens. In addition, the resistivity of a metal has a temperature-independent contribution due to the scattering of electrons from crystalline impurities. Hence, the absence of any electrical resistance indicates that electrons are not scattered in a superconductor. The mechanism behind this phenomenon will be illuminated in the following sections.

   Perfect conductivity does not only manifest in a vanishing resisitivity but also in a $1/\omega$ divergence of the electrical conductivity $\sigma(\omega)$, which can be understood on the level of the Drude model [8,9]. We start with the definition of the electrical conductivity. The electrical conductivity is a linear response function that describes the relation between the current density $\mathbf{J}$ and the electric field $\mathbf{E}$ at frequency ω inside a material,

$$\mathbf{J}(\omega) = \sigma(\omega)\mathbf{E}(\omega). \tag{1.1}$$

Here, the current and the electric field point in the same direction such that $\sigma(\omega)$ is a scalar function. Note that we refer to σ as the *optical conductivity* at frequencies in the terahertz range and above. According to the Drude model, the conductivity is given by

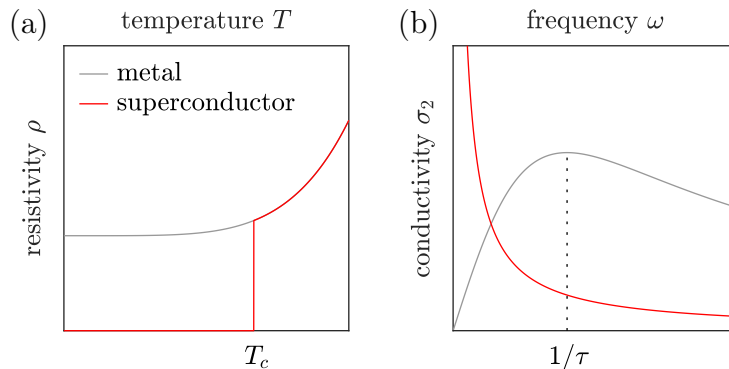$$\sigma(\omega) = \frac{ne^2\tau}{m(1 - i\omega\tau)}, \tag{1.2}$$

Figure 1.1: Signatures of perfect conductivity. (a) DC electrical resistivity of a super-conductor and a normal metal at low temperatures. (b) Imaginary part of the electrical conductivity of a superconductor and a normal metal at low frequencies. The metal has a finite scattering time τ.

where n is the density of free electrons, m is the (effective) electron mass, and τ is the mean free time between two collisions of an electron with the ion lattice. In the absence of scattering, $\tau \to \infty$, the real part of the conductivity diverges for $\omega = 0$ and vanishes for any finite frequency,

$$\sigma_1(\omega) = \frac{\pi n e^2}{m} \delta(\omega). \tag{1.3}$$

The divergence of the DC conductivity corresponds to a vanishing resistivity and is accompanied by a $1/\omega$ divergence of the imaginary part of the conductivity,

$$\sigma_2(\omega) = \frac{n e^2}{m \omega}. \tag{1.4}$$

The frequency dependence of σ_2 is shown in Fig. 1.1(b). In general, not all the free electrons inside a superconductor contribute to superconductivity. In that case, n is replaced by the density of superconducting electrons n_s. Equation (1.4) is then equivalent to the first London equation [10], relating the *supercurrent* to the electric field as

$$\partial_t \mathbf{J} = \frac{n_s e^2}{m} \mathbf{E}. \tag{1.5}$$

The second characteristic feature of superconductivity is perfect diamagnetism. A superconductor expels any magnetic field below a critical field strength from the bulk. This screening of magnetic fields, known as the Meissner effect [11], is provided by persistent surface currents. In general, the relation between supercurrents and the magnetic flux density $\mathbf{B}$ is described by the second London equation [10],

$$\boldsymbol{\nabla} \times \mathbf{J} = -\frac{n_s e^2}{m} \mathbf{B}. \tag{1.6}$$

Combining Eq. (1.6) with the Maxwell equation $\boldsymbol{\nabla} \times \mathbf{B} = \mu_0 \mathbf{J}$ [12], we obtain

$$\boldsymbol{\nabla}^2 \mathbf{B} = \frac{\mu_0 n_s e^2}{m} \mathbf{B}. \tag{1.7}$$
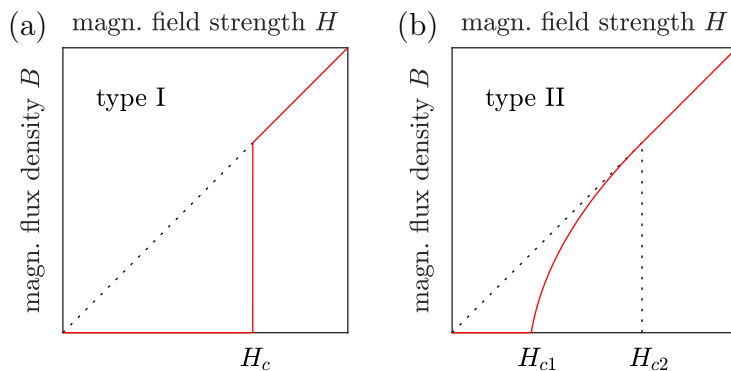
Figure 1.2: Response of type-I and type-II superconductors to an applied magnetic field. (a) Magnetic flux density in the bulk of a type-I superconductor as a function of the applied field strength. (b) Magnetic flux density in the bulk of a type-II superconductor as a function of the applied field strength.

Equation (1.7) implies that the magnetic flux density decays exponentially from the surface of a superconductor. The characteristic length scale of this exponential decay is the London penetration depth

$$\lambda = \sqrt{\frac{m}{\mu_0 n_s e^2}}. \tag{1.8}$$

The screening currents also decay exponentially on this length scale.

There are two classes of superconductors, which are distinguished based on their response to an applied magnetic field as illustrated in Fig. 1.2. Inside a type-I superconductor, the magnetic flux density $B = |\mathbf{B}|$ is zero as long as the strength of the applied field H is lower than the critical value H_c. When the critical field strength is exceeded, the superconducting state breaks down and the behavior of the normal state is retained. The critical field strength depends on temperature, following the empirical relation

$$H_c(T) \approx H_c(0) \left[1 - (T/T_c)^2 \right]. \tag{1.9}$$

Type-II superconductors are characterized by two critical field strengths. While magnetic fields are fully expelled up to the lower critical field strength H_{c1}, a mixed state is entered above H_{c1}. In this mixed state, the magnetic field partially penetrates into the bulk by creating normal conducting vortex tubes. The vortex tubes form a triangular lattice [13–15] and their density grows with increasing field strength. At the upper critical field H_{c2}, the vortex tubes essentially fill out the entire material such that the transition to the normal state is completed.

1.2   BCS theory

An important step towards a microscopic theory of superconductivity was the following insight by Leon Cooper [16]. He considered a normal metal at zero temperature, where the electrons occupy all the states up to the Fermi energy ϵ_F. Then, two electrons with an attractive interaction are added. It turns out that it is energetically favorable for the two electrons to form a bound pair with zero center-of-mass momentum. Remarkably,
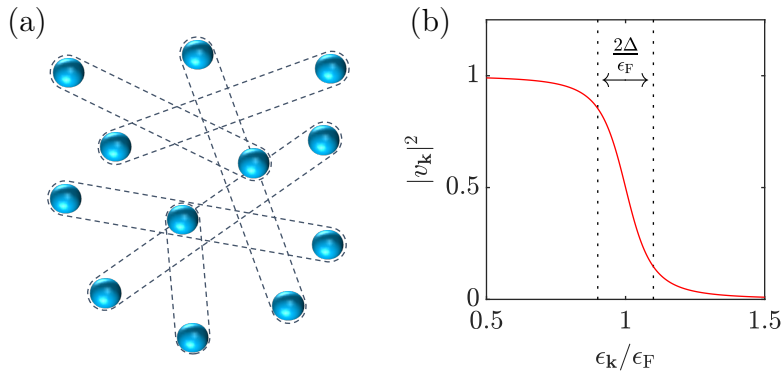
Figure 1.3: The BCS ground state. (a) Illustration of Cooper pairing in a conventional superconductor. (b) Occupation probability of pair states around the Fermi energy. In real conventional superconductors, the ratio $\Delta/\epsilon_\mathrm{F}$ is significantly smaller than in this example.

the presence of the Fermi sea enables this pairing of electrons with opposite momenta for arbitrarily weak interaction strengths.

Building on the discovery of *Cooper pairs*, Bardeen, Cooper and Schrieffer developed a theory that provides the framework of the microscopic understanding of superconductivity [17, 18]. The central ingredient of their so-called BCS theory is an attractive interaction between electrons close to the Fermi level. Due to this interaction, all the electrons are paired in the ground state and a minimal energy of 2Δ is required to break a Cooper pair. The superconducting gap Δ depends on the interaction strength. As the attractive interaction between the electrons is assumed to be isotropic and uniform in momentum space, the wavefunctions of the Cooper pairs and the superconducting gap exhibit *s*-wave symmetry. However, the total wavefunction of a Cooper pair has to be antisymmetric under particle exchange since electrons are fermions. This requires spin-singlet pairing, implying that the total spin of a Cooper pair is zero.

In second quantization, the superconducting ground state at $T = 0$ can be written as a product of pair states,

$$|\Psi\rangle = \prod_{\mathbf{k}} \left(u_{\mathbf{k}}|0\rangle_{\mathbf{k}} + v_{\mathbf{k}}|1\rangle_{\mathbf{k}}\right), \tag{1.10}$$

where $|0\rangle_{\mathbf{k}}$ denotes an empty pair state with electron momenta $(\mathbf{k}, -\mathbf{k})$ and $|1\rangle_{\mathbf{k}}$ corresponds to an occupied pair state. The probability of an occupied pair state is given by

$$|v_{\mathbf{k}}|^2 = \frac{1}{2}\left(1 - \frac{\epsilon_{\mathbf{k}} - \epsilon_{\mathrm{F}}}{\sqrt{(\epsilon_{\mathbf{k}} - \epsilon_{\mathrm{F}})^2 + \Delta^2}}\right), \tag{1.11}$$

with $\epsilon_{\mathbf{k}} = \hbar^2|\mathbf{k}|^2/2m$. As shown in Fig. 1.3(b), the electron distribution is smeared out around the Fermi energy. The probability of an empty pair state is $|u_{\mathbf{k}}|^2 = 1 - |v_{\mathbf{k}}|^2$. At nonzero temperature, there are also unpaired electrons, which we refer to as *quasiparticles*. With increasing temperature, an increasing fraction of Cooper pairs is broken and the superconducting gap decreases. The gap vanishes at T_c, consistent with a second-order phase transition.

In conventional superconductors, such as aluminium and niobium, the attraction between electrons close to the Fermi level is provided by an effective interaction via the

ionic lattice [19, 20]. As one electron moves through the lattice, it causes a positively charged ion cloud in its wake such that a second electron is attracted to it. Due to the relatively slow formation of the ion cloud, the typical distance between two bound electrons is $\xi_0 \sim 1\,\mu m$ [1, 4]. The screening of the Coulomb repulsion by the electron gas is very effective on these length scales, enabling a net attraction between the electrons. The large size of the Cooper pairs implies that many of them overlap in space as depicted in Fig. 1.3(a).

In general, experimental studies of conventional superconductors show good agreement with the predictions of the BCS theory. The existence of Cooper pairs was demonstrated by measurements of the magnetic flux quantum [21,22]. A phonon-mediated pairing mechanism is experimentally supported by the observation of the isotope effect [23,24]. Further experimental evidence for the validity of the BCS theory includes measurements of the superconducting gap and its temperature dependence [25–30]. We note that corrections of the original BCS theory must be taken into account for materials with strong electron-phonon coupling [31]. Most conventional superconductors are type-I superconductors and have critical temperatures below 10 K. At its critical temperature, a conventional superconductor enters a metallic state.

Unconventional superconductors cannot be described by the BCS theory. Some of these materials have significantly higher critical temperatures than conventional superconductors and exhibit anisotropic gap symmetries. As an example we mention cuprate superconductors, which will be introduced in Section 1.5. An overview of superconducting materials and their properties is given in Refs. [3,4], for example.

1.3   Ginzburg-Landau theory

The microscopic theory outlined in the previous section motivates a low-energy description of superconductors in terms of a condensate of charged bosons. Such a description is provided by the Ginzburg-Landau theory [32]. Following Landau's theory of second-order phase transitions [33], the superconducting state is represented by a complex order parameter $\psi(\mathbf{r})$ in the Ginzburg-Landau theory. The order parameter is assumed to vary slowly in space and to be small at temperatures near T_c. The free energy of a superconductor is then expanded in powers of $|\psi|^2$. Including the magnetic field energy and a gradient term with a gauge-invariant coupling to the electromagnetic field, the free energy density takes the form

$$\mathcal{F} = -\alpha|\psi|^2 + \frac{\beta}{2}|\psi|^4 + \frac{1}{2m^*}\left|(-i\hbar\boldsymbol{\nabla} - q\mathbf{A})\psi\right|^2 + \frac{|\mathbf{B}|^2}{2\mu_0}, \tag{1.12}$$

where α and β are real-valued expansion coefficients. As usual, the magnetic flux density is given by the curl of the vector potential, i.e., $\mathbf{B} = \boldsymbol{\nabla} \times \mathbf{A}$.

Although superconductivity was not understood microscopically at the time, Ginzburg and Landau already interpreted $\psi(\mathbf{r})$ as a macroscopic wavefunction of superconducting charge carriers. Based on the BCS theory, we consider $\psi(\mathbf{r})$ as the wavefunction of the Cooper pairs, describing the center-of-mass motion of bosons with effective mass $m^* = 2m$ and charge $q = -2e$. Note that the density of superconducting electrons is twice the density of Cooper pairs, i.e., $n_s(\mathbf{r}) = 2|\psi(\mathbf{r})|^2$.

Minimizing the free energy with respect to ψ^* and $\mathbf{A}$ leads to the Ginzburg-Landau equations

$$-\alpha\psi + \beta|\psi|^2\psi + \frac{1}{2m^*}\left(-i\hbar\boldsymbol{\nabla} + 2e\mathbf{A}\right)^2\psi = 0, \tag{1.13}$$

$$\boldsymbol{\nabla}\times\mathbf{B} - \frac{i\hbar e\mu_0}{m^*}\left(\psi^*\boldsymbol{\nabla}\psi - \psi\boldsymbol{\nabla}\psi^*\right) + \frac{4e^2\mu_0}{m^*}|\psi|^2\mathbf{A} = 0. \tag{1.14}$$

In the absence of magnetic fields, the minimum of the free energy corresponds to a spatially homogeneous configuration of the order parameter in the bulk. The order parameter has a magnitude of $|\psi_0| = \sqrt{\alpha/\beta}$ for $\alpha > 0$, while it vanishes for $\alpha \leq 0$. The phase transition is well captured by taking the temperature dependence of α as $\alpha = \alpha_0(1 - T/T_c)$ with $\alpha_0 > 0$ and keeping the other Ginzburg-Landau coefficient $\beta > 0$ temperature-independent [2].

Next, we consider a superconductor that occupies the half space $x > 0$ and suppose the magnetic field to be zero. In this case, the order parameter varies only along the x axis. It vanishes at the surface, $\psi(0) = 0$, and its magnitude approaches $|\psi_0|$ for large x. We choose the unitary gauge such that $\psi(x)$ is real-valued. Equation (1.13) then simplifies to

$$\alpha\psi + \beta\psi^3 - \frac{\hbar^2}{2m^*}\partial_x^2\psi = 0. \tag{1.15}$$

The solution of this equation,

$$\psi(x) = |\psi_0|\tanh\left(\frac{x}{\sqrt{2}\xi}\right), \tag{1.16}$$

describes the relaxation of the order parameter to its bulk value $|\psi_0|$. The rise of ψ from the surface is characterized by the Ginzburg-Landau coherence length

$$\xi = \frac{\hbar}{\sqrt{2m^*\alpha}}. \tag{1.17}$$

Remarkably, the ratio of the coherence length to the London penetration depth

$$\lambda = \sqrt{\frac{m}{\mu_0 n_s e^2}} = \sqrt{\frac{m^*}{4\mu_0|\psi_0|^2 e^2}}. \tag{1.18}$$

determines the response to magnetic fields. Type-I superconductors have a ratio of $\lambda/\xi < 1/\sqrt{2}$, while type-II superconductors have a ratio of $\lambda/\xi > 1/\sqrt{2}$.

The second Ginzburg-Landau equation (1.14) can be rewritten in the form of the Maxwell equation $\boldsymbol{\nabla}\times\mathbf{B} = \mu_0\mathbf{J}$ by identifying the current with

$$\mathbf{J} = \frac{i\hbar e}{m^*}\left(\psi^*\boldsymbol{\nabla}\psi - \psi\boldsymbol{\nabla}\psi^*\right) - \frac{4e^2}{m^*}|\psi|^2\mathbf{A}. \tag{1.19}$$

Now, we revisit the response of a superconductor to small electromagnetic fields, assuming a spatially homogeneous ground state $\psi(\mathbf{r}) = \psi_0$. Thus, we obtain a simplified expression for the current,

$$\mathbf{J} = -\frac{4e^2}{m^*}|\psi_0|^2\mathbf{A}. \tag{1.20}$$

Employing the temporal gauge, where $\mathbf{E} = -\partial_t \mathbf{A}$, we immediately recover the London equations

$$\partial_t \mathbf{J} = \frac{1}{\mu_0 \lambda^2} \mathbf{E}, \tag{1.21}$$

$$\boldsymbol{\nabla} \times \mathbf{J} = -\frac{1}{\mu_0 \lambda^2} \mathbf{B}. \tag{1.22}$$

Hence, the condensation of electrons into a macroscopic quantum state of bosonic pairs enables perfect conductivity and the Meissner effect.

Before concluding this section, we comment on the range of validity of the Ginzburg-Landau theory. In fact, Lev Gor'kov rigorously derived the Ginzburg-Landau theory from the BCS theory for temperatures near T_c [34]. He showed that the superconducting order parameter is identical to the superconducting gap in this limit. While this identity holds only near the phase transition, the Ginzburg-Landau theory is widely used also at lower temperatures. It has been argued that the effect of including higher order terms in the expansion of the free energy is rather quantitative than qualitative [5]. The Ginzburg-Landau theory is particularly useful to study superconductors for which no microscopic theory has been established. A general requirement for its validity is that ψ and $\mathbf{A}$ vary on length scales that are significantly larger than the size of a Cooper pair, i.e., $\xi, \lambda \gg \xi_0$. At temperatures far below T_c, the coherence length ξ is similar to ξ_0. However, it grows with increasing temperature and diverges at T_c. Therefore, the condition $\xi \gg \xi_0$ is usually fulfilled over a large temperature range. While the London penetration depth also diverges at T_c, its low-temperature value is smaller than ξ_0 in most conventional superconductors. For example, aluminium has a penetration depth of $\lambda \approx 0.01\,\xi_0$ at low temperatures [1]. In such a material, the condition $\lambda \gg \xi_0$ is fulfilled only close to the critical temperature. In many cuprate superconductors, on the other hand, the Cooper pairs are so small that the condition $\lambda \gg \xi_0$ is fulfilled at any temperature below T_c.

1.4 Josephson effect

The Josephson effect is a consequence of the macroscopic wavefunction of a superconductor. It enables a supercurrent between two superconducting leads that are separated by a thin insulating barrier [35, 36]. The setup of a Josephson junction is depicted in Fig. 1.4. Here, we consider two identical superconducting leads with volume $\mathcal{V}_0$ and Cooper pair density n_0 in equilibrium. Both superconductors are represented by spatially uniform wavefunctions of the form $\psi_j = \sqrt{n_j} \exp(i\theta_j)$. If the barrier thickness d is sufficiently small (a typical value is $d \sim 2$ nm), the wavefunctions of the superconductors overlap, enabling Cooper pairs to hop from one lead to the other. The strength of this coupling is characterized by the tunneling energy t_{J}. Including a voltage difference V between the two sites, the Schrödinger equations for the two wavefunctions read

$$i\hbar\partial_t \psi_1 = eV\psi_1 + t_{\mathrm{J}}\psi_2, \tag{1.23}$$
$$i\hbar\partial_t \psi_2 = -eV\psi_2 + t_{\mathrm{J}}\psi_1. \tag{1.24}$$

For small density variations, we find

$$\partial_t n_1 = \frac{2t_{\mathrm{J}} n_0}{\hbar} \sin(\theta_2 - \theta_1) = -\partial_t n_2, \tag{1.25}$$
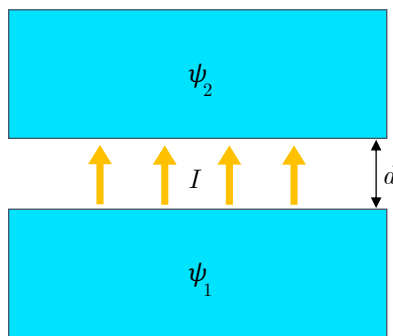
Figure 1.4: Setup of a Josephson junction. Two superconducting leads with wavefunctions ψ_1 and ψ_2 are separated by a thin insulating barrier. The overlap of the wavefunctions inside the barrier enables a supercurrent between the superconducting leads.

implying the Josephson current

$$I_{\mathrm{J}} = I_0 \sin \theta, \tag{1.26}$$

where $\theta = \theta_2 - \theta_1$ is the phase difference between the two superconductors and $I_0 = 4e t_{\mathrm{J}} n_0 \mathcal{V}_0 / \hbar$ is the critical current. Equation (1.26) is known as the first Josephson relation. The second Josephson relation describes the time evolution of the phase difference,

$$\partial_t \theta = \frac{2eV}{\hbar}. \tag{1.27}$$

To clarify the meaning of the Josephson relations, we consider two different cases. In the first case, the Josephson junction forms a circuit with a DC current source. According to the Josephson relations, the voltage is zero for DC currents below the critical current I_0. The current source also ensures the validity of the Josephson relations as it keeps the density of Cooper pairs in both superconducting leads constant. In the second case, the Josephson junction forms a circuit with a DC voltage source. The phase difference then grows linearly with time, leading to an AC Josephson current with the frequency $\omega = 2eV/\hbar$.

A realistic treatment of a Josephson junction is provided by the RCSJ (resistively and capacitively shunted junction) model [37–39]. It takes capacitive and resistive contributions to the total junction current I into account. The capacitive contribution is given by $I_{\mathrm{C}} = C \partial_t V$ with the junction capacitance C, and the resistive contribution is taken as $I_{\mathrm{R}} = V/R$ with the ohmic resistance R. Using the second Josephson relation, we obtain the following equation of motion for the phase difference,

$$\partial_t^2 \theta + \gamma \partial_t \theta + \omega_{\mathrm{J}}^2 \sin \theta = \frac{2eI}{\hbar C}, \tag{1.28}$$

where $\gamma = 1/RC$ and $\omega_{\mathrm{J}} = \sqrt{2eI_0/\hbar C}$. We see that plasma oscillations in a Josephson junction are described by a damped nonlinear oscillator, which can be driven by applying a current.

1.5   Cuprate superconductors

Cuprate superconductors are a family of high-temperature superconductors. Their crystal structure is characterized by copper oxide layers, which play a central role for the emergence of superconductivity in these materials. While the critical temperature of a conventional superconductor is usually below 10 K, values above 130 K have been reported for cuprate superconductors [40, 41]. The first cuprate superconductor was discovered by Bednorz and Müller in 1986 [42]. Strikingly, they observed critical temperatures in the range of 30 K for various $La_{2-x}Ba_xCuO_4$ (LBCO) samples. One year later, the material $YBa_2Cu_3O_{6+x}$ (YBCO) was reported to exhibit superconductivity at temperatures up to 93 K for values of x slightly below 1 [43]. Today, one knows about many cuprate superconductors with critical temperatures of $T_c \sim 100$ K at ambient pressure, which can be reached by cooling with liquid nitrogen.

Cuprates do not occur in nature but are synthesized in elaborate processes as described in Ref. [6], for instance. They consist of CuO_2 layers, separated by layers of charge reservoir groups and spacer atoms in the case of multilayer cuprates. The spacer atoms are alkaline earth or rare earth elements. As an example we consider the crystal structure of the bilayer cuprate $YBa_2Cu_3O_7$, depicted in Fig. 1.5. Here, the spacer element is yttrium and the charge reservoir group is Ba_2CuO_3. A specific feature of YBCO is the existence of CuO chains along the b axis in the charge reservoir group, leading to an anisotropic electromagnetic response in the ab plane [44, 45].

The parent compound of a cuprate superconductor, corresponding to $x = 0$ for LBCO and YBCO, is a Mott insulator at sufficiently low temperatures. This means that there is exactly one localized electron per CuO_2 unit and the spin configuration is antiferromagnetic. As x is increased, holes are injected into the material. In the following, we use the hole doping p to specify the number of holes injected into each CuO_2 unit. While we
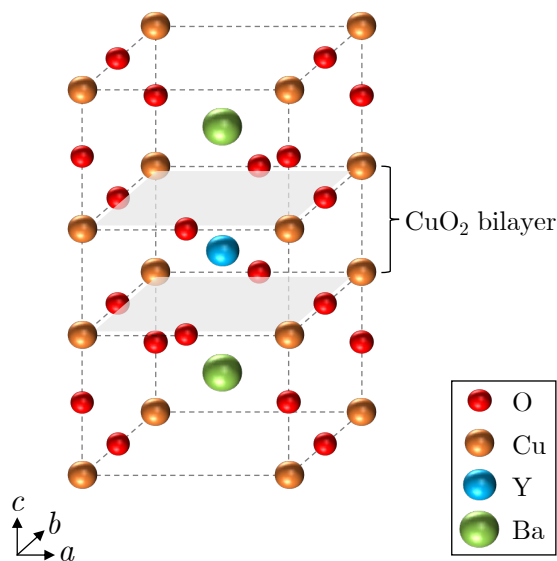

Figure 1.5: Crystal structure of $YBa_2Cu_3O_7$. The lattice parameters of the unit cell are $a_0 = 3.8$ Å, $b_0 = 3.9$ Å, and $c_0 = 11.7$ Å. The intrabilayer distance between CuO_2 layers amounts to 3.4 Å [6, 46].
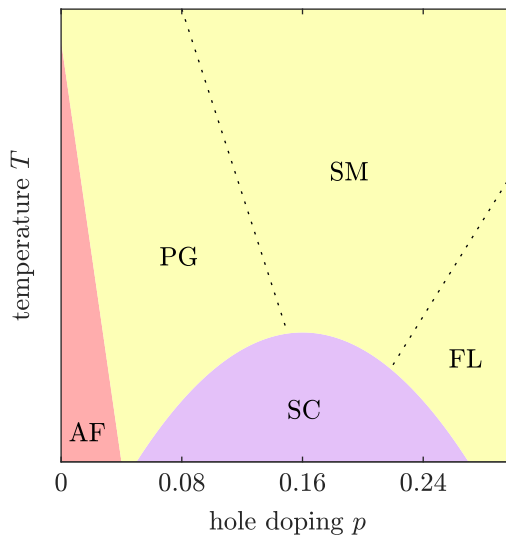
Figure 1.6: Schematic phase diagram of a typical cuprate superconductor, following Ref. [47]. At small doping, a cuprate is an insulating antiferromagnet (AF). The superconducting (SC) phase has a dome-like shape with a maximum of T_c around $p = 0.16$. The metallic phase is divided into three regimes: the pseudogap (PG) regime, the strange metal (SM) regime, and the Fermi liquid (FL) regime.

have $p \approx x$ for LBCO, there is only a phenomenological relation between the hole doping and the chemical composition in general. Remarkably, most cuprates have a similar phase diagram with respect to hole doping and temperature. The typical cuprate phase diagram is shown schematically in Fig. 1.6, based on Ref. [47]. We see that a cuprate remains an insulating antiferromagnet for small p.

The superconducting phase has a dome-like shape with a maximum of T_c for an optimal doping of $p \approx 0.16$. Cuprates with smaller p are *underdoped* and cuprates with larger p are *overdoped*. Measurements of the magnetic flux quantum show that the superconducting state in the cuprates is formed by electron pairs [48]. In contrast to conventional superconductors, the superconducting gap exhibits d-wave symmetry as demonstrated by phase-sensitive tunneling experiments [49–51] and angle-resolved photoemission spectroscopy (ARPES) [52–54]. More specifically, the superconducting gap displays $d_{x^2-y^2}$ symmetry,

$$\Delta(\mathbf{k}) \propto \big(\cos(k_x a_0) - \cos(k_y a_0)\big), \tag{1.29}$$

where a_0 denotes the lattice parameter of the (approximate) square lattice in the ab plane. The gap vanishes along the nodal lines, where $|k_x| = |k_y|$, while its absolute value reaches maxima on the antinodal lines for a given in-plane momentum k_{xy}, i.e., for $(k_x = \pm k_{xy}, k_y = 0)$ and $(k_x = 0, k_y = \pm k_{xy})$; see Refs. [55,56] for more details on the gap symmetry. An important consequence of the gap symmetry is the existence of quasiparticle excitations along the nodal lines down to very low temperatures. Besides, a gap with $d_{x^2-y^2}$ symmetry implies spin singlet pairing, which is corroborated by measurements of the Knight shift [57].

To date, the pairing mechanism in cuprate superconductors has not been identified unequivocally. Theoretical and experimental investigations indicate that Cooper pairing

in cuprate superconductors is possibly enabled by spin fluctuations [58–61]. Remarkably, a gap with $d_{x^2-y^2}$ symmetry is inherent to such a pairing mechanism [62]. On the other hand, there is also experimental evidence for the relevance of electron-phonon coupling to the emergence of superconductivity in the cuprates [63, 64].

The characteristic lengths of cuprate superconductors are very anisotropic due to their anisotropic structure. Depending on the material, the in-plane penetration depth λ_{ab} assumes a value between 1000 and 4000 Å in the zero-temperature limit [5, 65, 66]. The c-axis penetration depth λ_c is typically at least one order of magnitude larger than λ_{ab}. The coherence lengths of cuprate superconductors are found to be $\xi_{ab} \sim 30$ Å and $\xi_c \sim 2 - 3$ Å in the zero-temperature limit [5, 6, 67]. In addition to the anisotropy of the characteristic lengths, the small value of ξ_c supports the common understanding that the copper oxide layers are the primary seat of superconductivity in the cuprates. Since the coherence lengths set the scale of the Cooper pair size, we notice that the Cooper pairs in cuprate superconductors are tightly bound. Combining the determined penetrations depths with measurements of the effective electron mass, the density of Cooper pairs at $T = 0$ is estimated as $n_0 \sim (1-5) \cdot 10^{21}$ cm^{-3} [68, 69], consistent with valency calculations. Thus, the number of overlapping Cooper pairs is small, leading to pronounced fluctuation effects [2, 4, 5].

Only strongly overdoped cuprate superconductors transform into a relatively normal metallic state as the temperature is raised above T_c, corresponding to the *Fermi liquid* regime in Fig. 1.6. Optimally doped and weakly overdoped cuprates enter the so-called *strange metal* regime at higher temperatures. In this regime, the electrical conductivity is about two orders of magnitude smaller than in normal metals. Furthermore, the conductivity exhibits frequency and temperature dependencies that are incompatible with the conventional theory of metals [5, 47]. Notably, a similar behavior of the conductivity has been observed in other strongly correlated electron systems, indicating that the strange metal regime might not be directly linked to high-temperature superconductivity [47, 70]. While the phenomenology of the strange metal regime can be described by the *marginal Fermi liquid* theory [71], there exists no complete and generally accepted theory of this regime at present. We note that there is only a soft crossover between the strange metal regime and the Fermi liquid regime.

In contrast, the crossover from the strange metal regime to the *pseudogap* regime is fairly sharp, with an approximately linear dependence of the crossover temperature T^* on the doping. There are still many open questions regarding the pseudogap regime and it is possible that the pseudogap regime corresponds to a distinct phase of matter. The characteristic feature of the pseudogap regime is a strong suppression of the electronic density of states a low energies. This pseudogap was shown most clearly by tunneling experiments [72, 73] and ARPES studies [53, 54, 74–76], which also revealed that the pseudogap has a similar momentum dependence as the superconducting gap. In fact, the pseudogap smoothly evolves into the superconducting gap at T_c.

These findings suggest that the formation of electron pairs already sets in at T^*. Assuming the existence of preformed pairs, it was proposed that phase fluctuations of the superconducting order parameter cause the phase transition at T_c in underdoped cuprates [77, 78]. This scenario is consistent with the experimentally observed linear scaling of n_0 with the critical temperature [68, 69]. Related investigations of the anisotropic three-dimensional XY model indicate that vortex loop excitations play an important role
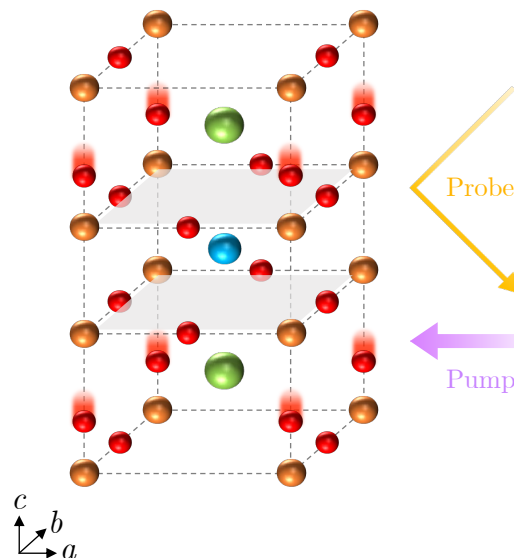
Figure 1.7: Pump-probe experiment on YBCO. The pump pulse excites oscillations of the apical oxygen atoms along the c axis. Subsequently, the sample is probed in reflection.

in the context of the phase transition [79–84], which is reminiscent of a Kosterlitz-Thouless transition in a two-dimensional Bose gas [85–88]. While optical spectroscopy and pump-probe experiments indicate fluctuating superconductivity far above T_c in the pseudogap regime [89–92], the existence of preformed pairs is still debated. Another important aspect regarding the breakdown of superconductivity in underdoped cuprates is the emergence of other orders, such as charge and spin stripes, near T_c. These intertwined orders seem to compete with superconductivity [93–96].

A modern technique for the study of cuprates and other materials with strong electronic correlations is provided by pump-probe experiments. In a pump-probe experiment, a material sample is first excited by an intense laser pulse called *pump*. The transiently excited material is then probed by a weak laser pulse called *probe*. As an example we consider a pump-probe experiment that was performed on underdoped YBCO [90,91]. In this experiment, a mid-infrared pump resonantly excited a phonon mode with a frequency of approximately 20 THz. The duration of the pump pulse was ~ 300 fs and the electric field strength reached up to $\sim 3\,\mathrm{MV\,cm^{-1}}$. The resulting oscillations of the *apical* oxygen atoms along the c axis are shown in Fig. 1.7. Using the reflected signal of a terahertz probe pulse, the c-axis optical conductivity of the sample was measured both in equilibrium and in the transiently excited state.

Below T_c, the imaginary part of the optical conductivity was significantly enhanced at small probe frequencies. Recalling the relation $\sigma_2(\omega) = n_s e^2/m\omega$ for superconductors in equilibrium, one can interpret the observed enhancement of σ_2 as an increase in the superfluid density n_s. Strikingly, an enhancement of σ_2 at low frequencies was also observed for temperatures between T_c and T^*, accompanied by the appearance of a reflectivity edge at low frequencies. These findings demonstrate light-induced coherence of interlayer transport and prompt the question whether a transient superconducting state is induced by resonantly driving specific phonon modes in underdoped YBCO. It was experimentally confirmed that only the excitation of oscillations of the apical oxygen atoms along

the c axis leads to enhanced interlayer transport with superconducting-like features [97]. Several mechanisms were proposed to explain the enhancement of interlayer transport, including nonlinear lattice dynamics [98], a redistribution of phase fluctuations [99, 100], parametric driving [101, 102], and the suppression of competing orders [103, 104]. Recent measurements of second-harmonic generation indicate that optically excited phonons decay into pairs of plasmons with opposite in-plane momenta, which give rise to spatial and temporal modulations of the superfluid density [92, 105]. This would explain the observed features in the optical response at temperatures below and above T_c if one assumes that superconducting fluctuations with sufficiently large correlation lengths preexist up to T^*.

The phenomenology presented in the previous paragraph is not limited to a single kind of experiment on underdoped YBCO. Features of a superconducting state were also induced in other cuprates by optical driving of specific phonon modes [106] or near-infrared excitation [107, 108]. Furthermore, signatures of light-induced superconductivity were reported for fullerides [109–111] and organic salts [112, 113] following excitation of molecular vibrations.

Now, we turn to the theoretical description of light-driven cuprate superconductors. To this end, the Ginzburg-Landau theory is a good starting point since it does not require any assumptions about the microscopic nature of the superconducting state in the cuprates. A natural approach to account for the layered structure of cuprate superconductors is given by the Lawrence-Doniac model [114]. Here, each copper oxide layer is described by a complex order parameter and the coupling between the layers is modeled as in Josephson junctions. Experiments on the current-voltage characteristics of cuprate superconductors indeed support a picture where superconducting layers form a stack of Josephson junctions [115]. In the superconducting state, a plasma excitation along the c axis corresponds to an oscillatory tunneling of Cooper pairs between copper oxide layers [116–119], leading to observable nonlinear effects [120–123]. The *Josephson plasma mode* with zero momentum is effectively described by the RCSJ model introduced in Section 1.4.

In the following chapter, we present a semiclassical $U(1)$ lattice gauge theory that builds on the Lawrence-Doniac model. To simulate the coupled dynamics of the superconducting order parameter and the electromagnetic field, we include time-dependent terms and discretize space in all three dimensions. Thus, the gradient terms in the ab plane also take the form of Josephson junctions. This lowest order gauge-invariant approximation of the in-plane gradient terms is justified as the discretization length is chosen to be well below the in-plane coherence length. Furthermore, our lattice gauge theory incorporates thermal fluctuations, which cause a phase transition to a fluctuating high-temperature state without global phase coherence. We highlight that our theory advances previous descriptions of driven cuprates [100, 101, 124] in two aspects. Firstly, it includes the in-plane dynamics of the order parameter and the electromagnetic field. Secondly, it allows for arbitrarily strong and phase-independent fluctuations of the amplitude of the order parameter.

Chapter 2

Semiclassical simulation method for bilayer cuprate superconductors

In this chapter, we present a semiclassical $U(1)$ lattice gauge theory developed for the simulation of fluctuating and light-induced dynamics in cuprate superconductors [H1–H3]. While our method can be utilized to simulate monolayer and bilayer cuprates, we consider only bilayer cuprates here. However, many of our considerations and results can be directly applied to monolayer cuprates.

Based on our semiclassical method, we first characterize the superconducting ground state in the absence of thermal fluctuations. Then, we investigate fluctuating dynamics at nonzero temperature. In particular, we present a scenario of the pseudogap regime in which vortex excitations play a central role. We discuss the temperature dependence of the plasma resonances and the optical conductivity. Throughout this chapter, we include analytical calculations to support our numerical results.

2.1   Lagrangian and equations of motion

Following the Ginzburg-Landau theory of superconductivity, we describe the superconducting state by a complex order parameter $\psi_{\mathbf{r}}$, which is discretized on a three-dimensional lattice with $\mathbf{r}$ denoting the position of a lattice site. Our lattice gauge model is depicted schematically in Fig. 2.1(a). The crystalline c axis is oriented along the z direction and each superconducting layer is represented by a square lattice. As the Cooper pairs carry a charge of $-2e$, the order parameter is coupled to the electromagnetic field. While the scalar potential $\Phi_{\mathbf{r}}$ is also located on the lattice sites, the vector potential $\mathbf{A}_{\mathbf{r}}$ is located on the bonds. The electric field on the bond from site $\mathbf{r}$ to its nearest neighbor $\mathbf{r}'(j)$ in the $j \in \{x, y, z\}$ direction is given by $E_{j,\mathbf{r}} = -\partial_t A_{j,\mathbf{r}} - \delta_j \Phi_{\mathbf{r}}$. We calculate the spatial derivative of the scalar potential using the finite-difference representation $\delta_j \Phi_{\mathbf{r}} = (\Phi_{\mathbf{r}'(j)} - \Phi_{\mathbf{r}})/d_{j,\mathbf{r}}$, where $d_{j,\mathbf{r}}$ is the length of the bond between the lattice sites $\mathbf{r}$ and $\mathbf{r}'(j)$. The magnetic field components $B_{j,\mathbf{r}} = \epsilon_{jkl} \delta_k A_{l,\mathbf{r}}$ are centered on the plaquettes of the lattice as shown in Fig. 2.1(b). This arrangement is consistent with the finite-difference time-domain (FDTD) method [125]. The in-plane lattice parameter $d_{x,\mathbf{r}} = d_{y,\mathbf{r}} = d_{ab}$ is introduced as a short-range cutoff that is small compared to the in-plane coherence length. The interlayer spacing $d_{z,\mathbf{r}}$ alternates between the intrabilayer distance d_s and the interbilayer distance d_w, reproducing the spacing of CuO_2 planes in the crystal.
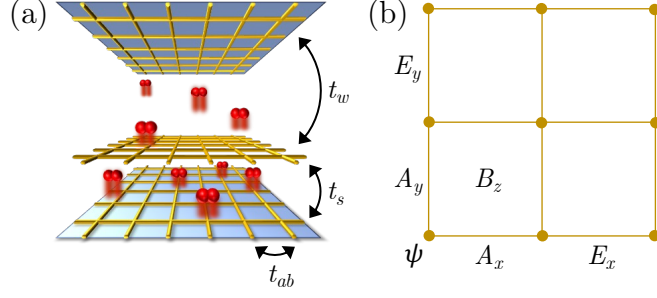
Figure 2.1: Schematic depiction of the lattice gauge model. (a) Cooper pairs tunnel between neighboring lattice sites on an anisotropic lattice. (b) Spatial configuration of the superconducting order parameter and the electromagnetic field in the xy plane. The order parameter is located on the lattice sites. The electromagnetic vector potential is located on the bonds, defining the magnetic field on the lattice plaquettes. The electric field is also located on the bonds. Panel (a) is adapted from Ref. [H5].

The Lagrangian of the lattice gauge model is

$$
\begin{aligned}
\mathcal{L} = & \sum_{\mathbf{r}} K |(\hbar \partial_t - 2ie\Phi_{\mathbf{r}})\psi_{\mathbf{r}}|^2 + \mu|\psi_{\mathbf{r}}|^2 - \frac{g}{2}|\psi_{\mathbf{r}}|^4 - \sum_{j,\mathbf{r}} t_{j,\mathbf{r}} |\psi_{\mathbf{r}'(j)} - \psi_{\mathbf{r}} e^{ia_{j,\mathbf{r}}}|^2 \\
& + \sum_{j,\mathbf{r}} \frac{\kappa_{j,\mathbf{r}} \epsilon_{\infty} \epsilon_0}{2} E_{j,\mathbf{r}}^2 - \frac{\kappa_{z,\mathbf{r}}}{\kappa_{j,\mathbf{r}} \beta_{j,\mathbf{r}}^2 \mu_0} \Big[1 - \cos\big(\beta_{j,\mathbf{r}} B_{j,\mathbf{r}}\big)\Big].
\end{aligned}
\tag{2.1}
$$

The Ginzburg-Landau coefficients μ and g are taken as temperature-independent throughout this work. The coefficient K describes the magnitude of the dynamical term. The physical meaning of these coefficients will be explained in the following section. The second sum in the Lagrangian (2.1) represents the kinetic energy of the superconducting condensate. As mentioned, the gradient terms from the Ginzburg-Landau theory take the form of Josephson junctions, corresponding to nearest-neighbor tunneling of Cooper pairs. The unitless vector potential $a_{j,\mathbf{r}} = -2ed_{j,\mathbf{r}}A_{j,\mathbf{r}}/\hbar$ couples to the phase of the order parameter, ensuring local gauge-invariance. The tunneling coefficients are $t_{x,\mathbf{r}} = t_{y,\mathbf{r}} = t_{ab}$ for in-plane junctions, $t_{z,\mathbf{r}} = t_s$ for intrabilayer (strong) junctions, and $t_{z,\mathbf{r}} = t_w$ for interbilayer (weak) junctions. The structure of a bilayer cuprate implies the hierarchy $t_w \ll t_s \ll t_{ab}$. The third sum is the Lagrangian of the electromagnetic field on an anisotropic lattice, formulated as a compact lattice gauge theory in the time-continuum limit [126]. The background dielectric constant ϵ_{∞} originates from bound charges. The other prefactors in the electromagnetic Lagrangian reflect the anisotropic lattice geometry. Introducing $d_c = (d_s + d_w)/2$, we write $\kappa_{x,\mathbf{r}} = \kappa_{y,\mathbf{r}} = 1$ and $\kappa_{z,\mathbf{r}} = d_{z,\mathbf{r}}/d_c$, while $\beta_{x,\mathbf{r}} = \beta_{y,\mathbf{r}} = 2ed_{ab}d_{z,\mathbf{r}}/\hbar$ and $\beta_{z,\mathbf{r}} = 2ed_{ab}^2/\hbar$.

The Lagrangian (2.1) is particle-hole symmetric due to its invariance under the simultaneous transformations $\psi_{\mathbf{r}} \to \psi_{\mathbf{r}}^*$ and $e \to -e$. Next, we derive the Euler-Lagrange equations from the Lagrangian. The equation of motion for the order parameter reads

$$
\begin{aligned}
& K\hbar^2 \partial_t^2 \psi_{\mathbf{r}} - 4ieK\hbar\Phi_{\mathbf{r}}\partial_t\psi_{\mathbf{r}} - (4e^2 K\Phi_{\mathbf{r}}^2 + 2ieK\hbar\partial_t\Phi_{\mathbf{r}})\psi_{\mathbf{r}} \\
& = (\mu - 4t_{ab} - t_s - t_w)\psi_{\mathbf{r}} - g|\psi_{\mathbf{r}}|^2\psi_{\mathbf{r}} + \sum_j \big(t_{j,\mathbf{r}''(j)}\psi_{\mathbf{r}''(j)}e^{ia_{j,\mathbf{r}''(j)}} + t_{j,\mathbf{r}}\psi_{\mathbf{r}'(j)}e^{-ia_{j,\mathbf{r}}} \big),
\end{aligned}
\tag{2.2}
$$

where $\mathbf{r}''(j)$ denotes the neighboring site of $\mathbf{r}$ in the $-j$ direction. The Euler-Lagrange equations with respect to $\Phi_{\mathbf{r}}$ and $\mathbf{A}_{\mathbf{r}}$ correspond to the inhomogeneous Maxwell equations on an anisotropic lattice,

$$\epsilon_{\infty}\epsilon_0 \sum_j \overline{\delta}_j E_{j,\mathbf{r}} = -2ieK\hbar\left(\psi_{\mathbf{r}}^*\partial_t\psi_{\mathbf{r}} - \text{c.c.}\right) - 8e^2K\Phi_{\mathbf{r}}|\psi_{\mathbf{r}}|^2, \tag{2.3}$$

$$\epsilon_{\infty}\epsilon_0 \partial_t E_{j,\mathbf{r}} = -\frac{2et_{j,\mathbf{r}}d_j}{i\hbar}\left(\psi_{\mathbf{r}'(j)}^*\psi_{\mathbf{r}}e^{ia_{j,\mathbf{r}}} - \text{c.c.}\right) + \epsilon_{jkl}\overline{\delta}_k \frac{\sin(\beta_{l,\mathbf{r}}B_{l,\mathbf{r}})}{\beta_{l,\mathbf{r}}\mu_0}, \tag{2.4}$$

where $d_x = d_y = d_{ab}$ and $d_z = d_c$. The backward-difference operator $\overline{\delta}_j$ acts on a discretized field $f_{\mathbf{r}}$ as $\overline{\delta}_j f_{\mathbf{r}} = (f_{\mathbf{r}} - f_{\mathbf{r}''(j)})/d_{j,\mathbf{r}}$. Based on Eqs. (2.3) and (2.4), we identify the charge density with

$$\rho_{\mathbf{r}} = -2ieK\hbar\left(\psi_{\mathbf{r}}^*\partial_t\psi_{\mathbf{r}} - \text{c.c.}\right) - 8e^2K\Phi_{\mathbf{r}}|\psi_{\mathbf{r}}|^2, \tag{2.5}$$

and the supercurrent density with

$$J_{j,\mathbf{r}} = \frac{2et_{j,\mathbf{r}}d_j}{i\hbar}\left(\psi_{\mathbf{r}'(j)}^*\psi_{\mathbf{r}}e^{ia_{j,\mathbf{r}}} - \text{c.c.}\right). \tag{2.6}$$

Multiplying Eq. (2.2) by $\psi_{\mathbf{r}}^*$ and then subtracting the complex conjugate, we find the continuity equation

$$\partial_t\rho_{\mathbf{r}} + \sum_j \overline{\delta}_j J_{j,\mathbf{r}} = 0. \tag{2.7}$$

We see that the electric charge is conserved in our model.

In our simulations and the remainder of this work, we use the temporal gauge $\Phi_{\mathbf{r}} \equiv 0$ such that the Lagrangian reduces to

$$\begin{aligned} \mathcal{L} = &\sum_{\mathbf{r}} K\hbar|\partial_t\psi_{\mathbf{r}}|^2 + \mu|\psi_{\mathbf{r}}|^2 - \frac{g}{2}|\psi_{\mathbf{r}}|^4 - \sum_{j,\mathbf{r}} t_{j,\mathbf{r}}|\psi_{\mathbf{r}'(j)} - \psi_{\mathbf{r}}e^{ia_{j,\mathbf{r}}}|^2 \\ &+ \sum_{j,\mathbf{r}} \frac{\kappa_{j,\mathbf{r}}\epsilon_{\infty}\epsilon_0}{2}E_{j,\mathbf{r}}^2 - \frac{\kappa_{z,\mathbf{r}}}{\kappa_{j,\mathbf{r}}\beta_{j,\mathbf{r}}^2\mu_0}\left[1 - \cos\left(\beta_{j,\mathbf{r}}B_{j,\mathbf{r}}\right)\right]. \end{aligned} \tag{2.8}$$

The equation of motion for the order parameter simplifies to

$$K\hbar^2\partial_t^2\psi_{\mathbf{r}} = (\mu - 4t_{ab} - t_s - t_w)\psi_{\mathbf{r}} - g|\psi_{\mathbf{r}}|^2\psi_{\mathbf{r}} + \sum_j \left(t_{j,\mathbf{r}''(j)}\psi_{\mathbf{r}''(j)}e^{ia_{j,\mathbf{r}''(j)}} + t_{j,\mathbf{r}}\psi_{\mathbf{r}'(j)}e^{-ia_{j,\mathbf{r}}}\right), \tag{2.9}$$

and the expression for the charge density simplifies to

$$\rho_{\mathbf{r}} = -2ieK\hbar\left(\psi_{\mathbf{r}}^*\partial_t\psi_{\mathbf{r}} - \text{c.c.}\right). \tag{2.10}$$

Furthermore, we add Langevin noise and damping terms to the equations of motions, which can be written in the form

$$\partial_t^2\psi_{\mathbf{r}} = \frac{1}{K\hbar^2}\frac{\partial\mathcal{L}}{\partial\psi_{\mathbf{r}}^*} - \gamma_{\text{sc}}\partial_t\psi_{\mathbf{r}} + \xi_{\mathbf{r}}, \tag{2.11}$$

$$\partial_t^2 A_{j,\mathbf{r}} = \frac{1}{\epsilon_{\infty}\epsilon_0}\frac{\partial\mathcal{L}}{\partial A_{j,\mathbf{r}}} - \gamma_{j,\mathbf{r}}\partial_t A_{j,\mathbf{r}} + \eta_{j,\mathbf{r}}. \tag{2.12}$$

Here, γ_{sc} and $\gamma_{j,\mathbf{r}}$ are phenomenological damping constants of the superconducting order parameter and the vector potential, respectively. The damping constants of the vector potential are $\gamma_{x,\mathbf{r}} = \gamma_{y,\mathbf{r}} = \gamma_{ab}$ for in-plane junctions, $\gamma_{z,\mathbf{r}} = \gamma_s$ for intrabilayer junctions, and $\gamma_{z,\mathbf{r}} = \gamma_w$ for interbilayer junctions. The Langevin noise terms $\xi_{\mathbf{r}}$ and $\boldsymbol{\eta}_{\mathbf{r}}$ are temporally uncorrelated and follow a Gaussian distribution with zero mean, representing thermal fluctuations. We employ periodic boundary conditions and integrate the stochastic differential equations using Heun's method. Details on the numerical implementation can be found in Appendix A, where we also present the equations of motion and the noise terms in more depth. In the temporal gauge, Gauss's law is not implied by the Euler-Lagrange equations. However, it has to be fulfilled and constitutes an additional constraint on the solutions.

2.2 Ground state at zero temperature

The ground state of the Lagrangian (2.8) in the temporal gauge is defined by the static solution of Eqs. (2.11) and (2.12),

$$\frac{\partial \mathcal{L}}{\partial \psi_{\mathbf{r}}^*} = 0, \quad \frac{\partial \mathcal{L}}{\partial A_{j,\mathbf{r}}} = 0 \text{ for } j \in \{x, y, z\}. \tag{2.13}$$

Note that the noise terms vanish at zero temperature. The conditions in Eq. (2.13) ensure that the free energy of the superconducting state is minimized. This is achieved for the spatially homogeneous configuration

$$\psi_{\mathbf{r}} \equiv \psi_0 = \sqrt{\mu/g}, \quad \mathbf{A}_{\mathbf{r}} \equiv 0. \tag{2.14}$$

Making this choice, we completely fix the gauge of the order parameter and the electromagnetic field. In the following, we characterize the ground state in Eq. (2.14) at zero temperature.

2.2.1 Collective excitations

It is instructive to consider a spatially homogeneous condensate of uncharged bosons first. The free energy of the condensate depends only on the order parameter ψ,

$$\mathcal{F} = -\mu|\psi|^2 + \frac{g}{2}|\psi|^4. \tag{2.15}$$

As visualized in Fig. 2.2, the free energy has the shape of a Mexican hat, with a continuum of ground states on its brim. Upon formation of the condensate, the order parameter spontaneously picks a phase such that the $U(1)$ symmetry is broken. There are two elementary collective excitations from the ground state, indicated by the arrows in Fig. 2.2. The *Higgs mode* corresponds to amplitude oscillations of the order parameter, and the *Goldstone mode* corresponds to phase oscillations. The Higgs mode is gapped due to the slope of the Mexican hat potential in the radial directions. Phases oscillations, on the other hand, cost a vanishing amount of energy. Therefore, the Goldstone mode is not gapped. In the case of a charged condensate, however, the phase couples to the electromagnetic vector potential. The arising plasma modes are gapped because of the
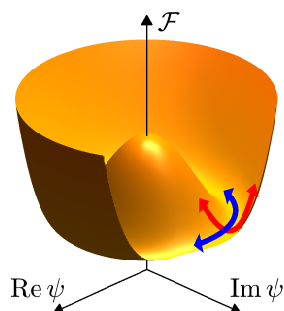
Figure 2.2: Free energy of a an uncharged condensate. The Higgs mode corresponds to amplitude oscillations (red arrow) of the order parameter, and the Goldstone mode corresponds to phase oscillations (blue arrow). This figure is adapted from Ref. [H1].

long-range Coulomb interaction between the charged particles. This is known as the *Anderson-Higgs mechanism* [127–130].

Starting from the ground state in Eq. (2.14), we write a spatially homogeneous excitation of the Higgs mode as $\psi_{\mathbf{r}} \equiv \psi_0(1+h)$. We assume that $h \ll 1$ and linearize Eq. (2.11), leading to the equation of motion

$$\partial_t^2 h + \gamma_{\mathrm{sc}}\partial_t h + \omega_{\mathrm{H}}^2 h = 0. \tag{2.16}$$

The Higgs frequency at zero momentum is $\omega_{\mathrm{H}} = \sqrt{2\mu/K\hbar^2}$. The Higgs frequency of a d-wave superconductor is approximated by twice the maximal superconducting gap [131]. In our idealized scenario, Higgs oscillations occur in the absence of any electromagnetic field. There are two experimental methods to excite the Higgs mode. Firstly, one quenches μ by suddenly heating up a superconductor with an intense laser pulse. Secondly, one continuously drives a superconductor with a laser operating at terahertz frequencies. The nonlinear coupling of the electromagnetic field to the Higgs mode and possible applications will be discussed in Sections 3.1–3.3. Both methods have been utilized to detect the Higgs mode in conventional superconductors and in cuprates [132–139].

We continue with a spatially homogeneous excitation of the in-plane vector potential, i.e., $A_{x,\mathbf{r}} \equiv A_x$. The corresponding electric field $E_x = -\partial_t A_x$ is polarized along the x axis, while the magnetic field is zero. As the order parameter is spatially homogeneous, the gauge-invariant phase along the x-axis junctions is $\theta_x = -2edA_x/\hbar$, corresponding to the Josephson relation $\partial_t\theta_x = 2ed_{ab}E_x/\hbar$. We assume that $|\theta_x| \ll 1$ and neglect variations of the amplitude of the order parameter. The dynamics then reduces to one equation of motion,

$$\epsilon_\infty\epsilon_0\partial_t^2 A_x + \gamma_{ab}\partial_t A_x - J_x = 0, \tag{2.17}$$

with the current J_x depending on θ_x. Using Eq. (2.6) and linearizing in θ_x, we can rewrite Eq. (2.17) as

$$\partial_t^2\theta_x + \gamma_{ab}\partial_t\theta_x + \omega_{ab}^2\theta_x = 0, \tag{2.18}$$

which describes damped in-plane plasma oscillations with zero momentum. The in-plane plasma frequency is

$$\omega_{ab} = \sqrt{\frac{8t_{ab}|\psi_0|^2 e^2 d_{ab}^2}{\epsilon_\infty\epsilon_0\hbar^2}}. \tag{2.19}$$

Next, we consider plasma excitations along the z axis. Consistent with the literature, we refer to these excitations as *Josephson plasma modes*. At zero momentum, all the intrabilayer junctions are characterized by the uniform gauge-invariant phase difference $\theta_s = a_s + \varphi_\downarrow - \varphi_\uparrow$, and all the interbilayer junctions are characterized by the uniform gauge-invariant phase difference $\theta_w = a_w + \varphi_\uparrow - \varphi_\downarrow$. Here, a_s and a_w denote the unitless vector potential along intra- and interbilayer junctions, respectively. The argument of $\psi_{\mathbf{r}}$ is $\varphi_\downarrow$ in the lower layer of each bilayer and $\varphi_\uparrow$ in the upper layer of each bilayer. According to Eq. (2.10), variations of $\varphi_\downarrow$ and $\varphi_\uparrow$ correspond to charge fluctuations,

$$\rho_{\downarrow,\uparrow} = 4eK\hbar|\psi_0|^2\partial_t\varphi_{\downarrow,\uparrow}. \tag{2.20}$$

Combining this relation with the continuity equation (2.7), we obtain

$$\partial_t^2\varphi_\downarrow = \frac{J_w - J_s}{4eK\hbar|\psi_0|^2} = -\partial_t^2\varphi_\uparrow. \tag{2.21}$$

In the following, we assume $\gamma_{\mathrm{sc}} = \gamma_s = \gamma_w \equiv \gamma$ and small plasma excitations. Including dissipation, the equations of motion for the on-site phases read

$$\partial_t^2\varphi_\downarrow + \gamma\partial_t\varphi_\downarrow + \frac{J_s - J_w}{4eK\hbar|\psi_0|^2} = 0, \tag{2.22}$$

$$\partial_t^2\varphi_\uparrow + \gamma\partial_t\varphi_\uparrow + \frac{J_w - J_s}{4eK\hbar|\psi_0|^2} = 0. \tag{2.23}$$

The unitless vector potential follows the equations

$$\partial_t^2 a_s + \gamma\partial_t a_s + \frac{2ed_s}{\epsilon_\infty\epsilon_0\hbar}J_s = 0, \tag{2.24}$$

$$\partial_t^2 a_w + \gamma\partial_t a_w + \frac{2ed_w}{\epsilon_\infty\epsilon_0\hbar}J_w = 0. \tag{2.25}$$

Thus, we find the linearized equations of motion

$$\partial_t^2\theta_s + \gamma\partial_t\theta_s + (1 + 2\alpha_s)\Omega_s^2\theta_s - 2\alpha_w\Omega_w^2\theta_w = 0, \tag{2.26}$$
$$\partial_t^2\theta_w + \gamma\partial_t\theta_w + (1 + 2\alpha_w)\Omega_w^2\theta_w - 2\alpha_s\Omega_s^2\theta_s = 0, \tag{2.27}$$

where

$$\Omega_{s,w} = \sqrt{\frac{8t_{s,w}|\psi_0|^2e^2d_cd_{s,w}}{\epsilon_\infty\epsilon_0\hbar^2}} \tag{2.28}$$

are the bare plasma frequencies of the interlayer junctions. The capacitive coupling constants

$$\alpha_{s,w} = \frac{\epsilon_\infty\epsilon_0}{8K|\psi_0|^2e^2d_cd_{s,w}} \tag{2.29}$$

are of the order of 1 in cuprate superconductors [124, 140, 141]. To decouple the equations of motions, we write the gauge-invariant interlayer phase differences in terms of new variables θ_1 and θ_2,

$$\theta_s = 2\alpha_w(\theta_1 + \theta_2), \tag{2.30}$$

$$\begin{aligned}\theta_w = &\left[\left(\frac{1}{2} + \alpha_s\right)\Omega_s^2 - \left(\frac{1}{2} + \alpha_w\right)\Omega_w^2 + W\right]\frac{\theta_1}{\Omega_w^2} \\ &+ \left[\left(\frac{1}{2} + \alpha_s\right)\Omega_s^2 - \left(\frac{1}{2} + \alpha_w\right)\Omega_w^2 - W\right]\frac{\theta_2}{\Omega_w^2},\end{aligned} \tag{2.31}$$
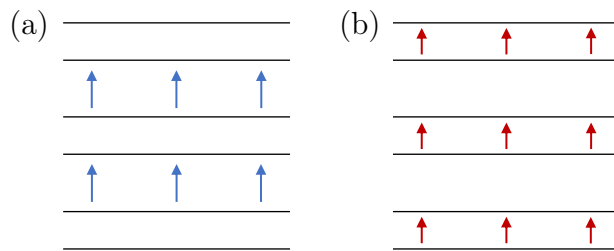
Figure 2.3: Sketch of the interlayer currents during excitation of the lower and upper Josephson plasma mode, respectively. (a) Interbilayer currents dominate in the case of the lower Josephson plasma mode. (b) Intrabilayer currents dominate in the case of the upper Josephson plasma mode.

where

$$W = \sqrt{\left[\left(\frac{1}{2}+\alpha_s\right)\Omega_s^2 - \left(\frac{1}{2}+\alpha_w\right)\Omega_w^2\right]^2 + 4\alpha_s\alpha_w\Omega_s^2\Omega_w^2}. \tag{2.32}$$

From Eqs. (2.26) and (2.27) we obtain

$$\partial_t^2\theta_1 + \gamma\partial_t\theta_1 + \omega_{J1}^2\theta_1 = 0, \tag{2.33}$$
$$\partial_t^2\theta_2 + \gamma\partial_t\theta_2 + \omega_{J2}^2\theta_2 = 0 \tag{2.34}$$

for the time evolution of the Josephson plasma modes. The lower and upper Josephson plasma frequency are

$$\omega_{J1,J2}^2 = \left(\frac{1}{2}+\alpha_s\right)\Omega_s^2 + \left(\frac{1}{2}+\alpha_w\right)\Omega_w^2 \mp W, \tag{2.35}$$

respectively. For the typical case of $\Omega_w \ll \Omega_s$, the upper Josephson plasma frequency is approximately $\omega_{J2} \approx \Omega_s\sqrt{1+2\alpha_s}$. The interlayer currents during excitation of the Josephson plasma modes are sketched in Fig. 2.3.

2.2.2 Choice of parameters

In the remainder of this chapter, we consider a bilayer cuprate with $N_z = 4$ layers and $N_{xy} = 40 \times 40$ sites per layer such that the total number of sites is $N = N_{xy}N_z = 6400$. The model parameters are specified in Table 2.1. The interlayer distances approximately reproduce the spacing of the CuO_2 layers in YBCO [6, 46]. Furthermore, we choose a background permittivity of $\epsilon_\infty = 4$, which is realistic for cuprate superconductors [142]. In the following, we relate the remaining parameters of our model to physical observables in the limit of zero temperature.

The ratio of the Ginzburg-Landau coefficients μ and g determines the Cooper pair density $|\psi_0|^2 = \mu/g$. According to Eq. (2.29), the capacitive coupling constants α_w and α_s then depend only on the coefficient K, which is related to the Thomas-Fermi screening length Λ_{TF} in the copper oxide layers [140],

$$K = \frac{\epsilon_0}{8e^2|\psi_0|^2\Lambda_{TF}^2}. \tag{2.36}$$

Our parameter choice implies $|\psi_0|^2 = 2 \times 10^{21}$ cm^{-3}, $\alpha_w \approx 1$, and $\alpha_s \approx 2$, which are realistic values for cuprate superconductors [68, 141]. Recalling the expressions for the bare plasma frequencies of the interlayer junctions,

$$\Omega_{s,w} = \sqrt{\frac{8t_{s,w}|\psi_0|^2 e^2 d_c d_{s,w}}{\epsilon_\infty \epsilon_0 \hbar^2}}, \tag{2.37}$$

we have $\Omega_w/2\pi \approx 0.9$ THz and $\Omega_s/2\pi \approx 6.3$ THz. The Josephson plasma frequencies $\omega_{\mathrm{J1}}/2\pi \approx 1.0$ THz and $\omega_{\mathrm{J2}}/2\pi \approx 14.1$ THz follow from Eq. (2.35). These frequencies are consistent with optical measurements on underdoped YBCO [90–92]. The Higgs frequency $\omega_{\mathrm{H}} = \sqrt{2\mu/K\hbar^2}$ and the in-plane plasma frequency

$$\omega_{ab} = \sqrt{\frac{8t_{ab}|\psi_0|^2 e^2 d_{ab}^2}{\epsilon_\infty \epsilon_0 \hbar^2}} \tag{2.38}$$

also have a realistic order of magnitude [45, 65, 134, 139]; confer Table 2.2. As we will see below, the in-plane parameters t_{ab} and d_{ab} determine not only the in-plane plasma frequency but also the critical temperature in our simulations. For the given system size, finite-temperature simulations are reliable only for samples with critical temperatures of up to ~ 30 K. We further mention that the in-plane London penetration depth,

$$\lambda_{ab} = \frac{c}{\omega_{ab}\sqrt{\epsilon_\infty}} \approx 3240 \text{ Å}, \tag{2.39}$$

Table 2.1: Model parameters of the simulated bilayer cuprate.

K (meV^{-1})	2.9×10^{-5}
μ (meV)	1.0×10^{-2}
g (meV Å^3)	5.0
ϵ_∞	4
d_{ab} (Å)	15
d_s (Å)	4
d_w (Å)	8
t_{ab} (meV)	5.7×10^{-1}
t_s (meV)	3.9×10^{-2}
t_w (meV)	3.6×10^{-4}
$\gamma_{\mathrm{H}}/2\pi$ (THz)	1.0
$\gamma_{ab}/2\pi$ (THz)	7.0
$\gamma_s/2\pi$ (THz)	1.2
$\gamma_w/2\pi$ (THz)	0.4

Table 2.2: Characteristic frequencies of the simulated bilayer cuprate.

$\omega_{\mathrm{H}}/2\pi$ (THz)	6.3
$\omega_{ab}/2\pi$ (THz)	73.7
$\omega_{\mathrm{J1}}/2\pi$ (THz)	1.0
$\omega_{\mathrm{J2}}/2\pi$ (THz)	14.1

is larger than the in-plane system size $L_{ab} = 40\,d_{ab} = 600$ Å. By comparison to the Ginzburg-Landau theory, we identify the in-plane coherence length with

$$\xi_{ab} = d_{ab}\sqrt{\frac{t_{ab}}{\mu}} \approx 113 \text{ Å}. \tag{2.40}$$

As mentioned, the coherence length is approximately one order of magnitude larger than d_{ab}. The specified damping constants ensure that the Higgs and plasma resonances have realistic widths [45, 92, 134].

2.2.3   Optical conductivity

First, we determine the in-plane conductivity of a bilayer cuprate in the spatially homogeneous ground state (2.14) at zero temperature. To this end, we recall Eq. (2.18) and add a small probe current to the right-hand side of the equation,

$$\partial_t^2 \theta_x + \gamma_{ab}\partial_t \theta_x + \omega_{ab}^2 \theta_x = \frac{2ed_{ab}}{\epsilon_\infty \epsilon_0 \hbar} J_0 \cos(\omega_{\mathrm{pr}}t). \tag{2.41}$$

Taking the Fourier transform of Eq. (2.41) leads to

$$\theta_x(\omega_{\mathrm{pr}}) = \frac{ed_{ab}J_0}{\epsilon_\infty \epsilon_0 \hbar(\omega_{ab}^2 - \omega_{\mathrm{pr}}^2 - i\gamma_{ab}\omega_{\mathrm{pr}})}. \tag{2.42}$$

As the Josephson relation $\partial_t \theta_x = 2ed_{ab}E_x/\hbar$ implies

$$E_x(\omega_{\mathrm{pr}}) = \frac{-i\hbar\omega_{\mathrm{pr}}}{2ed_{ab}}\theta_x(\omega_{\mathrm{pr}}), \tag{2.43}$$

we obtain the in-plane conductivity

$$\sigma_x(\omega_{\mathrm{pr}}) = \frac{J_0}{2E_x(\omega_{\mathrm{pr}})} = \epsilon_\infty \epsilon_0 \gamma_{ab} + i\epsilon_\infty \epsilon_0 \left(\frac{\omega_{ab}^2}{\omega_{\mathrm{pr}}} - \omega_{\mathrm{pr}}\right). \tag{2.44}$$

To measure the in-plane conductivity numerically, we add the probe current to the equation of motion for the x component of the vector potential,

$$\partial_t^2 A_{x,\mathbf{r}} = \frac{1}{\epsilon_\infty \epsilon_0}\frac{\partial \mathcal{L}}{\partial A_{x,\mathbf{r}}} - \gamma_{ab}\partial_t A_{x,\mathbf{r}} - \frac{J_0}{\epsilon_\infty \epsilon_0}\cos(\omega_{\mathrm{pr}}t). \tag{2.45}$$

Once a steady state is reached, we record the spatially uniform electric field E_x for 20 ps and compute its Fourier transform. Using this protocol, we find perfect agreement between the simulation and the analytical prediction (2.44), as evidenced by Fig. 2.4.
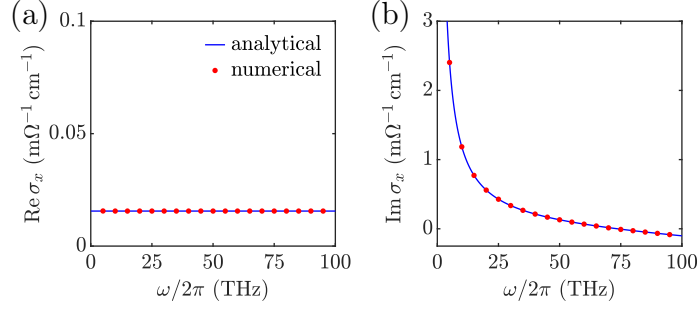
Figure 2.4: In-plane conductivity of a bilayer cuprate. For both the real part in (a) and the imaginary part in (b), the numerical results agree with the analytical prediction. In the simulation, we use a probe strength of $J_0 = 500 \text{ kA cm}^{-2}$.

Now, we turn to the out-of-plane conductivity of a bilayer cuprate at zero temperature. In analogy to the in-plane case, we add a small probe current to the linearized equations of motion (2.26) and (2.27),

$$\partial_t^2 \theta_s + \gamma \partial_t \theta_s + (1 + 2\alpha_s)\Omega_s^2 \theta_s - 2\alpha_w \Omega_w^2 \theta_w = \frac{2ed_s}{\epsilon_\infty \epsilon_0 \hbar} J_0 \cos(\omega_{\text{pr}} t), \qquad (2.46)$$

$$\partial_t^2 \theta_w + \gamma \partial_t \theta_w + (1 + 2\alpha_w)\Omega_w^2 \theta_w - 2\alpha_s \Omega_s^2 \theta_s = \frac{2ed_w}{\epsilon_\infty \epsilon_0 \hbar} J_0 \cos(\omega_{\text{pr}} t). \qquad (2.47)$$

Note that we assume $\gamma_{\text{sc}} = \gamma_s = \gamma_w \equiv \gamma$ here. Furthermore, we recall Eq. (2.20),

$$\rho_{\downarrow,\uparrow} = 4eK\hbar|\psi_0|^2 \partial_t \varphi_{\downarrow,\uparrow}. \qquad (2.48)$$

Combining this representation of the charge density with Gauss's law, we obtain

$$\partial_t \varphi_\downarrow = \frac{\epsilon_\infty \epsilon_0}{4eK\hbar|\psi_0|^2 d_c} \left(E_s - E_w\right) = -\partial_t \varphi_\uparrow. \qquad (2.49)$$

Thus, we recover the generalized Josephson relations [124, 143],

$$\frac{\hbar}{2e} \partial_t \theta_s = (1 + 2\alpha_s)d_s E_s - 2\alpha_w d_w E_w, \qquad (2.50)$$

$$\frac{\hbar}{2e} \partial_t \theta_w = (1 + 2\alpha_w)d_w E_w - 2\alpha_s d_s E_s. \qquad (2.51)$$

Next, we calculate the Fourier transforms of the equations of motion and the generalized Josephson relations. This leads to

$$d_s E_s(\omega_{\text{pr}}) = \frac{i\omega_{\text{pr}} J_0}{16K|\psi_0|^2 e^2 d_c} \frac{\alpha_s C_2 + \alpha_w C_4}{\alpha_s \alpha_w (C_1 C_4 - C_2 C_3)}, \qquad (2.52)$$

$$d_w E_w(\omega_{\text{pr}}) = \frac{i\omega_{\text{pr}} J_0}{16K|\psi_0|^2 e^2 d_c} \frac{\alpha_s C_1 + \alpha_w C_3}{\alpha_s \alpha_w (C_1 C_4 - C_2 C_3)}, \qquad (2.53)$$

where

$$C_1 = (1 + 2\alpha_s) \left[\omega_{\text{pr}}^2 + i\gamma\omega_{\text{pr}} - (1 + 2\alpha_s)\Omega_s^2\right] - 4\alpha_s \alpha_w \Omega_w^2, \qquad (2.54)$$

$$C_2 = 2\alpha_w \left[\omega_{\text{pr}}^2 + i\gamma\omega_{\text{pr}} - (1 + 2\alpha_s)\Omega_s^2\right] - 2\alpha_w \Omega_w^2(1 + 2\alpha_w), \qquad (2.55)$$

$$C_3 = 2\alpha_s \left[\omega_{\text{pr}}^2 + i\gamma\omega_{\text{pr}} - (1 + 2\alpha_w)\Omega_w^2\right] - 2\alpha_s \Omega_s^2(1 + 2\alpha_s), \qquad (2.56)$$

$$C_4 = (1 + 2\alpha_w) \left[\omega_{\text{pr}}^2 + i\gamma\omega_{\text{pr}} - (1 + 2\alpha_w)\Omega_w^2\right] - 4\alpha_s \alpha_w \Omega_s^2. \qquad (2.57)$$

Details of the calculation are included in Appendix B. The average electric field along the z axis is

$$E_z = \frac{d_s E_s + d_w E_w}{d_s + d_w}, \tag{2.58}$$

so that the out-of-plane conductivity reads

$$\sigma_z(\omega_{\mathrm{pr}}) = \frac{J_0}{2 E_z(\omega_{\mathrm{pr}})} = \frac{\epsilon_\infty \epsilon_0}{i\omega_{\mathrm{pr}}} \frac{(\omega_{\mathrm{pr}}^2 + i\gamma\omega_{\mathrm{pr}} - \omega_{\mathrm{J1}}^2)(\omega_{\mathrm{pr}}^2 + i\gamma\omega_{\mathrm{pr}} - \omega_{\mathrm{J2}}^2)}{\omega_{\mathrm{pr}}^2 + i\gamma\omega_{\mathrm{pr}} - \omega_\perp^2}. \tag{2.59}$$

This analytical result was also derived in Ref. [101]. The transverse Josephson plasma frequency $\omega_\perp$ [117, 143, 144] is given by

$$\omega_\perp^2 = \frac{1 + 2\alpha_s + 2\alpha_w}{\alpha_s + \alpha_w} \left(\alpha_s \Omega_s^2 + \alpha_w \Omega_w^2 \right). \tag{2.60}$$

To measure the out-of-plane conductivity numerically, we add the probe current to the equation of motion for the z component of the vector potential,

$$\partial_t^2 A_{z,\mathbf{r}} = \frac{1}{\epsilon_\infty \epsilon_0} \frac{\partial \mathcal{L}}{\partial A_{z,\mathbf{r}}} - \gamma_{z,\mathbf{r}} \partial_t A_{z,\mathbf{r}} - \frac{J_0}{\epsilon_\infty \epsilon_0} \cos(\omega_{\mathrm{pr}} t). \tag{2.61}$$

Once a steady state is reached, we record the average electric field E_z for 100 ps and compute its Fourier transform. In Fig. 2.5, we compare the out-of-plane conductivity of the simulated bilayer cuprate to the analytical prediction (2.44). Note that the damping constants in the simulation are $\gamma_w/2\pi = 0.4$ THz, $\gamma_s/2\pi = 1.2$ THz, and $\gamma_{\mathrm{sc}}/2\pi = 1$ THz. Thus, the analytical assumption $\gamma_{\mathrm{sc}} = \gamma_s = \gamma_w \equiv \gamma$ is not fulfilled. We use $\gamma/2\pi = 1$ THz for the analytical prediction, which yields good agreement with the numerical results for the imaginary part of the conductivity at all frequencies. Regarding the real part of the conductivity, the analytical prediction notably deviates from the numerical results at low frequencies. This is due to the overestimation of the damping constant γ_w. In Appendix B, we present simulations of a bilayer cuprate with $\gamma_{\mathrm{sc}}/2\pi = \gamma_s/2\pi = \gamma_w/2\pi = 0.4$ THz. Using $\gamma/2\pi = 0.4$ THz for the analytical prediction, we indeed find excellent agreement with the numerical results.
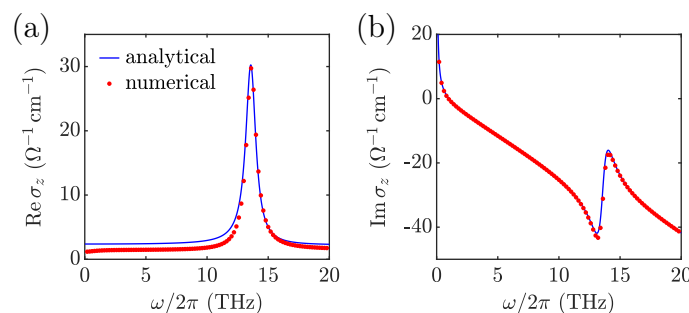

Figure 2.5: Out-of-plane conductivity of a bilayer cuprate. (a) At low frequencies, the analytical prediction for the real part of the conductivity deviates from the simulation. This is due to simplifications in the derivation of the analytical prediction. (b) These simplifications do not affect the analytical prediction for the imaginary part of the conductivity. In the simulation, we use a probe strength of $J_0 = 10$ kA cm^{-2}.

Qualitatively, the out-of-plane conductivity exhibits two characteristic features. Firstly, its imaginary part diverges as $1/\omega_{\mathrm{pr}}$ at low frequencies. Based on the analytical prediction (2.44), we identify the low-frequency response

$$[\operatorname{Im}\sigma_z(\omega_{\mathrm{pr}})]_{\omega_{\mathrm{pr}}\to 0} = \frac{\epsilon_\infty\epsilon_0\omega_{\mathrm{J}1}^2\omega_{\mathrm{J}2}^2}{\omega_{\mathrm{pr}}\omega_\perp^2}. \tag{2.62}$$

Secondly, the imaginary part of the conductivity is characterized by a sharp edge at $\omega_\perp/2\pi \approx 13.6$ THz, corresponding to an absorption peak in the real part.

2.3   Fluctuating dynamics at nonzero temperature

Parts of this section are taken from Ref. [H5]. For the rest of this work, we indicate the component of a vector field by a superscript when we write the site $\mathbf{r} = (l, m, n)$ explicitly. The two lowest layers $n = 0$ and $n = 1$ form a bilayer.

2.3.1   Thermal phase transition

An ensemble of thermal states is generated as follows. The system is initialized in the ground state and then evolves freely for 10 ps in the presence of dissipation and thermal fluctuations, which are different for each trajectory. At nonzero temperature, the tunneling coefficients are renormalized due to phase fluctuations. The gauge-invariant intrabilayer phase differences between layers $n = 0$ and $n = 1$ are $\theta_{l,m}^s = \mathcal{P}(\phi_{l,m,0} - \phi_{l,m,1} + a_{l,m,0}^z)$, and the gauge-invariant interbilayer phase differences between layers $n = 1$ and $n = 2$ are $\theta_{l,m}^w = \mathcal{P}(\phi_{l,m,1} - \phi_{l,m,2} + a_{l,m,1}^z)$. The gauge-invariant in-plane phase differences are $\theta_{l,m,n}^x = \mathcal{P}(\phi_{l,m,n} - \phi_{l+1,m,n} + a_{l,m,n}^x)$ and $\theta_{l,m,n}^y = \mathcal{P}(\phi_{l,m,n} - \phi_{l,m+1,n} + a_{l,m,n}^y)$. Note that the gauge-invariant phase differences are mapped onto the interval $(-\pi, \pi]$ by the projection operator $\mathcal{P}(\cdot)$. In the presence of thermal fluctuations, we determine the effective tunneling coefficients

$$t_{s,\mathrm{eff}} = t_s \left\langle \cos\theta_{l,m}^s \right\rangle, \tag{2.63}$$

$$t_{w,\mathrm{eff}} = t_w \left\langle \cos\theta_{l,m}^w \right\rangle, \tag{2.64}$$

$$t_{ab,\mathrm{eff}} = t_{ab} \left\langle \cos\theta_{l,m,n}^x \right\rangle. \tag{2.65}$$

Each expectation value bases on an average over space, a time interval of 2 ps (200 measurements), and an ensemble of 100 trajectories. The temperature dependence of the effective tunneling coefficients is shown in Fig. 2.6(a), indicating a crossover to a disordered state at a critical temperature of $T_c \sim 30$ K. Above this temperature, the interbilayer tunneling is strongly suppressed while the effective tunneling coefficients $t_{s,\mathrm{eff}}$ and $t_{ab,\mathrm{eff}}$ decrease significantly slower than below T_c. The temperature dependence of the superconducting order parameter is presented in Fig. 2.6(b). The amplitude of the order parameter first decreases with increasing temperature and reaches a minimum of $|\psi|/|\psi_0| \approx 0.66$ around T_c. Above T_c, it slowly increases with increasing temperature. This behavior is consistent with a thermal order-disorder transition [145].

The critical temperature T_c depends on the in-plane tunneling coefficient t_{ab} as shown in Fig. 2.7(a). To investigate this further, we recall the expression for the in-plane tun-
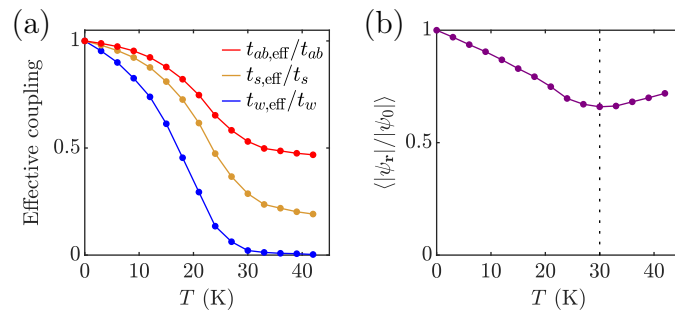
Figure 2.6: Thermal phase transition. (a) Temperature dependence of the effective tunneling coefficients. (b) Temperature dependence of the order parameter. Each data point is an ensemble average of 100 trajectories and the standard error is comparable to the point size. This figure is adapted from Ref. [H5].

neling energy from Eq. (2.1),

$$T_{ab} = \sum_{\mathbf{r}} t_{ab} V_0 \left(|\psi_{\mathbf{r}'(x)} - \psi_{\mathbf{r}} e^{ia_{x,\mathbf{r}}}|^2 + |\psi_{\mathbf{r}'(y)} - \psi_{\mathbf{r}} e^{ia_{y,\mathbf{r}}}|^2 \right), \qquad (2.66)$$

where $V_0 = d_{ab}^2 d_c$. Neglecting amplitude fluctuations, we can rewrite this as

$$T_{ab} \approx \sum_{\mathbf{r}} 2 t_{ab} V_0 |\psi_0|^2 \left(2 - \cos \theta_{\mathbf{r}}^x - \cos \theta_{\mathbf{r}}^y \right). \qquad (2.67)$$

Equation (2.67) has the form of the two-dimensional XY model with an in-plane coupling of $J_{ab} = 2 t_{ab} V_0 |\psi_0|^2$. However, the gauge-invariant phase differences couple to the electromagnetic field. Figure 2.7(b) indicates a linear relation between T_c and J_{ab}. Remarkably, the fitted slope $k_B T_c / J_{ab} = 0.87 \pm 0.03$ is comparable to the estimate $k_B T_c / J_{ab} \approx \pi/2$ for a Kosterlitz-Thouless transition [87,88]. Despite the coupling to the electromagnetic field and the presence of amplitude fluctuations, the phase transition in our model displays similarity to the phase transition in the anisotropic three-dimensional XY model. While the critical behavior of the anisotropic three-dimensional XY model is that of the isotropic
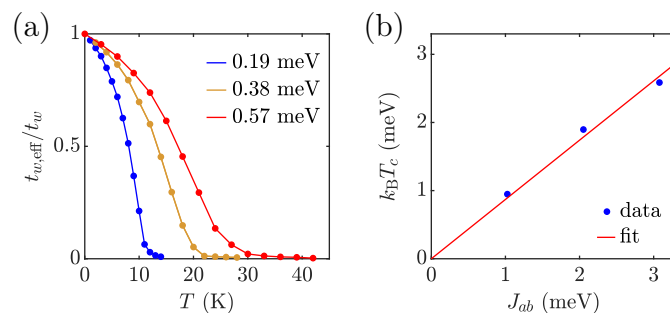

Figure 2.7: Influence of the in-plane tunneling coefficient t_{ab} on the phase transition. (a) Temperature dependence of the effective interbilayer coupling for various t_{ab} as specified in the legend. Each data point is an ensemble average of 100 trajectories and the standard error is comparable to the point size. (b) Relation between the critical temperature and the in-plane coupling. The data points are fitted by a straight line through the origin with $k_B T_c / J_{ab} = 0.87 \pm 0.03$.

three-dimensional XY model, the critical temperature approaches the Kosterlitz-Thouless estimate for large anisotropy [80,84,146]. This scaling of the critical temperature is associated with the appearance of vortex loops. Experiments indicate that the critical behavior of underdoped cuprate superconductors is indeed consistent with a three-dimensional XY model [147,148]. Nevertheless, the nature of the superconducting phase transition in these materials is not completely understood, particularly with regard to the role of magnetic fluctuations [83,149,150] and competing orders [96].

2.3.2   Vortex excitations

The thermal phase transition is accompanied by the appearance of vortex excitations. In continuum, the phase winding of the order parameter along a closed path is given by

$$\Phi = \oint \boldsymbol{\nabla}\phi \cdot \mathrm{d}\mathbf{r} = \oint \left(\boldsymbol{\nabla}\phi + \frac{2e}{\hbar}\mathbf{A} \right) \cdot \mathrm{d}\mathbf{r} - \oint \frac{2e}{\hbar}\mathbf{A} \cdot \mathrm{d}\mathbf{r}. \tag{2.68}$$

In the simulation, we use the latter representation as it is based on quantities that directly enter the Lagrangian. We define the vorticity of a single plaquette in the xy plane as

$$\begin{aligned} v_{l,m,n} = {} & \frac{1}{2\pi}\left(a^x_{l,m,n} + a^y_{l+1,m,n} - a^x_{l,m+1,n} - a^y_{l,m,n} \right) \\ & - \frac{1}{2\pi}\left(\theta^x_{l,m,n} + \theta^y_{l+1,m,n} - \theta^x_{l,m+1,n} - \theta^y_{l,m,n} \right). \end{aligned} \tag{2.69}$$

The vorticity can assume the values -1, 0, and $+1$. A vorticity of $+1$ corresponds to a vortex, while a vorticity of -1 corresponds to an antivortex. In Fig. 2.8(a), we show a snapshot of the vorticity in the lowest layer at a temperature of 36 K $\sim 1.2\,T_c$. One can see a strong tendency of vortices and antivortices to form pairs. This is highlighted by the equal-time in-plane vortex correlation function displayed in Fig. 2.8(b). The definition of the in-plane vortex correlation function is

$$V_{ab}(x_i, y_j, t) = \frac{\langle v_{l,m,n}(0) v_{l+i,m+j,n}(t) \rangle}{\langle v^2_{l,m,n}(0) \rangle}. \tag{2.70}$$

Here, we evaluate the ensemble average of 1000 trajectories. The accumulated probability to find an antivortex on the nearest or next-nearest plaquettes of a vortex amounts to 94%.
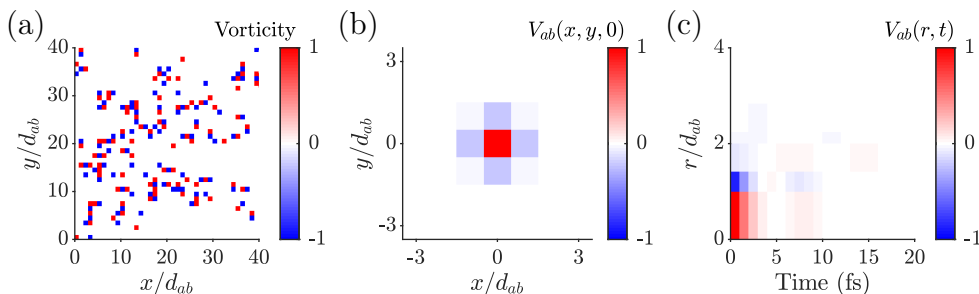

Figure 2.8: Vortices in the xy plane at 36 K $\sim 1.2\,T_c$. (a) Snapshot of the vorticity in the lowest layer. (b) Equal-time in-plane vortex correlation function. (c) Time-resolved in-plane vortex correlation function, where $r^2 = x^2 + y^2$. This figure is adapted from Ref. [H5].

On larger length scales, in-plane vortex correlations are negligible. Next, we consider the cumulative correlation function

$$V_{ab}(r,t) = \sum_{|(x_i,y_j)|=r} V_{ab}(x_i, y_j, t), \tag{2.71}$$

where the sum is taken over all (x_i, y_j) with $x_i^2 + y_j^2 = r^2$. The time dependence of the in-plane vortex correlations reveals that vortex-antivortex pairs annihilate on a time scale of a few femtoseconds, as visible in Fig. 2.8(c). For comparison, we now present an analytical estimate of the annihilation time. Following Refs. [3, 151], the energy of a vortex-antivortex pair with separation $r \ll \lambda_{ab}$ is

$$U(r) \approx 2\pi J_{ab} \ln(r/d_{ab}) = 2\pi t_{ab} V_0 |\psi_0|^2 \ln(r/d_{ab}), \tag{2.72}$$

implying the attractive force

$$F(r) \approx -\frac{2\pi t_{ab} V_0 |\psi_0|^2}{r}. \tag{2.73}$$

The mass of a vortex was derived in Ref. [152],

$$m_{\mathrm{v}} \approx \pi K \hbar^2 d_c |\psi_0|^2. \tag{2.74}$$

Thus, we obtain

$$\partial_t^2 r \approx -\frac{8 t_{ab} d_{ab}}{K \hbar^2} \tag{2.75}$$

for $r \approx d_{ab}$ and estimate the annihilation time as

$$\tau = \sqrt{\frac{K \hbar^2}{4 t_{ab}}} \approx 2.3 \text{ fs}, \tag{2.76}$$

which is consistent with the simulation. In addition to this fast decay, the in-plane vortex correlations are characterized by weak temporal oscillations for small r.
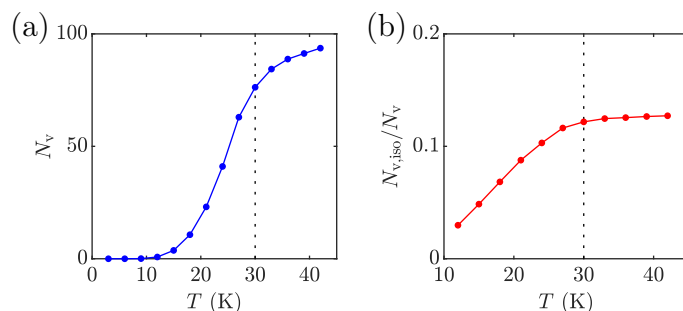

Figure 2.9: Temperature dependence of vortex excitations. (a) Number of vortices per layer at different temperatures. Each layer contains an equal amount of antivortices. (b) Relative amount of isolated vortices at different temperatures. Isolated vortices are vortices without an antivortex on the nearest or next-nearest neighbor plaquettes. Each data point is an ensemble average of 100 trajectories and the standard error is comparable to the point size. The critical temperature is $T_c \sim 30$ K.

Figure 2.9(a) shows that the number of vortices is negligible for temperatures up to 15 K. While the number of vortices rises rapidly with temperature between 15 K and 30 K, it rises only slowly at temperatures above $T_c \sim 30$ K. In Fig. 2.9(b), we show the relative amount of isolated vortices as a function of temperature. An isolated vortex is a vortex without an antivortex on the nearest or next-nearest neighbor plaquettes. The percentage of isolated vortices grows below T_c and saturates at higher temperature. This possibly indicates a transition from bound to unbound vortices akin to a Kosterlitz-Thouless transition. The percentage of isolated vortices is limited by the areal density of vortices. We also note that the in-plane system size of 60 nm is smaller than the in-plane penetration depth $\lambda_{ab} \approx 324$ nm. Thus, magnetic interactions between vortices are strongly suppressed in the simulation.

2.3.3 Plasma excitations

In the following, we investigate the temperature dependence of the plasma resonances. We begin with the in-plane plasma resonance. To this end, we compute the power spectrum of the supercurrent along the x axis at different temperatures. We average the x-axis supercurrent over one bilayer,

$$J_x = \frac{1}{2N_{xy}} \sum_{l,m} \sum_{n=1}^{2} J^x_{l,m,n}, \tag{2.77}$$

where

$$J^x_{l,m,n} = \frac{2et_{ab}d_{ab}}{i\hbar} \left(\psi^*_{l+1,m,n} \psi_{l,m,n} e^{ia^x_{l,m,n}} - \text{c.c.} \right). \tag{2.78}$$

For each trajectory, we record $J_x(t)$ for 10 ps. We then compute the Fourier transform $J_x(\omega)$ and determine the power spectrum $\langle |J_x(\omega)|^2 \rangle$ based on an ensemble average of 1000 trajectories. As one can see in Fig. 2.10(a), the in-plane plasma resonance broadens with increasing temperature. The peak frequency $\omega_{x,\text{peak}}$ decreases monotonically with increasing temperature below T_c, which is also visible in Fig. 2.10(b). Consistent with the temperature dependence of the order parameter, the peak frequency slowly increases

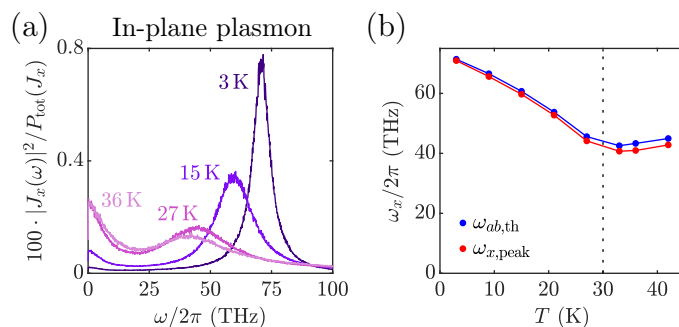**Figure 2.10:** Temperature dependence of the in-plane plasma resonance. (a) Power spectrum of the supercurrent along the x axis at different temperatures. The spectral power is normalized by the total power. (b) Temperature dependence of the peak frequency and the thermal average of the in-plane plasma frequency. The critical temperature is $T_c \sim 30$ K. This figure is adapted from Ref. [H5].

above T_c. We find that the temperature dependence of $\omega_{x,\text{peak}}$ is well described by the thermal average

$$\omega_{ab,\text{th}} = \omega_{ab} \sqrt{\frac{\langle \psi_{l+1,m,n}^* \psi_{l,m,n} e^{ia_{l,m,n}^x} + \text{c.c.} \rangle}{2|\psi_0|^2}}, \tag{2.79}$$

which accounts for the average renormalization of the in-plane coupling and the order parameter due to thermal fluctuations.

To study the temperature dependence of the lower and upper Josephson plasma resonances, we compute the power spectra of the inter- and intrabilayer supercurrents analogously to $\langle |J_x(\omega)|^2 \rangle$. We take the planar average of the interbilayer supercurrent,

$$J_w = \frac{1}{N_{xy}} \sum_{l,m} J_{l,m,1}^z, \tag{2.80}$$

and the planar average of the intrabilayer supercurrent,

$$J_s = \frac{1}{N_{xy}} \sum_{l,m} J_{l,m,0}^z, \tag{2.81}$$

where

$$J_{l,m,n}^z = \frac{2et_{z,\mathbf{r}}d_c}{i\hbar} \left(\psi_{l,m,n+1}^* \psi_{l,m,n} e^{ia_{l,m,n}^z} - \text{c.c.} \right). \tag{2.82}$$

The temperature dependence of the power spectra $\langle |J_w(\omega)|^2 \rangle$ and $\langle |J_s(\omega)|^2 \rangle$ is shown in Fig. 2.11. The lower Josephson plasma resonance shifts to lower frequencies with increasing temperature and vanishes around T_c. This is also observed in experiments [92, 118].

Similarly to the in-plane plasma resonance, the upper Josephson plasma resonance broadens with increasing temperature and shifts to lower frequencies. In Figure 2.12(a), the temperature dependence of the peak frequency $\omega_{s,\text{peak}}$ is compared to that of the thermal average

$$\omega_{\text{J2,th}} = \Omega_s \sqrt{\frac{\langle C_s \rangle}{|\psi_0|^2} + \alpha_s \left\langle \frac{C_s}{|\psi_{l,m,0}|^2} + \frac{C_s}{|\psi_{l,m,1}|^2} \right\rangle}, \tag{2.83}$$
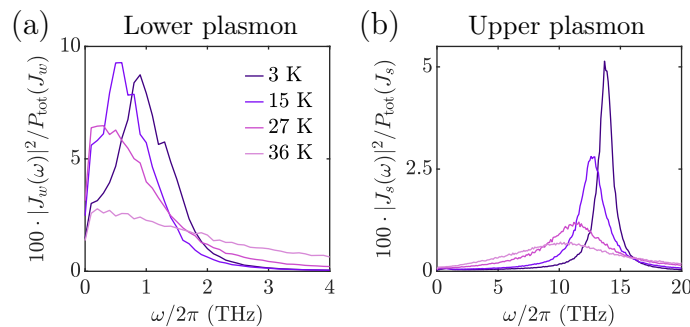

Figure 2.11: Temperature dependence of the Josephson plasma resonances. (a) Power spectrum of the interbilayer supercurrent at different temperatures. (b) Power spectrum of the intrabilayer supercurrent at different temperatures. In both panels, the spectral power is normalized by the total power. The critical temperature is $T_c \sim 30$ K. This figure is adapted from Ref. [H5].
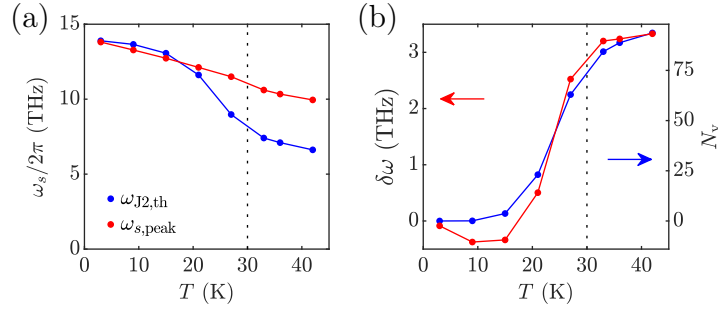
Figure 2.12: Temperature dependence of the upper Josephson plasma frequency. (a) Temperature dependence of the peak frequency and the thermal average of the upper Josephson plasma frequency $\omega_{\text{J2,th}}$. (b) The discrepancy $\delta\omega = \omega_{s,\text{peak}} - \omega_{\text{J2,th}}$ has a similar temperature dependence as the number of vortices per layer. The critical temperature is $T_c \sim 30$ K. This figure is adapted from Ref. [H5].

with

$$C_s = \frac{1}{2}\left(\psi_{l,m,1}^* \psi_{l,m,0} e^{ia_{l,m,0}^z} + \text{c.c.}\right). \tag{2.84}$$

The definition in Eq. (2.83) is motivated by the zero-temperature expression $\omega_{\text{J2}} \approx \Omega_s\sqrt{1 + 2\alpha_s}$. While $\omega_{s,\text{peak}}$ and $\omega_{\text{J2,th}}$ approximately agree at temperatures below 20 K, $\omega_{\text{J2,th}}$ is clearly smaller than $\omega_{s,\text{peak}}$ at higher temperatures. Remarkably, the discrepancy $\delta\omega = \omega_{s,\text{peak}} - \omega_{\text{J2,th}}$ follows a similar temperature dependence as the average density of vortices, which is highlighted by Fig. 2.12(b). This suggests that the emergence of vortices stabilizes the upper Josephson plasma frequency.

Now, we present an analytical model of the upper Josephson plasma mode including thermal fluctuations and disorder [H5]. Parts of the calculation follow Ref. [153]. Assuming that the bilayers are weakly coupled, we consider the following equation of motion for the gauge-invariant intrabilayer phase $\theta(\mathbf{r}, t)$,

$$\partial_t^2\theta + \gamma\partial_t\theta + \mathcal{D}(\boldsymbol{\nabla}\theta) + \omega_{\text{J2}}^2 \sin\theta = \xi, \tag{2.85}$$

where $\mathcal{D}(\boldsymbol{\nabla}\theta)$ depends on the plasma dispersion and $\xi(\mathbf{r}, t)$ is Langevin noise. We assume that Eq. (2.85) is solved for $\theta = \theta_T$ at a given temperature T. Next, we add a spatially uniform driving term $f(t)$ to the right-hand side of Eq. (2.85),

$$\partial_t^2\theta + \gamma\partial_t\theta + \mathcal{D}(\boldsymbol{\nabla}\theta) + \omega_{\text{J2}}^2 \sin\theta = \xi + f. \tag{2.86}$$

We then write the gauge-invariant intrabilayer phase as $\theta = \theta_T + \theta_f$. Assuming θ_f to be small, we find

$$\partial_t^2\theta_f + \gamma\partial_t\theta_f + \mathcal{D}(\boldsymbol{\nabla}\theta_f) + \omega_{\text{J2}}^2 \cos(\theta_T)\theta_f \approx f. \tag{2.87}$$

Splitting θ_f into zero-momentum and finite-momentum contributions,

$$\theta_f(\mathbf{r}, t) = \Theta_f(t) + \delta\theta_f(\mathbf{r}, t), \tag{2.88}$$

we obtain the two equations of motion

$$\partial_t^2\Theta_f + \gamma\partial_t\Theta_f + \omega_{\text{J2}}^2\langle\cos\theta_T\rangle_{\text{sp}}\Theta_f + \omega_{\text{J2}}^2\left\langle(\cos\theta_T - \langle\cos\theta_T\rangle_{\text{sp}})\,\delta\theta_f\right\rangle_{\text{sp}} \approx f, \tag{2.89}$$

$$\partial_t^2\delta\theta_f + \gamma\partial_t\delta\theta_f + \mathcal{D}(\boldsymbol{\nabla}\delta\theta_f) + \omega_{\text{J2}}^2\langle\cos\theta_T\rangle_{\text{sp}}\delta\theta_f + \omega_{\text{J2}}^2\left(\cos\theta_T - \langle\cos\theta_T\rangle_{\text{sp}}\right)\Theta_f \approx 0, \tag{2.90}$$

where $\langle \cdot \rangle_{\mathrm{sp}}$ denotes a spatial average over the entire superconductor. Next, we rewrite $\delta\theta_f$ in terms of its Fourier components,

$$\delta\theta_f(\mathbf{r}, t) = \int \frac{\mathrm{d}\omega}{2\pi} \frac{1}{N/2} \sum_{\mathbf{k}} \delta\theta_f(\mathbf{k}, \omega)\, e^{i(\mathbf{k}\cdot\mathbf{r} - \omega t)}. \tag{2.91}$$

The solution of Eq. (2.90) is then

$$\delta\theta_f(\mathbf{k}, \omega) \approx -\frac{\omega_{\mathrm{J2}}^2}{-\omega^2 - i\gamma\omega + \omega_{\mathrm{J2},T}^2 + \mathcal{D}(\mathbf{k})} \int \frac{\mathrm{d}\nu}{2\pi}\, F_T(\mathbf{k}, \nu)\Theta_f(\omega - \nu), \tag{2.92}$$

with $\omega_{\mathrm{J2},T} = \omega_{\mathrm{J2}}\langle \cos\theta_T \rangle_{\mathrm{sp}}$. The function

$$F_T(\mathbf{k}, \nu) = \big(\cos\theta_T - \langle \cos\theta_T \rangle_{\mathrm{sp}}\big)(\mathbf{k}, \nu) \tag{2.93}$$

is related to the disorder of the gauge-invariant intrabilayer phase at a given temperature. Inserting Eq. (2.92) into Eq. (2.89) yields

$$\begin{aligned}
f(\omega) &\approx \big(-\omega^2 - i\gamma\omega + \omega_{\mathrm{J2},T}^2\big)\, \Theta_f(\omega) \\
&\quad - \omega_{\mathrm{J2}}^4 \int \frac{\mathrm{d}\nu_1 \mathrm{d}\nu_2}{(2\pi)^2} \frac{1}{(N/2)^2} \sum_{\mathbf{k}} \frac{F_T(\mathbf{k}, \nu_1)F_T(-\mathbf{k}, \nu_2)\Theta_f(\omega - \nu_1 - \nu_2)}{-(\omega - \nu_1)^2 - i\gamma(\omega - \nu_1) + \omega_{\mathrm{J2},T}^2 + \mathcal{D}(\mathbf{k})}.
\end{aligned} \tag{2.94}$$

Taking the ensemble average of Eq. (2.94), we obtain the general expression for the susceptibility of the upper Josephson plasma mode at zero momentum,

$$\chi(\omega) = \frac{\Theta_f(\omega)}{f(\omega)} = \frac{1}{-\omega^2 - i\gamma\omega + \Omega^2(\omega)}, \tag{2.95}$$

where

$$\Omega^2(\omega) = \omega_{\mathrm{J2},T}^2 + \omega_{\mathrm{J2}}^4 \int \frac{\mathrm{d}\nu}{2\pi} \frac{1}{(N/2)^2} \sum_{\mathbf{k}} \frac{\langle |F_T(\mathbf{k}, \nu)|^2 \rangle_{\mathrm{ens}}}{(\omega - \nu)^2 + i\gamma(\omega - \nu) - \omega_{\mathrm{J2},T}^2 - \mathcal{D}(\mathbf{k})}. \tag{2.96}$$

According to the fluctuation-dissipation theorem [154, 155], the power spectrum of the intrabilayer current follows the relation

$$\langle |J_s(\omega)|^2 \rangle \sim \langle |\Theta_f(\omega)|^2 \rangle \sim \mathrm{Im}\,\chi(\omega). \tag{2.97}$$

Before we proceed with the calculation of the susceptibility, we consider the dispersion relations of the Josephson plasma modes in a bilayer cuprate. The dispersion of the Josephson plasma modes is nearly flat for propagation along the z axis. However, the dispersion of these longitudinal modes acquires a quadratic term if the direction of propagation has a small in-plane component $k_{xy} = \sqrt{k_x^2 + k_y^2} \ll |k_z|$. We also assume $|k_z| \gg \omega_{ab}\sqrt{\epsilon_\infty}/c$ such that the dispersion relations for the longitudinal modes [123, 156] can be written as

$$\omega_{\mathrm{J1,J2}}^2(k_{xy}, k_z) \approx \omega_{\mathrm{J1,J2}}^2 + \frac{k_{xy}^2}{k_z^2}\, \omega_{ab}^2. \tag{2.98}$$

The dispersion relations for transverse propagation were derived in Refs. [143, 144],

$$\omega_{\mathrm{J1,J2}}^2(k_{xy}, 0) = \frac{1}{2}\left(\omega_{\mathrm{J1}}^2 + \omega_{\mathrm{J2}}^2 + \frac{c^2 k_{xy}^2}{\epsilon_\infty}\right) \mp \sqrt{\frac{1}{4}\left(\omega_{\mathrm{J1}}^2 + \omega_{\mathrm{J2}}^2 + \frac{c^2 k_{xy}^2}{\epsilon_\infty}\right)^2 - \omega_{\mathrm{J1}}^2 \omega_{\mathrm{J2}}^2 - \frac{c^2 k_{xy}^2 \omega_\perp^2}{\epsilon_\infty}}. \tag{2.99}$$
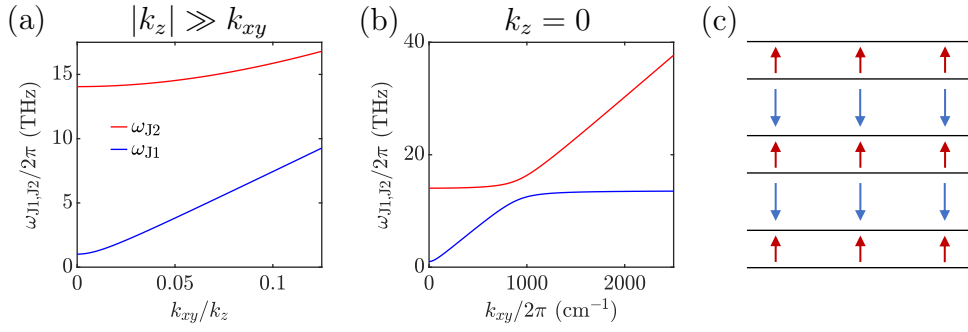
Figure 2.13: Propagating Josephson plasma modes at zero temperature. (a) Dispersion for longitudinal propagation. (b) Dispersion for transverse propagation. Note that $k_{xy}/2\pi \geq L_{ab}^{-1} \approx 1.7 \cdot 10^5$ cm^{-1} in the simulation. (c) Interlayer currents during excitation of the transverse Josephson plasma mode, corresponding to the lower branch in (b) for large k_{xy}.

In Figs. 2.13(a) and 2.13(b), we show the dispersion of the Josephson plasma modes for longitudinal and transverse propagation, respectively, using the parameters specified in Section 2.2.2. While the Josephson plasma modes retain their character for longitudinal propagation with $k_{xy} \ll |k_z|$, their character changes qualitatively for transverse propagation with $k_{xy} \gg \omega_{J2}\sqrt{\epsilon_\infty}/c$. The upper plasma mode attains photonic character as the dispersion merges with the light cone. The lower plasma mode hybridizes with the transverse Josephson plasma mode as $\omega_{J1}(k_{xy}, 0)$ converges to the frequency $\omega_\perp$, which is slightly smaller than ω_{J2} according to Eq. (2.60). As depicted in Fig. 2.13(c), the transverse plasma mode is characterized by intra- and interbilayer currents oscillating with a comparable amplitude and a phase shift of π; see also Ref. [144].

Strictly speaking, the dispersion relations in Eqs. (2.98) and (2.99) are only valid in the limit of zero temperature. Nonetheless, we also employ them for temperatures around T_c, replacing the fundamental plasma frequencies by their thermal averages, e.g., $\omega_{J2} \to \omega_{J2,T}$. We consider only the out-of-plane momenta $k_z = 0$ and $k_z = \pi/2d_c$, which are the only out-of-plane momenta included in our simulation. Furthermore, the dispersion relations for transverse propagation simplify to

$$\omega_{J1}(k_{xy}, 0) \approx \omega_{\perp,T}, \tag{2.100}$$

$$\omega_{J2}(k_{xy}, 0) \approx ck_{xy}/\sqrt{\epsilon_\infty} \tag{2.101}$$

for the in-plane momenta included in the simulation. For longitudinal propagation, only the upper Josephson plasma mode delivers a significant contribution to $\Omega^2(\omega)$ since the lower Josephson plasma mode is primarily associated with oscillations of the gauge-invariant interlayer phase. As we will see below, the spectral weight of the disorder function $F_T(\mathbf{k}, \nu)$ is concentrated on small in-plane momenta and small frequencies. Thus, we can neglect the photonic mode in the case of transverse propagation. The transverse Josephson plasma mode, on the other hand, is relevant for our discussion since its frequency is close to $\omega_{J2,T}$.

In the following, we analyze the effects of longitudinal and transverse disorder. We begin with transverse disorder. As mentioned, the dispersion of the transverse Josephson

plasma mode is flat, so that the general expression in Eq. (2.96) takes the form

$$\Omega^2(\omega) = \omega_{\mathrm{J2},T}^2 + \omega_{\mathrm{J2}}^4 \int \frac{\mathrm{d}\nu}{2\pi} \frac{1}{(N/2)^2} \sum_{k_x,k_y} \frac{\langle |F_T(k_x, k_y, 0, \nu)|^2 \rangle_{\mathrm{ens}}}{(\omega - \nu)^2 + i\gamma(\omega - \nu) - \omega_{\perp,T}^2}. \tag{2.102}$$

The disorder function rapidly decreases with increasing k_{xy} as evidenced by Fig. 2.14(a); see also Appendix C. Note that $F_T(\mathbf{k} = 0, \nu) = 0$. Therefore, we use the approximation

$$\langle |F_T(k_x, k_y, 0, \nu)|^2 \rangle_{\mathrm{ens}} = \begin{cases} |F_{\perp,T}(\nu)|^2 & \text{for } 2\pi/L_{ab} \leq k_{xy} \leq k_{\max}, \\ 0 & \text{else.} \end{cases} \tag{2.103}$$

Converting the momentum sum to an integral and performing the integration, we find

$$\Omega^2(\omega) = \omega_{\mathrm{J2},T}^2 + \frac{(k_{\max}^2 L_{ab}^2 - 4\pi^2)\,\omega_{\mathrm{J2}}^4}{\pi N^2} \int \frac{\mathrm{d}\nu}{2\pi} \frac{|F_{\perp,T}(\nu)|^2}{(\omega - \nu)^2 + i\gamma(\omega - \nu) - \omega_{\perp,T}^2}. \tag{2.104}$$

Figure 2.14(a) also shows that $|F_{\perp,T}(\nu)|^2$ decays for frequencies well below $\omega_{\mathrm{J2},T} \sim \omega_{\mathrm{J2,th}}$. Therefore, we consider the limit of static disorder,

$$|F_{\perp,T}(\nu)|^2 = 2\pi F_{\perp,T}^2 \delta(\nu). \tag{2.105}$$

Thus, we obtain

$$\Omega^2(\omega) = \omega_{\mathrm{J2},T}^2 + \frac{S_\perp (k_{\max}^2 L_{ab}^2 - 4\pi^2)\,\omega_{\mathrm{J2}}^4}{\omega^2 + i\gamma\omega - \omega_{\perp,T}^2}, \tag{2.106}$$

where $S_\perp = F_{\perp,T}^2/\pi N^2$ quantifies the strength of transverse disorder. Corresponding to the numerically obtained disorder spectra in Fig. 2.14, we choose a momentum cutoff of $k_{\max} = 4\pi/L_{ab}$. Based on the numerical results for $\omega_{\mathrm{J2,th}}$ and $\omega_{ab,\mathrm{th}}$ at $36\,\mathrm{K} \sim 1.2\,T_c$, we use $\omega_{\mathrm{J2},T} = 0.5\,\omega_{\mathrm{J2}}$ and $\omega_{ab,T} = 3\,\omega_{\mathrm{J2}}$ in the following. Furthermore, we use $\gamma = 0.1\,\omega_{\mathrm{J2}}$ for the damping constant. In Figs. 2.14(b) and 2.14(c), the imaginary part of the susceptibility is displayed for varying disorder strength $S_\perp$ and two different values of the transverse
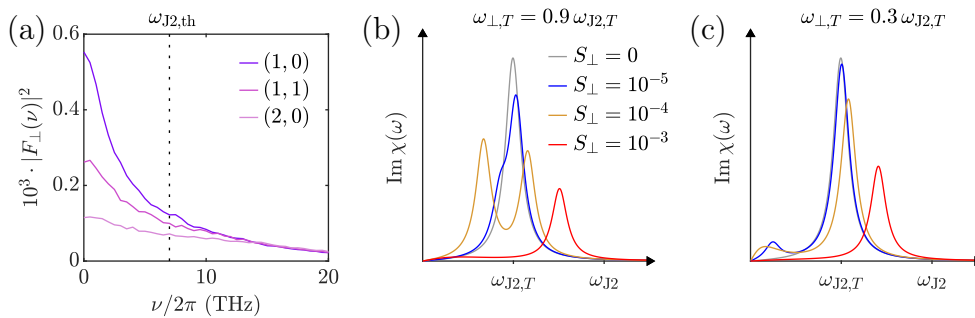

Figure 2.14: Influence of transverse disorder on the susceptibility of the upper Josephson plasma mode. (a) Fourier spectrum of transverse disorder for various in-plane momenta (k_x, k_y) specified in units of $2\pi/L_{ab}$. The data is obtained from an ensemble average of 1000 trajectories at $36\,\mathrm{K} \sim 1.2\,T_c$. (b) Analytical solution for the imaginary part of the susceptibility, assuming $\omega_{\perp,T} = 0.9\,\omega_{\mathrm{J2},T}$. (c) Analytical solution for the imaginary part of the susceptibility, assuming $\omega_{\perp,T} = 0.3\,\omega_{\mathrm{J2},T}$.

plasma frequency $\omega_{\perp,T}$. If the transverse plasma frequency is slightly below $\omega_{J2,T}$, as in Fig. 2.14(b), the susceptibility of the upper Josephson plasma mode reveals three different regimes of transverse disorder. For small disorder strength, the maximum of $\text{Im}\,\chi(\omega)$ is slightly asymmetric such that the peak is slightly blue-shifted with respect to the perfectly ordered case. For intermediate disorder strength, the maximum of $\text{Im}\,\chi(\omega)$ splits into two peaks. For large disorder strength, $\text{Im}\,\chi(\omega)$ exhibits only a significantly blue-shifted peak. By contrast, the imaginary part of the susceptibility always exhibits a clearly dominant, blue-shifted maximum if the transverse plasma frequency is well below $\omega_{J2,T}$ as in Fig. 2.14(c). The blue-shift of the maximum grows with increasing disorder. In Appendix C, we demonstrate that the analytical solution for the susceptibility does not change qualitatively when the finite spectral width of $|F_{\perp,T}(\nu)|^2$ is taken into account.

Next, we consider longitudinal disorder. The general expression in Eq. (2.96) takes the form

$$\Omega^2(\omega) = \omega_{J2,T}^2 + \omega_{J2}^4 \int \frac{d\nu}{2\pi} \frac{1}{(N/2)^2} \sum_{k_x,k_y} \frac{\langle |F_T(k_x,k_y,\pi/2d_c,\nu)|^2 \rangle_{\text{ens}}}{(\omega-\nu)^2 + i\gamma(\omega-\nu) - \omega_{J2,T}^2 - 4\omega_{ab,T}^2 k_{xy}^2 d_c^2/\pi^2}.$$
(2.107)

Figure 2.15(a) shows that longitudinal disorder has a similar dependence on k_{xy} and ν as transverse disorder. Therefore, we use the approximation

$$\langle |F_T(k_x,k_y,\pi/2d_c,\nu)|^2 \rangle_{\text{ens}} = \begin{cases} 2\pi F_{\parallel,T}^2 \delta(\nu) & \text{for } k_{xy} \leq k_{\max}, \\ 0 & \text{for } k_{xy} > k_{\max}. \end{cases}$$
(2.108)

Converting the momentum sum to an integral and performing the integration, we find

$$\Omega^2(\omega) = \omega_{J2,T}^2 - \frac{\pi^2 S_\parallel L_{ab}^2 \omega_{J2}^4}{4d_c^2 \omega_{ab,T}^2} \ln\left(\frac{\omega^2 + i\gamma\omega - \omega_{\max}^2}{\omega^2 + i\gamma\omega - \omega_{J2,T}^2} \right),$$
(2.109)

where the cutoff frequency

$$\omega_{\max,T}^2 = \omega_{J2,T}^2 + \frac{4\omega_{ab,T}^2 k_{\max}^2 d_c^2}{\pi^2}$$
(2.110)

is determined by the momentum cutoff and $S_\parallel = F_{\parallel,T}^2/\pi N^2$ quantifies the strength of longitudinal disorder. As before, we use $\gamma = 0.1\,\omega_{J2}$, $\omega_{J2,T} = 0.5\,\omega_{J2}$, $\omega_{ab,T} = 3\,\omega_{J2}$, and $k_{\max} = 4\pi/L_{ab}$. This implies $\omega_{\max} \approx 1.1\,\omega_{J2,T}$. In Figs. 2.15(b) and 2.15(c), the imaginary part of the susceptibility is displayed for varying disorder strength $S_\parallel$ and two different values of the cutoff frequency $\omega_{\max}$. For both values of the cutoff frequency, we find three regimes of longitudinal disorder, which are qualitatively similar to the case of transverse disorder. However, the asymmetry of the maximum is inverted for weak disorder, such that the peak is slightly red-shifted with respect to the perfectly ordered case. This inverted asymmetry is due to the fact that the plasma frequencies of the longitudinal mode are larger than $\omega_{J2,T}$ while the transverse plasma frequency is smaller than $\omega_{J2,T}$.

Finally, we combine transverse and longitudinal disorder, leading to

$$\Omega^2(\omega) = \omega_{J2,T}^2 + \frac{S_\perp(k_{\max}^2 L_{ab}^2 - 4\pi^2)\,\omega_{J2}^4}{\omega^2 + i\gamma\omega - \omega_{\perp,T}^2} - \frac{\pi^2 S_\parallel L_{ab}^2 \omega_{J2}^4}{4d_c^2 \omega_{ab,T}^2} \ln\left(\frac{\omega^2 + i\gamma_\parallel\omega - \omega_{\max}^2}{\omega^2 + i\gamma_\parallel\omega - \omega_{J2,T}^2} \right),$$
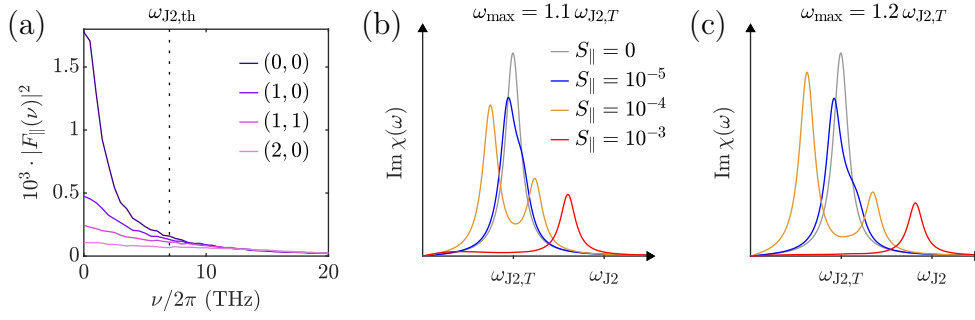(2.111)

Figure 2.15: Influence of longitudinal disorder on the susceptibility of the upper Josephson plasma mode. (a) Fourier spectrum of longitudinal disorder for various in-plane momenta (k_x, k_y) specified in units of $2\pi/L_{ab}$. The data is obtained from an ensemble average of 1000 trajectories at $36\,\mathrm{K} \sim 1.2\,T_c$. (b) Analytical solution for the imaginary part of the susceptibility, assuming $\omega_{\max} = 1.1\,\omega_{\mathrm{J2},T}$. (c) Analytical solution for the imaginary part of the susceptibility, assuming $\omega_{\max} = 1.2\,\omega_{\mathrm{J2},T}$.

where we introduced $\gamma_\parallel$ as the damping constant of the longitudinal mode. Our simulations indicate that the strength of transverse disorder is comparable to that of longitudinal disorder. Therefore, we utilize $S_\perp = S_\parallel \equiv S$ here. In Figs. 2.16(a) and 2.16(b), we show the imaginary part of the susceptibility of the upper Josephson plasma mode using $\gamma_\parallel = \gamma = 0.1\,\omega_{\mathrm{J2}}$, $\omega_{\mathrm{J2},T} = 0.5\,\omega_{\mathrm{J2}}$, $\omega_{ab,T} = 3\,\omega_{\mathrm{J2}}$, and $k_{\max} = 4\pi/L_{ab}$. For these parameters, we find a qualitatively similar dependence of the susceptibility on the disorder strength as in the case of purely longitudinal disorder. Comparing these results with the simulation, one notes that the power spectrum of the plane-averaged intrabilayer current exhibits only one visible peak at all simulated temperatures. A possible explanation for this observation is that there is a sharp jump of the disorder strength from the weakly disordered regime to the strongly disordered regime. Thus, the regime of intermediate disorder might correspond to a very narrow temperature region which is not captured by our simulations. The numerical results in Fig. 2.12 indeed feature a steep rise of the discrepancy between the peak frequency $\omega_{s,\mathrm{peak}}$ and $\omega_{\mathrm{J2,th}}$. However, we find a disorder
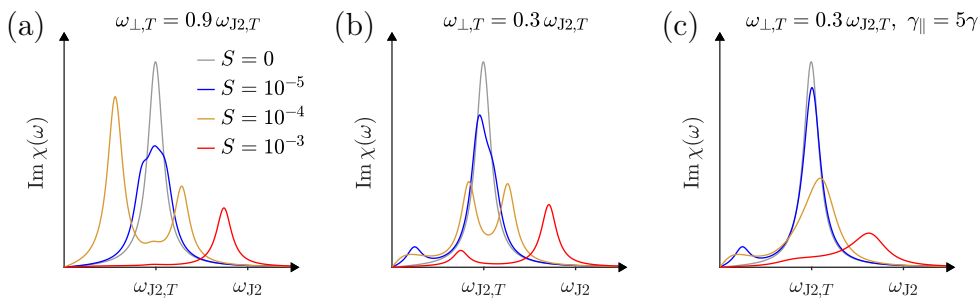

Figure 2.16: Analytical solution for the imaginary part of the susceptibility of the upper Josephson plasma mode, including transverse and longitudinal disorder with the same disorder strength S. (a) Analytical solution for $\omega_{\perp,T} = 0.9\,\omega_{\mathrm{J2},T}$ and $\gamma_\parallel = \gamma$. (b) Analytical solution for $\omega_{\perp,T} = 0.3\,\omega_{\mathrm{J2},T}$ and $\gamma_\parallel = \gamma$. (c) Analytical solution for $\omega_{\perp,T} = 0.3\,\omega_{\mathrm{J2},T}$ and $\gamma_\parallel = 5\,\gamma$.

strength of $S \sim 10^{-4}$ at 36 K $\sim 1.2\,T_c$, corresponding to the regime of intermediate disorder strength. We evaluate

$$S = \frac{F_{\perp,T}^2}{\pi N^2} = \frac{1}{\pi N^2} \int \frac{\mathrm{d}\nu}{2\pi} \, |F_T(2\pi/L_{ab}, 0, 0, \nu)|^2 \tag{2.112}$$

from the numerically obtained disorder spectrum shown in Fig. 2.14(a).

An alternative scenario is presented in Fig. 2.16(c). In this scenario, the longitudinal plasma mode is overdamped such that the susceptibility is mainly affected by transverse disorder. The imaginary part of the susceptibility then exhibits only one pronounced maximum, which is blue-shifted with respect to the perfectly ordered case. The blue-shift grows monotonically with increasing disorder. Furthermore, the significant broadening of the maximum of Im $\chi(\omega)$ is consistent with the simulation.

In both scenarios, the susceptibility of the upper Josephson plasma mode is modified by scattering with a continuum of finite-momentum modes, which is conceptually related to a *Fano resonance* [157]. The broadening of the plasma resonance can be regarded as *inhomogeneous broadening*. To conclude our analysis, we elaborate on the relation between disorder and vortices. For this purpose, we consider a superconducting bilayer in the ground state, in which the gauge-invariant intrabilayer phase is $\theta(x, y) \equiv 0$. Then, we add a single vortex-antivortex pair to one of the two layers. We assume that the vortex has the coordinates $(0,0)$ while the antivortex is located at $(0, \delta y)$. Thus, the spatial profile of the gauge-invariant intrabilayer phase is modified to

$$\theta(x, y) = \arctan\left(\frac{y}{x}\right) - \arctan\left(\frac{y - \delta y}{x}\right) \approx \arctan\left(\frac{x \cdot \delta y}{x^2 + y^2}\right) \tag{2.113}$$

for $x, y \gg \delta y$. This induces the disorder

$$F(x, y) \approx \cos\theta - 1 = \frac{1}{\sqrt{1 + (x \cdot \delta y)^2/(x^2 + y^2)^2}} - 1 \approx -\frac{1}{2}\left(\frac{x \cdot \delta y}{x^2 + y^2}\right)^2. \tag{2.114}$$

2.3.4   Optical conductivity

Now, we investigate how vortices affect the in-plane conductivity. To measure the in-plane conductivity, we add a spatially homogeneous probe current $J_{\mathrm{ext}} = J_0 \cos(\omega_{\mathrm{pr}}t)$ to the equation of motion for $A_{x,\mathbf{r}}$ as described in Section 2.2.3. Once a steady state is reached, we record the average electric field $E_x = \frac{1}{N}\sum_{\mathbf{r}} E_{x,\mathbf{r}}$ and the average current $J_{x,\mathrm{tot}}$ along the x axis for 4 ps. The average current $J_{x,\mathrm{tot}}$ includes superconducting, normal and capacitive contributions,

$$J_{x,\mathrm{tot}} = J_{x,\mathrm{sup}} + J_{x,\mathrm{nor}} + J_{x,\mathrm{cap}}. \tag{2.115}$$

The superconducting current is given by

$$J_{x,\mathrm{sup}} = \frac{1}{N}\sum_{\mathbf{r}} \frac{2et_{ab}d_{ab}}{i\hbar}\left(\psi_{\mathbf{r}'(x)}^* \psi_{\mathbf{r}} e^{ia_{\mathbf{r}}^x} - \mathrm{c.c.}\right). \tag{2.116}$$

The normal current is defined as

$$J_{x,\mathrm{nor}} = \frac{1}{N}\sum_{\mathbf{r}} \epsilon_\infty \epsilon_0 \gamma_{ab} E_{x,\mathbf{r}}. \tag{2.117}$$
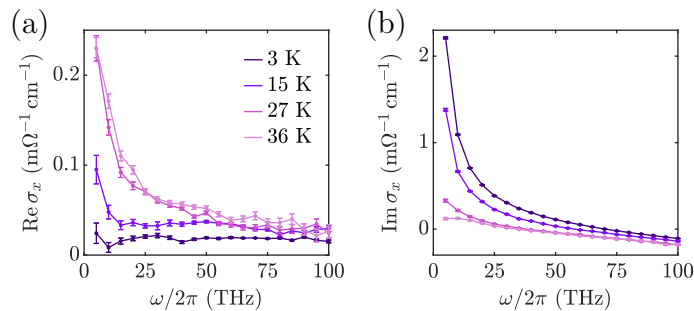
Figure 2.17: In-plane conductivity at different temperatures. (a) Real part. (b) Imaginary part. The probe strength is $J_0 = 500$ kA cm^{-2}, and the error bars indicate the standard errors of the ensemble averages. The critical temperature is $T_c \sim 30$ K. This figure is adapted from Ref. [H5].

The capacitive current is given by

$$J_{x,\text{cap}} = \frac{1}{N} \sum_{\mathbf{r}} \epsilon_\infty \epsilon_0 \partial_t E_{x,\mathbf{r}}. \tag{2.118}$$

From the steady-state dynamics of E_x and $J_{x,\text{tot}}$, we evaluate the in-plane conductivity $\sigma_x(\omega_{\text{pr}}) = J_{x,\text{tot}}(\omega_{\text{pr}})/E_x(\omega_{\text{pr}})$ for 100–1000 trajectories and take the ensemble average. We demonstrate in Appendix B that the linear response is probed for $J_0 = 500$ kA cm^{-2}. In Fig. 2.17, the in-plane conductivity is shown for different temperatures. At 3 K, the real part of the in-plane conductivity is relatively flat and its magnitude is close to the zero-temperature value $\epsilon_\infty \epsilon_0 \gamma_{ab}$. We note that the numerical convergence of Re σ_x is very slow for small frequencies at low temperature. The imaginary part of the in-plane conductivity exhibits the characteristic $1/\omega_{\text{pr}}$ behavior of a superconductor at 3 K. The prefactor of this divergence is slightly reduced with respect to zero temperature, consistent with the reduction of the in-plane plasma frequency. At higher temperatures, we observe a steep rise of the real part of σ_x for small frequencies, which is less pronounced at 15 K than at 27 K and 36 K. While we find an approximate $1/\omega_{\text{pr}}$ behavior of the imaginary part of σ_x at 15 K and 27 K, this feature of superconductivity does not seem to be present at 36 K. This indicates that the appearance of vortices causes a transition to a resistive state as proposed to occur in superconducting films [158]. The underlying mechanism is the unbinding of vortex-antivortex pairs due to an applied current. The vortices and antivortices are exposed to a Magnus force and drift in opposite directions, perpendicular to the current. The drift of the vortices leads to phase slips along the current direction, giving rise to an electric field.

Next, we measure the out-of-plane conductivity at nonzero temperature. For this purpose, we add a spatially homogeneous probe current $J_{\text{ext}} = J_0 \cos(\omega_{\text{pr}} t)$ to the equation of motion for $A_{z,\mathbf{r}}$ as described in Section 2.2.3. Once a steady state is reached, we record the average electric field E_z and the average current $J_{z,\text{tot}}$ along the z axis for 20 ps. The average electric field is given by

$$E_z = \frac{1}{N} \sum_{\mathbf{r}} \frac{d_{z,\mathbf{r}} E_{z,\mathbf{r}}}{d_c} \tag{2.119}$$
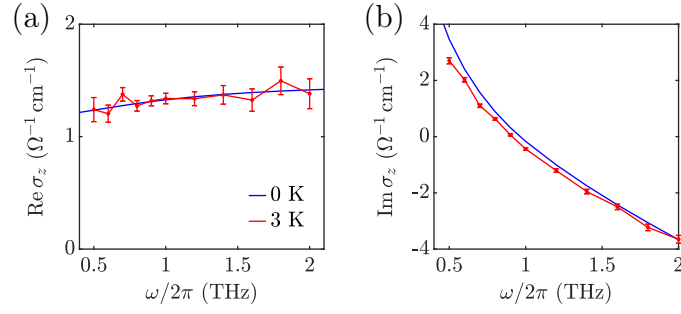
Figure 2.18: Out-of-plane conductivity at 3 K $\sim 0.1\,T_c$, compared to the out-of-plane conductivity at zero temperature. (a) Real part. (b) Imaginary part. The probe strength is $J_0 = 10\ \text{kA}\,\text{cm}^{-2}$, and the error bars indicate the standard errors of the ensemble averages.

In analogy to the in-plane case, the average current $J_{z,\text{tot}}$ includes superconducting, normal and capacitive contributions,

$$J_{z,\text{tot}} = J_{z,\text{sup}} + J_{z,\text{nor}} + J_{z,\text{cap}}, \tag{2.120}$$

with

$$J_{z,\text{sup}} = \frac{1}{N} \sum_{\mathbf{r}} \frac{2e t_{z,\mathbf{r}} d_{z,\mathbf{r}}}{i\hbar} \left(\psi^*_{\mathbf{r}'(z)} \psi_{\mathbf{r}} e^{i a_{\mathbf{r}}^z} - \text{c.c.} \right), \tag{2.121}$$

$$J_{z,\text{nor}} = \frac{1}{N} \sum_{\mathbf{r}} \frac{\epsilon_\infty \epsilon_0 \gamma_{z,\mathbf{r}} d_{z,\mathbf{r}} E_{z,\mathbf{r}}}{d_c}, \tag{2.122}$$

$$J_{z,\text{cap}} = \frac{1}{N} \sum_{\mathbf{r}} \frac{\epsilon_\infty \epsilon_0 d_{z,\mathbf{r}} \partial_t E_{z,\mathbf{r}}}{d_c}. \tag{2.123}$$

From the steady-state dynamics of E_z and $J_{z,\text{tot}}$, we evaluate the out-of-plane conductivity $\sigma_z(\omega_{\text{pr}}) = J_{z,\text{tot}}(\omega_{\text{pr}})/E_z(\omega_{\text{pr}})$ for 1000 trajectories and take the ensemble average. As the numerical convergence of σ_z is generally slow, we present results only for a relatively low temperature of 3 K $\sim 0.1\,T_c$ in Fig. 2.18. One can see that the real part of σ_z does not significantly change compared to zero temperature. The imaginary part of σ_z still exhibits a $1/\omega_{\text{pr}}$ behavior with a slightly reduced prefactor, corresponding to the reduction of the lower plasma frequency. In the following chapter, we discuss among other things how the out-of-plane conductivity is modified in various scenarios of driving.

Chapter 3

Light-induced nonequilibrium phenomena in cuprate superconductors

In this chapter, we discuss light-induced nonequilibrium phenomena in cuprate superconductors based on our semiclassical method. Each section summarizes one of the author's publications [H1–H4].

3.1   Higgs time crystal

Time crystals are physical systems in a particular dynamical phase of matter that was first proposed in 2012 [159, 160]. Originally, a time crystal was defined as a closed many-body system that spontaneously breaks time-translation symmetry in its ground state. This symmetry-broken state also has to be robust against perturbations. However, it was shown that time crystalline states do not exist in closed quantum systems in equilibrium [161, 162]. Since then, two modified variants of time crystals have been proposed and experimentally demonstrated, namely discrete time crystals [163–167] and dissipative time crystals [168–170]. In the latter class of time crystals, dissipation stabilizes a state that spontaneously breaks continuous time symmetry. A discrete time crystal is a periodically driven system that does not respond with the driving frequency or an integer multiple of the driving frequency. Instead, the response is subharmonic, i.e., the response frequency is smaller than the driving frequency. Discrete time-crystalline states can be induced in closed and dissipative systems. Reviews on time crystals can be found in Refs. [171, 172].

In Ref. [H1], we propose to induce a time-crystalline state in a cuprate superconductor by optical driving. As this discrete time crystal is enabled by the nonlinear coupling between the Higgs mode and a Josephson plasma mode, we call it a *Higgs time crystal*. We identify the Higgs time crystal based on a minimal model of a light-driven monolayer cuprate. Then, we demonstrate that a Higgs time crystal can also be induced in a bilayer cuprate. The robustness of the subharmonic response against thermal fluctuations is confirmed by finite-temperature simulations.

First, we consider a monolayer cuprate that is periodically driven by an electric field polarized along the z axis as depicted in Fig. 3.1. We take the driving to be spatially uniform as the wavelength of the terahertz drive ($> 10~\mu$m) is significantly larger than the system size ($< 0.1~\mu$m). At zero temperature, the superconducting order parameter and the z-axis electric field then perform a spatially homogeneous motion, while the in-plane
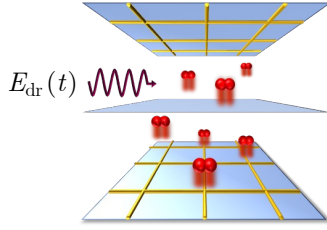
Figure 3.1: Light-driven monolayer cuprate. The electric field $E_{\mathrm{dr}}(t) = E_0 \cos(\omega_{\mathrm{dr}} t)$ is polarized along the z axis, driving Josephson plasma oscillations. This figure is adapted from Ref. [H2].

components of the electric field and all components of the magnetic field vanish. As the superconductor is spatially homogeneous, we can take the order parameter to be real and expand it around its ground state ψ_0, i.e., $\psi = \psi_0(1 + h)$. We use the gauge-invariant interlayer phase θ_z to describe the motion of the z-axis electric field $E_z = \hbar \partial_t \theta_z / 2 e d_z$, where d_z is the interlayer distance. Thus, the dynamics governed by Eqs. (2.11) and (2.12) simplifies to the two-mode model

$$\partial_t^2 \theta_z + \gamma_z \partial_t \theta_z + \omega_{\mathrm{J}}^2 (1 + h)^2 \sin \theta_z = j_{\mathrm{dr}} \cos(\omega_{\mathrm{dr}} t), \quad (3.1)$$

$$\partial_t^2 h + \gamma_{\mathrm{sc}} \partial_t h + \omega_{\mathrm{H}}^2 \left(h + \frac{3}{2} h^2 + \frac{1}{2} h^3 \right) + 2\alpha \omega_{\mathrm{J}}^2 (1 + h)(1 - \cos \theta_z) = 0, \quad (3.2)$$

where γ_z is the damping constant of the gauge-invariant interlayer phase and α is the capacitive coupling constant. The fundamental frequencies are the Higgs frequency ω_{H} and the Josephson plasma frequency ω_{J}. The optical drive with the frequency ω_{dr} couples directly to the Josephson plasma mode and enters as a driving current on the right-hand side of Eq. (3.1). The relation between the current amplitude j_{dr} and the electric field strength E_0 is $j_{\mathrm{dr}} = 2 e d_z \omega_{\mathrm{dr}} E_0 / \epsilon_\infty \hbar$. We then perform numerical simulations of the coupled equations (3.1) and (3.2), using the parameters $\omega_{\mathrm{H}}/2\pi = 6.3$ THz, $\omega_{\mathrm{J}}/2\pi = 16$ THz, $\gamma_{\mathrm{sc}}/2\pi = \gamma_z/2\pi = 0.5$ THz, $\alpha = 0.33$, $d_z = 6$ Å, and $\epsilon_\infty = 1$. Based on the dynamics in the steady state, we obtain the dynamical phase diagram shown in Fig. 3.2(a). In the normal phase, θ_z oscillates at the driving frequency and h oscillates at twice the driving frequency. The latter is a consequence of the nonlinear coupling between the Higgs mode and the Josephson plasma mode. To see this, we neglect all nonlinear terms in Eqs. (3.1) and (3.2) except for the lowest order coupling between the two modes,

$$\partial_t^2 \theta_z + \gamma_z \partial_t \theta_z + \omega_{\mathrm{J}}^2 \theta_z + 2\omega_{\mathrm{J}}^2 \theta_z h = j_{\mathrm{dr}} \cos(\omega_{\mathrm{dr}} t), \quad (3.3)$$

$$\partial_t^2 h + \gamma_{\mathrm{sc}} \partial_t h + \omega_{\mathrm{H}}^2 h + \alpha \omega_{\mathrm{J}}^2 \theta_z^2 = 0. \quad (3.4)$$

For $\omega_{\mathrm{dr}} = \omega_{\mathrm{H}}/2$, the Higgs mode is resonantly excited as one can see in Fig. 3.2(b). The underlying nonlinear process is visualized in Fig. 3.2(c). For large field strengths, we identify a heating regime, which is characterized by the suppression of superconducting order. The tongue-like shape of the heating regime is associated with the Josephson plasma resonance. The tip of the heating tongue is slightly red-shifted from ω_{J} due to the presence of nonlinearities and dissipation in the dynamics; see also Ref. [173].

   The main finding of Ref. [H1] is the emergence of a time-crystalline phase for driving frequencies of $\omega_{\mathrm{dr}} \approx \omega_{\mathrm{H}} + \omega_{\mathrm{J}}$ and intermediate driving strengths. This Higgs time crystal
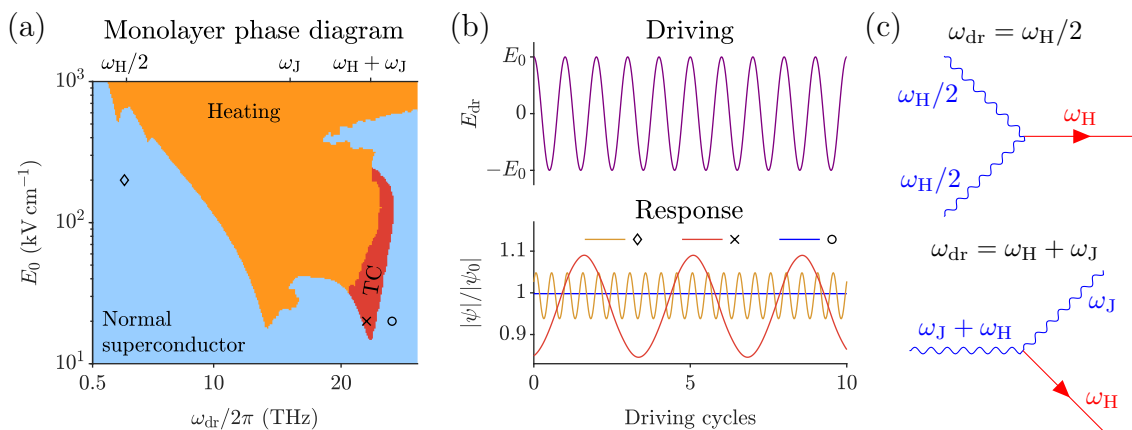
Figure 3.2: Response of a monolayer cuprate to periodic driving by an electric field $E_{dr}(t) = E_0 \cos(\omega_{dr} t)$ polarized along the z axis. (a) Dynamical phase diagram at zero temperature. The time crystalline (TC) phase is encoded in red. (b) Response of the order parameter to the optical drive for the Higgs resonance at $\omega_{dr} = \omega_H/2$ (diamond), the time crystal (cross), and an off-resonantly driven superconductor (circle). The driving parameters are indicated by the symbols in (a). (c) Resonant excitation of the Higgs mode by two different nonlinear processes. This figure is adapted from Ref. [H1].

is enabled by a sum resonance of the Higgs mode and the Josephson plasma mode, which can also be derived analytically from Eqs. (3.3) and (3.4). As shown in Fig. 3.2(c), the optical drive resonantly excites the Higgs mode and the Josephson plasma mode at the same time. Thus, the amplitude of the order parameter mainly oscillates at the Higgs frequency ω_H in the time-crystalline phase. Furthermore, the amplitude of the Josephson plasma oscillations at the Josephson plasma frequency ω_J is comparable to the amplitude of the Josephson plasma oscillations at the driving frequency ω_{dr}. We emphasize that the Higgs time crystal originates from the same cubic coupling term $\sim \theta_z^2 h$ in the Lagrangian as the Higgs resonance for $\omega_{dr} = \omega_H/2$. In general, the subharmonic response of the Higgs mode and the Josephson plasma mode is incommensurate to the drive.

A Higgs time crystal can also be induced in a bilayer cuprate superconductor. Here, it is enabled by a sum resonance of the Higgs mode and the upper Josephson plasma mode. Importantly, we demonstrate the robustness of the subharmonic response against thermal fluctuations by simulating a bilayer cuprate with $48 \times 48 \times 4$ lattice sites in Ref. [H1]. Unlike the monolayer example above, the simulated bilayer cuprate has realistic parameters in comparison to known materials. At zero temperature, the Higgs frequency is $\omega_H/2\pi \approx 6.3$ THz and the upper Josephson plasma frequency is $\omega_{J2}/2\pi \approx 14.3$ THz. As discussed in Section 2.3, the Josephson plasma frequency decreases with increasing temperature. Remarkably, the Higgs frequency increases with increasing temperature in our simulations, which is scrutinized in the Supplemental Material of Ref. [H1]. The critical temperature of the simulated bilayer cuprate is $T_c \sim 30$ K.

In Fig. 3.3(a), we show the power spectrum of the zero-momentum amplitude of the order parameter for different driving frequencies at 3 K. All power spectra exhibit a sharp peak at twice the driving frequency and a second peak near the Higgs frequency. However, the power spectrum is qualitatively unique for $\omega_{dr}/2\pi = 22.4$ THz, corresponding to the sum of the Higgs frequency ω_H^* and the upper Josephson plasma frequency ω_{J2}^* at
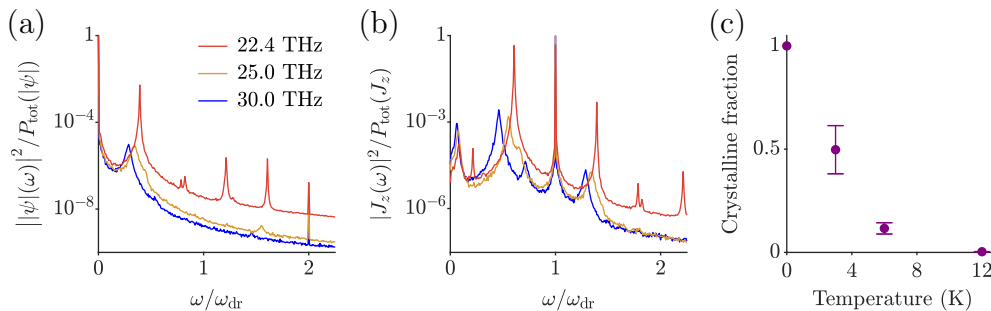
Figure 3.3: Higgs time crystal in a bilayer cuprate at nonzero temperature. (a) Power spectrum of the amplitude of the order parameter for different driving frequencies at 3 K $\sim 0.1\,T_c$. The driving strength is $E_0 = 200$ kV cm^{-1}. (b) Corresponding power spectra of the supercurrent along the z axis. In both panels, we show power spectra at zero momentum, averaged over 100 trajectories. The spectral power is normalized by the total power. (c) Temperature dependence of the optimal time-crystalline fraction, normalized by its value at $T = 0$. The optimal crystalline fraction at a given temperature is determined by the maximum height of the blue-detuned side peak in the power spectrum of the z-axis supercurrent. This figure is adapted from Ref. [H1].

3 K. In this case, the peak near the Higgs frequency is significantly more pronounced, and additional sharp peaks at $2\omega_{\text{dr}} - \omega_{\text{H}}^*$ and $2\omega_{\text{dr}} - 2\omega_{\text{H}}^*$ emerge. The collective sub-harmonic response of the order parameter at a temperature of $\sim 0.1\,T_c$ confirms that a time-crystalline state is induced by driving a sum resonance of the Higgs mode and the upper Josephson plasma mode. The emergence of the time-crystalline state gives rise to pronounced side peaks at $\omega_{\text{dr}} \pm \omega_{\text{H}}^*$ in the power spectrum of the zero-momentum super-current along the z axis, as evidenced by Fig. 3.3(b). Thus, we identify an experimentally relevant signature of the Higgs time crystal.

Next, we investigate the temperature dependence of the Higgs time crystal in Ref [H1]. For this purpose, we introduce the *time-crystalline fraction* as the height of the blue-detuned side peak in the power spectrum of the z-axis supercurrent. We evaluate the time-crystalline fraction for a variety of driving parameters at different temperatures and identify the optimum at each temperature. The temperature dependence of the optimal time-crystalline fraction is presented in Fig. 3.3(c). As expected, the time-crystalline fraction decreases with increasing temperature. Nonetheless, the subharmonic response of the bilayer cuprate is robust against thermal fluctuations for temperatures up to $\sim 0.2\,T_c$. Furthermore, we demonstrate that the subharmonic response is robust against perturbations of the drive and observable for pulsed driving with a pulse duration of ~ 2 ps. Therefore, a Higgs time crystal can possibly be realized and detected in state-of-the-art experiments using techniques from Refs. [92, 97, 111].

3.2 Higgs mode mediated enhancement of interlayer transport

In Ref. [H2], we present a mechanism for light-enhanced interlayer transport in monolayer cuprate superconductors which is mediated by the Higgs mode. This enhancement of

interlayer transport is achieved by periodic driving with an electric field that is polarized along the z axis and whose frequency is blue-detuned from the Higgs frequency. To derive this, we consider the simplified two-mode model from the previous section and add a probe current,

$$\partial_t^2\theta_z + \gamma_z\partial_t\theta_z + \omega_J^2\theta_z + 2\omega_J^2\theta_z h = j_{dr}\cos(\omega_{dr}t) + j_{pr}\cos(\omega_{pr}t), \tag{3.5}$$

$$\partial_t^2 h + \gamma_{sc}\partial_t h + \omega_H^2 h + \alpha\omega_J^2\theta_z^2 = 0. \tag{3.6}$$

Due to the θ_z^2 term in Eq. (3.6), the amplitude of the order parameter oscillates at the frequencies $2\omega_{dr}$, $2\omega_{pr}$, and $\omega_{dr} \pm \omega_{pr}$. Thus, Eq. (3.5) takes the form of a parametrically driven oscillator. The coupling of amplitude oscillations at $\omega_{dr} \pm \omega_{pr}$ to Josephson plasma oscillations at ω_{dr} renormalizes $\theta_z(\omega_{pr})$. A perturbative expansion of h and θ_z shows that $\theta_z(\omega_{pr})$ is reduced if the driving frequency is blue-detuned from the Higgs frequency. The renormalization of $\theta_z(\omega_{pr})$ is particularly strong for $\omega_{dr} \approx \omega_H$ as the amplitude oscillations at $\omega_{dr} \pm \omega_{pr}$ are close to resonance in this case. Note that we assume the probing frequency ω_{pr} to be very small. Our perturbative expansion leads to the analytical prediction

$$\omega_{pr}\sigma_z(\omega_{pr}) = \frac{i\epsilon_\infty\epsilon_0 j_{pr}}{2\theta_z(\omega_{pr})}$$

$$\approx \frac{i\epsilon_\infty\epsilon_0\omega_J^2\omega_H^2(\omega_{dr}^2 - \omega_H^2 + i\gamma_{sc}\omega_{dr})\left[(\omega_{dr}^2 - \omega_J^2)^2 + \gamma_z^2\omega_{dr}^2\right]}{\omega_H^2(\omega_{dr}^2 - \omega_H^2 + i\gamma_{sc}\omega_{dr})\left[(\omega_{dr}^2 - \omega_J^2)^2 + \gamma_z^2\omega_{dr}^2\right] + \alpha\omega_J^2 j_{dr}^2(\omega_{dr}^2 - 3\omega_H^2 + i\gamma_{sc}\omega_{dr})}. \tag{3.7}$$

for the z-axis conductivity in the limit of $\omega_{pr} \to 0$. In general, one has to distinguish three different cases regarding Eq. (3.7): $\omega_J < \omega_H$, $\omega_H < \omega_J < \sqrt{3}\omega_H$, and $\sqrt{3}\omega_H < \omega_J$. All these cases are discussed in Ref. [H2]. Here, we focus on the case of $\omega_J < \omega_H$, which is realized in known monolayer cuprates, such as La$_{2-x}$Sr$_x$CuO$_4$ (LSCO) [174, 175]. We choose the parameters $\omega_J/2\pi = 2$ THz, $\omega_H/2\pi = 6$ THz, $\gamma_{sc}/2\pi = \gamma_z/2\pi = 0.5$ THz, $\alpha = 1$, $d_z = 10$ Å, and $\epsilon_\infty = 4$.

Motivated by Eqs. (1.3) and (1.4), we define the superconducting weight

$$D = \text{Im}\left[\pi\omega_{pr}\sigma_z(\omega_{pr})\right]_{\omega_{pr}\to 0}. \tag{3.8}$$

In equilibrium, the superconducting weight is given by $D_0 = \pi\epsilon_\infty\epsilon_0\omega_J^2$. Figure 3.4(a) displays the superconducting weight in the driven state as a function of the driving frequency for a fixed driving strength. While the superconducting weight is enhanced for driving frequencies that are blue-detuned from the Higgs frequency, it is reduced for red-detuned driving frequencies. The analytical prediction is in qualitative agreement with numerical simulations of Eqs. (3.1) and (3.2), which include all nonlinearities of the lattice gauge model. In the simulations, we determine the superconducting weight based on the z-axis conductivity at $\omega_{pr}/2\pi = 0.05$ THz. At this frequency, the imaginary part of σ_z approaches a $1/\omega_{pr}$ behavior as exemplified by Fig. 3.4(b). Remarkably, the enhancement of interlayer transport reaches nearly 50% in this example. One can see in Fig. 3.4(c) that the corresponding driving parameters belong to the regime of maximal enhancement. In general, the interlayer transport is enhanced for driving frequencies that are slightly blue-detuned from the Higgs frequency, while it is diminished on the red-detuned side. Increasing the driving strength amplifies the suppression/enhancement
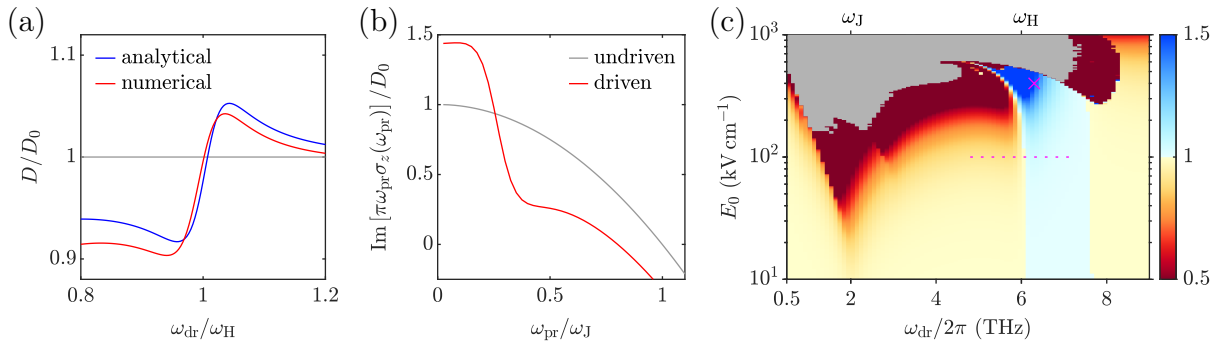
Figure 3.4: Higgs mode mediated enhancement of interlayer transport in a light-driven monolayer cuprate at zero temperature. (a) Dependence of the superconducting weight on the driving frequency, normalized by its equilibrium value. The driving strength is fixed at $E_0 = 100 \text{ kV cm}^{-1}$ as indicated by the dotted line in (c). (b) Imaginary part of the z-axis conductivity multiplied by the probing frequency. The driving parameters are $\omega_{\mathrm{dr}} = 1.05 \, \omega_{\mathrm{H}}$ and $E_0 = 400 \text{ kV cm}^{-1}$ as indicated by the cross in (c). (c) Superconducting weight as a function of the driving frequency and the driving strength. The gray area marks the heating regime. The results in (b) and (c) are obtained numerically. This figure is adapted from Ref. [H2].

effects and additionally renormalizes the resonance frequencies, which is inherent to non-linear oscillators [173]. The renormalization of the Higgs frequency results in the bending of the enhancement regime towards lower driving frequencies for stronger driving. The enhancement regime is limited by the onset of heating for large driving strengths.

For driving frequencies below ω_{H}, the strongest suppression of interlayer transport occurs close to the Josephson plasma frequency. Strikingly, there is a second suppression regime for driving frequencies of $\omega_{\mathrm{dr}} \approx \omega_{\mathrm{H}} + \omega_{\mathrm{J}}$. In fact, this regime corresponds to the time-crystalline phase discussed in the previous section, demonstrating that the emergence of a Higgs time crystal does not depend on the ratio of the Higgs frequency and the Josephson plasma frequency. In particular, we also find a Higgs time crystal for realistic parameters of a monolayer cuprate. Furthermore, we note that the sum frequency $\omega_{\mathrm{H}} + \omega_{\mathrm{J}}$

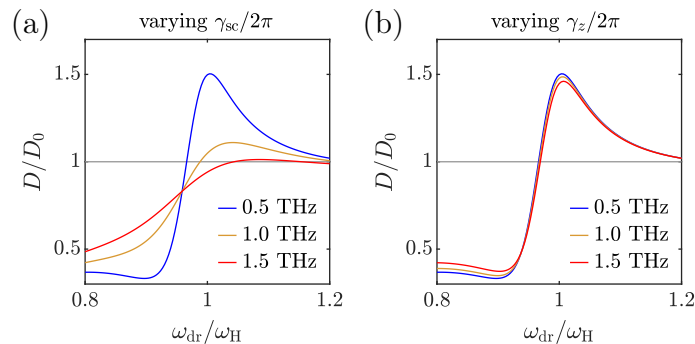**Figure 3.5:** Dependence of Higgs mode mediated enhancement of interlayer transport on the damping constants. (a) γ_{H} is varied while $\gamma_{\mathrm{J}}/2\pi = 0.5$ THz is fixed. (b) γ_{J} is varied while $\gamma_{\mathrm{H}}/2\pi = 0.5$ THz is fixed. The driving strength is $E_0 = 300 \text{ kV cm}^{-1}$. This figure is adapted from Ref. [H2].

bounds the enhancement regime with respect to the driving frequency. This upper bound originates from higher order terms that are not included in our analytical calculation. According to the analytical prediction for the z-axis conductivity in Eq. (3.7), we expect an upper bound of $\omega_{\mathrm{dr}} = \sqrt{3}\omega_{\mathrm{H}}$ for the enhancement regime.

We continue our analysis in Ref. [H2] by varying the damping constants in the simulation. Considering higher values of γ_{sc} is particularly interesting because the Higgs mode is strongly damped in cuprate superconductors [134, 135, 176, 177]. Figure 3.5 shows that the enhancement of interlayer transport significantly decreases for larger values of γ_{sc} while stronger damping of the Josephson plasma mode has a negligible effect. Finite-temperature simulations indicate Higgs mode mediated enhancement of interlayer transport for temperatures up to $\sim 0.1\,T_c$; see Supplemental Material of Ref. [H2]. Therefore, we propose to experimentally study this effect at low temperature first. We emphasize that the enhancement mechanism presented in this section is broadly applicable to cuprate superconductors because it does not rely on the existence of suitable phonon modes. The main limiting factor is the damping of the Higgs mode.

3.3 Parametric amplification of terahertz radiation

In Ref. [H3], we show how the nonlinear coupling of a plasma mode and another collective mode can be exploited for parametric amplification of terahertz radiation. Specifically, we demonstrate gain reflectivity for two examples. Firstly, we consider the nonlinear coupling between the Higgs mode and the Josephson plasma mode in a monolayer cuprate. Secondly, we consider the nonlinear coupling between a phonon mode and the upper Josephson plasma mode in a bilayer cuprate.

As in the previous sections, we assume that the monolayer cuprate is periodically driven by an electric field polarized along the z axis. We simulate the fully nonlinear two-mode model given by Eqs. (3.1) and (3.2) with the parameters $\omega_{\mathrm{J}}/2\pi = 2$ THz,
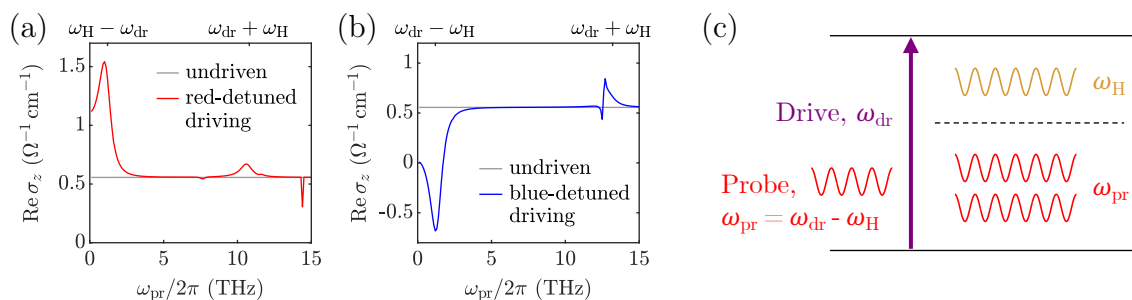

Figure 3.6: Parametric amplification of terahertz radiation in a light-driven monolayer cuprate, mediated by the Higgs mode. (a) Real part of the z-axis conductivity for $\omega_{\mathrm{dr}} < \omega_{\mathrm{H}}$. The driving frequency is $\omega_{\mathrm{dr}}/2\pi = 4.8$ THz and the driving strength is $E_0 = 150\,\mathrm{kV\,cm^{-1}}$. (b) Real part of the z-axis conductivity for $\omega_{\mathrm{dr}} > \omega_{\mathrm{H}}$. The driving frequency is $\omega_{\mathrm{dr}}/2\pi = 7.2$ THz and the driving strength is $E_0 = 300\,\mathrm{kV\,cm^{-1}}$. (c) Schematic illustration of the amplification process corresponding to the negative conductivity in (b). The drive induces Josephson plasma oscillations, which are down-converted to the probe frequency by simultaneous excitation of the Higgs mode. This figure is adapted from Ref. [H3].
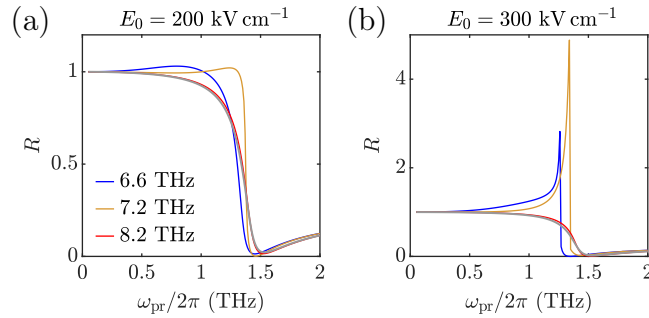
Figure 3.7: Higgs mode mediated gain reflectivity in a light-driven monolayer cuprate. The reflectivity at normal incidence is shown for two choices of the driving strength: (a) $E_0 = 200 \text{ kV cm}^{-1}$, (b) $E_0 = 300 \text{ kV cm}^{-1}$. The driving frequencies are indicated in (a). Gray lines correspond to the undriven case. The probe strength is $E_{\text{pr}} = 1 \text{ kV cm}^{-1}$. This figure is adapted from Ref. [H2].

$\omega_{\text{H}}/2\pi = 6$ THz, $\gamma_z/2\pi = 0.25$ THz, $\gamma_{\text{sc}}/2\pi = 1$ THz, $\alpha = 1$, $d_z = 10$ Å, and $\epsilon_\infty = 4$. The real part of the z-axis conductivity is displayed for two different sets of driving parameters in Figs. 3.6(a) and 3.6(b). For a driving frequency that is red-detuned from the Higgs frequency, the conductivity exhibits a pronounced absorption peak at $\omega_{\text{pr}} \approx \omega_{\text{H}} - \omega_{\text{dr}}$. In this case, the Higgs mode is resonantly excited due to the mixing of the probe with Josephson plasma oscillations induced by the drive. This process is enabled by the cubic coupling Lagrangian $\theta_z^2 h$ and leads to parametric attenuation of the probe. When the driving frequency is blue-detuned from the Higgs frequency, the probe is parametrically amplified as Josephson plasma oscillations at the driving frequency are down-converted to the probing frequency by simultaneous excitation of the Higgs mode, which serves as an idler mode. Thus, we find a minimum of the conductivity at $\omega_{\text{pr}} \approx \omega_{\text{dr}} - \omega_{\text{H}}$. In the example shown in 3.6(b), parametric amplification dominates over absorption due to quasiparticles, resulting in a negative conductivity.

In the following, we focus on blue-detuned driving and compute the reflectivity at normal incidence from the optical conductivity using the Fresnel equation

$$R(\omega) = \left| \frac{1 - n(\omega)}{1 + n(\omega)} \right|^2. \tag{3.9}$$

The refractive index $n(\omega) = \pm\sqrt{\epsilon_z(\omega)}$ is a function of the dielectric permittivity $\epsilon_z(\omega) = \epsilon_\infty + i\sigma_z(\omega)/\epsilon_0\omega$. The sign of the refractive index for a given frequency is fixed by causality [178–180]. We choose the positive sign unless both the real part and the imaginary part of $\epsilon_z(\omega)$ are negative. Thus, incident radiation penetrates the bulk at frequencies above the Josephson plasma edge around $\omega_{\text{J}}/\sqrt{2}$ while it is screened from the bulk at lower frequencies. In fact, the reflectivity is larger than 1 at probe frequencies below the Josephson plasma edge as one can see in Fig. 3.7. This is a direct consequence of the negative conductivity for driving frequencies blue-detuned from the Higgs frequency. Naturally, the enhancement of the reflectivity is more pronounced for the larger driving strength in Fig. 3.7(b) than for the smaller driving strength in Fig. 3.7(a). The amplification mechanism is particularly effective if the detuning $\omega_{\text{dr}} - \omega_{\text{H}}$ approaches the Josephson plasma edge. The latter is the case for $\omega_{\text{dr}}/2\pi = 7.2$ THz. We note that the
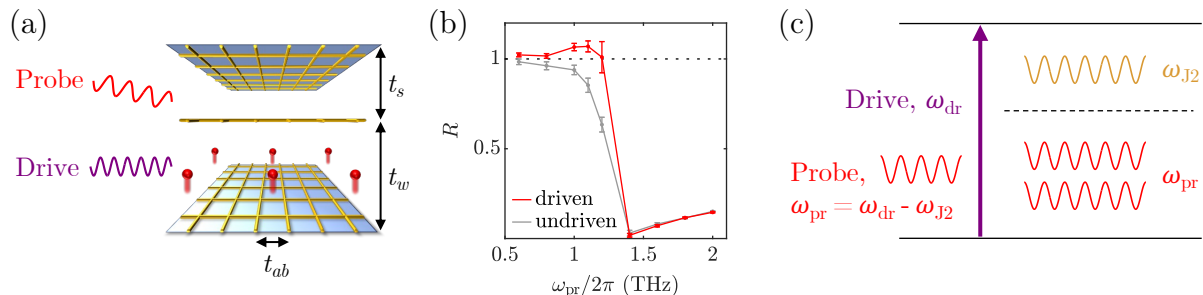
Figure 3.8: Parametric amplification of terahertz radiation in a light-driven bilayer cuprate, mediated by a phonon mode. (a) The optical drive resonantly excites a phonon mode, represented by the red atoms moving along the z axis. (b) Reflectivity at normal incidence in the presence of driving at $T = 5$ K $\sim 0.2\,T_c$. The driving frequency is $\omega_{dr}/2\pi = 14.8$ THz, and the modulation amplitudes are $M_s = 0.2$ and $M_w = 0.8$. The upper Josephson plasma frequency is $\omega^*_{J2} \approx 13.8$ THz at this temperature. The error bars indicate the standard errors of the ensemble averages. The probe strength is $E_{pr} = 30$ kV cm^{-1}. (c) Schematic illustration of the amplification process corresponding to the gain reflectivity in (b). This figure is adapted from Ref. [H3].

driving causes a small reduction of the time-averaged order parameter, resulting in a shift of the Josephson plasma edge to a slightly lower frequency.

Next, we put forth a phonon mediated mechanism for parametric amplification of terahertz radiation in Ref. [H3]. To this end, we simulate a bilayer cuprate with $40 \times 40 \times 4$ lattice sites at nonzero temperature. We assume that the bilayer cuprate has an infrared-active phonon mode whose resonance frequency is slightly blue-detuned from the upper Josephson plasma frequency. Furthermore, we assume that the interlayer tunneling is modulated by resonantly driving the phonon mode as depicted in Fig. 3.8(a). We include the phononic excitation in our model by making the interlayer tunneling coefficients time-dependent [101, 102], i.e.,

$$t_{s,w} \to t_{s,w} \left[1 \pm M_{s,w} \cos(\omega_{dr} t) \right] \tag{3.10}$$

in the limit of large wavelengths. We then evaluate the ensemble average of the z-axis conductivity as described in Section 2.3.4 and determine the reflectivity via the Fresnel equation. In Fig. 3.8(b), we show that phonon mediated driving induces a reflectivity of $R > 1$ in the low-terahertz regime despite the presence of thermal broadening at a temperature of $\sim 0.2\,T_c$. Here, the cubic coupling $\sim t_{z,\mathbf{r}}\theta^2_{z,\mathbf{r}}$ of the tunneling coefficients and the plasmonic degrees of freedom enables the parametric amplification of terahertz radiation. Remarkably, this parametric amplification is effective for probe frequencies below the lower Josephson plasma edge around $\omega_{J1}/\sqrt{2}$ while the upper Josephson plasma mode serves as an idler mode. In principle, the lower Josephson plasma mode can also act as an idler mode. However, this is not useful for the amplification of radiation with frequencies of ~ 1 THz since it requires the driving frequency to be in the same regime. We note that phonon mediated amplification of terahertz radiation is feasible for probe strengths up to 100 kV cm^{-1} according to our simulations. In addition to gain reflectivity, we observe a parametric enhancement of the imaginary part of σ_z at low frequencies, which was previously discussed in Refs. [101, 102]. We will investigate this enhancement of interlayer transport more closely in the following section.
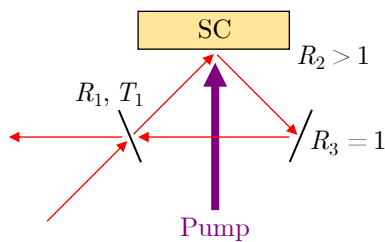
Figure 3.9: Setup of a terahertz amplifier using a light-driven superconductor (SC) with reflectivity $R_2 > 1$ as a gain medium. This figure is adapted from Ref. [H3].

A key feature of both amplification mechanisms presented in this section is that the enhancement of the reflectivity is controlled by the driving frequency and the driving strength. We emphasize that the phonon mediated amplification mechanism requires the existence of a suitable phonon mode. In many cases, parametric amplification of terahertz radiation is limited by the fact that the penetration depth of the drive is smaller than the penetration depth of the probe [90, 91, 113]. To reduce the mismatch of the penetration depths, we recommend to choose a large incident angle for the probe beam while orienting the pump beam parallel to the surface normal. The general idea to exploit the nonlinear coupling of light to collective modes can also be applied to other materials. To achieve gain reflectivity, one should consider only materials with a reflectivity of nearly 1 in equilibrium.

We suggest to first test our proposal using pump pulses with a duration of ~ 1 ps. If a significant net amplification of terahertz radiation is observed, one could aim to implement a terahertz amplifier as sketched in Fig. 3.9. In this setup, a light-driven superconductor with reflectivity $R_2 = R(\omega_{\mathrm{pr}}) > 1$ serves as one of three mirrors forming an optical resonator. The probe enters the resonator through a partially transparent mirror with reflectivity $R_1 < 1$ and transmissivity $T_1 > 0$. Assuming the third mirror to have perfect reflectivity $R_3 = 1$, the probe is amplified for $R_2 > 1/R_1$. Above this threshold, the gain saturates once the probe strength enters the nonlinear response regime, where $R(\omega_{\mathrm{pr}})$ decreases. The realization of such a terahertz amplifier requires to overcome several technical challenges. Most importantly, the duration of the pump pulse has to be extended to ~ 1 ns as in Ref. [111] so that the probe pulse can travel several times around the optical resonator. This would allow for a terahertz amplifier in pulsed operation, which is also advantageous with respect to surface heating. Ultimately, it should be tested experimentally whether there are materials and conditions for which a terahertz amplifier can be realized. The development of a terahertz amplifier is relevant since the intensity of existing sources of coherent terahertz radiation [181–185] limits their application for spectroscopy and imaging [186–190].

3.4 Parametric control of Meissner screening

In Ref. [H4], we investigate the Meissner effect in a parametrically driven superconductor. Specifically, we consider periodic driving of the z-axis tunneling, which has been proposed as a possible mechanism for light-enhanced interlayer transport in YBCO [101, 102]. First, we confirm that the superconducting weight in the z-axis conductivity is enhanced if the
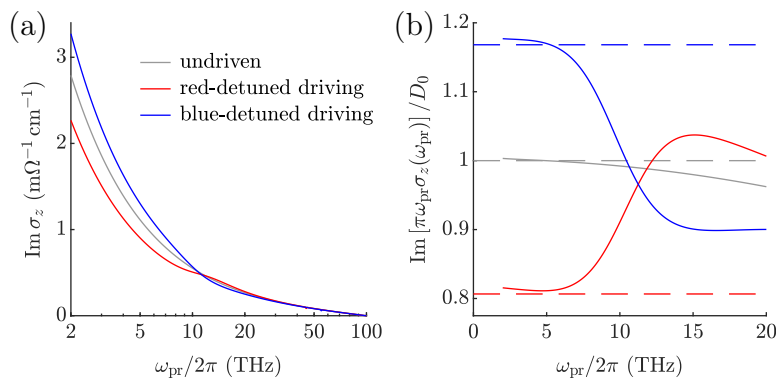
Figure 3.10: Renormalization of z-axis transport in a parametrically driven superconductor. (a) Imaginary part of the z-axis conductivity. (b) Imaginary part of the z-axis conductivity multiplied by the probe frequency. The dashed lines indicate the analytical prediction for the superconducting weight, which corresponds to the zero-frequency limit of $\mathrm{Im}\,[\pi\omega_{\mathrm{pr}}\sigma_z(\omega_{\mathrm{pr}})]$. The z-axis tunneling coefficient is driven with the frequency $\omega_{\mathrm{dr}} = 0.9\,\omega_{\mathrm{pl}}$ in the red-detuned case and with the frequency $\omega_{\mathrm{dr}} = 1.1\,\omega_{\mathrm{pl}}$ in the blue-detuned case. The driving strength is $M = 0.3$ in both cases. The plasma frequency is $\omega_{\mathrm{pl}}/2\pi = 100$ THz and the sample height is $100\,\mu$m. This figure is adapted from Ref. [H4].

driving frequency is blue-detuned from the z-axis plasma frequency. We then examine the response to an applied magnetic field analytically and numerically. Our calculations demonstrate a reduction of the Meissner screening for blue-detuned driving, which is in contrast to the enhancement of z-axis transport. For red-detuned driving, on the other hand, the Meissner screening displays a tendency to be enhanced while the z-axis transport is reduced.

Due to computational constraints, we focus on an isotropic superconductor with plasma frequency ω_{pl}. Additionally, we restrict our analysis to zero temperature and neglect spatial variations along the y axis. In the simulation, we employ open boundary conditions in the x and z direction, which enables us to impose a magnetic field at the surfaces of the superconductor. The superconductor is driven by a periodic modulation of the tunneling coefficients of all z-axis junctions,

$$t_z \rightarrow t_z \left[1 + M \cos(\omega_{\mathrm{dr}}t)\right]. \tag{3.11}$$

In Fig. 3.10(a), we show the effect of this parametric driving on the imaginary part of the z-axis conductivity. While the imaginary part of σ_z is reduced for $\omega_{\mathrm{dr}} < \omega_{\mathrm{pl}}$ at probe frequencies $\omega_{\mathrm{pr}} \lesssim |\omega_{\mathrm{pl}} - \omega_{\mathrm{dr}}|$, the imaginary part of σ_z is enhanced for $\omega_{\mathrm{dr}} > \omega_{\mathrm{pl}}$. According to Ref. [101], the imaginary part of the z-axis conductivity approaches a $1/\omega_{\mathrm{pr}}$ behavior at low probe frequencies also in the driven state. The superconducting weight is predicted as

$$D = D_0 \left(1 - \frac{M^2\omega_{\mathrm{pl}}^2(\omega_{\mathrm{pl}}^2 - \omega_{\mathrm{dr}}^2)}{2(\omega_{\mathrm{pl}}^2 - \omega_{\mathrm{dr}}^2)^2 + 2\gamma_z^2\omega_{\mathrm{dr}}^2}\right), \tag{3.12}$$

where $D_0 = \pi\epsilon_\infty\epsilon_0\omega_{\mathrm{pl}}^2$ is the superconducting weight in equilibrium. This prediction is in good agreement with our numerical results for $M = 0.3$ as highlighted by Fig. 3.10(b). In the blue-detuned case of $\omega_{\mathrm{dr}} = 1.1\,\omega_{\mathrm{pl}}$, the superconducting weight is enhanced by
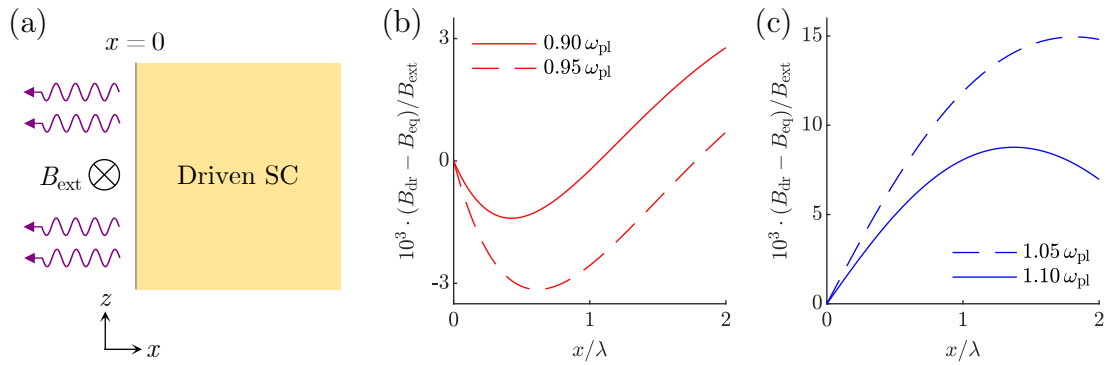
Figure 3.11: Analytical results for the Meissner screening in a parametrically driven superconductor. (a) A static magnetic field is applied at the surface of a parametrically driven superconductor, inducing the emission of electromagnetic waves. The magnetic field is oriented along the y axis. (b) Spatial dependence of the DC magnetic field for $M = 0.3$ and two different red-detuned driving frequencies. (c) Spatial dependence of the DC magnetic field for $M = 0.3$ and two different blue-detuned driving frequencies. In (b) and (c), the equilibrium magnetic field $B_{\mathrm{eq}} = B_{\mathrm{ext}} \exp(-x/\lambda)$ is subtracted. Panels (b) and (c) are adapted from Ref. [H4].

approximately 17%. In the red-detuned case of $\omega_{\mathrm{dr}} = 0.9\,\omega_{\mathrm{pl}}$, the superconducting weight is reduced by approximately 19%. We note that the numerical results slightly deviate from the predicted $1/\omega_{\mathrm{pr}}$ behavior due to the insufficiently small probe frequencies and the finite system size.

We now turn to the response of a parametrically driven superconductor to an applied static magnetic field. In Ref. [H4], we derive an analytical prediction for the magnetic field inside a parametrically driven superconductor. Specifically, we apply a weak DC magnetic field B_{ext} at the surface and allow for the emission of electromagnetic waves induced by the driving. The considered geometry is depicted in Fig. 3.11(a). Our prediction is valid close to the center of the surface. In general, parametric driving has two effects on the DC magnetic field inside the superconductor. Firstly, the London penetration depth $\lambda = c/\omega_{\mathrm{pl}}\sqrt{\epsilon_\infty}$ is slightly reduced. This renormalization alone would imply an enhanced screening. However, the driving also induces an additional contribution to the DC magnetic field, which is screened similarly to an AC magnetic field in equilibrium, The penetration depth of this contribution is approximately

$$\lambda(\omega_{\mathrm{dr}}) = \frac{\lambda}{\sqrt{1 - \omega_{\mathrm{dr}}^2/\omega_{\mathrm{pl}}^2}}, \tag{3.13}$$

implying less effective screening for driving frequencies that are red-detuned from the plasma frequency. Taking both contributions to the DC magnetic field into account, the Meissner screening close to the surface is slightly enhanced for red-detuned driving, as visible in Fig. 3.11(b). Further away from the surface, the slower decaying contribution dominates such that the DC magnetic field is larger than in the absence of driving. The length scale of enhanced screening grows with decreasing detuning $\omega_{\mathrm{pl}} - \omega_{\mathrm{dr}}$. In the case of blue-detuned driving, the second contribution to the DC magnetic field is not screened but oscillates in space. Thus, the Meissner screening is generally lessened for blue-detuned driving. This is evidenced by Fig. 3.11(c).
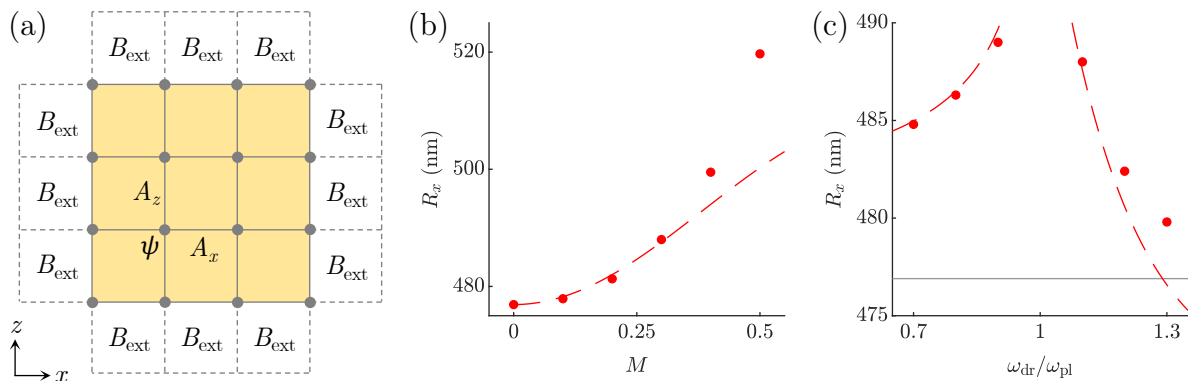
Figure 3.12: Numerical results for the Meissner screening in a parametrically driven superconductor. (a) Setup of the lattice gauge simulation with a fixed magnetic field at the surface. (b) Attenuation length for $\omega_{\mathrm{dr}} = 1.1\,\omega_{\mathrm{pl}}$ and different driving strengths. (c) Attenuation length for $M = 0.3$ and different driving frequencies. The gray line indicates the equilibrium value $\lambda = 477$ nm. In panels (b) and (c), the dashed red line indicates the analytical solution for the attenuation length. The system size is $12 \times 12\ \mu\mathrm{m}^2$, except for the two largest driving frequencies in (c), where converged results are obtained for a system size of $16 \times 16\ \mu\mathrm{m}^2$. This figure is adapted from Ref. [H4].

In our simulations, we impose a weak DC magnetic field $\mathbf{B} = B_{\mathrm{ext}}\hat{\mathbf{y}}$ at the surface of the superconductor as shown in Fig. 3.12(a), neglecting the emission of electromagnetic waves. We also determine the analytical solution for this boundary condition and compare it our numerical results below. We find that the analytical solution is not affected in the case of blue-detuned driving. However, the modified boundary condition suppresses the enhancement regime for red-detuned driving.

In Ref. [H4], we simulate the Meissner effect in an isotropic superconductor with a plasma frequency of $\omega_{\mathrm{pl}}/2\pi = 100$ THz. In the presence of driving, the magnetic field inside the superconductor oscillates with the driving frequency. While the magnetic field is screened from the bulk for red-detuned driving, blue-detuned driving stimulates the transmission of electromagnetic waves into the bulk. Nevertheless, the magnitude of the magnetic field inside the superconductor is strongly suppressed compared to the surface field B_{ext} even in this case. To evaluate the DC magnetic field, we average the magnetic field over 1 ps with a detection rate of 5 PHz. We then characterize the Meissner screening in the driven state by the attenuation length R_x, which is defined by the condition $B_y(x = R_x) = B_{\mathrm{ext}} \exp(-1)$. In equilibrium, the attenuation length equals the London penetration depth, i.e., $R_x = \lambda$. The attenuation length R_x grows monotonically with increasing driving amplitude as shown in Fig. 3.12(b). The numerical results show good agreement with the analytical solution for $M \leq 0.3$. The dependence of R_x on the driving frequency is displayed in Figure 3.12(c). As mentioned, the Meissner screening is reduced also for red-detuned driving if the emission of electromagnetic waves is surpressed. We note that the screening of AC magnetic fields with frequencies of ~ 1 THz is consistent with the screening of a DC magnetic field; see Supplemental Material of Ref. [H4]. Furthermore, we simulate an anisotropic superconductor whose in-plane plasma frequency is six times as large as the z-axis plasma frequency. We find a similar renormalization of the attenuation length as in the isotropic case, consistent with the fact that our analytical prediction is

also valid for anisotropic superconductors. Therefore, we expect that our results apply to cuprate superconductors, at least qualitatively.

Our analysis suggests that the enhancement of the low-frequency conductivity is naturally accompanied by a suppression of the Meissner effect when the z-axis tunneling is periodically driven with a frequency blue-detuned from the z-axis plasma frequency. While the admixture of the plasma resonance into the low-frequency response provides an enhanced conductivity, it results in a reduced Meissner screening due to the transmission of unscreened plasma waves into the superconductor.

Chapter 4

Conclusion

In this dissertation, we have presented a newly developed semiclassical method for the simulation of cuprate superconductors, based on the Ginzburg-Landau theory of superconductivity. Using this method, we have analyzed the fluctuating dynamics in a bilayer cuprate at nonzero temperature and discussed several light-induced nonequilibrium phenomena in monolayer and bilayer cuprates. An important feature of our method is the possibility to implement various driving mechanisms and to simulate the response to electric and magnetic probes.

Our method explicitly captures the coupled dynamics of the superconducting order parameter and the electromagnetic field on a layered lattice. The coupling to other degrees of freedom, such as quasiparticles and the ionic lattice, is included in the form of dissipation and thermal fluctuations. After characterizing the superconducting ground state of a bilayer cuprate at zero temperature, we investigate its fluctuating dynamics at nonzero temperature. Thermal fluctuations reduce the phase coherence of the superconducting state at low temperature and cause a phase transition to a resistive state at high temperature. This resistive state is characterized by a strong suppression of the interbilayer tunneling of Cooper pairs and the emergence of vortex excitations. Remarkably, the upper Josephson plasma frequency decreases slower than the thermal average of the intrabilayer coupling. While analytical calculations indicate two possible mechanisms for a stabilization of the upper Josephson plasma frequency due to vortex-induced disorder, a complete understanding of its temperature dependence requires further research.

The resistive state that we find constitutes a possible scenario of the pseudogap regime in underdoped cuprates. The dependence of the critical temperature on the in-plane coupling seems to follow the scaling of a Kosterlitz-Thouless transition. Investigating the phase transition in more detail might be an interesting direction for future work. To this end, it would be desirable to simulate larger systems. Increasing the system size would allow to vary the in-plane coupling over a larger range and to explore the influence of magnetic fluctuations. At this stage, magnetic interactions between vortices are strongly suppressed as the system size is smaller than the London penetration depth.

In our discussion of light-induced nonequilibrium phenomena, we focus on temperatures well below T_c. Specifically, we consider the periodic driving of a cuprate superconductor by an electric field polarized along the crystalline c axis, implementing two different scenarios. In the first scenario, the electric field directly couples to the superconducting order parameter. In the second scenario, the electric field resonantly couples to an

infrared-active phonon mode, resulting in a periodic modulation of the coupling between the superconducting layers. In both cases, the properties of the driven state critically depend on the driving strength and the driving frequency.

Driving a superconductor via the nonlinear coupling of the electric field to the order parameter gives rise to Higgs oscillations. We propose to induce a time-crystalline state in a mono- or bilayer cuprate by driving a sum resonance of the Higgs mode and the Josephson plasma mode or the upper Josephson plasma mode, respectively. We identify the emergence of two pronounced side peaks in the power spectrum of the c-axis supercurrents as a possible experimentally accessible signature of this Higgs time crystal, which is visible also for pulsed driving. It remains an open question whether a Higgs time crystal can be observed experimentally since the Higgs mode is strongly damped in cuprate superconductors. Another noteworthy aspect is that the time-crystalline state emerges for optical driving with photon energies above the superconducting gap. Thus, pair-breaking is a competing process, which is not fully captured by our method. The importance of pair breaking depends on the microscopic nature of the superconducting state in the cuprates. The creation of a Higgs time crystal is favored by the scenario of preformed pairs in underdoped cuprates, with the pseudogap corresponding to an effective pairing energy.

Based on the nonlinear coupling between the electric field and the Higgs mode, we put forth a mechanism for the enhancement of interlayer transport in monolayer cuprates, which is qualitatively different from previous proposals [98–105]. We demonstrate that the superconducting weight in the c-axis conductivity is enhanced when the frequency of the optical driving is slightly blue-detuned from the Higgs frequency. The enhancement effect is limited by the damping of the Higgs mode, and we recommend to first test our proposal in experiments at low temperature.

Furthermore, we show how the nonlinear coupling of a plasma mode to another collective mode can be exploited for parametric amplification of terahertz radiation. We present two specific protocols to implement this general proposal. The first protocol applies to monolayer cuprates and exploits the nonlinear coupling to the Higgs mode. The second protocol applies to bilayer cuprates and exploits the nonlinear coupling to an infrared-active phonon mode that modulates the interlayer coupling. Here, parametric amplification of terahertz radiation is possible only if the resonance frequency of the phonon mode is slightly blue-detuned from the upper Josephson plasma frequency. We also propose a design of a terahertz amplifier using a light-driven superconductor as a gain medium. The realization of such a terahertz amplifier is associated with several technical challenges and its feasibility remains an open question.

Parametric driving of a cuprate superconductor via a suitable phonon mode also enables an enhancement of interlayer transport as reported in Ref. [101, 102]. This was proposed as a possible explanation for the observation of light-enhanced transport in YBCO [90, 91]. We confirm that the superconducting weight in the c-axis conductivity is enhanced when the driving frequency is blue-detuned from a Josephson plasma frequency, while it is diminished by red-detuned driving. In contrast, both our analytical and numerical calculations show that blue-detuned driving reduces the Meissner screening as plasma waves generated at the surface are transmitted into the superconductor. For red-detuned driving, on the other hand, we find a tendency to an enhanced Meissner screening. These results suggest that the light-induced state considered here is a genuinely non-equilibrium

state, rather than a renormalized equilibrium state, in which some of the reasoning derived from equilibrium superconductors does not apply. This insight is generally relevant for the interpretation of pump-probe experiments indicating light-enhanced or light-induced superconductivity.

It would be interesting to investigate the enhancement mechanism presented in Refs. [92, 105] with our method. According to these works, the enhancement of inter-layer transport in YBCO is mediated by the decay of optically excited phonons into pairs of Josephson plasmons with opposite in-plane momenta, which give rise to spatial and temporal modulations of the superfluid density. However, the limitation of computational resources does not currently allow for the simulation of sufficiently large systems with an in-plane discretization of the order of the coherence length. Our present simulations do not include the range of in-plane momenta that are relevant for the mechanism reported in Refs. [92, 105]. In principle, this problem can be circumvented by choosing an artificially high background permittivity of $\epsilon_\infty \sim 10^5$. In addition to increasing the system size, larger computational resources might enable convergent measurements of the c-axis conductivity at temperatures around T_c as one could simulate larger ensembles.

Appendix A

Details on the numerical implementation

Here, we elaborate on the numerical integration of the stochastic differential equations (2.11) and (2.12),

$$\partial_t^2 \psi_{\mathbf{r}} = \frac{1}{K\hbar^2} \frac{\partial \mathcal{L}}{\partial \psi_{\mathbf{r}}^*} - \gamma_{\text{sc}} \partial_t \psi_{\mathbf{r}} + \xi_{\mathbf{r}}, \tag{A.1}$$

$$\partial_t^2 A_{j,\mathbf{r}} = \frac{1}{\epsilon_\infty \epsilon_0} \frac{\partial \mathcal{L}}{\partial A_{j,\mathbf{r}}} - \gamma_{j,\mathbf{r}} \partial_t A_{j,\mathbf{r}} + \eta_{j,\mathbf{r}} \text{ for } j \in \{x, y, z\}. \tag{A.2}$$

The Langevin noise terms $\xi_{\mathbf{r}}$ and $\boldsymbol{\eta}_{\mathbf{r}}$ have zero mean and follow Gaussian distributions [191, 192]. The noise of the superconducting order parameter has the properties

$$\langle \text{Re}\{\xi_{\mathbf{r}}(t)\} \text{Re}\{\xi_{\mathbf{r}'}(t')\}\rangle = \frac{\gamma_{\text{sc}} k_{\text{B}} T}{K\hbar^2 V_0} \delta_{\mathbf{r}\mathbf{r}'} \delta(t - t'), \tag{A.3}$$

$$\langle \text{Im}\{\xi_{\mathbf{r}}(t)\} \text{Im}\{\xi_{\mathbf{r}'}(t')\}\rangle = \frac{\gamma_{\text{sc}} k_{\text{B}} T}{K\hbar^2 V_0} \delta_{\mathbf{r}\mathbf{r}'} \delta(t - t'), \tag{A.4}$$

$$\langle \text{Re}\{\xi_{\mathbf{r}}(t)\} \text{Im}\{\xi_{\mathbf{r}'}(t')\}\rangle = 0, \tag{A.5}$$

where $V_0 = d_{ab}^2 d_c$. The noise correlations for the vector potential are

$$\langle \eta_{x,\mathbf{r}}(t)\eta_{x,\mathbf{r}'}(t')\rangle = \frac{2\gamma_{ab} k_{\text{B}} T}{\epsilon_\infty \epsilon_0 V_0} \delta_{\mathbf{r}\mathbf{r}'} \delta(t - t'), \tag{A.6}$$

$$\langle \eta_{y,\mathbf{r}}(t)\eta_{y,\mathbf{r}'}(t')\rangle = \frac{2\gamma_{ab} k_{\text{B}} T}{\epsilon_\infty \epsilon_0 V_0} \delta_{\mathbf{r}\mathbf{r}'} \delta(t - t'), \tag{A.7}$$

$$\langle \eta_{z,\mathbf{r}}(t)\eta_{z,\mathbf{r}'}(t')\rangle = \frac{2\gamma_{z,\mathbf{r}} k_{\text{B}} T}{\kappa_{z,\mathbf{r}} \epsilon_\infty \epsilon_0 V_0} \delta_{\mathbf{r}\mathbf{r}'} \delta(t - t'). \tag{A.8}$$

We introduce the conjugate fields $\pi_{\mathbf{r}}$ and $\mathbf{E}_{\mathbf{r}}$ in order to obtain two sets of first order differential equations,

$$\partial_t \psi_{\mathbf{r}} = \frac{\pi_{\mathbf{r}}}{K\hbar^2}, \tag{A.9}$$

$$\partial_t A_{j,\mathbf{r}} = -E_{j,\mathbf{r}}. \tag{A.10}$$

$$t + \Delta t \quad \text{---} \quad \psi, \mathbf{A}$$
$$t + \Delta t/2 \quad \text{---} \quad \pi, \mathbf{E}$$
$$t \quad \text{---} \quad \psi, \mathbf{A}$$
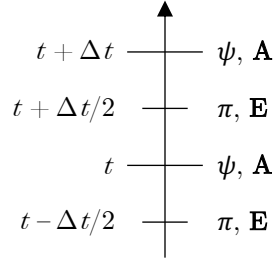$$t - \Delta t/2 \quad \text{---} \quad \pi, \mathbf{E}$$

Figure A.1: The temporal discretization is consistent with a leapfrog scheme.

The equations of motion for the conjugate fields are shown explicitly at the end of this section. The general form of the equations of motion is

$$\partial_t Q_i(t) = f[P_i(t)], \tag{A.11}$$

$$\partial_t P_i(t) = g[\{Q_i(t)\}] - \gamma_i P_i(t) + \xi_i(t), \tag{A.12}$$

where $\{Q_i\} = \{\psi_{\mathbf{r}}, A_{\mathbf{r}}^x, A_{\mathbf{r}}^y, A_{\mathbf{r}}^z\}$ and $\{P_i\} = \{\pi_{\mathbf{r}}, E_{\mathbf{r}}^x, E_{\mathbf{r}}^y, E_{\mathbf{r}}^z\}$. Our numerical implementation picks up on elements of the leapfrog scheme [193] and Heun's method [194, 195]. The fields Q_i and their conjugate fields P_i are staggered in time as depicted in Fig. A.1. The integration steps are performed according to

$$Q_i(t + \Delta t) = Q_i(t) + f[P_i(t + \Delta t/2)] \cdot \Delta t, \tag{A.13}$$

$$
\begin{aligned}
P_i(t + \Delta t/2) = {}& P_i(t - \Delta t/2) + g[\{Q_i(t)\}] \cdot \Delta t \\
& + \left(-\gamma_i P_i(t - \Delta t/2) + \xi_i(t - \Delta t/2) \right) \cdot \Delta t/2 \\
& + \left(-\gamma_i \tilde{P}_i(t + \Delta t/2) + \xi_i(t + \Delta t/2) \right) \cdot \Delta t/2,
\end{aligned} \tag{A.14}
$$

with $\tilde{P}_i(t + \Delta t/2) = P_i(t - \Delta t/2) + \left(g[\{Q_i(t)\}] - \gamma_i P_i(t - \Delta t/2) + \xi_i(t - \Delta t/2) \right) \cdot \Delta t$. The last two lines in Eq. (A.14) correspond to the predictor and corrector, respectively, in Heun's method. We implement the equations of motion in C++, compatible with the language standard ISO/IEC 14882:2011. We employ the random number generator mt19937 for the noise terms and draw new random numbers for both the predictor and corrector in each time step. Note that $\delta(t - t')$ transforms to $\delta_{tt'}/\Delta t$ in the simulation. We use a time step of $\Delta t = 1.25$ as $\approx d_s/c$, which yields convergent results as evidenced by Fig. A.2.

The explicit equation of motion for the conjugate field of the order parameter is

$$
\begin{aligned}
\partial_t \pi_{l,m,n} = {}& (\mu - 4t_{ab} - t_s - t_w)\psi_{l,m,n} - g|\psi_{l,m,n}|^2 \psi_{l,m,n} - \gamma_{\mathrm{sc}}\pi_{l,m,n} + \xi_{l,m,n} \\
& + t_{ab} \left(\psi_{l-1,m,n}e^{ia_{l-1,m,n}^x} + \psi_{l+1,m,n}e^{-ia_{l,m,n}^x} + \psi_{l,m-1,n}e^{ia_{l,m-1,n}^y} + \psi_{l,m+1,n}e^{-ia_{l,m,n}^y} \right) \\
& + t_{z,n-1}\psi_{l,m,n-1}e^{ia_{l,m,n-1}^z} + t_{z,n}\psi_{l,m,n+1}e^{-ia_{l,m,n}^z}.
\end{aligned} \tag{A.15}
$$

The explicit equations of motion for the electric field are

$$
\begin{aligned}
\partial_t & E^x_{l,m,n} \\
= & -\frac{J^x_{l,m,n}}{\epsilon_\infty \epsilon_0} - \gamma_{ab} E^x_{l,m,n} + \eta^x_{l,m,n} \\
& + \frac{c^2}{\beta_z d_{ab} \epsilon_\infty} \sin\left(\frac{\beta_z(A^y_{l+1,m,n} - A^y_{l,m,n})}{d_{ab}} - \frac{\beta_z(A^x_{l,m+1,n} - A^x_{l,m,n})}{d_{ab}} \right) \\
& - \frac{c^2}{\beta_z d_{ab} \epsilon_\infty} \sin\left(\frac{\beta_z(A^y_{l+1,m-1,n} - A^y_{l,m-1,n})}{d_{ab}} - \frac{\beta_z(A^x_{l,m,n} - A^x_{l,m-1,n})}{d_{ab}} \right) \\
& - \frac{c^2}{\beta_{y,n} d_c \epsilon_\infty} \sin\left(\frac{\beta_{y,n}(A^x_{l,m,n+1} - A^x_{l,m,n})}{d_{z,n}} - \frac{\beta_{y,n}(A^z_{l+1,m,n} - A^z_{l,m,n})}{d_{ab}} \right) \\
& + \frac{c^2}{\beta_{y,n} d_c \epsilon_\infty} \sin\left(\frac{\beta_{y,n}(A^x_{l,m,n} - A^x_{l,m,n-1})}{d_{z,n}} - \frac{\beta_{y,n}(A^x_{l+1,m,n-1} - A^x_{l,m,n-1})}{d_{ab}} \right),
\end{aligned}
\tag{A.16}
$$

$$
\begin{aligned}
\partial_t & E^y_{l,m,n} \\
= & -\frac{J^y_{l,m,n}}{\epsilon_\infty \epsilon_0} - \gamma_{ab} E^y_{l,m,n} + \eta^y_{l,m,n} \\
& + \frac{c^2}{\beta_{x,n} d_c \epsilon_\infty} \sin\left(\frac{\beta_{x,n}(A^z_{l,m+1,n} - A^z_{l,m,n})}{d_{ab}} - \frac{\beta_{x,n}(A^y_{l,m,n+1} - A^y_{l,m,n})}{d_{z,n}} \right) \\
& - \frac{c^2}{\beta_{x,n} d_c \epsilon_\infty} \sin\left(\frac{\beta_{x,n}(A^z_{l,m+1,n-1} - A^z_{l,m,n-1})}{d_{ab}} - \frac{\beta_{x,n}(A^y_{l,m,n} - A^y_{l,m,n-1})}{d_{z,n}} \right) \\
& - \frac{c^2}{\beta_z d_{ab} \epsilon_\infty} \sin\left(\frac{\beta_z(A^y_{l+1,m,n} - A^y_{l,m,n})}{d_{ab}} - \frac{\beta_z(A^x_{l,m+1,n} - A^x_{l,m,n})}{d_{ab}} \right) \\
& + \frac{c^2}{\beta_z d_{ab} \epsilon_\infty} \sin\left(\frac{\beta_z(A^y_{l,m,n} - A^y_{l-1,m,n})}{d_{ab}} - \frac{\beta_z(A^x_{l-1,m+1,n} - A^x_{l-1,m,n})}{d_{ab}} \right),
\end{aligned}
\tag{A.17}
$$

$$
\begin{aligned}
\partial_t & E^z_{l,m,n} \\
= & -\frac{J^z_{l,m,n}}{\epsilon_\infty \epsilon_0} - \gamma_{z,n} E^z_{l,m,n} + \eta^z_{l,m,n} \\
& + \frac{c^2}{\beta_{y,n} d_{ab} \epsilon_\infty} \sin\left(\frac{\beta_{y,n}(A^x_{l,m,n+1} - A^x_{l,m,n})}{d_{z,n}} - \frac{\beta_{y,n}(A^z_{l+1,m,n} - A^z_{l,m,n})}{d_{ab}} \right) \\
& - \frac{c^2}{\beta_{y,n} d_{ab} \epsilon_\infty} \sin\left(\frac{\beta_{y,n}(A^x_{l-1,m,n+1} - A^x_{l-1,m,n})}{d_{z,n}} - \frac{\beta_{y,n}(A^z_{l,m,n} - A^z_{l-1,m,n})}{d_{ab}} \right) \\
& - \frac{c^2}{\beta_{x,n} d_{ab} \epsilon_\infty} \sin\left(\frac{\beta_{x,n}(A^z_{l,m+1,n} - A^z_{l,m,n})}{d_{ab}} - \frac{\beta_{x,n}(A^y_{l,m,n+1} - A^y_{l,m,n})}{d_{z,n}} \right) \\
& + \frac{c^2}{\beta_{x,n} d_{ab} \epsilon_\infty} \sin\left(\frac{\beta_{x,n}(A^z_{l,m,n} - A^z_{l,m-1,n})}{d_{ab}} - \frac{\beta_{x,n}(A^y_{l,m-1,n+1} - A^y_{l,m-1,n})}{d_{z,n}} \right),
\end{aligned}
\tag{A.18}
$$

where $\beta_{x,n} = \beta_{y,n} = 2e d_{ab} d_{z,n}/\hbar$ and $\beta_z = 2e d_{ab}^2/\hbar$.
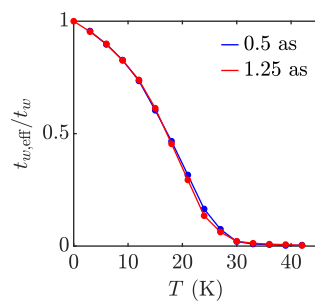
Figure A.2: Temperature dependence of the effective interbilayer tunneling coefficient for two different time steps. Each data point is an ensemble average of 100 trajectories and the standard error is comparable to the point size.

Appendix B

Details on the optical conductivity of a bilayer cuprate

B.1   Out-of-plane conductivity at zero temperature

In the following, we consider the case $\gamma_{\mathrm{sc}} = \gamma_s = \gamma_w \equiv \gamma$. We recall the equations of motion

$$\partial_t^2 \theta_s + \gamma \partial_t \theta_s + (1 + 2\alpha_s)\Omega_s^2 \theta_s - 2\alpha_w \Omega_w^2 \theta_w = \frac{2ed_s}{\epsilon_\infty \epsilon_0 \hbar} J_0 \cos(\omega_{\mathrm{pr}} t), \qquad (\text{B.1})$$

$$\partial_t^2 \theta_w + \gamma \partial_t \theta_w + (1 + 2\alpha_w)\Omega_w^2 \theta_w - 2\alpha_s \Omega_s^2 \theta_s = \frac{2ed_w}{\epsilon_\infty \epsilon_0 \hbar} J_0 \cos(\omega_{\mathrm{pr}} t) \qquad (\text{B.2})$$

from Section 2.2.3. We transform these equations into the frequency domain,

$$\left[-\omega_{\mathrm{pr}}^2 - i\gamma\omega_{\mathrm{pr}} + (1 + 2\alpha_s)\Omega_s^2 \right] \theta_s(\omega_{\mathrm{pr}}) - 2\alpha_w \Omega_w^2 \theta_w(\omega_{\mathrm{pr}}) = \frac{ed_s J_0}{\epsilon_\infty \epsilon_0 \hbar}, \qquad (\text{B.3})$$

$$\left[-\omega_{\mathrm{pr}}^2 - i\gamma\omega_{\mathrm{pr}} + (1 + 2\alpha_w)\Omega_w^2 \right] \theta_w(\omega_{\mathrm{pr}}) - 2\alpha_s \Omega_s^2 \theta_s(\omega_{\mathrm{pr}}) = \frac{ed_w J_0}{\epsilon_\infty \epsilon_0 \hbar}. \qquad (\text{B.4})$$

We also recall the generalized Josephson equations

$$\frac{\hbar}{2e} \partial_t \theta_s = (1 + 2\alpha_s)d_s E_s - 2\alpha_w d_w E_w, \qquad (\text{B.5})$$

$$\frac{\hbar}{2e} \partial_t \theta_w = (1 + 2\alpha_w)d_w E_w - 2\alpha_s d_s E_s, \qquad (\text{B.6})$$

and transform them into the frequency domain,

$$-\frac{i\omega\hbar}{2e} \theta_s(\omega_{\mathrm{pr}}) = (1 + 2\alpha_s)d_s E_s(\omega_{\mathrm{pr}}) - 2\alpha_w d_w E_w(\omega_{\mathrm{pr}}), \qquad (\text{B.7})$$

$$-\frac{i\omega\hbar}{2e} \theta_w(\omega_{\mathrm{pr}}) = (1 + 2\alpha_w)d_w E_w(\omega_{\mathrm{pr}}) - 2\alpha_s d_s E_s(\omega_{\mathrm{pr}}). \qquad (\text{B.8})$$

Inserting Eqs. (B.7) and (B.8) into Eqs. (B.3) and (B.4) yields

$$C_1 d_s E_s(\omega_{\mathrm{pr}}) - C_2 d_w E_w(\omega_{\mathrm{pr}}) = \frac{i\omega_{\mathrm{pr}} J_0}{16K|\psi_0|^2 e^2 d_c \alpha_s}, \qquad (\text{B.9})$$

$$-C_3 d_s E_s(\omega_{\mathrm{pr}}) + C_4 d_w E_w(\omega_{\mathrm{pr}}) = \frac{i\omega_{\mathrm{pr}} J_0}{16K|\psi_0|^2 e^2 d_c \alpha_w}, \qquad (\text{B.10})$$
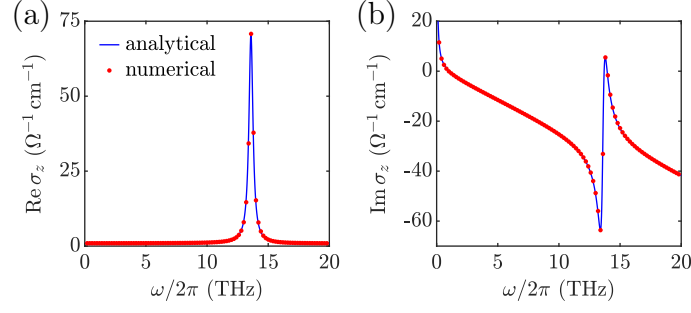
Figure B.1: Out-of-plane conductivity of a bilayer cuprate with uniform damping constants. For both the real part in (a) and the imaginary part in (b), the numerical results agree with the analytical prediction. In the simulation, we use a probe strength of $J_0 = 10 \text{ kA cm}^{-2}$.

where

$$C_1 = (1 + 2\alpha_s) \left[\omega_{\text{pr}}^2 + i\gamma\omega_{\text{pr}} - (1 + 2\alpha_s)\Omega_s^2 \right] - 4\alpha_s\alpha_w\Omega_w^2, \tag{B.11}$$

$$C_2 = 2\alpha_w \left[\omega_{\text{pr}}^2 + i\gamma\omega_{\text{pr}} - (1 + 2\alpha_s)\Omega_s^2 \right] - 2\alpha_w\Omega_w^2(1 + 2\alpha_w), \tag{B.12}$$

$$C_3 = 2\alpha_s \left[\omega_{\text{pr}}^2 + i\gamma\omega_{\text{pr}} - (1 + 2\alpha_w)\Omega_w^2 \right] - 2\alpha_s\Omega_s^2(1 + 2\alpha_s), \tag{B.13}$$

$$C_4 = (1 + 2\alpha_w) \left[\omega_{\text{pr}}^2 + i\gamma\omega_{\text{pr}} - (1 + 2\alpha_w)\Omega_w^2 \right] - 4\alpha_s\alpha_w\Omega_s^2. \tag{B.14}$$

As shown in Section 2.2.3, this leads to the analytical prediction

$$\sigma_z(\omega_{\text{pr}}) = \frac{\epsilon_\infty\epsilon_0}{i\omega_{\text{pr}}} \frac{(\omega_{\text{pr}}^2 + i\gamma\omega_{\text{pr}} - \omega_{\text{J1}}^2)(\omega_{\text{pr}}^2 + i\gamma\omega_{\text{pr}} - \omega_{\text{J2}}^2)}{\omega_{\text{pr}}^2 + i\gamma\omega_{\text{pr}} - \omega_\perp^2} \tag{B.15}$$

for the out-of-plane conductivity. In Fig. B.1, we compare the analytical prediction to simulations of a bilayer cuprate with $\gamma/2\pi = 0.4$ THz. We find excellent agreement between the numerical results and the analytical prediction.

B.2 In-plane conductivity at nonzero temperature

Here, we repeat the measurements of the in-plane conductivity from Section 2.3.4 using a smaller probe strength. Figure B.2 demonstrates that the linear response at nonzero temperature is probed for $J_0 = 500$ kA cm^{-2}, consistent with the measurements at zero temperature in Section 2.2.3.
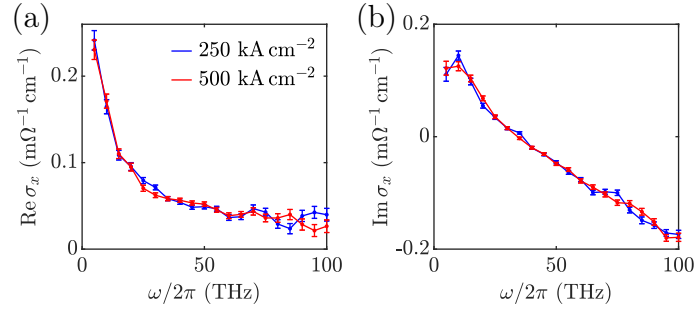

Figure B.2: In-plane conductivity for different probe strengths at 36 K $\sim 1.2\,T_c$. (a) Real part. (b) Imaginary part. The error bars indicate the standard errors of the ensemble averages.

Appendix C

Details on the temperature dependence of the upper Josephson plasma mode

C.1   Disorder at large in-plane momenta

In Fig. C.1, we show the disorder function for large in-plane momenta at a temperature of 36 K $\sim 1.2\,T_c$. The small disorder strength for $k_{xy} > 4\pi/L_{ab}$ justifies the momentum cutoff at $k_{\mathrm{max}} = 4\pi/L_{ab}$ in the analytical calculations in Section 2.3.3.
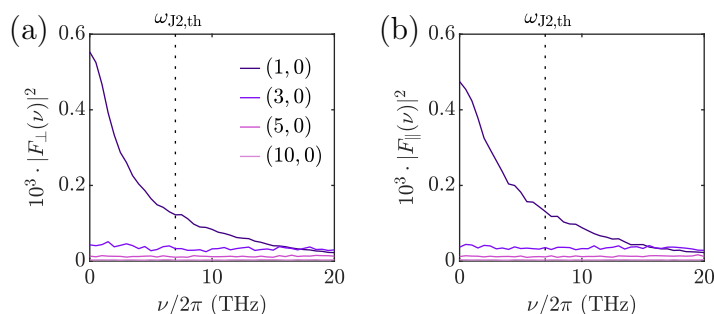

Figure C.1: Fourier spectra of transverse and longitudinal disorder for large in-plane momenta (k_x, k_y) specified in units of $2\pi/L_{ab}$. (a) Transverse disorder, $k_z = 0$. (b) Longitudinal disorder, $k_z = \pi/2d_c$. The data is obtained from an ensemble average of 1000 trajectories at 36 K $\sim 1.2\,T_c$.

C.2   Influence of dynamical disorder

The disorder function is not completely static as one can see in Fig. C.1, for example. To include dynamical effects in our description of transverse disorder, we consider a white spectrum with a width of Γ, i.e.,

$$|F_{\perp,T}(\nu)|^2 = \begin{cases} \pi F_{\perp,T}^2/\Gamma & \text{for } 0 \le |\nu| \le \Gamma, \\ 0 & \text{for } |\nu| > \Gamma. \end{cases} \tag{C.1}$$
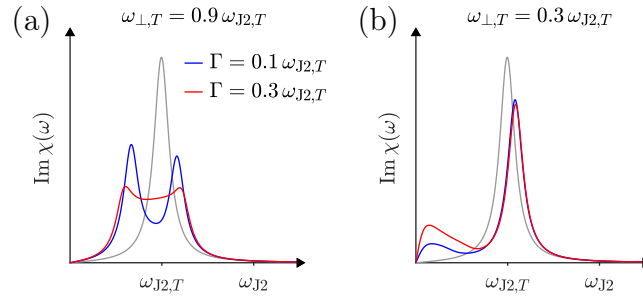
Figure C.2: Analytical solution for the susceptibility of the upper Josephson plasma mode, including transverse disorder with spectral width Γ. (a) Analytical solution for $\omega_{\perp,T} = 0.9\,\omega_{J2,T}$. (b) Analytical solution for $\omega_{\perp,T} = 0.3\,\omega_{J2,T}$. In both panels, the disorder strength is $S_\perp = 10^{-4}$ and the gray curve indicates the solution in the absence of disorder.

In this case, the frequency integral in Eq. (2.104) yields

$$\Omega^2(\omega) = \omega_{J2,T}^2 + \frac{S_\perp(k_{\max}^2 L_{ab}^2 - 4\pi^2)\,\omega_{J2}^4}{2\omega_{\perp,T}\Gamma}\left[\operatorname{artanh}\left(\frac{\omega - \Gamma + i\gamma/2}{\omega_{\perp,T}}\right)\right.$$
$$\left. - \operatorname{artanh}\left(\frac{\omega + \Gamma + i\gamma/2}{\omega_{\perp,T}}\right)\right], \tag{C.2}$$

with $S_\perp = F_{\perp,T}^2/\pi N^2$. In Fig. C.2, the imaginary part of the susceptibility is displayed for $\gamma = 0.1\,\omega_{J2}$, $\omega_{J2,T} = 0.5\,\omega_{J2}$, and $k_{\max} = 4\pi/L_{ab}$. For $\Gamma = 0.1\,\omega_{J2,T}$, the analytical solution is only weakly modified in comparison to the case of static disorder; confer Fig. 2.14. Even for a spectral width of $\Gamma = 0.3\,\omega_{J2,T}$, the qualitative character of the analytical solution does not change.

C.3   Influence of the system size

The system size analysis of the intrabilayer supercurrent in Fig. C.3 indicates that the system size has no significant influence on the upper Josephson plasma resonance.

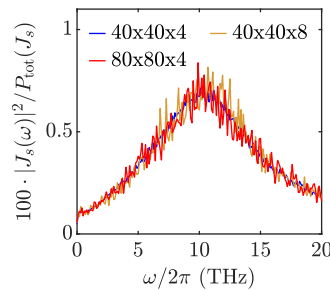**Figure C.3:** Power spectrum of the intrabilayer supercurrent at 36 K $\sim 1.2\,T_c$ for different system sizes. While the data for the system with $40 \times 40 \times 4$ sites is based on an ensemble average of 1000 trajectories, the data for the two larger systems is based on an ensemble average of 100 trajectories.

Appendix D

Publications

D.1 Higgs time crystal in a high-T_c superconductor

Higgs time crystal in a high-T_c superconductor

Guido Homann [1,*] Jayson G. Cosme [1,2,3] and Ludwig Mathey[1,2]

[1]*Zentrum für Optische Quantentechnologien and Institut für Laserphysik, Universität Hamburg, 22761 Hamburg, Germany*
[2]*The Hamburg Centre for Ultrafast Imaging, Luruper Chaussee 149, 22761 Hamburg, Germany*
[3]*National Institute of Physics, University of the Philippines, Diliman, Quezon City 1101, Philippines*

We propose to induce a time-crystalline state in a high-T_c superconductor, by optically driving a sum resonance of the Higgs mode and a Josephson plasma mode. The generic cubic process that couples these fundamental excitations converts driving of the sum resonance into simultaneous resonant driving of both modes, resulting in an incommensurate subharmonic motion. We use a numerical implementation of a semiclassical driven-dissipative lattice gauge theory on a three-dimensional layered lattice, which models the geometry of cuprate superconductors, to demonstrate the robustness of this motion against thermal fluctuations. We demonstrate this light-induced time-crystalline phase for mono- and bilayer systems and show that this order can be detected for pulsed driving under realistic technological conditions.

I. INTRODUCTION

Optical driving of solids constitutes a new method of designing many-body states. Striking examples of this approach include light-induced superconductivity [1–3] as well as optical control of charge density wave phases [4]. For these states, the carefully tuned light field either renormalizes the phase boundary of the equilibrium phase, as is the case for light-induced superconductivity, or renormalizes a nearby metastable state into a stable state of the driven system, as is the case for light-controlled charge density waves.

These observations are part of a larger effort to determine the steady states of periodically driven many-body systems. In a parallel development in cold atom systems, serving as well-defined many-body toy models, the generic regimes that were proposed (see Refs. [5,6]) firstly include renormalized equilibrium states, for which the above-mentioned states are examples. Secondly, regimes beyond the equilibrium states emerge, in particular, genuine nonequilibrium orders, which have no equilibrium counterpart, and only exist in the driven state. A striking example of a nonequilibrium order is time crystals [7–13], reported in systems such as ion traps or nitrogen-vacancy centers [14,15]. Thirdly, for strong driving, chaotic states emerge. These different regimes are achieved for different driving amplitudes and driving frequencies, which constitutes the dynamical phase diagram of the system.

In this paper, we propose to create a light-induced time-crystalline state in a high-T_c superconductor. This advances light control of superconductors towards genuine nonequilibrium orders and furthers time crystals in the solid-state domain [16]. We characterize the observed nonequilibrium state as a time crystal based on the following criteria [12]: (i) A time crystal spontaneously breaks time-translation symmetry; that is, it exhibits a subharmonic response to the drive. (ii) The subharmonic response is robust against perturbations which respect the time-translation symmetry of the Hamiltonian. (iii) The subharmonic response emerges in a many-body system with a large number of locally coupled degrees of freedom, and it persists for an infinite time.

We call the novel dynamical phase a Higgs time crystal because we induce it via optical driving of a sum resonance of the Higgs mode and a Josephson plasma mode. The Higgs mode and the Josephson plasma mode correspond to the two fundamental collective excitations of a system with broken $U(1)$ symmetry and with an underlying approximate particle-hole symmetry. The Higgs mode is an amplitude oscillation of the order parameter, as depicted in Fig. 1(a) for the $|\psi|^4$ theory used in the following. The Higgs mode is a gapped excitation due to the increase of the potential energy in the radial direction. The Josephson plasma mode is a phase oscillation, as indicated. This mode also has a gapped excitation spectrum owing to the electromagnetic interaction of the system. Because of the approximate particle-hole symmetry, these two oscillations are orthogonal to each other [17,18].

To identify the Higgs time-crystalline phase, we map out the dynamical phase diagram of optically driven high-T_c superconductors as a function of the driving frequency ω_{dr} and the driving amplitude E_0, which is shown in Fig. 2(a), for instance. The time-crystalline state is induced by driving the superconductor via the nonlinear coupling $\sim a^2 h$ of the electromagnetic field a and the Higgs field h. We demonstrate that driving at the frequency $\omega_{dr} = \omega_H + \omega_J$ induces a
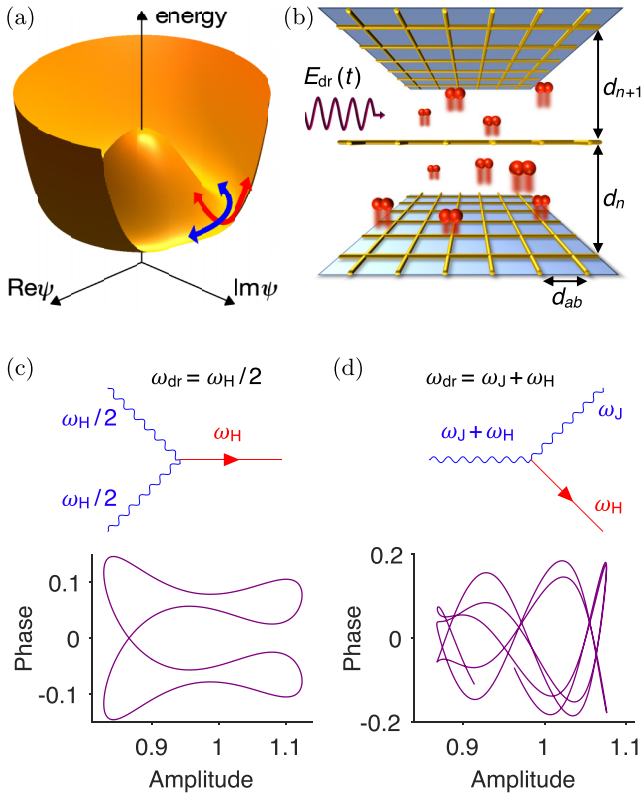
*ghomann@physnet.uni-hamburg.de

FIG. 1. Exciting the Higgs and plasma modes. (a) Illustration of the free energy of a state with broken $U(1)$ symmetry. (b) Illustration of a driven cuprate superconductor modeled as a $U(1)$ gauge theory on an anisotropic lattice. In-plane dynamics is captured by discretizing the condensate field in the ab plane. (c) The Higgs mode can be excited resonantly with a driving frequency of $\omega_{\mathrm{dr}} \lesssim \omega_{\mathrm{H}}/2$, by utilizing the nonlinear coupling between the electromagnetic field and the Higgs field. Upper panel: Diagrammatic representation of the nonlinear process. Lower panel: Exemplary dynamical portrait of the phase difference between the superconducting layers and the condensate amplitude in the steady state for 10 driving cycles at zero temperature. (d) We propose to utilize the same nonlinear coupling to induce a time-crystalline state by driving the sum resonance of the system at $\omega_{\mathrm{dr}} = \omega_{\mathrm{H}} + \omega_{\mathrm{J}}$. The phase-space trajectories shown in the lower panels of (c) and (d) are obtained using a Josephson junction model for a monolayer cuprate with Higgs frequency $\omega_{\mathrm{H}}/2\pi \approx 6.3$ THz and plasma frequency $\omega_{\mathrm{J}}/2\pi \approx 16.0$ THz; see Table I for full parameter set.

time-crystalline phase, where ω_{H} is the Higgs frequency and ω_{J} is the plasma frequency, as depicted in Fig. 1(d). We note that this nonlinear coupling has been confirmed in conventional superconductors [19–22], while a direct probe of the Higgs field is challenging due to its scalar nature. Further studies on the Higgs mode in high-T_c cuprates and organic superconductors are reported in Refs. [23–29]. Persistent multifrequency dynamics of the superconducting order parameter has been investigated in Ref. [30].

To describe the dynamics of optically driven superconductors, we develop a lattice gauge simulation that describes the motion of the order parameter of the superconducting state $\psi(\mathbf{r}, t)$ and the electromagnetic field $\mathbf{A}(\mathbf{r}, t)$. We first

utilize our method to show how to induce the time-crystalline state and to determine its regime in the dynamical phase diagram. Furthermore, we demonstrate the robustness of the time-crystalline phase against thermal fluctuations and show that it can be realized and identified under pulsed operation.

II. THREE-DIMENSIONAL LATTICE GAUGE MODEL

We represent the layered structure of high-T_c superconductors via the lattice geometry illustrated in Fig. 1(b). We note that this geometry of CuO_2 layers perpendicular to the c axis has motivated a low-energy description of stacks of Josephson junctions [31–33], which captures the appearance of Josephson plasma excitations reported in Refs. [34–36]. Each layer is represented by a square lattice, leading to a discretization of the fields of the form $\psi(\mathbf{r}, t) \rightarrow \psi_{l,m,n}(t) \equiv \psi_{\mathbf{r}}(t)$. The in-plane discretization length d_{ab} constitutes a short-range cutoff well below the in-plane coherence length. In doing so, we generalize the modeling of layered cuprates to a three-dimensional (3D) lattice of Josephson junctions. Each component of the vector potential $A_{i,\mathbf{r}}(t)$ is located between a lattice site $\mathbf{r}$ and its nearest neighbor $\mathbf{r}'(i)$ in the i direction, where $i \in \{x, y, z\}$. According to the Peierls substitution, it describes the averaged electric field along the bond of a plaquette in Fig. 1(b).

We focus on temperatures below T_c, where the dominant low-energy degrees of freedom are Cooper pairs. We describe the Cooper pairs as a condensate of interacting bosons with charge $-2e$, represented by the complex field $\psi_{\mathbf{r}}(t)$. To construct the Hamiltonian of the lattice gauge model, we discretize the Ginzburg-Landau free energy [37] on a layered lattice and add time-dependent terms. We explicitly simulate the coupled dynamics of the condensate and the electromagnetic field. We discretize space by mapping it on a lattice, as mentioned, but implement the compact $U(1)$ lattice gauge theory in the time-continuum limit [38]. The particle-hole symmetry inherent to our relativistic model creates stable Higgs oscillations, even in bilayer cuprates where the Higgs frequency is between the two longitudinal Josephson plasma frequencies.

We consider mono- and bilayer cuprate superconductors. For bilayer cuprates, we assign the strong (weak) junctions to the even (odd) layers. The corresponding tunneling coefficients are $t_{2n} = t_s$ and $t_{2n+1} = t_w$. The interlayer spacings $d_{2n,2n+1} = d_{s,w}$ are the distances between the CuO_2 planes in the crystal. Note that we suppose the z direction to be aligned with the c axis of the crystal throughout this paper. The Hamiltonian of the lattice gauge model is

$$\mathcal{H} = \mathcal{H}_{\mathrm{sc}} + \mathcal{H}_{\mathrm{em}} + \mathcal{H}_{\mathrm{kin}}. \tag{1}$$

The first term is the $|\psi|^4$ model of the superconducting condensate in the absence of Cooper pair tunneling:

$$\mathcal{H}_{\mathrm{sc}} = \sum_{\mathbf{r}} \frac{|\pi_{\mathbf{r}}|^2}{K\hbar^2} - \mu|\psi_{\mathbf{r}}|^2 + \frac{g}{2}|\psi_{\mathbf{r}}|^4, \tag{2}$$

where $\pi_{\mathbf{r}} = K\hbar^2 \partial_t \psi_{\mathbf{r}}^*$ is the conjugate momentum of $\psi_{\mathbf{r}}$, μ is the chemical potential, and g is the interaction strength. This Hamiltonian is particle-hole symmetric due to its invariance

under $\psi_{\mathbf{r}} \to \psi_{\mathbf{r}}^*$. The coefficient K describes the magnitude of the dynamical term.

The electromagnetic part $\mathcal{H}_{\mathrm{em}}$ is the discretized form of the free-field Hamiltonian, modified by tunable interlayer permittivities $\epsilon_{s,w}$ to capture the screening due to bound charges in the material:

$$\mathcal{H}_{\mathrm{em}} = \sum_{i,\mathbf{r}} \frac{\kappa_{i,\mathbf{r}} \epsilon_{i,\mathbf{r}} \epsilon_0}{2} E_{i,\mathbf{r}}^2 + \frac{\kappa_{z,\mathbf{r}}}{\kappa_{i,\mathbf{r}} \beta_{i,\mathbf{r}}^2 \mu_0} [1 - \cos(\beta_{i,\mathbf{r}} B_{i,\mathbf{r}})],$$
(3)

where $E_{i,\mathbf{r}}$ denotes the i component of the electric field. The vector potential is located on the bonds between the superconducting sites. Consequently, this applies to the electric field as well. Note that we choose the temporal gauge for our calculations, i.e., $E_{i,\mathbf{r}} = -\partial_t A_{i,\mathbf{r}}$. Meanwhile, the magnetic field components $B_{i,\mathbf{r}} = \epsilon_{ijk} \delta_j A_{k,\mathbf{r}}$ are centered about the plaquettes. This arrangement is consistent with the finite-difference time-domain (FDTD) method for solving Maxwell's equations [39]. We calculate the spatial derivatives according to $\delta_j A_{k,\mathbf{r}} = (A_{k,\mathbf{r}'(j)} - A_{k,\mathbf{r}})/d_{j,\mathbf{r}}$, where $d_{j,\mathbf{r}}$ is the length of the bond. The dielectric permittivities are $\epsilon_{x,\mathbf{r}} = \epsilon_{y,\mathbf{r}} = 1$ and $\epsilon_{z,\mathbf{r}} = \epsilon_n$. The other prefactors in Eq. (3) account for the anisotropic lattice geometry. They are defined as $\kappa_{x,\mathbf{r}} = \kappa_{y,\mathbf{r}} = 1$ and $\kappa_{z,\mathbf{r}} = d_n/d_c$, while $\beta_{x,\mathbf{r}} = \beta_{y,\mathbf{r}} = 2ed_{ab}d_n/\hbar$ and $\beta_{z,\mathbf{r}} = 2ed_{ab}^2/\hbar$, where $d_c = (d_s + d_w)/2$.

The nonlinear coupling between the Higgs field and the electromagnetic field derives from the tunneling term

$$\mathcal{H}_{\mathrm{kin}} = \sum_{i,\mathbf{r}} t_{i,\mathbf{r}} |\psi_{\mathbf{r}'(i)} - \psi_{\mathbf{r}} e^{ia_{i,\mathbf{r}}}|^2.$$
(4)

The unitless vector potential $a_{i,\mathbf{r}} = -2ed_{i,\mathbf{r}} A_{i,\mathbf{r}}/\hbar$ couples to the phase of the superconducting field, ensuring the gauge invariance of $\mathcal{H}_{\mathrm{kin}}$. The in-plane tunneling coefficient is t_{ab}, and the c-axis tunneling coefficients are $t_{s,w}$.

We solve the equations of motion for $\psi_{\mathbf{r}}(t)$ and $\mathbf{A}_{\mathbf{r}}(t)$ obtained from the Hamiltonian numerically, employing Heun's method with an integration step size $\Delta t = 1.6$ as. Thermal fluctuations are included by adding dissipation and Langevin noise to the equations of motion for both fields. For example, the time evolution of the superconducting field is given by

$$\partial_t \pi_{\mathbf{r}} = -\frac{\partial \mathcal{H}}{\partial \psi_{\mathbf{r}}} - \gamma \pi_{\mathbf{r}} + \xi_{\mathbf{r}},$$
(5)

where γ is a damping constant and $\xi_{\mathbf{r}}$ represents white Gaussian noise with zero mean; see Appendix A for noise correlations. We note that the inclusion of in-plane dynamics and arbitrarily strong amplitude fluctuations constitutes a qualitative advance of previous descriptions, such as 1D sine-Gordon models [40,41].

We determine the response of the superconductor to periodic driving of the electric field along the c axis. The external drive $E_{\mathrm{dr}}(t)$ has the frequency ω_{dr} and the effective field strength E_0. We consider the long-wavelength limit such that the external drive is assumed to be homogeneous in the bulk of the sample. Thus the time evolution of $E_{z,\mathbf{r}}(t)$ reads

$$\partial_t E_{z,\mathbf{r}} = \frac{d_c}{d_n \epsilon_n \epsilon_0} \frac{\partial \mathcal{H}}{\partial A_{z,\mathbf{r}}} - \gamma E_{z,\mathbf{r}} + \eta_{z,\mathbf{r}} + \frac{\partial_t E_{\mathrm{dr}}}{\epsilon_n},$$
(6)

where $\eta_{z,\mathbf{r}}$ is white Gaussian noise with zero mean. The equations of motion for $E_{x,\mathbf{r}}(t)$ and $E_{y,\mathbf{r}}(t)$ are analogous to Eq. (6), except for the driving term. We characterize the response by evaluating the sample averages of the condensate amplitude $|\psi(t)|$ and the supercurrent density $J(t)$; see also Appendix B.

By applying the optical driving as described, we obtain the full dynamical phase diagram due to the direct coupling of the electromagnetic field to the superconducting order parameter. We note that resonant optical driving of phonon modes has been utilized and discussed in Refs. [1–3,40–42]. Here, we ignore the phononic resonances, so that our predictions are valid away from these resonances. A combined description will be given elsewhere.

III. TWO-MODE MODEL

Before we present the full numerical simulation, we identify the main resonant phenomena of the system. We consider the zero-temperature limit, where the in-plane dynamics can be neglected and the model simplifies to a 1D chain along the c axis. Furthermore, we restrict ourselves to weak driving and a monolayer structure with $t_s = t_w \equiv t_J$ and $d_s = d_w \equiv d$. For periodic boundary conditions, the time evolution then reduces to two coupled equations of motion. Keeping only linear terms except for the lowest-order coupling between the Higgs field and the unitless vector potential, we find

$$\partial_t^2 a + \gamma \partial_t a + \omega_J^2 a + 2\omega_J^2 ah \approx j_{\mathrm{dr}},$$
(7)

$$\partial_t^2 h + \gamma \partial_t h + \omega_H^2 h + \alpha \omega_J^2 a^2 \approx 0,$$
(8)

where $h = (\psi - \psi_0)/\psi_0$ is the Higgs field with ψ_0 being the equilibrium condensate amplitude, γ is the damping constant, and α is the capacitive coupling constant of the junction. Note that the unitless vector potential a equals the phase difference between adjacent planes in this setting. The external drive appears through the current j_{dr}. The Higgs and plasma frequencies are $\omega_H = \sqrt{2\mu/K\hbar^2}$ and $\omega_J = \sqrt{t_J/\alpha K\hbar^2}$, respectively.

The main finding of this work is the emergence of a time-crystalline phase by driving at the sum of the Higgs and plasma frequencies, $\omega_{\mathrm{dr}} = \omega_J + \omega_H$. A cubic interaction process, visualized in Fig. 1(d), allows for simultaneous resonant driving of both the Higgs and the plasma modes [43].

In addition to the sum resonance, we identify various other resonances from the simplified equations of motion. For a response of the vector potential at the driving frequency, i.e., $a = a_1 \cos(\omega_{\mathrm{dr}} t)$, Eq. (8) simplifies to a forced oscillator with a resonance at $\omega_{\mathrm{dr}} = \omega_H/2$. This recovers the subgap Higgs resonance [22]. The subgap resonance and the sum resonance originate from the same cubic coupling term $\sim a^2 h$, as illustrated in Figs. 1(c) and 1(d). Next, we consider the range of driving frequencies where the Higgs field exhibits a second-harmonic response; that is, the external drive induces Higgs oscillations of the form $h = h_0 + h_1 \cos(2\omega_{\mathrm{dr}} t)$ through the a^2 term in Eq. (8). For small driving amplitudes, the ah term in Eq. (7) can be neglected so that the equation reduces to a forced oscillator with a resonance at $\omega_{\mathrm{dr}} = \omega_J$. However, the response is modified once the coupling to the Higgs field becomes significant. Then, Eq. (7) approaches a parametri-
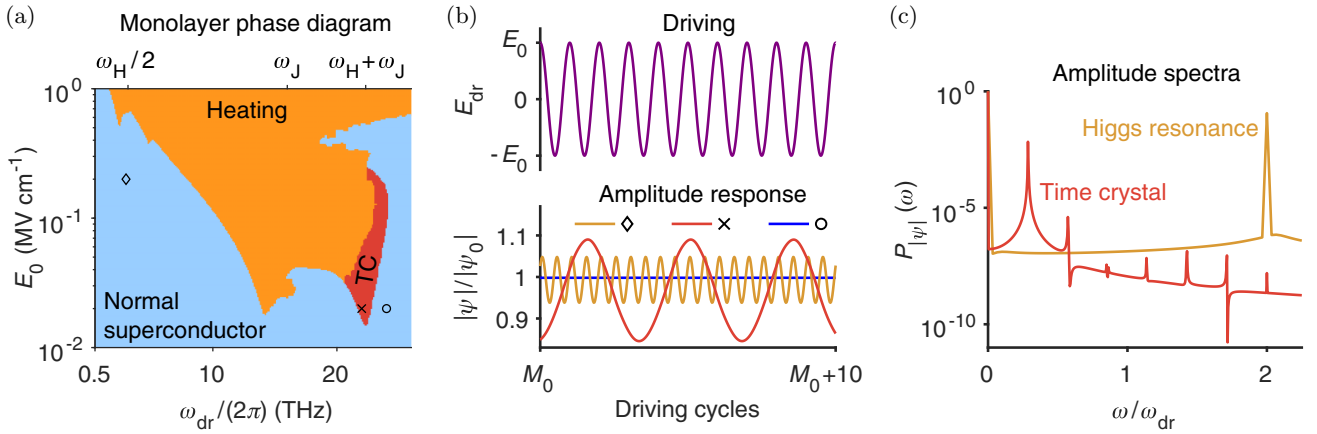
FIG. 2. Dynamical phases of a light-driven monolayer cuprate superconductor. (a) Dynamical phase diagram of a monolayer cuprate continuously driven by an electric field with frequency ω_{dr} and effective field strength E_0 at $T = 0$. The time-crystalline (TC) phase is encoded in red. (b) Driving $E_{dr}(t)$ and response of the condensate amplitude $|\psi|/|\psi_0|(t)$ for the Higgs resonance at $\omega_{dr} = \omega_H/2$ (diamond), the time crystal (cross), and an off-resonantly driven superconductor (circle). The driving parameters are indicated by the symbols in (a). (c) Power spectra of the condensate amplitude, corresponding to the trajectories of the Higgs resonance and the time crystal presented in (b). The parameters for the monolayer system are the same as in Fig. 1.

cally driven oscillator. The parametric resonances emerge at $\omega_{dr} = \omega_J/k$, where $k \in \mathbb{N}$.

IV. DYNAMICAL PHASE DIAGRAM

We now present our numerical results in two steps. Firstly, we verify our analytical predictions for the resonances and, in particular, the Higgs time crystal by mapping out the dynamical phase diagrams of mono- and bilayer cuprate superconductors at zero temperature. We will show how the sum resonance is modified in a bilayer system, which has two plasma modes. Secondly, we test the robustness of this phase against thermal fluctuations using finite-temperature simulations.

A. Monolayer cuprate superconductor

Here, we consider a monolayer cuprate with $\omega_H/2\pi \approx 6.3$ THz, $\omega_J/2\pi \approx 16.0$ THz, $\gamma/2\pi = 0.5$ THz, and $\alpha = 0.33$; see Table I for full parameter set. The system is continuously driven at various amplitudes and frequencies in the terahertz regime. In each realization, the drive is applied for 20 ps, and the relevant frequency spectra are computed using the final 10 ps, which amounts to $5 < M_{tot} < 300$ driving cycles in the frequency range of interest. The dynamical phase diagram in Fig. 2(a) is mapped out by analyzing the normalized power spectra of $|\psi(t)|$ and $J(t)$ defined as $P_f(\omega) = \langle f(\omega) f(-\omega) \rangle$, where $\int P_f(\omega) d\omega = 1$, $f(\omega) = 1/\sqrt{T_s} \int dt' \exp(-i\omega t') f(t')$, and $T_s = 10$ ps is the sampling interval. Specifically, we obtain the spectral entropy for the dynamics of the condensate amplitude, $\mathcal{S}_{|\psi|} = -\int d\omega P_{|\psi|}(\omega) \ln P_{|\psi|}(\omega)$.

The heating regime, which is characterized by a strong depletion of the condensate, is identified based on the threshold $\mathcal{S}_{|\psi|} > 2.2 \times 10^{-2}$. It indicates the appearance of resonant phases associated with the Higgs and plasma excitations. We note that the two dominant heating tongues are weakly

red-detuned from the expected resonance frequencies $\omega_H/2$ and ω_J, respectively. Such a renormalization of the fundamental frequencies is inherent to strongly driven nonlinear systems [44]. This effect is further amplified by the damping terms present in our model. We identify the small tongue at $\omega_{dr}/2\pi \approx 4.8$ THz as the third-order parametric resonance of the Josephson plasma mode around $\omega_J/3$.

For intermediate driving intensity, we observe several dynamical regimes due to resonances. The resonance with the lowest frequency is the Higgs resonance at $\omega_{dr} = \omega_H/2$. In general, resonant excitation of the Higgs mode is marked by strong modulation of the condensate amplitude as exemplified in Fig. 2(b). Moreover, the Higgs resonance exhibits a commensurate and superharmonic response of $|\psi(t)|$ with respect to the driving $E_{dr}(t)$ as seen from the closed trajectory in Fig. 1(c) and the sharp peak at $2\omega_{dr}$ of the condensate amplitude spectrum in Fig. 2(c). We emphasize that driving away from any noticeable resonance, indicated as the blue regime in Fig. 2(a), induces only a single sharp peak in the supercurrent spectrum, namely, at the driving frequency. The condensate amplitude oscillates at twice the driving frequency in the blue regime. This also applies to the regime near the Josephson plasma resonance at $\omega_{dr} = \omega_J$, where the system responds with strong oscillations of the supercurrent.

The red regime in Fig. 2(a), identified via the condition $10^{-4} < \mathcal{S}_{|\psi|} < 2.2 \times 10^{-2}$, is the Higgs time crystal introduced earlier. We emphasize that its resonance condition $\omega_{dr} = \omega_J + \omega_H$ differs from the subgap frequencies $\omega_{dr} \lesssim \omega_H/2$ used in standard Higgs spectroscopy. The sum resonance simultaneously couples to the Higgs and plasma resonances as evident from the exemplary mean-field trajectory in Fig. 1(d), where the amplitude oscillation is accompanied by a strong oscillation of the phase difference between the junctions. Despite a smaller driving amplitude E_0, the plasma mode is excited with larger amplitude than for the Higgs resonance. The strong activation of the plasma mode
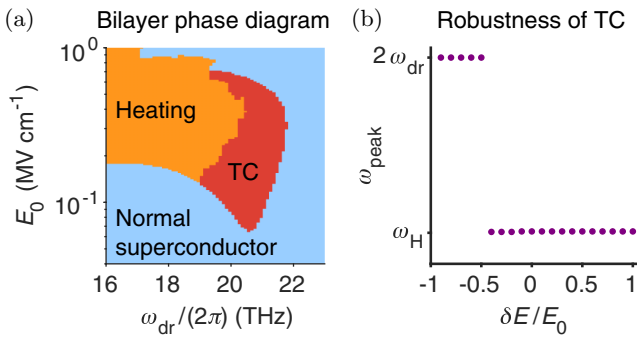
FIG. 3. Higgs time crystal in a light-driven bilayer cuprate superconductor. (a) Dynamical phase diagram of a bilayer cuprate continuously driven by an electric field with frequency ω_{dr} and effective field strength E_0 at $T = 0$. (b) Robustness of the time crystal (TC) against perturbations of the drive as described in the text. Values of the dominant amplitude frequency ω_{peak} close to ω_H indicate a subharmonic response, whereas maxima at $2\omega_{dr}$ mark a normal response. The bilayer system has the Higgs frequency $\omega_H/2\pi \approx$ 6.3 THz and the two longitudinal Josephson plasma frequencies $\omega_{J1}/2\pi \approx 2.0$ THz and $\omega_{J2}/2\pi \approx 14.3$ THz at $T = 0$; see Table I for full parameter set.

results in a partial depletion of the condensate as visible in Fig. 2(b), where the time average of the oscillatory motion of the condensate amplitude is below 1. The key feature of the novel phase is the subharmonic response of the condensate amplitude as $|\psi(t)|$ oscillates at ω_H when the superconductor is driven at $\omega_{dr} = \omega_J + \omega_H$. This phenomenon is highlighted in Fig. 2(b) and in the strong subharmonic peak in the power spectrum of $|\psi(t)|$ shown in Fig. 2(c). The other dynamical phases respect the time-translation symmetry imposed by the external drive as evidenced by Figs. 2(b) and 2(c).

The subharmonic collective motion is one of the defining features of a time crystal. In addition to being subharmonic, the response of the time-crystalline state is also incommensurate to the external driving. That is, the phase-space trajectory traces an open loop for any number of driving cycles; see also Fig. 1(d). Therefore, and more specifically, the state that we propose to create is an incommensurate time crystal in high-T_c superconductors. We will confirm its robustness against perturbations of the drive and thermal fluctuations for the bilayer case. We note that the subharmonic response can be expected to be rigid as it emerges for a broad regime of driving parameters rather than a fine-tuned point in the dynamical phase diagram. In addition, our finite-temperature calculations with a large number of lattice sites will highlight the many-body nature of the Higgs time crystal.

B. Bilayer superconductor

We now focus on bilayer cuprates. Due to the staggered tunneling coefficients t_s and t_w along the c axis, the system has two fundamental longitudinal plasma excitations with frequencies ω_{J1} and ω_{J2}. The dynamical phase diagram at zero temperature in Fig. 3(a) displays a regime in which a Higgs time crystal is induced by optical driving at a sum resonance. Here, the resonance condition is $\omega_{dr} = \omega_H + \omega_{J2}$, so it is the sum of the Higgs frequency and the upper plasma frequency.

First, we examine how perturbing the optical drive itself affects the subharmonic response. To excite the sum resonance, we initially drive the bilayer superconductor with $E_0 = 0.1$ MV/cm and $\omega_{dr}/2\pi = 21$ THz. At some instant of time t_0, the driving is altered so that the oscillation amplitude of the field strength depends on its sign for $t > t_0$:

$$E_{dr}(t) = \begin{cases} E_0 \cos(\omega_{dr}t) & \text{for } \cos(\omega_{dr}t) \geqslant 0 \\ (E_0 + \delta E)\cos(\omega_{dr}t) & \text{for } \cos(\omega_{dr}t) < 0. \end{cases} \quad (9)$$

After allowing the system to relax to a steady state, we take the power spectrum of the condensate amplitude and determine the dominant frequency ω_{peak}. The robustness of the subharmonic response is demonstrated by Fig. 3(b), where perturbations of the driving amplitude between $\delta E/E_0 = -0.4$ and $\delta E/E_0 = 1$ do not destroy the sum resonance. We have also verified the persistence of the subharmonic response for 10^5 cycles of continuous driving at $T = 0$ [43]. Because of experimental and numerical limitations in accessible time scales ($\sim 10^2$ driving cycles for our finite-temperature calculations), we will not distinguish here between a "true" time crystal and a slowly decaying time crystal [13,14].

We note that the time-crystalline response is stabilized by the nonlinear coupling between the Higgs and plasma modes, which further highlights the collective nature of the Higgs time crystal. Furthermore, the amplitudes of the oscillations are saturated by nonlinear processes in the system (see Ref. [45] for example) while the dissipative coupling to the environment limits heating.

Next, we demonstrate the robustness of the Higgs time crystal against thermal fluctuations modeled as Langevin noise in the dynamics of the fields. These fluctuations are a natural test for the rigidity of the subharmonic response against temporal perturbations [13]. When considering thermal fluctuations, we include the in-plane dynamics of the fields in a full 3D simulation. The complete parameter set is summarized in Table I, implying the Higgs frequency $\omega_H/2\pi \approx 6.3$ THz and the two longitudinal Josephson plasma frequencies $\omega_{J1}/2\pi \approx 2.0$ THz and $\omega_{J2}/2\pi \approx 14.3$ THz at $T = 0$. For simplicity, we keep the chemical potential fixed in the following finite-temperature calculations, $\mu(T) \equiv \mu$. We choose the parameters within the CuO_2 planes to yield a critical temperature of $T_c \sim 30$ K. We find that a discretization of $48 \times 48 \times 4$ lattice sites with periodic boundaries is sufficient to obtain fully converged results with respect to the system size. Note that both the Higgs and Josephson plasma frequencies are renormalized at finite temperature [43].

Examples of the power spectra of the condensate amplitude and the supercurrent density at $T = 3$ K are shown in Figs. 4(a) and 4(b), respectively. When the sum resonance is driven, the condensate amplitude exhibits strong subharmonic modulation as evidenced by a sharp peak in the amplitude spectrum in Fig. 4(a). Moreover, we observe in Fig. 4(a) how the modulation of the condensate amplitude is suppressed as the driving frequency is tuned away from the resonance frequency. As shown in Fig. 4(b), we identify an experimentally relevant signature of the superconducting time-crystalline phase, which is the appearance of two side peaks at $\omega_{dr} \pm \omega_H$ in the power spectrum of the supercurrent density. The side peaks vanish as the driving frequency is
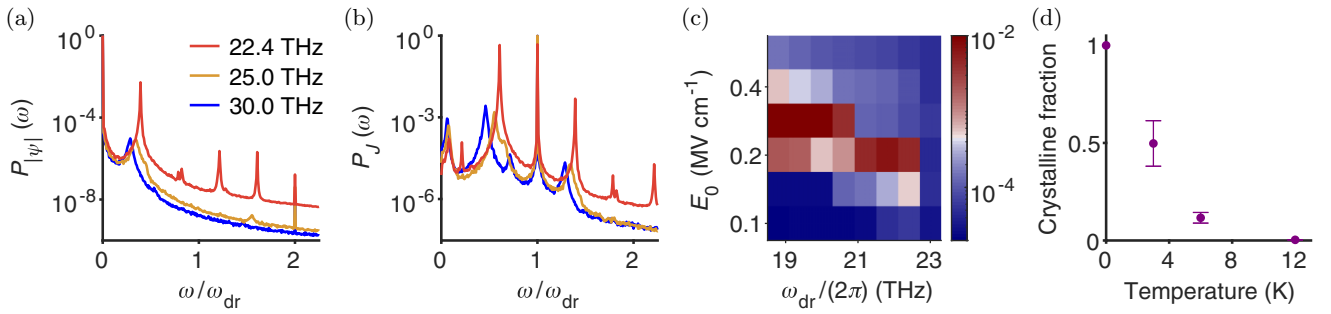
FIG. 4. Higgs time crystal at nonzero temperatures. (a) Comparison between the power spectra of the condensate amplitude at $T = 3$ K $\sim$ $0.1T_c$ for $E_0 = 0.2$ MV/cm and different driving frequencies indicated in the legend. The time-crystalline state at $\omega_{dr}/2\pi = 22.4$ THz is demonstrated by the strongly enhanced subharmonic peak at ω_H. (b) Power spectra of the supercurrent density for the same parameters as in (a). The time-crystalline state creates strongly enhanced side peaks at $\omega_{dr} \pm \omega_H$. (c) Time-crystalline fraction $P_J(\omega_{dr} + \omega_H)$ in a section of the dynamical phase diagram at $T = 3$ K $\sim 0.1T_c$, containing the time-crystalline phase. (d) Temperature dependence of the optimal time-crystalline fraction for a bilayer cuprate superconductor, rescaled by its value at $T = 0$. The optimal crystalline fraction at a given temperature corresponds to the maximum value of $P_J(\omega_{dr} + \omega_H)$ in the relevant section of the dynamical phase diagram, as exemplified in (c). The error bars in (d) arise from the standard errors of Lorentzian fits to the blue-detuned side peaks. The parameters for the bilayer system are the same as in Fig. 3. The resonance frequencies are shifted at finite temperature.

tuned away from the resonance frequency. Coherent dynamics of supercurrents can be experimentally probed using second-harmonic measurements [46,47].

To quantify the time-crystalline fraction, we use the height of the blue-detuned side peak in the power spectrum of the supercurrent density, $P_J(\omega_{dr} + \omega_H)$. Figure 4(d) displays the temperature dependence of the optimal crystalline fraction for a bilayer cuprate, normalized to the optimal time-crystalline fraction at $T = 0$. The optimal driving parameters at each temperature were inferred from coarse scans such as that in Fig. 4(c). As we expect for time crystals under increasingly strong perturbation, the crystalline fraction decreases with temperature. Nevertheless, the subharmonic response is robust against thermal noise for temperatures up to $T = 6$ K $\sim$ $0.2T_c$.

V. PULSED EXCITATION OF THE HIGGS TIME CRYSTAL

While significant progress has been made in generating continuous-wave terahertz sources [48], typical experiments in optically driven superconductors utilize pulsed excitation, as in most pump-probe experiments. We now point out that the time-crystalline phase can be detected when the system is driven with a short pulse, rather than the steady state discussed so far. We consider a pulsed driving scheme by introducing a Gaussian envelope of the periodic driving; that is, $E_{dr}(t) = E_0\cos(\omega_{dr}t)\exp(-t^2/2\sigma^2)$ with the pulse width σ. In Fig. 5, we present an example of the dynamical response of the bilayer system under pulsed excitation. The response shown in Fig. 5(b) is approximately the Fourier-broadened form of Fig. 4(b). The similarity between the two results suggests that the defining features of the Higgs time crystal of continuously driven superconductors are detectable for pulsed driving protocols with realistic pulse lengths. The response can be clearly distinguished from normal dynamical phases by probing the coherent dynamics of the supercurrent. Thus the Higgs time crystal predicted here can be observed in current state-of-the-art experiments with optically driven high-T_c superconductors.

VI. DISCUSSION

In conclusion, we have demonstrated the emergence of a time-crystalline phase in a high-T_c superconductor, which is
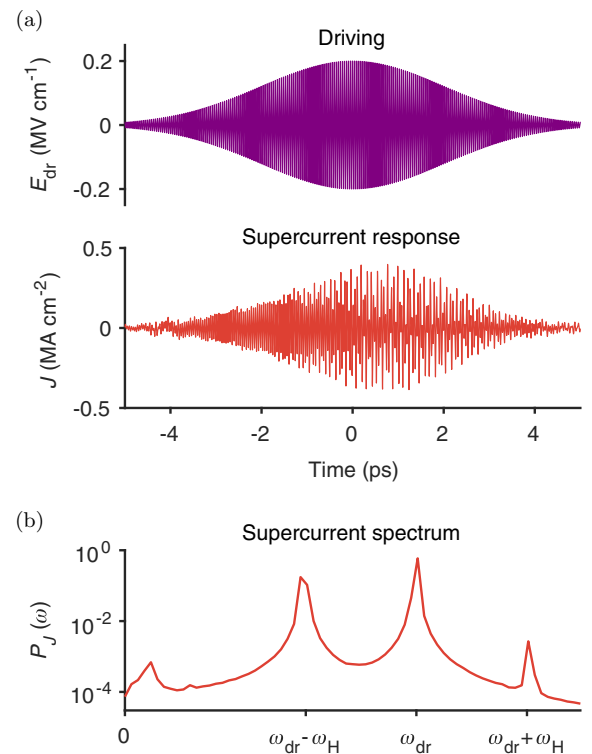
FIG. 5. Time-crystalline response of a bilayer cuprate superconductor to a driving pulse. (a) Temporal wave form of the pulsed electric field and the induced motion of the supercurrent density shown for one representative trajectory at $T = 3$ K $\sim 0.1T_c$ with an effective field strength $E_0 = 0.2$ MV/cm, driving frequency $\omega_{dr}/2\pi = 22.4$ THz, and pulse width $\sigma = 2$ ps. (b) Power spectrum of the supercurrent density, measured in the interval between 0 and 2 ps. The parameters for the bilayer system are the same as in Fig. 3.

induced by optical driving of a sum resonance of the Higgs mode and a Josephson plasma mode. Using a newly developed lattice gauge simulator, we demonstrate this time crystal for mono- and bilayer cuprates and show its robustness against thermal fluctuations, for up to ~20% of the critical temperature. As an experimentally accessible signature we observe the emergence of two side peaks at $\omega_{\rm dr} \pm \omega_{\rm H}$ in the supercurrent spectra. This signature is also visible in pulsed operation, which mimics realistic experimental conditions.

The emergent time-crystalline order that we propose to induce constitutes a qualitative departure from previous light-induced states in solids, because it is a genuine nonequilibrium state with no equilibrium counterpart. The realization of such a state expands the scope of the scientific effort to design many-body states by optical driving beyond the paradigm of renormalizing equilibrium orders. While even this existing paradigm has been and continues to be thought provoking and stimulating, the work presented here urges the design and exploration of light-induced nonequilibrium states beyond that framework and thereby expands the scope of the effort to design quantum matter on demand.

ACKNOWLEDGMENTS

APPENDIX A: NOISE CORRELATIONS

The fluctuation-dissipation theorem requires

$$\langle {\rm Re}\{\xi_{\mathbf{r}}(t)\}{\rm Re}\{\xi_{\mathbf{r}'}(t')\}\rangle = \frac{\gamma K \hbar^2 k_{\rm B} T}{V_0}\delta_{\mathbf{rr}'}\delta(t-t'), \qquad {\rm (A1)}$$

$$\langle {\rm Im}\{\xi_{\mathbf{r}}(t)\}{\rm Im}\{\xi_{\mathbf{r}'}(t')\}\rangle = \frac{\gamma K \hbar^2 k_{\rm B} T}{V_0}\delta_{\mathbf{rr}'}\delta(t-t'), \qquad {\rm (A2)}$$

$$\langle {\rm Re}\{\xi_{\mathbf{r}}(t)\}{\rm Im}\{\xi_{\mathbf{r}'}(t')\}\rangle = 0 \qquad {\rm (A3)}$$

for the noise term of the superconducting field, where $V_0 = d_{ab}^2 d_c$ is the discretization volume of a single superconducting

TABLE I. Model parameters used in the simulations.

	Monolayer	Bilayer
K (meV^{-1})	2.9×10^{-5}	2.9×10^{-5}
μ (meV)	1.0×10^{-2}	1.0×10^{-2}
g (meV Å^3)	5.0	5.0
$\gamma/2\pi$ (THz)	0.5	0.5
t_{ab} (meV)	6.2×10^{-1}	6.2×10^{-1}
t_s (meV)	4.2×10^{-2}	2.5×10^{-2}
t_w (meV)	4.2×10^{-2}	1.0×10^{-3}
d_{ab} (Å)	15	15
d_s (Å)	6	4
d_w (Å)	6	8
ϵ_s	1	1
ϵ_w	1	4

site. The noise correlations for the electric field are

$$\langle \eta_{x,\mathbf{r}}(t)\eta_{x,\mathbf{r}'}(t')\rangle = \frac{2\gamma k_{\rm B} T}{\epsilon_0 V_0}\delta_{\mathbf{rr}'}\delta(t-t'), \qquad {\rm (A4)}$$

$$\langle \eta_{y,\mathbf{r}}(t)\eta_{y,\mathbf{r}'}(t')\rangle = \frac{2\gamma k_{\rm B} T}{\epsilon_0 V_0}\delta_{\mathbf{rr}'}\delta(t-t'), \qquad {\rm (A5)}$$

$$\langle \eta_{z,\mathbf{r}}(t)\eta_{z,\mathbf{r}'}(t')\rangle = \frac{d_c}{d_n\epsilon_n}\frac{2\gamma k_{\rm B} T}{\epsilon_0 V_0}\delta_{\mathbf{rr}'}\delta(t-t'). \qquad {\rm (A6)}$$

APPENDIX B: CHARACTERIZATION OF THE RESPONSE

We characterize the response of the system to the periodic driving by studying the dynamics of the sample averages of the condensate amplitude and the supercurrent along the c axis. The supercurrent along a single junction in the c direction is given by the Josephson relation

$$J_{l,m,n}^z = \frac{4et_nd_c}{\hbar}{\rm Im}\{\psi_{l,m,n+1}^*\psi_{l,m,n}e^{ia_{l,m,n}^z}\}. \qquad {\rm (B1)}$$

The sample average of the supercurrent density along the c axis can be obtained from

$$J(t) = \frac{d_s\overline{J_s(t)} + d_w\overline{J_w(t)}}{d_s + d_w}, \qquad {\rm (B2)}$$

where $\overline{J_{s,w}(t)}$ denotes the spatial average of Josephson currents along either strong or weak junctions. In the case of nonzero temperatures, we average the power spectra $P_{|\psi|}(\omega)$ and $P_J(\omega)$ over an ensemble of trajectories. We find that 100 trajectories are enough to obtain convergent results for sampling thermal fluctuations at nonzero temperatures.

APPENDIX C: MODEL PARAMETERS

Table I summarizes the parameters of our numerical calculations for mono- and bilayer systems, respectively. In both cases, our parameter choice of μ and g implies an equilibrium condensate density $n_0 = \mu/g = 2 \times 10^{21}$ cm^{-3} at $T = 0$. The bilayer system has two longitudinal c-axis plasma modes. Their eigenfrequencies are

$$\omega_{\rm J1,J2}^2 = \left(\frac{1}{2}+\alpha_s\right)\Omega_s^2 + \left(\frac{1}{2}+\alpha_w\right)\Omega_w^2 \mp \sqrt{\left[\left(\frac{1}{2}+\alpha_s\right)\Omega_s^2 - \left(\frac{1}{2}+\alpha_w\right)\Omega_w^2\right]^2 + 4\alpha_s\alpha_w\Omega_s^2\Omega_w^2}, \qquad {\rm (C1)}$$

as follows from a sine-Gordon analysis at $T = 0$ [32,33]. Here, we introduced the bare plasma frequencies of the strong and weak junctions

$$\Omega_{s,w} = \sqrt{\frac{8t_{s,w}n_0e^2d_cd_{s,w}}{\hbar^2\epsilon_{s,w}\epsilon_0}},$$ (C2)

where $d_c = (d_s + d_w)/2$. The capacitive coupling constants are given by

$$\alpha_{s,w} = \frac{\epsilon_{s,w}\epsilon_0}{8Kn_0e^2d_cd_{s,w}}.$$ (C3)

Besides, there is a transverse c-axis plasma mode with the eigenfrequency

$$\omega_{\mathrm{T}}^2 = \frac{1 + 2\alpha_s + 2\alpha_w}{\alpha_s + \alpha_w}\left(\alpha_s\Omega_s^2 + \alpha_w\Omega_w^2\right).$$ (C4)

We have $\alpha_s = 0.5$, $\alpha_w = 1$, $\omega_{\mathrm{J1}}/2\pi \approx 2.0$ THz, $\omega_{\mathrm{J2}}/2\pi \approx 14.3$ THz, and $\omega_{\mathrm{T}}/2\pi \approx 11.8$ THz for the parameters specified in Table I. The in-plane plasma frequency amounts to 154 THz.

---

[1] D. Fausti, R. I. Tobey, N. Dean, S. Kaiser, A. Dienst, M. C. Hoffmann, S. Pyon, T. Takayama, H. Takagi, and A. Cavalleri, Light-induced superconductivity in a stripe-ordered cuprate, Science **331**, 189 (2011).

[2] W. Hu, S. Kaiser, D. Nicoletti, C. R. Hunt, I. Gierz, M. C. Hoffmann, M. Le Tacon, T. Loew, B. Keimer, and A. Cavalleri, Optically enhanced coherent transport in YBa$_2$Cu$_3$O$_{6.5}$ by ultrafast redistribution of interlayer coupling, Nat. Mater. **13**, 705 (2014).

[3] K. A. Cremin, J. Zhang, C. C. Homes, G. D. Gu, Z. Sun, M. M. Fogler, A. J. Millis, D. N. Basov, and R. D. Averitt, Photoenhanced metastable c-axis electrodynamics in stripe-ordered cuprate La$_{1.885}$Ba$_{0.115}$CuO$_4$, Proc. Natl. Acad. Sci. USA **116**, 19875 (2019).

[4] A. Kogar, A. Zong, P. E. Dolgirev, X. Shen, J. Straquadine, Y.-Q. Bie, X. Wang, T. Rohwer, I.-C. Tung, Y. Yang, R. Li, J. Yang, S. Weathersby, S. Park, M. E. Kozina, E. J. Sie, H. Wen, P. Jarillo-Herrero, I. R. Fisher, X. Wang *et al.*, Light-induced charge density wave in LaTe$_3$, Nat. Phys. **16**, 159 (2019).

[5] J. G. Cosme, C. Georges, A. Hemmerich, and L. Mathey, Dynamical Control of Order in a Cavity-BEC System, Phys. Rev. Lett. **121**, 153001 (2018).

[6] C. Georges, J. G. Cosme, L. Mathey, and A. Hemmerich, Light-Induced Coherence in an Atom-Cavity System, Phys. Rev. Lett. **121**, 220405 (2018).

[7] F. Wilczek, Superfluidity and Space-Time Translation Symmetry Breaking, Phys. Rev. Lett. **111**, 250402 (2013).

[8] K. Sacha and J. Zakrzewski, Time crystals: A review, Rep. Prog. Phys. **81**, 016401 (2018).

[9] F. M. Gambetta, F. Carollo, M. Marcuzzi, J. P. Garrahan, and I. Lesanovsky, Discrete Time Crystals in the Absence of Manifest Symmetries or Disorder in Open Quantum Systems, Phys. Rev. Lett. **122**, 015701 (2019).

[10] B. Buca, J. Tindall, and D. Jaksch, Non-stationary coherent quantum many-body dynamics through dissipation, Nat. Commun. **10**, 1730 (2019).

[11] T. L. Heugel, M. Oscity, A. Eichler, O. Zilberberg, and R. Chitra, Classical Many-Body Time Crystals, Phys. Rev. Lett. **123**, 124301 (2019).

[12] D. V. Else, C. Monroe, C. Nayak, and N. Y. Yao, Discrete time crystals, Annu. Rev. Condens. Matter Phys. **11**, 467 (2020).

[13] N. Y. Yao, C. Nayak, L. Balents, and M. P. Zaletel, Classical discrete time crystals, Nat. Phys. **16**, 438 (2020).

[14] S. Choi, J. Choi, R. Landig, G. Kucsko, H. Zhou, J. Isoya, F. Jelezko, S. Onoda, H. Sumiya, V. Khemani, C. von Keyserlingk, N. Y. Yao, E. Demler, and M. D. Lukin, Observation of discrete time-crystalline order in a disordered dipolar many-body system, Nature (London) **543**, 221 (2017).

[15] J. Zhang, P. W. Hess, A. Kyprianidis, P. Becker, A. Lee, J. Smith, G. Pagano, I.-D. Potirniche, A. C. Potter, A. Vishwanath, N. Y. Yao, and C. Monroe, Observation of a discrete time crystal, Nature (London) **543**, 217 (2017).

[16] A. Chew, D. F. Mross, and J. Alicea, Time-Crystalline Topological Superconductors, Phys. Rev. Lett. **124**, 096802 (2020).

[17] C. M. Varma, Higgs boson in superconductors, J. Low Temp. Phys. **126**, 901 (2002).

[18] D. Pekker and C. Varma, Amplitude/Higgs modes in condensed matter physics, Annu. Rev. Condens. Matter Phys. **6**, 269 (2015).

[19] R. Matsunaga, N. Tsuji, H. Fujita, A. Sugioka, K. Makise, Y. Uzawa, H. Terai, Z. Wang, H. Aoki, and R. Shimano, Light-induced collective pseudospin precession resonating with Higgs mode in a superconductor, Science **345**, 1145 (2014).

[20] N. Tsuji and H. Aoki, Theory of Anderson pseudospin resonance with Higgs mode in superconductors, Phys. Rev. B **92**, 064508 (2015).

[21] S. Nakamura, Y. Iida, Y. Murotani, R. Matsunaga, H. Terai, and R. Shimano, Infrared Activation of the Higgs Mode by Supercurrent Injection in Superconducting NbN, Phys. Rev. Lett. **122**, 257001 (2019).

[22] R. Shimano and N. Tsuji, Higgs mode in superconductors, Annu. Rev. Condens. Matter Phys. **11**, 103 (2020).

[23] F. Peronaci, M. Schiró, and M. Capone, Transient Dynamics of *d*-Wave Superconductors after a Sudden Excitation, Phys. Rev. Lett. **115**, 257001 (2015).

[24] K. Katsumi, N. Tsuji, Y. I. Hamada, R. Matsunaga, J. Schneeloch, R. D. Zhong, G. D. Gu, H. Aoki, Y. Gallais, and R. Shimano, Higgs Mode in the *d*-Wave Superconductor Bi$_2$Sr$_2$CaCu$_2$O$_{8+x}$ Driven by an Intense Terahertz Pulse, Phys. Rev. Lett. **120**, 117001 (2018).

[25] M. Buzzi, G. Jotzu, A. Cavalleri, J. I. Cirac, E. A. Demler, B. I. Halperin, M. D. Lukin, T. Shi, Y. Wang, and D. Podolsky,

Higgs-mediated optical amplification in a non-equilibrium superconductor, arXiv:1908.10879 [cond-mat.supr-con].

[26] H. Chu, M.-J. Kim, K. Katsumi, S. Kovalev, R. D. Dawson, L. Schwarz, N. Yoshikawa, G. Kim, D. Putzky, Z. Z. Li, H. Raffy, S. Germanskiy, J.-C. Deinert, N. Awari, I. Ilyakov, B. Green, M. Chen, M. Bawatna, G. Christiani, G. Logvenov *et al.*, Phase-resolved Higgs response in superconducting cuprates, Nat. Commun. **11**, 1793 (2020).

[27] L. Schwarz, B. Fauseweh, N. Tsuji, N. Cheng, N. Bittner, H. Krull, M. Berciu, G. S. Uhrig, A. P. Schnyder, S. Kaiser, and D. Manske, Classification and characterization of nonequilibrium Higgs modes in unconventional superconductors, Nat. Commun. **11**, 287 (2020).

[28] M. Puviani, L. Schwarz, X.-X. Zhang, S. Kaiser, and D. Manske, Current-assisted Raman activation of the Higgs mode in superconductors, Phys. Rev. B **101**, 220507(R) (2020).

[29] F. Yang and M. W. Wu, Theory of Higgs modes in d-wave superconductors, Phys. Rev. B **102**, 014511 (2020).

[30] E. A. Yuzbashyan, O. Tsyplyatyev, and B. L. Altshuler, Relaxation and Persistent Oscillations of the Order Parameter in Fermionic Condensates, Phys. Rev. Lett. **96**, 097005 (2006).

[31] T. Koyama and M. Tachiki, I-V characteristics of Josephson-coupled layered superconductors with longitudinal plasma excitations, Phys. Rev. B **54**, 16183 (1996).

[32] D. van der Marel and A. A. Tsvetkov, Transverse-optical Josephson plasmons: Equations of motion, Phys. Rev. B **64**, 024530 (2001).

[33] T. Koyama, Josephson plasma resonances and optical properties in high-T_c superconductors with alternating junction parameters, J. Phys. Soc. Jpn. **71**, 2986 (2002).

[34] H. Shibata and T. Yamada, Double Josephson Plasma Resonance in T^* Phase SmLa$_{1-x}$Sr$_x$CuO$_{4-\delta}$, Phys. Rev. Lett. **81**, 3519 (1998).

[35] D. Dulić, A. Pimenov, D. van der Marel, D. M. Broun, S. Kamal, W. N. Hardy, A. A. Tsvetkov, I. M. Sutjaha, R. Liang, A. A. Menovsky, A. Loidl, and S. S. Saxena, Observation of the Transverse Optical Plasmon in SmLa$_{0.8}$Sr$_{0.2}$CuO$_{4-\delta}$, Phys. Rev. Lett. **86**, 4144 (2001).

[36] D. N. Basov and T. Timusk, Electrodynamics of high-T_c superconductors, Rev. Mod. Phys. **77**, 721 (2005).

[37] V. L. Ginzburg and L. D. Landau, On the theory of superconductivity, Zh. Eksp. Teor. Fiz. **20**, 1064 (1950).

[38] J. B. Kogut, An introduction to lattice gauge theory and spin systems, Rev. Mod. Phys. **51**, 659 (1979).

[39] K. Yee, Numerical solution of initial boundary value problems involving Maxwell's equations in isotropic media, IEEE Trans. Antennas Propag. **14**, 302 (1966).

[40] S. J. Denny, S. R. Clark, Y. Laplace, A. Cavalleri, and D. Jaksch, Proposed Parametric Cooling of Bilayer Cuprate Superconductors by Terahertz Excitation, Phys. Rev. Lett. **114**, 137001 (2015).

[41] J.-i. Okamoto, A. Cavalleri, and L. Mathey, Theory of Enhanced Interlayer Tunneling in Optically Driven High-T_c Superconductors, Phys. Rev. Lett. **117**, 227001 (2016).

[42] J.-i. Okamoto, W. Hu, A. Cavalleri, and L. Mathey, Transiently enhanced interlayer tunneling in optically driven high-T_c superconductors, Phys. Rev. B **96**, 144505 (2017).

[43] See Supplemental Material at http://link.aps.org/supplemental/10.1103/PhysRevResearch.2.043214 for a multiple-scale analysis of the sum resonance, rigidity of the Higgs time crystal, conductivity measurements in the time-crystalline phase, and information on the thermal phase transition and the temperature dependence of the resonance frequencies.

[44] L. D. Landau and E. M. Lific, *Mechanics*, 3rd ed. (Butterworth-Heinemann, Oxford, 1976).

[45] A. H. Nayfeh, Combination resonances in the non-linear response of bowed structures to a harmonic excitation, J. Sound Vib. **90**, 457 (1983).

[46] A. von Hoegen, R. Mankowsky, M. Fechner, M. Först, and A. Cavalleri, Probing the interatomic potential of solids with strong-field nonlinear phononics, Nature (London) **555**, 79 (2018).

[47] A. von Hoegen, M. Fechner, M. Först, J. Porras, B. Keimer, M. Michael, E. Demler, and A. Cavalleri, Probing coherent charge fluctuations in YBa$_2$Cu$_3$O$_{6+x}$ at wavevectors outside the light cone, arXiv:1911.08284 [cond-mat.supr-con].

[48] U. Welp, K. Kadowaki, and R. Kleiner, Superconducting emitters of THz radiation, Nat. Photonics **7**, 702 (2013).

Supplemental Material for
Higgs Time Crystal in a High-T_c Superconductor

Guido Homann,[1, *] Jayson G. Cosme,[1, 2, 3] and Ludwig Mathey[1, 2]

[1] *Zentrum für Optische Quantentechnologien und Institut für Laserphysik, Universität Hamburg, 22761 Hamburg, Germany*
[2] *The Hamburg Centre for Ultrafast Imaging, Luruper Chaussee 149, 22761 Hamburg, Germany*
[3] *National Institute of Physics, University of the Philippines, Diliman, Quezon City 1101, Philippines*

CONTENTS

* ghomann@physnet.uni-hamburg.de

I. MULTIPLE-SCALE ANALYSIS OF THE SUM RESONANCE

Here, we derive the sum resonance of the Higgs mode and the Josephson plasmon of a monolayer cuprate superconductor in the zero-temperature limit, where the model simplifies to a 1D chain along the c-axis. We consider the two-mode model discussed in the main text:

$$\partial_t^2 a + \gamma \partial_t a + \omega_J^2 a + 2\omega_J^2 ah \approx j_{dr}, \tag{1}$$

$$\partial_t^2 h + \gamma \partial_t h + \omega_H^2 h + \alpha \omega_J^2 a^2 \approx 0. \tag{2}$$

The Higgs field is given by $h = (\psi - \psi_0)/\psi_0$ with ψ_0 being the equilibrium condensate amplitude, and j_{dr} is the current due to the drive. Note that the unitless vector potential a equals the phase difference between adjacent planes in this setting. The Higgs and plasma frequencies are $\omega_H = \sqrt{2\mu/K\hbar^2}$ and $\omega_J = \sqrt{t_J/\alpha K\hbar^2}$, respectively. Next, we expand j_{dr}, a, and h according to

$$f = f^{(0)} + \lambda f^{(1)} + \lambda^2 f^{(2)} + \mathcal{O}(\lambda^3), \tag{3}$$

where $\lambda \ll 1$ is a small expansion parameter. Moreover, we take the driving as

$$j_{dr}^{(1)} = j_1 e^{-i\omega_{dr}t} + \text{c.c.}, \tag{4}$$

where

$$\lambda |j_1| = \frac{ed\omega_{dr}E_0}{\hbar\epsilon} \tag{5}$$

for $E_{dr}(t) = E_0 \cos(\omega_{dr}t)$. From now on, we assume weak damping, that is, $\gamma = \lambda\tilde{\gamma}$. The expansion parameter λ is also used to define multiple time scales:

$$T_0 \equiv t, \quad T_1 \equiv \lambda t. \tag{6}$$

The time derivatives transform as

$$\partial_t = D_0 + \lambda D_1 + \mathcal{O}(\lambda^2), \quad \partial_t^2 = D_0^2 + 2\lambda D_0 D_1 + \mathcal{O}(\lambda^2), \tag{7}$$

where $D_n \equiv \frac{\partial}{\partial T_n}$. Since all the zeroth order contributions vanish, the first non-trivial contribution comes from the first order

$$D_0^2 a^{(1)} + \omega_J^2 a^{(1)} = j_1 e^{-i\omega_{dr}t} + \text{c.c.}, \tag{8}$$

$$D_0^2 h^{(1)} + \omega_H^2 h^{(1)} = 0. \tag{9}$$

This implies solutions of the form

$$a^{(1)} = C_J e^{-i\omega_J T_0} + F e^{-i\omega_{dr}T_0} + \text{c.c.}, \tag{10}$$

$$h^{(1)} = C_H e^{-i\omega_H T_0} + \text{c.c.}, \tag{11}$$

where F is given by

$$F = \frac{j_1}{\omega_J^2 - \omega_{dr}^2}. \tag{12}$$

Introducing the amplitudes $C_J(T_1)$ and $C_H(T_1)$ allows to describe a possible sum resonance. These amplitudes are determined in the following. In second order, we have

$$D_0^2 a^{(2)} + \omega_J^2 a^{(2)} = -2D_0 D_1 a^{(1)} - \tilde{\gamma} D_0 a^{(1)} - 2\omega_J^2 a^{(1)} h^{(1)}, \tag{13}$$

$$D_0^2 h^{(2)} + \omega_H^2 h^{(2)} = -2D_0 D_1 h^{(1)} - \tilde{\gamma} D_0 h^{(1)} - \alpha\omega_J^2 [a^{(1)}]^2. \tag{14}$$

Substituting the first order solutions into the second order equations leads to

$$D_0^2 a^{(2)} + \omega_J^2 a^{(2)} = i(2D_1 + \tilde{\gamma})\left(\omega_J C_J e^{-i\omega_J T_0} + \omega_{dr} F e^{-i\omega_{dr}T_0}\right)$$
$$- 2\omega_J^2\left(C_J C_H e^{-i(\omega_J + \omega_H)T_0} + C_J C_H^* e^{-i(\omega_J - \omega_H)T_0} + F C_H e^{-i(\omega_{dr} + \omega_H)T_0} + F C_H^* e^{-i(\omega_{dr} - \omega_H)T_0}\right) + \text{c.c.}, \tag{15}$$

$$D_0^2 h^{(2)} + \omega_H^2 h^{(2)} = i(2D_1 + \tilde{\gamma})\omega_H C_H e^{-i\omega_H T_0} - \alpha\omega_J^2\Big(|C_J|^2 + |F|^2 + C_J^2 e^{-2i\omega_J T_0} + F^2 e^{-2i\omega_{dr}T_0}$$
$$+ 2F C_J e^{-i(\omega_{dr} + \omega_J)T_0} + 2F C_J^* e^{-i(\omega_{dr} - \omega_J)T_0}\Big) + \text{c.c.}. \tag{16}$$

To study the behavior near the sum resonance, we write

$$\omega_{\text{dr}} = \omega_{\text{J}} + \omega_{\text{H}} + \lambda\delta \tag{17}$$

with the detuning δ. Inserting this into the second order equations induces secular terms, which we demand to vanish:

$$\text{i}(2D_1 + \tilde{\gamma})\omega_{\text{J}}C_{\text{J}} - 2\omega_{\text{J}}^2 F C_{\text{H}}^* \text{e}^{-\text{i}\delta T_1} = 0, \tag{18}$$

$$\text{i}(2D_1 + \tilde{\gamma})\omega_{\text{H}}C_{\text{H}} - 2\alpha\omega_{\text{J}}^2 F C_{\text{J}}^* \text{e}^{-\text{i}\delta T_1} = 0. \tag{19}$$

The conditions (18) and (19) imply solutions of the form

$$C_{\text{J}} = \tilde{C}_{\text{J}} \text{e}^{(r-\text{i}\delta)T_1}, \tag{20}$$

$$C_{\text{H}} = \tilde{C}_{\text{J}} \text{e}^{r^* T_1}. \tag{21}$$

Using this ansatz, we find

$$r = -\frac{(\tilde{\gamma} - \text{i}\delta)}{2} \pm \frac{1}{2}\sqrt{\frac{4\alpha\omega_{\text{J}}^3}{\omega_{\text{H}}}|F|^2 - \delta^2}. \tag{22}$$

If the real part of r is positive, the amplitudes C_{J} and C_{H} grow exponentially. Such a behaviour signals the excitation of the sum resonance. It requires a sufficient driving amplitude given by the condition

$$|F|^2 > \left(\tilde{\gamma}^2 + \delta^2\right)\frac{\omega_{\text{H}}}{4\alpha\omega_{\text{J}}^3}. \tag{23}$$

Let us consider the case $\omega_{\text{dr}} = \omega_{\text{J}} + \omega_{\text{H}}$, i.e., $\delta = 0$. In this case, the required driving amplitude to induce the sum resonance is

$$E_0 > \gamma\sqrt{\frac{2n_0 K\hbar^2}{\epsilon\epsilon_0}}\left(\frac{2\omega_{\text{J}} + \omega_{\text{H}}}{\omega_{\text{J}} + \omega_{\text{H}}}\right)\left(\frac{\omega_{\text{H}}}{\omega_{\text{J}}}\right)^{3/2} \approx 8 \times 10^{-3} \text{ MV cm}^{-1} \tag{24}$$

for the parameters specified in the main text. Higher order terms play an important role in saturating the amplitude of oscillations [1], which can be understood from the perspective of non-linear oscillators having amplitude dependent eigenfrequencies.

In the case of driving close to the difference frequency,

$$\omega_{\text{dr}} = \omega_{\text{J}} - \omega_{\text{H}} + \lambda\delta, \tag{25}$$

we find

$$r = -\frac{(\tilde{\gamma} - \text{i}\delta)}{2} \pm \frac{1}{2}\sqrt{-\frac{4\alpha\omega_{\text{J}}^3}{\omega_{\text{H}}}|F|^2 - \delta^2}. \tag{26}$$

Here the real part of r is always negative. Hence, there is no difference resonance in the system.

II. RIGIDITY OF THE HIGGS TIME CRYSTAL

The following zero-temperature simulations refer to the bilayer cuprate superconductor specified in the main text. We take the driving as

$$E_{\text{dr}}(t) = \frac{E_0}{2}\cos(\omega_{\text{dr}}t)\left[1 + \tanh\left(\frac{t}{\tau}\right)\right], \tag{27}$$

where E_0 is the strength of the external field effectively penetrating the sample. Additionally, the external drive is characterised by the frequency ω_{dr} and the rise time τ.

To realise the sum resonance of the Higgs mode and the upper Josephson plasmon, we drive the electric field with $E_0 = 0.2$ MV cm^{-1} and $\omega_{\text{dr}}/2\pi = 21$ THz. The long-time persistence of the time-translation symmetry breaking is exemplified in Fig. 1, where the subharmonic oscillations in the condensate amplitude are found to survive even after 10^5 driving cycles.

As discussed in Ref. [2], a signature of a phase transition to a time crystalline order in classical systems is the hysteretic behaviour across a critical point. Here, we demonstrate an indicator of such hysteresis in the response of the condensate amplitude. This can be seen in Fig. 2 as we tune the driving amplitude across the time crystal-normal response transition from $E_0 = 0.08$ MV cm^{-1} to $E_0 = 0.1$ MV cm^{-1} and vice versa, while keeping the driving frequency fixed at $\omega_{\text{dr}}/2\pi = 21$ THz. In particular, there is a clear difference in the time that it takes the system to enter and leave the time crystalline phase.
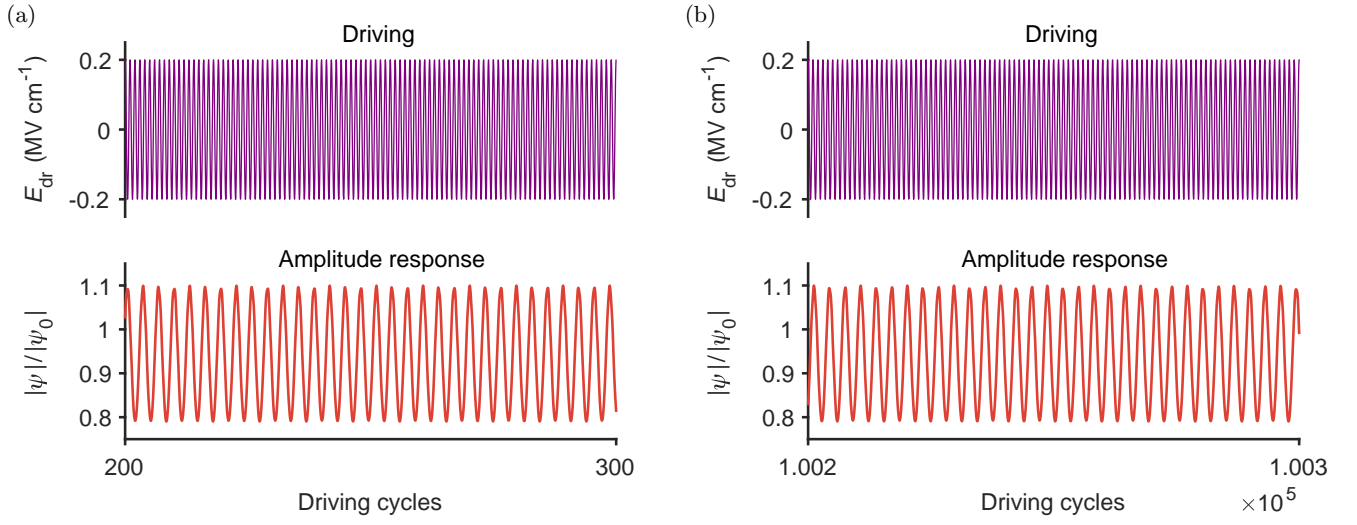
FIG. 1. Long-time persistence of the subharmonic response at $T = 0$. (a) Amplitude response after 200 driving cycles. (b) Amplitude response after 1.002×10^5 driving cycles.
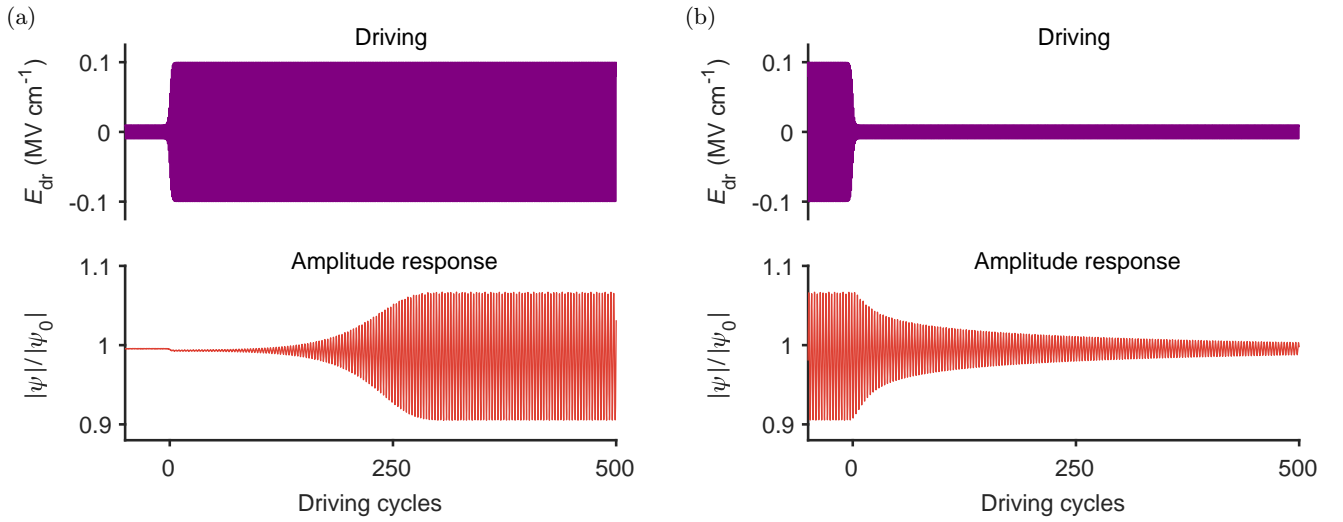

FIG. 2. Dynamical transitions between normal and time crystalline phase. (a) Transition from normal to time crystalline phase. (b) Transition from time crystalline to normal phase.

III. OPTICAL CONDUCTIVITY OF THE HIGGS TIME CRYSTAL

The optical conductivity $\sigma(\omega)$ is a crucial quantity to characterise the electric transport properties of a superconductor in the linear response regime. It is a macroscopic observable that can be measured in pump-probe experiments [3, 4]. Here, we investigate how the emergence of the Higgs time crystal alters the c-axis optical conductivity of a bilayer cuprate superconductor with parameters as specified in the main text. For this purpose, the system is driven into the time crystalline phase with $E_0 = 0.2$ MV cm^{-1} and $\omega_{\mathrm{dr}}/2\pi = 21$ THz at $T = 0$. Then, we add a probing term to the external drive,

$$E_{\mathrm{dr}}(t) = E_0\cos(\omega_{\mathrm{dr}}t) + \frac{E_{\mathrm{pr}}}{2}\cos(\omega_{\mathrm{pr}}t)\left[1 + \tanh\left(\frac{\omega_{\mathrm{pr}}(t - t_{\mathrm{pr}})}{2\pi}\right)\right], \tag{28}$$

where $t_{\mathrm{pr}} = 10$ ps. The probing amplitude E_{pr} has to be one order of magnitude smaller than E_0 to enter the linear response regime. We evaluate $\sigma(\omega) = J_{\mathrm{tot}}(\omega)/E(\omega)$ from a Fourier analysis over 50 ps in the steady state. The average electric field along the c-axis is given by

$$E(t) = \frac{d_s\overline{E_s(t)} + d_w\overline{E_w(t)}}{d_s + d_w}, \tag{29}$$

where $\overline{E_{s,w}(t)}$ denotes the spatial average of electric fields along either strong or weak junctions. The total current is the sum of the average supercurrent and the average displacement current inside the sample, that is,

$$J_{\mathrm{tot}}(t) = J(t) + \frac{d_s\epsilon_s\epsilon_0\overline{\partial_t E_s} + d_w\epsilon_w\epsilon_0\overline{\partial_t E_w}}{d_s + d_w}, \tag{30}$$

where $J(t)$ is the supercurrent given in the main text. As visible in Fig. 3(a), the real part of the optical conductivity acquires additional resonance peaks in the time crystalline phase, especially at $\omega_{\mathrm{L}} = \omega_{\mathrm{dr}} - \omega_{\mathrm{H}}$ and $\omega_{\mathrm{R}} = \omega_{\mathrm{dr}} + \omega_{\mathrm{H}}$. These frequencies correspond to the side peaks previously observed in the supercurrent spectra. Remarkably, the current response is amplified at the left side peak while attenuated at the right side peak. The counterparts of the peaks in σ_1 are sharp edges in σ_2 as evidenced by Fig. 3(b). The depletion of the condensate tends to reduce the plasma frequencies in the time crystalline phase. This effect is most apparent for the transverse Josephson plasmon shifting from 11.8 THz to 11.4 THz. For the same reason, we find a smaller prefactor of the $1/\omega$ divergence of σ_2 at low frequencies.
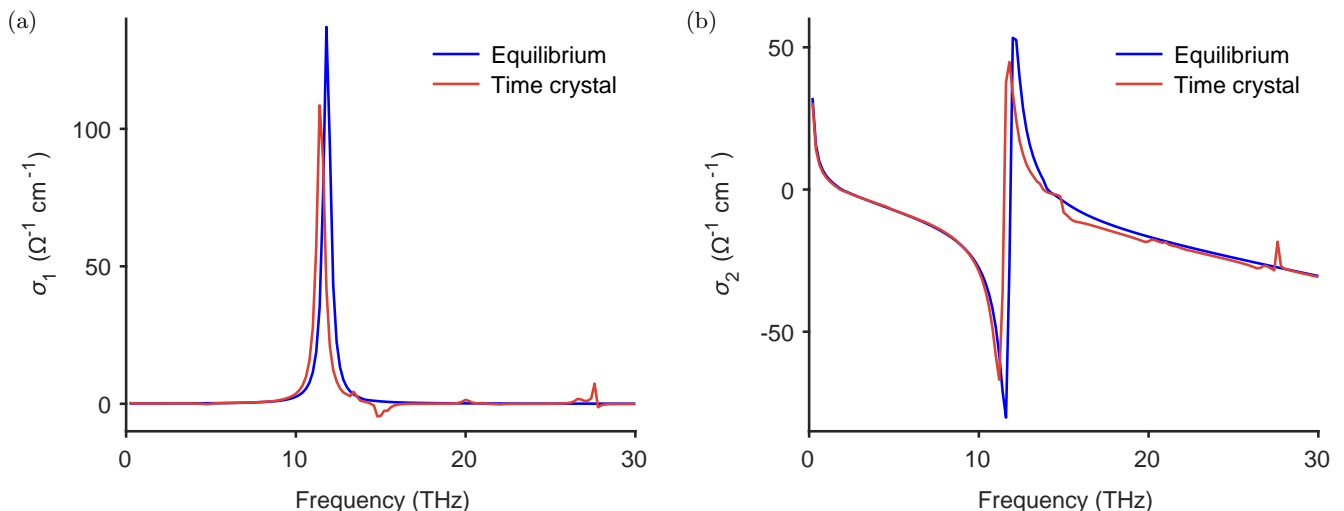

FIG. 3. Optical conductivity in the time crystalline phase. (a) Real part of the optical conductivity. (b) Imaginary part of the optical conductivity.

IV. THERMAL PHASE TRANSITION

Here, we elaborate on the thermal phase transition of the simulated bilayer cuprate superconductor, see main text for parameters. The thermal equilibrium at a given temperature is established as follows. We initialise the system in its ground state at $T = 0$ and let the dynamics evolve without external driving, influenced only by thermal fluctuations and dissipation. After 10 ps, the average condensate density $n = \frac{1}{N} \sum_{\mathbf{r}} |\psi_{\mathbf{r}}|^2$ and the phase coherence are converged, indicating thermal equilbrium. To characterise the phase transition, we introduce the order parameter

$$O = \frac{1}{n} \left| \frac{1}{N/2} \sum_{l,m,n \in \text{odd}} \psi_{l,m,n+1}^* \psi_{l,m,n} \, \mathrm{e}^{\mathrm{i} a_{l,m,n}^z} \right|. \tag{31}$$

The order parameter measures the phase coherence of the condensate across different bilayers. For each trajectory, it is evaluated from the average of 200 measurements within a time interval of 2 ps. Finally, we take the ensemble average of 100 trajectories. As shown in Fig. 4(a), the temperature dependence of the order parameter is reminiscent of a second order phase transition. Due to the finite size of the simulated system, the order parameter converges to a plateau with non-zero value for high temperatures. Instead of a sharp discontinuity, one finds a distinct crossover at $T_c \sim 30$ K. We also note that the lower Josephson plasmon vanishes in this temperature regime, which agrees with experimental observations [5]. Figure 4(b) reveals that the condensate density does not drop below $0.4 \, n_0$ through the phase transition. Strikingly, the condensate density decreases almost linearly with temperature below T_c. By contrast, it undergoes a nearly linear increase above the transition temperature. We see in Figs. 4(c) and 4(d) that the phase transition is only weakly modified by increasing the system size.
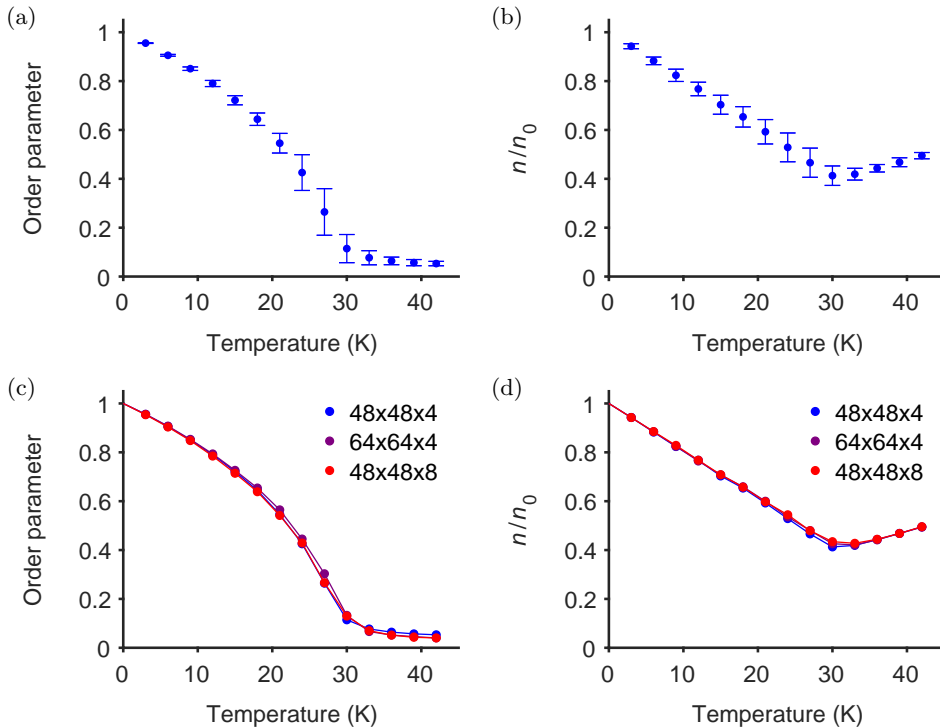
FIG. 4. Phase transition of a bilayer cuprate superconductor. (a) Order parameter for a system of $48 \times 48 \times 4$ lattice sites. (b) Condensate density for a system of $48 \times 48 \times 4$ lattice sites. The error bars indicate the standard deviations of the ensemble averages. (c) Order parameter for various system sizes. (d) Condensate density for various system sizes. The physical parameters are the same as for the bilayer system considered in the main text.

V. TEMPERATURE DEPENDENCE OF THE RESONANCE FREQUENCIES

In this section, we discuss the temperature dependence of the resonance frequencies, which can be deduced from the undriven dynamics of the superconductor in thermal equilibrium. More precisely, the Higgs mode and the longitudinal Josephson plasmons appear as peaks in the amplitude and supercurrent spectra, respectively. We fit a Lorentzian to the corresponding maxima in the thermal spectra (ensemble average of 100 trajectories). Figure 5 displays the temperature dependence of the Higgs and upper Josephson plasma frequencies up to $\sim 0.4\,T_{\rm c}$ for various system sizes.

While the upper Josephson plasmon is weakly shifted towards smaller frequencies, the Higgs frequency notably increases with temperature. The temperature dependence of the Higgs frequency does not significantly depend on the system size, but on the in-plane tunnelling t_{ab} as inferred from additional simulations. Additionally, a comparison to thermal spectra with different t_{ab} indicates a minor role of the condensate density in this process. That is why our analysis is focused on the correction of the Higgs frequency arising from fourth order coupling terms between the Higgs field and the vector potential. Due to the dominant role of the in-plane dynamics in this process, we perform the following calculations in 2D. Expanding around the thermal equilibrium at a given temperature yields

$$\partial_t^2 h_{\bf r} + \gamma\partial_t h_{\bf r} + \frac{2\mu}{K\hbar^2}h_{\bf r} + \frac{t_{ab}}{K\hbar^2}\sum_{{\bf r}'\in{\rm NN}}(h_{\bf r}-h_{{\bf r}'}) + \frac{t_{ab}}{2K\hbar^2}\sum_{{\bf r}'\in{\rm NN}}\theta_{{\bf r}{\bf r}'}^2 h_{{\bf r}'} \approx 0, \tag{32}$$

where the sum is restricted to the nearest neighbours (NN) of ${\bf r}$ in the ab-plane, and $\theta_{{\bf r}{\bf r}'} = a_{{\bf r}{\bf r}'} + \arg(\psi_{\bf r}) - \arg(\psi_{{\bf r}'})$ denotes the gauge-invariant phase between neighbouring sites. The notation $a_{{\bf r}{\bf r}'}$ means the bond-directed component of the vector potential at $({\bf r}+{\bf r}')/2$ with $a_{{\bf r}'{\bf r}} = -a_{{\bf r}{\bf r}'}$. A Fourier transform leads to

$$\sum_{\bf k}\left(\partial_t^2 h_{\bf k} + \gamma\partial_t h_{\bf k} + \omega_{\rm H}^2({\bf k})h_{\bf k}\right){\rm e}^{{\rm i}{\bf k}\cdot{\bf r}} \approx -\frac{t_{ab}}{K\hbar^2 M}\sum_{\bf p,q}\left[\cos\left(\frac{p_x+2q_x}{2}d_{ab}\right)(\theta_x^2)_{\bf p} + \cos\left(\frac{p_y+2q_y}{2}d_{ab}\right)(\theta_y^2)_{\bf p}\right]h_{\bf q}{\rm e}^{{\rm i}({\bf p}+{\bf q})\cdot{\bf r}}, \tag{33}$$

where M is the total number of sites in the ab-plane, and

$$\omega_{\rm H}^2({\bf k}) = \frac{2\mu}{K\hbar^2} + \frac{2t_{ab}}{K\hbar^2}\left[2 - \cos(k_x d_{ab}) - \cos(k_y d_{ab})\right]. \tag{34}$$

The equation of motion for a given momentum mode reads

$$\partial_t^2 h_{\bf k} + \gamma\partial_t h_{\bf k} + \omega_{\rm H}^2({\bf k})h_{\bf k} \approx -\frac{t_{ab}}{K\hbar^2 M}\sum_{\bf q}\left[\cos\left(\frac{k_x+q_x}{2}d_{ab}\right)(\theta_x^2)_{\bf k-q} + \cos\left(\frac{k_y+q_y}{2}d_{ab}\right)(\theta_y^2)_{\bf k-q}\right]h_{\bf q}. \tag{35}$$
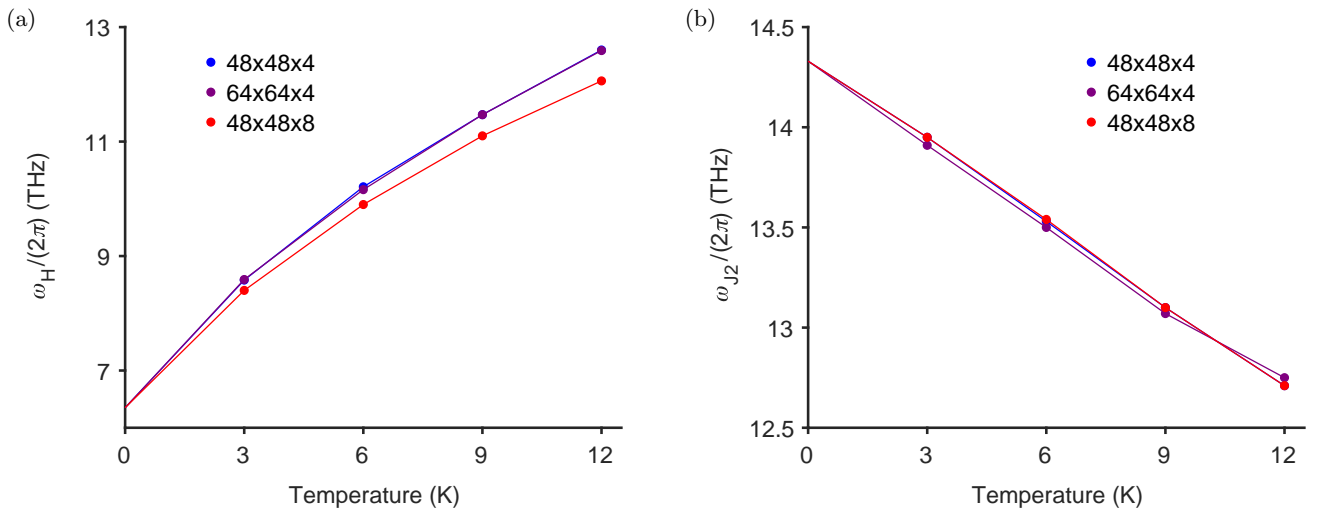

FIG. 5. Temperature dependence of the the resonance frequencies. (a) Temperature dependence of the Higgs frequency. (b) Temperature dependence of the upper Josephson plasma frequency.
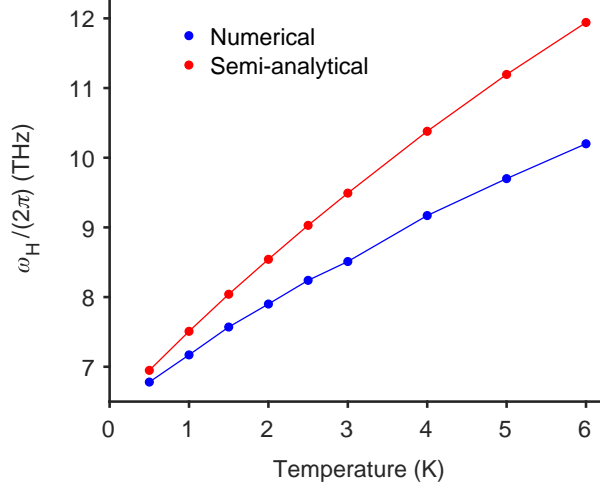
FIG. 6. Increase of the Higgs frequency at low temperatures. The numerical results are compared to a semi-analytical estimate.

So, we have

$$\partial_t^2 h_0 + \gamma \partial_t h_0 + \omega_{\mathrm{H}}^2(0) h_0 \approx -\frac{t_{ab}}{K\hbar^2} \frac{(\theta_x^2)_0 + (\theta_y^2)_0}{M} h_0 - \frac{t_{ab}}{K\hbar^2 M} \sum_{\mathbf{q}\neq 0}\left[\cos\left(\frac{q_x d_{ab}}{2}\right)(\theta_x^2)_{-\mathbf{q}} + \cos\left(\frac{q_y d_{ab}}{2}\right)(\theta_y^2)_{-\mathbf{q}}\right] h_{\mathbf{q}}. \quad (36)$$

To determine the finite-momentum modes on the right-hand side of equation (36), we apply a rotating wave approximation:

$$h_{\mathbf{q}} \approx -\frac{t_{ab}}{K\hbar^2 \omega_{\mathrm{H}}^2(\mathbf{q}) M} \sum_{\mathbf{k}}\left[\cos\left(\frac{k_x + q_x}{2} d_{ab}\right)(\theta_x^2)_{\mathbf{q}-\mathbf{k}} + \cos\left(\frac{k_y + q_y}{2} d_{ab}\right)(\theta_y^2)_{\mathbf{q}-\mathbf{k}}\right] h_{\mathbf{k}}. \quad (37)$$

Furthermore, we assume that the zero-momentum mode provides the main contribution to the sum in equation (37), leading to

$$h_{\mathbf{q}} \approx -\frac{t_{ab}}{K\hbar^2 \omega_{\mathrm{H}}^2(\mathbf{q}) M}\left[\cos\left(\frac{q_x d_{ab}}{2}\right)(\theta_x^2)_{\mathbf{q}} + \cos\left(\frac{q_y d_{ab}}{2}\right)(\theta_y^2)_{\mathbf{q}}\right] h_0. \quad (38)$$

Inserting this into equation (36) yields

$$\begin{aligned}
&\partial_t^2 h_0 + \gamma \partial_t h_0 + \omega_{\mathrm{H}}^2(0) h_0 \\
&\approx -\frac{t_{ab}}{K\hbar^2} \frac{(\theta_x^2)_0 + (\theta_y^2)_0}{M} h_0 + \frac{t_{ab}^2}{K^2 \hbar^4} \sum_{\mathbf{q}\neq 0}\left[\frac{F_x(\mathbf{q})(\theta_x^2)_{\mathbf{q}}(\theta_x^2)_{-\mathbf{q}}}{M^2} + \frac{F_y(\mathbf{q})(\theta_y^2)_{\mathbf{q}}(\theta_y^2)_{-\mathbf{q}}}{M^2} + \frac{2 F_{xy}(\mathbf{q})(\theta_x^2)_{\mathbf{q}}(\theta_y^2)_{-\mathbf{q}}}{M^2}\right] h_0,
\end{aligned} \quad (39)$$

where

$$F_x(\mathbf{q}) = \frac{1}{\omega_{\mathrm{H}}^2(\mathbf{q})} \cos^2\left(\frac{q_x d_{ab}}{2}\right), \quad (40)$$

$$F_y(\mathbf{q}) = \frac{1}{\omega_{\mathrm{H}}^2(\mathbf{q})} \cos^2\left(\frac{q_y d_{ab}}{2}\right), \quad (41)$$

$$F_{xy}(\mathbf{q}) = \frac{1}{\omega_{\mathrm{H}}^2(\mathbf{q})} \cos\left(\frac{q_x d_{ab}}{2}\right)\cos\left(\frac{q_y d_{ab}}{2}\right). \quad (42)$$

This implies the temperature-dependent Higgs frequency

$$\omega_{\mathrm{H}}(\mathbf{k} = 0, T) = \omega_{\mathrm{H}}(0, 0)\sqrt{1 + \Delta_1(T) + \Delta_2(T)}, \quad (43)$$

with the corrections

$$\Delta_1(T) = \frac{t_{ab}}{2\mu} \left\langle \frac{(\theta_x^2)_0 + (\theta_y^2)_0}{M} \right\rangle, \tag{44}$$

$$\Delta_2(T) = -\frac{t_{ab}^2}{2\mu K \hbar^2} \sum_{\mathbf{q} \neq 0} \left\langle \frac{F_x(\mathbf{q})(\theta_x^2)_{\mathbf{q}}(\theta_x^2)_{-\mathbf{q}}}{M^2} + \frac{F_y(\mathbf{q})(\theta_y^2)_{\mathbf{q}}(\theta_y^2)_{-\mathbf{q}}}{M^2} + \frac{2F_{xy}(\mathbf{q})(\theta_x^2)_{\mathbf{q}}(\theta_y^2)_{-\mathbf{q}}}{M^2} \right\rangle. \tag{45}$$

The estimate in Eq. (43) is compared to the purely numerical results in Fig. 6. For both curves, we take the ensemble average of 100 trajectories. The discrepancy between the the numerical and semi-analytical values can be ascribed to the approximations made in equations (37) and (38). Moreover, we have ignored the c-axis dynamics and higher order terms as present in the Mexican hat potential, for example. Nonetheless, our estimate distils the effect of the fourth order coupling terms $\sim a^2 h^2$ on the Higgs frequency. For fixed model parameters, the Higgs frequency is shifted to a higher value because of thermally activated phase fluctuations in the ab-plane. In realistic systems, however, the chemical potential $\mu(T)$ decreases with temperature such that the Higgs frequency does not necessarily increase.

[1] A. H. Nayfeh, Combination resonances in the non-linear response of bowed structures to a harmonic excitation, J. Sound Vib. **90**, 457 (1983).

[2] N. Y. Yao, C. Nayak, L. Balents, and M. P. Zaletel, Classical discrete time crystals, Nat. Phys. **16**, 438 (2020).

[3] W. Hu, S. Kaiser, D. Nicoletti, C. R. Hunt, I. Gierz, M. C. Hoffmann, M. Le Tacon, T. Loew, B. Keimer, and A. Cavalleri, Optically enhanced coherent transport in YBa$_2$Cu$_3$O$_{6.5}$ by ultrafast redistribution of interlayer coupling, Nat. Mater. **13**, 705 (2014).

[4] K. A. Cremin, J. Zhang, C. C. Homes, G. D. Gu, Z. Sun, M. M. Fogler, A. J. Millis, D. N. Basov, and R. D. Averitt, Photoenhanced metastable c-axis electrodynamics in stripe-ordered cuprate La$_{1.885}$Ba$_{0.115}$CuO$_4$, Proc. Natl. Acad. Sci. USA **116**, 19875 (2019).

[5] A. von Hoegen, M. Fechner, M. Först, J. Porras, B. Keimer, M. Michael, E. Demler, and A. Cavalleri, Probing coherent charge fluctuations in YBa$_2$Cu$_3$O$_{6+x}$ at wavevectors outside the light cone, arXiv e-prints (2019), arXiv:1911.08284 [cond-mat.supr-con].

D.2 Higgs mode mediated enhancement of interlayer transport in high-T_c cuprate superconductors

Higgs mode mediated enhancement of interlayer transport in high-T_c cuprate superconductors

Guido Homann [1], Jayson G. Cosme [1,2,3] Junichi Okamoto [4,5] and Ludwig Mathey[1,2]

[1]*Zentrum für Optische Quantentechnologien and Institut für Laserphysik, Universität Hamburg, 22761 Hamburg, Germany*
[2]*The Hamburg Centre for Ultrafast Imaging, Luruper Chaussee 149, 22761 Hamburg, Germany*
[3]*National Institute of Physics, University of the Philippines, Diliman, Quezon City 1101, Philippines*
[4]*Institute of Physics, University of Freiburg, Hermann-Herder-Strasse 3, 79104 Freiburg, Germany*
[5]*EUCOR Centre for Quantum Science and Quantum Computing, University of Freiburg,*
Hermann-Herder-Strasse 3, 79104 Freiburg, Germany

We put forth a mechanism for enhancing the interlayer transport in cuprate superconductors, by optically driving plasmonic excitations along the c axis with a frequency that is blue-detuned from the Higgs frequency. The plasmonic excitations induce a collective oscillation of the Higgs field which induces a parametric enhancement of the superconducting response, as we demonstrate with a minimal analytical model. Furthermore, we perform simulations of a particle-hole symmetric $U(1)$ lattice gauge theory and find good agreement with our analytical prediction. We map out the renormalization of the interlayer coupling as a function of the parameters of the optical field and demonstrate that the Higgs mode mediated enhancement can be larger than 50%.

I. INTRODUCTION

The observation of light-induced superconductivity in cuprates and organic salts has been associated with exciting lattice or molecular vibrations [1–3]. Related experiments on light-enhanced interlayer transport in the bilayer cuprate YBa$_2$Cu$_3$O$_{7-\delta}$ (YBCO) above and below the critical temperature T_c have been reported in Refs. [4–7]. Several mechanisms for these observations have been proposed in Refs. [8–14]. These proposed mechanisms focus on inducing phononic motion and its influence on the superconducting response. Here, we propose to enhance the interlayer transport in cuprates by optically exciting Higgs oscillations. This collective motion of the Higgs field couples parametrically to the plasma field, which results in the enhancement of the superconducting response. Our primary example will be monolayer cuprates. We expect that similar results emerge for other lattice geometries as well. We demonstrate that the enhancement of the superconducting response, in particular the low-frequency behavior of the imaginary conductivity, is achieved via driving of the electric field along the c axis with frequencies that are slightly blue-detuned from the Higgs frequency. Thus, we expand the scope of dynamical control of the superconducting state in the cuprates by exploiting nonlinear plasmonics [15,16].

In this paper, we first consider a two-mode model with a cubic coupling of the Higgs and plasma modes [17]. Based on this minimal model, we provide an analytical expression for the Higgs mode mediated renormalization of the interlayer coupling in monolayer cuprates. We then extend our treatment to a $U(1)$ lattice gauge theory with inherent particle-hole symmetry and simulate the c-axis optical conductivity for different ratios of the Higgs and plasma frequencies at zero temperature. The numerical results confirm our analytical prediction,

and we identify the optimal parameter regime for observing the Higgs mode mediated enhancement of interlayer transport. Finally, we discuss the feasibility of the effect and possible challenges brought by damping.

II. ANALYTICAL PREDICTION

Expanding on previous works [18–21], we model a layered superconductor as a stack of intrinsic Josephson junctions. In addition to Josephson plasma resonances [22–24], recent experiments have revealed the existence of another fundamental excitation in cuprate superconductors, the Higgs mode [25–27]. This mode corresponds to amplitude oscillations of the superconducting order parameter ψ, which decouples from the plasma mode in a system with approximate particle-hole symmetry [28,29]. The two distinct low-energy modes of a monolayer cuprate superconductor are depicted in Fig. 1(a), where the phase of ψ shall be interpreted as the gauge-invariant phase difference between adjacent layers. At zero momentum, the lowest-order coupling between the Higgs field h and the unitless vector potential a is given by the cubic interaction Lagrangian $\mathcal{L}_{\text{int}} \sim a^2 h$ [27,30]. The equations of motion corresponding to such a minimal model for describing the dynamics of a light-driven monolayer cuprate at zero temperature are

$$\ddot{a} + \gamma_J \dot{a} + \omega_J^2 a + 2\omega_J^2 ah = j, \quad (1)$$

$$\ddot{h} + \gamma_H \dot{h} + \omega_H^2 h + \alpha\omega_J^2 a^2 = 0, \quad (2)$$

where ω_H is the Higgs frequency, ω_J is the plasma frequency, and γ_H and γ_J are damping coefficients. The capacitive coupling constant α is of the order of 1 in the cuprates [31]. The interlayer current j is induced by an external electric field.

We use $\gamma_H/2\pi = \gamma_J/2\pi = 0.5$ THz and $\alpha = 1$ unless stated otherwise [32], and we assume the z axis to be aligned with the c axis of the crystal.

For weak pump-probe strengths, we perform a perturbative expansion for a and h around their equilibrium values [32]. To calculate the c-axis optical conductivity $\sigma(\omega)$ in the driven state, we apply both driving and probing currents. We take the current as a first-order term in the expansion, i.e.,

$$j = \lambda(j_{\mathrm{dr},1} e^{-i\omega_{\mathrm{dr}}t} + j_{\mathrm{pr},1} e^{-i\omega_{\mathrm{pr}}t} + \text{c.c.}), \qquad (3)$$

where $\lambda \ll 1$ is a small expansion parameter. Hence, the leading contribution to a is of first order and the leading contribution to h is of second order. The coupling term $\sim ah$

gives a third-order correction to a. Additionally, we assume that the probing frequency ω_{pr} is much smaller than the driving frequency ω_{dr} and the eigenfrequencies ω_H and ω_J. Thus, we obtain an approximate expression for the Fourier component $a(\omega_{\mathrm{pr}}) = \lambda a_{\mathrm{pr},1} + \lambda^3 a_{\mathrm{pr},3}$. The contributions are $a_{\mathrm{pr},1} \approx j_{\mathrm{pr},1}/\omega_J^2$ and

$$a_{\mathrm{pr},3} \approx \frac{4\alpha |j_{\mathrm{dr},1}|^2 j_{\mathrm{pr},1} (\omega_{\mathrm{dr}}^2 - 3\omega_H^2 + i\gamma_H\omega_{\mathrm{dr}})}{\omega_H^2 (\omega_{\mathrm{dr}}^2 - \omega_H^2 + i\gamma_H\omega_{\mathrm{dr}}) [(\omega_{\mathrm{dr}}^2 - \omega_J^2)^2 + \gamma_J^2\omega_{\mathrm{dr}}^2]}. \qquad (4)$$

This leads to the analytical prediction

$$\omega_{\mathrm{pr}}\sigma(\omega_{\mathrm{pr}}) = \frac{i\epsilon_z\epsilon_0 j(\omega_{\mathrm{pr}})}{a(\omega_{\mathrm{pr}})} \approx \frac{i\epsilon_z\epsilon_0\omega_J^2\omega_H^2(\omega_{\mathrm{dr}}^2 - \omega_H^2 + i\gamma_H\omega_{\mathrm{dr}})[(\omega_{\mathrm{dr}}^2 - \omega_J^2)^2 + \gamma_J^2\omega_{\mathrm{dr}}^2]}{\omega_H^2(\omega_{\mathrm{dr}}^2 - \omega_H^2 + i\gamma_H\omega_{\mathrm{dr}})[(\omega_{\mathrm{dr}}^2 - \omega_J^2)^2 + \gamma_J^2\omega_{\mathrm{dr}}^2] + 4\alpha\omega_J^2|j_{\mathrm{dr}}|^2(\omega_{\mathrm{dr}}^2 - 3\omega_H^2 + i\gamma_H\omega_{\mathrm{dr}})}, \qquad (5)$$

where ϵ_z denotes the dielectric permittivity of the junctions, and $j_{\mathrm{dr}} = \lambda j_{\mathrm{dr},1}$ is the driving amplitude. We define an effective Josephson coupling [13] based on the $1/\omega$ divergence of the conductivity,

$$J_{\mathrm{eff}} = \frac{\hbar}{2ed_z}\mathrm{Im}[\omega_{\mathrm{pr}}\sigma(\omega_{\mathrm{pr}})]_{\omega_{\mathrm{pr}}\to 0}, \qquad (6)$$

with the interlayer spacing d_z. In the absence of driving, the Josephson coupling is $J_0 = \hbar\epsilon_z\epsilon_0\omega_J^2/(2ed_z)$ according to

Eq. (5). The analytical prediction for J_{eff}/J_0 in the presence of driving is shown in Fig. 1(c). The key result of this work is the enhancement of the effective interlayer coupling when the pump frequency is slightly blue-detuned from the Higgs frequency. This enhancement phenomenon is due to parametric amplification. Indeed, Eq. (1) takes the form of a parametric oscillator due to the two-wave mixing of drive and probe in Eq. (2), inducing amplitude oscillations at frequencies $2\omega_{\mathrm{dr}}$, $2\omega_{\mathrm{pr}}$, and $\omega_{\mathrm{dr}} \pm \omega_{\mathrm{pr}}$. The coupling of amplitude oscillations with $\omega_{\mathrm{dr}} \pm \omega_{\mathrm{pr}}$ to the drive amplifies the current response at the probing frequency. The numerical results in Figs. 1(c) and 1(d), further highlighting the enhancement of interlayer transport, are obtained by simulating a full lattice gauge model discussed in the following.

III. LATTICE GAUGE MODEL

We now turn to our relativistic $U(1)$ lattice gauge theory in three dimensions, which is inherently particle-hole symmetric. The layered structure of cuprate superconductors is encoded in the lattice parameters. Our approach allows us to explicitly simulate the coupled dynamics of the order parameter of the superconducting state $\psi_{\mathbf{r}}(t)$ and the electromagnetic field $\mathbf{A}_{\mathbf{r}}(t)$ at temperatures below T_c. To this end, we describe the Cooper pairs as a condensate of interacting bosons with charge $-2e$, represented by the complex field $\psi_{\mathbf{r}}(t)$. The time-independent part of our model Lagrangian has the form of the Ginzburg-Landau free energy [33], discretized on an anisotropic lattice. We model the layered structure of high-T_c cuprates using an anisotropic lattice geometry as illustrated in Fig. 1(b). The in-plane discretization length d_{xy} constitutes a short-range cutoff around the coherence length, while the interlayer spacing d_z is the distance between the CuO$_2$ planes in the crystal. Each component of the vector potential $A_{s,\mathbf{r}}(t)$ is located at half a lattice site from site $\mathbf{r}$ in the s direction, where $s \in \{x, y, z\}$. According to the Peierls substitution, it describes the averaged electric field along the bond of a plaquette in Fig. 1(b).

We discretize space by mapping it on a lattice and implement the compact $U(1)$ lattice gauge theory in the time
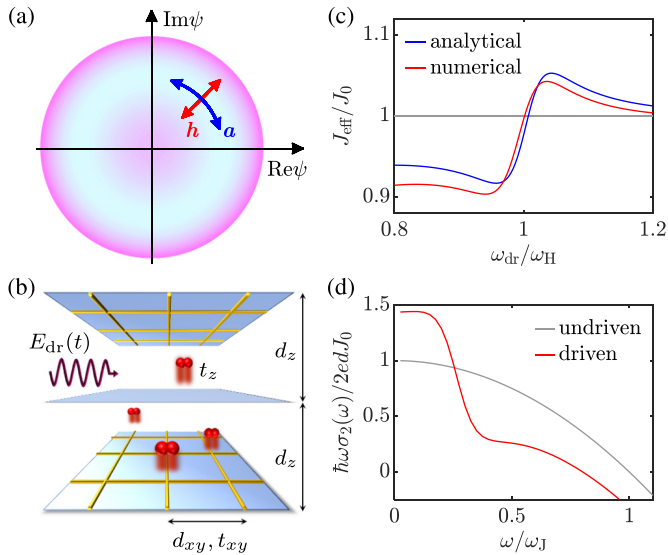
FIG. 1. (a) Higgs and plasma modes of a monolayer cuprate superconductor, illustrated with a Mexican hat potential for the superconducting order parameter. (b) Schematic representation of a layered superconductor periodically driven by a c-axis polarized electric field with frequency ω_{dr} and field strength E_0. (c) Effective interlayer coupling J_{eff} rescaled by its equilibrium value J_0. The field strength is fixed at $E_0 = 100$ kV/cm. (d) Numerical results for the imaginary conductivity σ_2. The driving parameters are $\omega_{\mathrm{dr}} = 1.05\,\omega_H$ and $E_0 = 400$ kV/cm. The cuprate considered in (c) and (d) has the Josephson plasma frequency $\omega_J/2\pi = 2$ THz and the Higgs frequency $\omega_H/2\pi = 6$ THz.

continuum limit [34]. The Lagrangian of the lattice gauge model is

$$\mathcal{L} = \mathcal{L}_{\text{sc}} + \mathcal{L}_{\text{em}} + \mathcal{L}_{\text{kin}}. \qquad (7)$$

The first term is the $|\psi|^4$ model of the superconducting condensate in the absence of Cooper pair tunneling,

$$\mathcal{L}_{\text{sc}} = \sum_{\mathbf{r}} K\hbar^2 |\partial_t \psi_{\mathbf{r}}|^2 + \mu |\psi_{\mathbf{r}}|^2 - \frac{g}{2}|\psi_{\mathbf{r}}|^4, \qquad (8)$$

where μ is the chemical potential, and g is the interaction strength. This Lagrangian is particle-hole symmetric due to its invariance under $\psi_{\mathbf{r}} \to \psi_{\mathbf{r}}^*$. The coefficient K describes the magnitude of the dynamical term [27,29].

The electromagnetic part $\mathcal{L}_{\text{em}}$ is the discretized form of the free-field Lagrangian:

$$\mathcal{L}_{\text{em}} = \sum_{s,\mathbf{r}} \frac{\epsilon_s \epsilon_0}{2} E_{s,\mathbf{r}}^2 - \frac{1}{\mu_0 \beta_s^2}[1 - \cos(\beta_s B_{s,\mathbf{r}})]. \qquad (9)$$

Here, $E_{s,\mathbf{r}}$ denotes the s component of the electric field, and ϵ_s is the dielectric permittivity along that axis. The magnetic field components $B_{s,\mathbf{r}}$ follow from the finite-difference representation of $\nabla \times \mathbf{A}$. The temporal and spatial arrangement of the electromagnetic field is consistent with the finite-difference time-domain (FDTD) method for solving Maxwell's equations [35]. Note that we choose the temporal gauge for our calculations, i.e., $E_{s,\mathbf{r}} = -\partial_t A_{s,\mathbf{r}}$. The coefficients for the magnetic field are $\beta_x = \beta_y = 2ed_{xy}d_z/\hbar$ and $\beta_z = 2ed_{xy}^2/\hbar$.

The nonlinear coupling between the Higgs field and the electromagnetic field derives from the tunneling term

$$\mathcal{L}_{\text{kin}} = -\sum_{s,\mathbf{r}} t_s |\psi_{\mathbf{r}'(s)} - \psi_{\mathbf{r}} e^{ia_{s,\mathbf{r}}}|^2, \qquad (10)$$

where $\mathbf{r}'(s)$ denotes the neighboring lattice site of $\mathbf{r}$ in the positive s direction. The unitless vector potential $a_{s,\mathbf{r}} = -2ed_s A_{s,\mathbf{r}}/\hbar$ couples to the phase of the superconducting field, ensuring the local gauge invariance of $\mathcal{L}_{\text{kin}}$. The in-plane tunneling coefficient is t_{xy}, and the interlayer tunneling coefficient is t_z.

We numerically solve the equations of motion derived from the Lagrangian, including damping terms. We employ periodic boundary conditions and integrate the differential equations using Heun's method with a step size $\Delta t = 2.5$ as. Here, we focus on zero temperature, where the in-plane dynamics is silent. An example of Higgs mode mediated enhancement at nonzero temperature is included in the Supplemental Material [32].

We drive the system by adding $(\omega_{\text{dr}} E_0/\epsilon_z)\sin(\omega_{\text{dr}}t)$ to the equations of motion for the vector potential $A_{z,\mathbf{r}}(t)$ on all interlayer bonds, which describes a spatially homogeneous driving field. Note that Eqs. (1) and (2) can be derived as the Euler-Lagrange equations of the Lagrangian (7) at zero temperature. In that case, the fields are uniform in the bulk, i.e., $\psi_{\mathbf{r}} \equiv \psi$, $A_{x,\mathbf{r}} = A_{y,\mathbf{r}} \equiv 0$, and $A_{z,\mathbf{r}} \equiv A$. The equations of motion read

$$\partial_t^2 A = \frac{2ed_z t_z}{i\hbar \epsilon_z \epsilon_0}|\psi|^2(e^{ia} - e^{-ia}) - \gamma_{\text{J}}\partial_t A + \frac{\omega_{\text{dr}} E_0}{\epsilon_z}\sin(\omega_{\text{dr}}t) \qquad (11)$$

and

$$\partial_t^2 \psi = \frac{\mu - g|\psi|^2 + t_z(e^{ia} + e^{-ia} - 2)}{K\hbar^2}\psi - \gamma_{\text{H}}\partial_t \psi, \qquad (12)$$

where $a = -2ed_z A/\hbar$. To recover Eqs. (1) and (2), the order parameter is expanded around its equilibrium value $\psi_0 = \sqrt{\mu/g}$, i.e., $\psi = \psi_0 + h$, and only linear terms in a and h except for the coupling term $\sim ah$ are retained. Thus, one can identify the plasma frequency with $\omega_{\text{J}} = \sqrt{t_z/\alpha K\hbar^2}$ and the Higgs frequency with $\omega_{\text{H}} = \sqrt{2\mu/K\hbar^2}$, where $\alpha = (\epsilon_z \epsilon_0)/(8K\psi_0^2 e^2 d_z^2)$ is the capacitive coupling constant of the c-axis junctions. The drive induces a current with Fourier amplitude $|j_{\text{dr}}| = ed_z \omega_{\text{dr}} E_0/\hbar \epsilon_z$.

IV. NUMERICAL RESULTS

In the following, we present our numerical results. We evaluate the effective interlayer coupling based on the optical conductivity at $\omega_{\text{pr}} = \omega_{\text{H}}/120$. For weak driving, we find decent agreement between the analytical prediction in Eq. (5) and the numerical results of the full lattice gauge model, as shown in Fig. 2. The deviations are due to higher-order terms ignored in the minimal model and the perturbative expansion. They grow with increasing field strength. Nevertheless, our simulations demonstrate that the enhancement effect persists for strong driving, even in the presence of higher-order nonlinearities, fully included in our $U(1)$ lattice gauge theory.

We find that the renormalization of the interlayer coupling does not only depend on the driving parameters, but also on the ratio of the Higgs frequency and the plasma frequency of the system. Our main proposal consists of driving the superconductor slightly blue-detuned from the Higgs frequency ω_{H}. This mechanism is effective for all ratios of $\omega_{\text{J}}/\omega_{\text{H}}$. As we discuss below, there is a second regime in which dynamical stabilization can be achieved, if the system fulfills the requirement $\omega_{\text{H}} < \omega_{\text{J}} < \sqrt{3}\omega_{\text{H}}$.

Figure 3 displays the renormalized interlayer coupling as a function of the driving parameters for a monolayer cuprate with $\omega_{\text{J}} < \omega_{\text{H}}$ [the same system as in Figs. 1 and 2(a)]. Consistent with our analytical prediction, the interlayer transport is enhanced for driving frequencies blue-detuned from the Higgs frequency, while it is diminished on the red-detuned side, as immediately apparent for weak driving. In general, higher field strengths amplify the suppression/enhancement effects and additionally renormalize the Higgs frequency and the plasma frequency. The frequency renormalization of the Higgs mode results in the bending of the enhancement regime towards lower driving frequencies for larger driving fields. This observation reflects the general behavior of nonlinear oscillators to display amplitude-dependent eigenfrequencies [36]. We emphasize that the interlayer coupling can be increased by more than 50% in this example. The strongest suppression of interlayer transport occurs for driving close to the plasma frequency. This is generally the case if $\omega_{\text{J}} < \omega_{\text{H}}$ or $\omega_{\text{J}} > \sqrt{3}\omega_{\text{H}}$.

The enhancement and suppression effects are limited by heating that dominates for larger field strengths (see also Ref. [17]). We identify the heating regime based on the condition that the condensate is completely depleted. Specifically, we observe the driven dynamics for 100 ps and apply
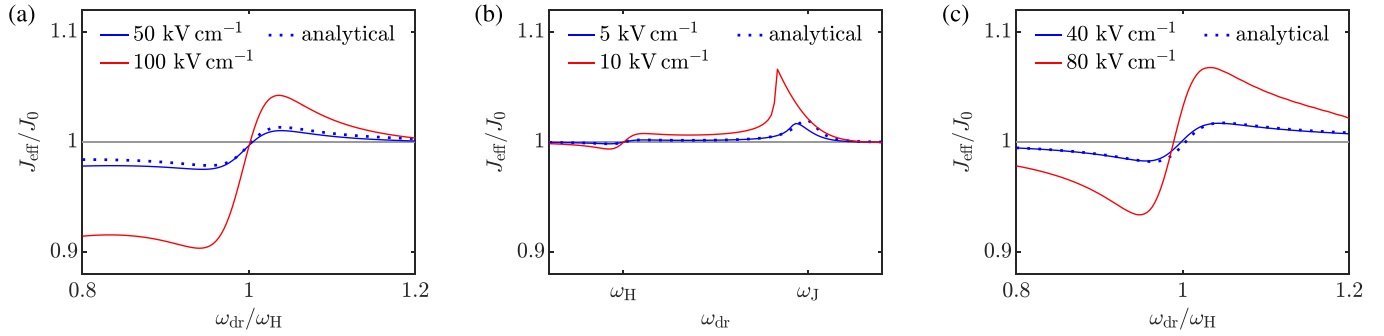
FIG. 2. Effective interlayer coupling for three light-driven monolayer cuprate superconductors with different ratios ω_J/ω_H. (a) $\omega_J < \omega_H$, (b) $\omega_H < \omega_J < \sqrt{3}\omega_H$, (c) $\sqrt{3}\omega_H < \omega_J$. Each panel shows the dependence on the driving frequency ω_{dr} for two fixed values of the field strength E_0. Solid lines correspond to numerical results, and dotted lines indicate analytical results for the lower field strength. In all cases, the Higgs frequency is fixed at $\omega_H/2\pi = 6$ THz, while the plasma frequency $\omega_J/2\pi$ is varied: (a) 2 THz, (b) 9 THz, and (c) 15 THz.

the condition $\min(|\psi|/|\psi_0|) < 10^{-3}$ to determine unstable states. We note that the heating regime has a similar shape as the parameter set for which no stable solutions can be found by applying the harmonic balance method with ten harmonics [32,37].

Within our analytical solution for the optical conductivity in Eq. (5), we have determined an upper boundary for the driving frequency of $\sqrt{3}\omega_H$ for the enhancement effect to occur. At this boundary, the second term in the denominator of Eq. (5) switches sign. Our simulations confirm this prediction for $\omega_H < \omega_J$. However, as visible in Fig. 3, an additional suppression lowers this upper bound for superconductors with $\omega_J < (\sqrt{3} - 1)\omega_H$. Here, the enhancement regime is approximately limited by the resonance frequency of the time crystalline state at $\omega_{dr} = \omega_H + \omega_J$ [17]. This modified upper bound derives from higher-order terms not included in the analytical solution.

We continue our analysis by varying the damping coefficients, as shown in Fig. 4. Studying higher values of γ_H is particularly interesting because the damping of the Higgs mode is typically strong in cuprate superconductors [25,26]. It can be seen in Fig. 4(a) that increasing γ_H significantly decreases the enhancement of the interlayer coupling for a given field strength. By contrast, stronger damping of the

plasma mode has a negligible effect. In the Supplemental Material [32], we provide a parameter scan of the renormalized interlayer coupling with higher damping coefficients $\gamma_H/2\pi = \gamma_J/2\pi = 1$ THz. Compared to Fig. 3, we find that the parameter regime with an enhancement of more than 10% is smaller and shifted to higher field strengths.

Finally, we consider cuprates with $\omega_H < \omega_J < \sqrt{3}\omega_H$. In this case, the previous suppression of interlayer transport for $\omega_{dr} \approx \omega_J$ switches to strong enhancement, as exemplified in Fig. 2(b). Therefore, we propose to drive these particular systems near the plasma frequency ω_J. In typical monolayer cuprates, such as La$_{2-x}$Sr$_x$CuO$_4$ (LSCO), the superconducting gap 2Δ is larger than the Josephson plasma energy $\hbar\omega_J$ [38–40]. At low temperatures, the Higgs frequency approximately equals $2\Delta/\hbar$ [27,41], so it is larger than the Josephson plasma frequency in these materials, i.e., $\omega_J < \omega_H$. However, while the temperature dependence of the Higgs mode in cuprate superconductors is the subject of debate [25,26,42,43], the case $\omega_H < \omega_J < \sqrt{3}\omega_H$ might be realized for higher temperatures. For these temperatures, stronger damping and thermal fluctuations might suppress or reduce the enhancement mechanism. This regime will be discussed elsewhere. Further decay channels of the Higgs mode have been studied in Refs. [44,45].
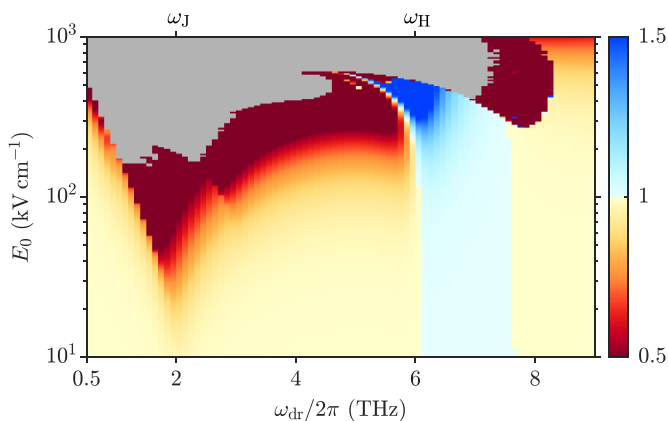
FIG. 3. Dependence of the effective interlayer coupling J_{eff}/J_0 on the driving frequency ω_{dr} and the field strength E_0. The gray area marks the heating regime.
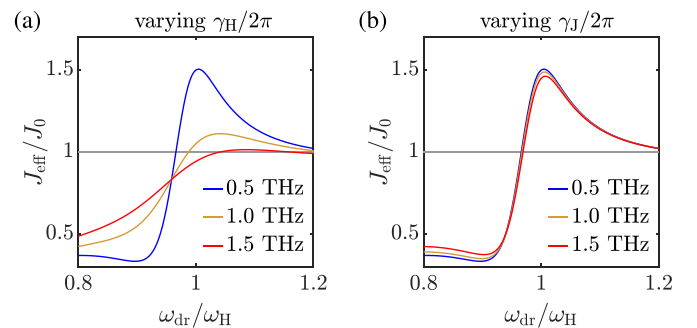
FIG. 4. Dependence of the Higgs mode mediated renormalization of the interlayer coupling on the damping coefficients. (a) γ_H is varied while $\gamma_J/2\pi = 0.5$ THz is fixed. (b) γ_J is varied while $\gamma_H/2\pi = 0.5$ THz is fixed. The cuprate with Josephson plasma frequency $\omega_J/2\pi = 2$ THz and Higgs frequency $\omega_H/2\pi = 6$ THz is driven with the field strength $E_0 = 300$ kV/cm.

V. CONCLUSION

In conclusion, we propose a mechanism for light-enhanced interlayer transport in cuprate superconductors by optically exciting Higgs oscillations which then induce a parametric amplification of the superconducting response. Both our analytical and numerical calculations show that the superconducting response of a monolayer cuprate is significantly amplified when the optical driving is slightly blue-detuned from the Higgs frequency. Our calculations demonstrate that the regime of driving parameters, for which a significant Higgs mode mediated enhancement of interlayer transport is achieved, crucially depends on the damping of the Higgs mode. Therefore, we propose to verify this effect first for low temperatures. The enhancement mechanism presented in this work is broadly applicable to cuprate superconductors because it does not rely on the existence of suitable phonons. Instead, the light-driven renormalization of interlayer transport is mediated by Higgs oscillations of the Cooper pair condensate itself. This effect amounts to dynamical control of a functionality in high-temperature superconductors, utilizing the intrinsic collective modes of these materials and their nonlinear coupling.

TABLE I. Model parameters used in the simulations.

K (meV^{-1})	1.38×10^{-5}
μ (meV)	4.24×10^{-3}
g (meV Å^3)	2.12
ϵ_{xy}	1
ϵ_z	4
d_{xy} (Å)	20
d_z (Å)	10
t_{xy} (meV)	2.2×10^{-1}
t_z (meV)	$9.44 \times 10^{-4}, 1.91 \times 10^{-2}, 5.31 \times 10^{-2}$

APPENDIX: MODEL PARAMETERS

Table I summarizes the parameters of the monolayer cuprate superconductors studied in this paper. Our parameter choice of μ and g implies an equilibrium condensate density $n_0 = \mu/g = 2 \times 10^{21}$ cm^{-3} at zero temperature. The capacitive coupling constant is given by

$$\alpha = \frac{g\epsilon_z\epsilon_0}{8\mu K e^2 d_z^2} = 1. \tag{A1}$$

For the c-axis plasma frequency, we consider the three cases $\omega_J/2\pi = 2$ THz, $\omega_J/2\pi = 9$ THz, and $\omega_J/2\pi = 15$ THz. The Higgs frequency is $\omega_H/2\pi = 6$ THz in each case.

[1] D. Fausti, R. I. Tobey, N. Dean, S. Kaiser, A. Dienst, M. C. Hoffmann, S. Pyon, T. Takayama, H. Takagi, and A. Cavalleri, Light-induced superconductivity in a stripe-ordered cuprate, Science **331**, 189 (2011).

[2] M. Buzzi, D. Nicoletti, M. Fechner, N. Tancogne-Dejean, M. A. Sentef, A. Georges, T. Biesner, E. Uykur, M. Dressel, A. Henderson, T. Siegrist, J. A. Schlueter, K. Miyagawa, K. Kanoda, M.-S. Nam, A. Ardavan, J. Coulthard, J. Tindall, F. Schlawin, D. Jaksch *et al.*, Photomolecular High-Temperature Superconductivity, Phys. Rev. X **10**, 031028 (2020).

[3] M. Budden, T. Gebert, M. Buzzi, G. Jotzu, E. Wang, T. Matsuyama, G. Meier, Y. Laplace, D. Pontiroli, M. Riccò, F. Schlawin, D. Jaksch, and A. Cavalleri, Evidence for metastable photo-induced superconductivity in K$_3$C$_{60}$, Nat. Phys. **17**, 611 (2021).

[4] W. Hu, S. Kaiser, D. Nicoletti, C. R. Hunt, I. Gierz, M. C. Hoffmann, M. Le Tacon, T. Loew, B. Keimer, and A. Cavalleri, Optically enhanced coherent transport in YBa$_2$Cu$_3$O$_{6.5}$ by ultrafast redistribution of interlayer coupling, Nat. Mater. **13**, 705 (2014).

[5] S. Kaiser, C. R. Hunt, D. Nicoletti, W. Hu, I. Gierz, H. Y. Liu, M. Le Tacon, T. Loew, D. Haug, B. Keimer, and A. Cavalleri, Optically induced coherent transport far above T_c in underdoped YBa$_2$Cu$_3$O$_{6+\delta}$, Phys. Rev. B **89**, 184516 (2014).

[6] M. Först, A. Frano, S. Kaiser, R. Mankowsky, C. R. Hunt, J. J. Turner, G. L. Dakovski, M. P. Minitti, J. Robinson, T. Loew, M. Le Tacon, B. Keimer, J. P. Hill, A. Cavalleri, and S. S. Dhesi, Femtosecond x rays link melting of charge-density wave correlations and light-enhanced coherent transport in YBa$_2$Cu$_3$O$_{6.6}$, Phys. Rev. B **90**, 184514 (2014).

[7] K. A. Cremin, J. Zhang, C. C. Homes, G. D. Gu, Z. Sun, M. M. Fogler, A. J. Millis, D. N. Basov, and R. D. Averitt, Photoenhanced metastable c-axis electrodynamics in stripe-ordered cuprate La$_{1.885}$Ba$_{0.115}$CuO$_4$, Proc. Natl. Acad. Sci. USA **116**, 19875 (2019).

[8] R. Mankowsky, A. Subedi, M. Först, S. O. Mariager, M. Chollet, H. T. Lemke, J. S. Robinson, J. M. Glownia, M. P. Minitti, A. Frano, M. Fechner, N. A. Spaldin, T. Loew, B. Keimer, A. Georges, and A. Cavalleri, Nonlinear lattice dynamics as a basis for enhanced superconductivity in YBa$_2$Cu$_3$O$_{6.5}$, Nature (London) **516**, 71 (2014).

[9] S. J. Denny, S. R. Clark, Y. Laplace, A. Cavalleri, and D. Jaksch, Proposed Parametric Cooling of Bilayer Cuprate Superconductors by Terahertz Excitation, Phys. Rev. Lett. **114**, 137001 (2015).

[10] R. Höppner, B. Zhu, T. Rexin, A. Cavalleri, and L. Mathey, Redistribution of phase fluctuations in a periodically driven cuprate superconductor, Phys. Rev. B **91**, 104507 (2015).

[11] Z. M. Raines, V. Stanev, and V. M. Galitski, Enhancement of superconductivity via periodic modulation in a three-dimensional model of cuprates, Phys. Rev. B **91**, 184506 (2015).

[12] A. A. Patel and A. Eberlein, Light-induced enhancement of superconductivity via melting of competing bond-density wave order in underdoped cuprates, Phys. Rev. B **93**, 195139 (2016).

[13] J.-i. Okamoto, A. Cavalleri, and L. Mathey, Theory of Enhanced Interlayer Tunneling in Optically Driven High-T_c Superconductors, Phys. Rev. Lett. **117**, 227001 (2016).

[14] J.-i. Okamoto, W. Hu, A. Cavalleri, and L. Mathey, Transiently enhanced interlayer tunneling in optically driven high-T_c superconductors, Phys. Rev. B **96**, 144505 (2017).

[15] S. Rajasekaran, E. Casandruc, Y. Laplace, D. Nicoletti, G. D. Gu, S. R. Clark, D. Jaksch, and A. Cavalleri, Parametric amplification of a superconducting plasma wave, Nat. Phys. **12**, 1012 (2016).

[16] F. Schlawin, A. S. D. Dietrich, M. Kiffner, A. Cavalleri, and D. Jaksch, Terahertz field control of interlayer transport modes in cuprate superconductors, Phys. Rev. B **96**, 064526 (2017).

[17] G. Homann, J. G. Cosme, and L. Mathey, Higgs time crystal in a high-T_c superconductor, Phys. Rev. Research **2**, 043214 (2020).

[18] T. Koyama and M. Tachiki, *I-V* characteristics of Josephson-coupled layered superconductors with longitudinal plasma excitations, Phys. Rev. B **54**, 16183 (1996).

[19] D. van der Marel and A. A. Tsvetkov, Transverse-optical Josephson plasmons: Equations of motion, Phys. Rev. B **64**, 024530 (2001).

[20] T. Koyama, Josephson plasma resonances and optical properties in high-T_c superconductors with alternating junction parameters, J. Phys. Soc. Jpn. **71**, 2986 (2002).

[21] M. Harland, S. Brener, A. I. Lichtenstein, and M. I. Katsnelson, Josephson lattice model for phase fluctuations of local pairs in copper oxide superconductors, Phys. Rev. B **100**, 024510 (2019).

[22] D. Dulić, A. Pimenov, D. van der Marel, D. M. Broun, S. Kamal, W. N. Hardy, A. A. Tsvetkov, I. M. Sutjaha, R. Liang, A. A. Menovsky, A. Loidl, and S. S. Saxena, Observation of the Transverse Optical Plasmon in SmLa$_{0.8}$Sr$_{0.2}$CuO$_{4-\delta}$, Phys. Rev. Lett. **86**, 4144 (2001).

[23] H. Shibata and T. Yamada, Double Josephson Plasma Resonance in T^* Phase SmLa$_{1-x}$Sr$_x$CuO$_{4-\delta}$, Phys. Rev. Lett. **81**, 3519 (1998).

[24] D. N. Basov and T. Timusk, Electrodynamics of high-T_c superconductors, Rev. Mod. Phys. **77**, 721 (2005).

[25] K. Katsumi, N. Tsuji, Y. I. Hamada, R. Matsunaga, J. Schneeloch, R. D. Zhong, G. D. Gu, H. Aoki, Y. Gallais, and R. Shimano, Higgs Mode in the *d*-Wave Superconductor Bi$_2$Sr$_2$CaCu$_2$O$_{8+x}$ Driven by an Intense Terahertz Pulse, Phys. Rev. Lett. **120**, 117001 (2018).

[26] H. Chu, M.-J. Kim, K. Katsumi, S. Kovalev, R. D. Dawson, L. Schwarz, N. Yoshikawa, G. Kim, D. Putzky, Z. Z. Li, H. Raffy, S. Germanskiy, J.-C. Deinert, N. Awari, I. Ilyakov, B. Green, M. Chen, M. Bawatna, G. Christiani, G. Logvenov *et al.*, Phase-resolved Higgs response in superconducting cuprates, Nat. Commun. **11**, 1793 (2020).

[27] R. Shimano and N. Tsuji, Higgs mode in superconductors, Annu. Rev. Condens. Matter Phys. **11**, 103 (2020).

[28] C. M. Varma, Higgs boson in superconductors, J. Low Temp. Phys. **126**, 901 (2002).

[29] D. Pekker and C. Varma, Amplitude/Higgs modes in condensed matter physics, Annu. Rev. Condens. Matter Phys. **6**, 269 (2015).

[30] Z. Sun, M. M. Fogler, D. N. Basov, and A. J. Millis, Collective modes and terahertz near-field response of superconductors, Phys. Rev. Research **2**, 023413 (2020).

[31] M. Machida and T. Koyama, Localized rotating-modes in capacitively coupled intrinsic Josephson junctions: Systematic study of branching structure and collective dynamical instability, Phys. Rev. B **70**, 024523 (2004).

[32] See Supplemental Material at http://link.aps.org/supplemental/10.1103/PhysRevB.103.224503 for a detailed derivation of the analytical prediction in Eq. (5), details of the lattice gauge model, a comparison between the quadratic and fully nonlinear models, a discussion of the condensate depletion, results for different values of the damping coefficients and the capacitive coupling constant, and finite-temperature results.

[33] V. L. Ginzburg and L. D. Landau, On the theory of superconductivity, Zh. Eksp. Teor. Fiz. **20**, 1064 (1950).

[34] J. B. Kogut, An introduction to lattice gauge theory and spin systems, Rev. Mod. Phys. **51**, 659 (1979).

[35] K. Yee, Numerical solution of initial boundary value problems involving Maxwell's equations in isotropic media, IEEE Trans. Antennas Propag. **14**, 302 (1966).

[36] L. D. Landau and E. M. Lifshitz, *Mechanics*, 3rd ed. (Butterworth-Heinemann, Oxford, U.K., 1976).

[37] J. C. Slater, Mousai: An open-source general purpose harmonic balance solver, 13th ASME Dayton Engineering Sciences Symposium, 2017, https://josephcslater.github.io/DESS2017/.

[38] S. V. Dordevic, S. Komiya, Y. Ando, and D. N. Basov, Josephson Plasmon and Inhomogeneous Superconducting State in La$_{2-x}$Sr$_x$CuO$_4$, Phys. Rev. Lett. **91**, 167401 (2003).

[39] G. Deutscher, Coherence and single-particle excitations in the high-temperature superconductors, Nature (London) **397**, 410 (1999).

[40] M. Hashimoto, T. Yoshida, K. Tanaka, A. Fujimori, M. Okusawa, S. Wakimoto, K. Yamada, T. Kakeshita, H. Eisaki, and S. Uchida, Distinct doping dependences of the pseudogap and superconducting gap of La$_{2-x}$Sr$_x$CuO$_4$ cuprate superconductors, Phys. Rev. B **75**, 140503(R) (2007).

[41] F. Yang and M. W. Wu, Theory of Higgs modes in *d*-wave superconductors, Phys. Rev. B **102**, 014511 (2020).

[42] M. Puviani, A. Baum, S. Ono, Y. Ando, R. Hackl, and D. Manske, Enhanced A_{1g} Raman response in cuprates due to Higgs oscillations, arXiv:2012.01922.

[43] F. Gabriele, M. Udina, and L. Benfatto, Non-linear terahertz driving of plasma waves in layered cuprates, Nat. Commun. **12**, 752 (2021).

[44] F. Peronaci, M. Schiró, and M. Capone, Transient Dynamics of *d*-Wave Superconductors After a Sudden Excitation, Phys. Rev. Lett. **115**, 257001 (2015).

[45] Y. Murakami, P. Werner, N. Tsuji, and H. Aoki, Damping of the collective amplitude mode in superconductors with strong electron-phonon coupling, Phys. Rev. B **94**, 115126 (2016).

Supplemental Material for
Higgs mode mediated enhancement of interlayer transport in high-T_c cuprate superconductors

Guido Homann,[1] Jayson G. Cosme,[1, 2, 3] Junichi Okamoto,[4, 5] and Ludwig Mathey[1, 2]

[1]*Zentrum für Optische Quantentechnologien and Institut für Laserphysik, Universität Hamburg, 22761 Hamburg, Germany*
[2]*The Hamburg Centre for Ultrafast Imaging, Luruper Chaussee 149, 22761 Hamburg, Germany*
[3]*National Institute of Physics, University of the Philippines, Diliman, Quezon City 1101, Philippines*
[4]*Institute of Physics, University of Freiburg, Hermann-Herder-Strasse 3, 79104 Freiburg, Germany*
[5]*EUCOR Centre for Quantum Science and Quantum Computing,*
University of Freiburg, Hermann-Herder-Strasse 3, 79104 Freiburg, Germany

CONTENTS

I. ANALYTICAL DERIVATION OF THE HIGGS MODE MEDIATED ENHANCEMENT OF INTERLAYER TRANSPORT

Here, we consider a monolayer cuprate superconductor at zero temperature. Since the system is driven along the c axis, it exhibits no in-plane dynamics. We rewrite Eqs. (11) and (12) from the main text as

$$\ddot{a} + \gamma_{\mathrm{J}}\dot{a} + \omega_{\mathrm{J}}^2 \sin(a)(1+h)^2 = j, \tag{1}$$

$$\ddot{h} + \gamma_{\mathrm{H}}\dot{h} + \omega_{\mathrm{H}}^2\left(h + \frac{3}{2}h^2 + \frac{1}{2}h^3\right) + 2\alpha\omega_{\mathrm{J}}^2\left[1 - \cos(a)\right](1+h) = 0. \tag{2}$$

Neglecting all nonlinear terms except for the quadratic coupling between the Higgs field h and the unitless vector potential a, we find

$$\ddot{a} + \gamma_{\mathrm{J}}\dot{a} + \omega_{\mathrm{J}}^2 a + 2\omega_{\mathrm{J}}^2 ah = j, \tag{3}$$

$$\ddot{h} + \gamma_{\mathrm{H}}\dot{h} + \omega_{\mathrm{H}}^2 h + \alpha\omega_{\mathrm{J}}^2 a^2 = 0. \tag{4}$$

Now, we expand j, a, and h in the form

$$f = f^{(0)} + \lambda f^{(1)} + \lambda^2 f^{(2)} + \lambda^3 f^{(3)} + \mathcal{O}(\lambda^4), \tag{5}$$

where $\lambda \ll 1$ is a small expansion parameter. We take the current j induced by driving and probing as

$$j^{(1)} = j_{\mathrm{dr},1}e^{-i\omega_{\mathrm{dr}}t} + j_{\mathrm{pr},1}e^{-i\omega_{\mathrm{pr}}t} + \mathrm{c.c.}. \tag{6}$$

Hence, there are no zeroth order contributions and we obtain

$$a^{(1)} = a_{\mathrm{dr},1}e^{-i\omega_{\mathrm{dr}}t} + a_{\mathrm{pr},1}e^{-i\omega_{\mathrm{pr}}t} + \mathrm{c.c.}, \tag{7}$$

$$h^{(1)} = 0 \tag{8}$$

in first order, where

$$a_{\mathrm{dr},1} = \frac{j_{\mathrm{dr},1}}{\omega_{\mathrm{J}}^2 - \omega_{\mathrm{dr}}^2 - i\gamma_{\mathrm{J}}\omega_{\mathrm{dr}}}, \tag{9}$$

$$a_{\mathrm{pr},1} = \frac{j_{\mathrm{pr},1}}{\omega_{\mathrm{J}}^2 - \omega_{\mathrm{pr}}^2 - i\gamma_{\mathrm{J}}\omega_{\mathrm{pr}}}. \tag{10}$$

In second order, we have

$$a^{(2)} = 0, \tag{11}$$

$$h^{(2)} = h_0 + h_1 e^{-2i\omega_{\mathrm{dr}}t} + h_2 e^{-2i\omega_{\mathrm{pr}}t} + h_3 e^{-i(\omega_{\mathrm{dr}}-\omega_{\mathrm{pr}})t} + h_4 e^{-i(\omega_{\mathrm{dr}}+\omega_{\mathrm{pr}})t} + \mathrm{c.c.}, \tag{12}$$

where

$$h_0 = -\frac{2\alpha\omega_{\mathrm{J}}^2}{\omega_{\mathrm{H}}^2}\left(|a_{\mathrm{dr},1}|^2 + |a_{\mathrm{pr},1}|^2\right), \tag{13}$$

$$h_1 = \frac{\alpha\omega_{\mathrm{J}}^2 a_{\mathrm{dr},1}^2}{4\omega_{\mathrm{dr}}^2 - \omega_{\mathrm{H}}^2 + 2i\gamma_{\mathrm{H}}\omega_{\mathrm{dr}}}, \tag{14}$$

$$h_2 = \frac{\alpha\omega_{\mathrm{J}}^2 a_{\mathrm{pr},1}^2}{4\omega_{\mathrm{pr}}^2 - \omega_{\mathrm{H}}^2 + 2i\gamma_{\mathrm{H}}\omega_{\mathrm{pr}}}, \tag{15}$$

$$h_3 = \frac{2\alpha\omega_{\mathrm{J}}^2 a_{\mathrm{dr},1}a_{\mathrm{pr},1}^*}{(\omega_{\mathrm{dr}} - \omega_{\mathrm{pr}})^2 - \omega_{\mathrm{H}}^2 + i\gamma_{\mathrm{H}}(\omega_{\mathrm{dr}} - \omega_{\mathrm{pr}})}, \tag{16}$$

$$h_4 = \frac{2\alpha\omega_{\mathrm{J}}^2 a_{\mathrm{dr},1}a_{\mathrm{pr},1}}{(\omega_{\mathrm{dr}} + \omega_{\mathrm{pr}})^2 - \omega_{\mathrm{H}}^2 + i\gamma_{\mathrm{H}}(\omega_{\mathrm{dr}} + \omega_{\mathrm{pr}})}. \tag{17}$$

In third order, we find the following correction for the vector potential at the probing frequency:

$$a_{\mathrm{pr},3} = \frac{2\omega_{\mathrm{J}}^2\left(h_0 a_{\mathrm{pr},1} + h_2 a_{\mathrm{pr},1}^* + h_3^* a_{\mathrm{dr},1} + h_4 a_{\mathrm{dr},1}^*\right)}{\omega_{\mathrm{pr}}^2 - \omega_{\mathrm{J}}^2 + i\gamma_{\mathrm{J}}\omega_{\mathrm{pr}}}. \tag{18}$$

Using $|j_{\mathrm{pr},1}| \ll |j_{\mathrm{dr},1}|$ and $\omega_{\mathrm{pr}} \ll \omega_{\mathrm{dr}}, \omega_{\mathrm{H}}, \omega_{\mathrm{J}}$, we can neglect terms proportional to $|a_{\mathrm{pr},1}|^2 a_{\mathrm{pr},1}$ and simplify the denominators of Eqs. (10), (16), (17), and (18):

$$
\begin{aligned}
a_{\mathrm{pr},3} &\approx \frac{4\alpha \omega_{\mathrm{J}}^2 |a_{\mathrm{dr},1}|^2 a_{\mathrm{pr},1}}{\omega_{\mathrm{H}}^2} \left(1 - \frac{2\omega_{\mathrm{H}}^2}{\omega_{\mathrm{dr}}^2 - \omega_{\mathrm{H}}^2 + i\gamma_{\mathrm{H}}\omega_{\mathrm{dr}}} \right) \\
&\approx \frac{4\alpha |j_{\mathrm{dr},1}|^2 j_{\mathrm{pr},1} (\omega_{\mathrm{dr}}^2 - 3\omega_{\mathrm{H}}^2 + i\gamma_{\mathrm{H}}\omega_{\mathrm{dr}})}{\omega_{\mathrm{H}}^2 (\omega_{\mathrm{dr}}^2 - \omega_{\mathrm{H}}^2 + i\gamma_{\mathrm{H}}\omega_{\mathrm{dr}}) \left[(\omega_{\mathrm{dr}}^2 - \omega_{\mathrm{J}}^2)^2 + \gamma_{\mathrm{J}}^2 \omega_{\mathrm{dr}}^2 \right]}.
\end{aligned}
\tag{19}
$$

Thus, we obtain

$$
\begin{aligned}
\omega_{\mathrm{pr}}\sigma(\omega_{\mathrm{pr}}) &= \frac{i\epsilon_z \epsilon_0 j(\omega_{\mathrm{pr}})}{a(\omega_{\mathrm{pr}})} \\
&= \frac{i\epsilon_z \epsilon_0 \lambda j_{\mathrm{pr},1}}{\lambda a_{\mathrm{pr},1} + \lambda^3 a_{\mathrm{pr},3}} \\
&\approx \frac{i\epsilon_z \epsilon_0 \omega_{\mathrm{J}}^2 \omega_{\mathrm{H}}^2 (\omega_{\mathrm{dr}}^2 - \omega_{\mathrm{H}}^2 + i\gamma_{\mathrm{H}}\omega_{\mathrm{dr}}) \left[(\omega_{\mathrm{dr}}^2 - \omega_{\mathrm{J}}^2)^2 + \gamma_{\mathrm{J}}^2 \omega_{\mathrm{dr}}^2 \right]}{\omega_{\mathrm{H}}^2 (\omega_{\mathrm{dr}}^2 - \omega_{\mathrm{H}}^2 + i\gamma_{\mathrm{H}}\omega_{\mathrm{dr}}) \left[(\omega_{\mathrm{dr}}^2 - \omega_{\mathrm{J}}^2)^2 + \gamma_{\mathrm{J}}^2 \omega_{\mathrm{dr}}^2 \right] + 4\alpha \omega_{\mathrm{J}}^2 |j_{\mathrm{dr}}|^2 (\omega_{\mathrm{dr}}^2 - 3\omega_{\mathrm{H}}^2 + i\gamma_{\mathrm{H}}\omega_{\mathrm{dr}})},
\end{aligned}
\tag{20}
$$

with the original driving amplitude $j_{\mathrm{dr}} = \lambda j_{\mathrm{dr},1}$. Taking $j_{\mathrm{dr}} = 0$ leads to the equilibrium solution

$$
\omega_{\mathrm{pr}}\sigma(\omega_{\mathrm{pr}}) \approx i\epsilon_z \epsilon_0 \omega_{\mathrm{J}}^2.
\tag{21}
$$

II. LATTICE GAUGE MODEL

The discretization of the fields on the lattice is sketched in Fig. 1. As mentioned in the main text, the superconducting order parameter is located on the sites and the vector potential is located on the bonds. The time derivative of the vector potential leads to the electric field, which has the same spatial structure. The magnetic field inside a plaquette is defined by the discretized curl of the vector potential on the enclosing bonds. While we take the vector potential to be constant along each bond, the spatially dependent terms in the electromagnetic part of the Lagrangian describe variations of the electric and magnetic fields on length scales above the discretization length. In particular, we note that for a system at nonzero temperature, the order parameter and the electromagnetic field display spatial fluctuations, even if the driving field has a much longer wavelength. These fluctuations are captured in our simulation method.
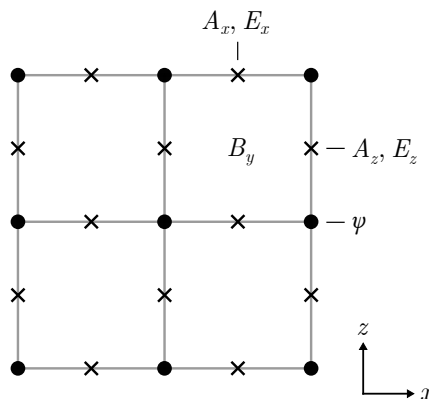

FIG. 1. Discretization of the fields in the xz plane.

III. COMPARISON BETWEEN THE QUADRATIC AND FULLY NONLINEAR MODELS

We refer to Eqs. (3) and (4) as the quadratic model, which approximates the fully nonlinear model given by Eqs. (1) and (2). In Fig. 2, we investigate the effect of the higher order terms on the effective interlayer coupling. We also compare the numerical results for the two models to the analytical prediction from Section I. While the analytical prediction shows excellent agreement with the numerical results for the quadratic model, simulating the fully nonlinear model leads to slightly different results, even for weak driving.
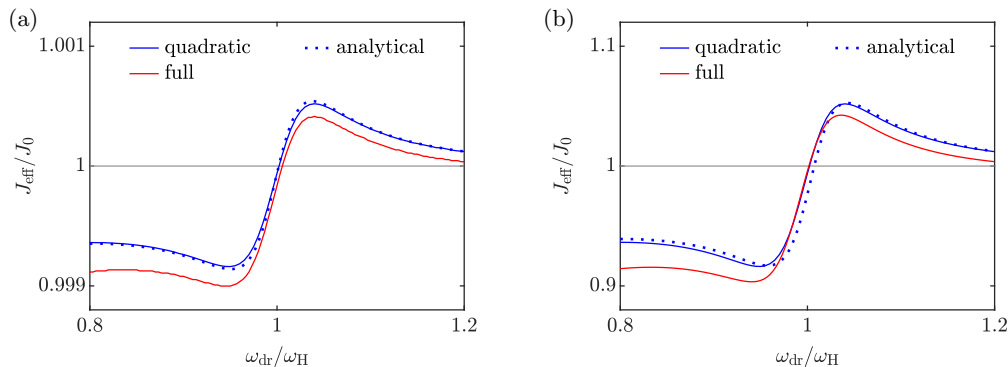

FIG. 2. Effective interlayer coupling for the quadratic and fully nonlinear models. The driving amplitudes are $E_0 = 10 \, \text{kV} \, \text{cm}^{-1}$ in (a) and $E_0 = 100 \, \text{kV} \, \text{cm}^{-1}$ in (b). The dotted lines indicate the analytical predictions based on the quadratic model. The model parameters are consistent with Section II, with $\omega_\text{J}/2\pi = 2$ THz.

IV. DEPLETION OF THE CONDENSATE

In our model, we explicitly include the drive in the time evolution of the electric field, keeping μ and α fixed. In fact, the gauge field effectively rescales μ, which leads to a (partial) suppression of the order parameter. For simplicity, we consider the spatially homogeneous case and expand the tunneling term of the Lagrangian up to quadratic order in the vector potential:

$$\mathcal{L}_\text{kin} = -\sum_{s,\mathbf{r}} t_s |\psi_\mathbf{r}|^2 |1 - e^{i a_{s,\mathbf{r}}}|^2 \approx -\sum_{s,\mathbf{r}} t_s |\psi_\mathbf{r}|^2 a_{s,\mathbf{r}}^2, \tag{22}$$

where $\psi_\mathbf{r} \equiv \psi$ and $a_{s,\mathbf{r}} \equiv a_s$ are homogeneous in space. Comparing the above expression with Eq. (6) in the manuscript, we find an effective reduction $\mu \to \mu - \sum_s t_s a_s^2$ due to the gauge field. The effective reduction of the order parameter is displayed as a function of the driving parameters in Fig. 3(a). While the gauge field is small away from the resonances, it leads to a significant depletion of the condensate in the resonant regimes. Entering the heating regime results in a complete depletion of the condensate. Note that the gauge field accounts for both the external drive and the supercurrents inside the sample.

Furthermore, we scrutinize the dynamical stability of the Higgs field and the vector potential using the harmonic balance method. Given a set of nonlinear ordinary differential equations with periodically changing parameters, the harmonic balance method maps the problem into an algebraic one by expanding solutions by multiple harmonics. The obtained algebraic equation is solved by the Newton or secant method. In order to solve the fully nonlinear equations of motion (1) and (2), we use the Krylov-Newton method with ten harmonics in Mousai [1].

In Fig. 3(b), we plot the absolute value of the time-averaged Higgs field for various driving frequencies ω_dr and amplitudes E_0 (corresponding to Fig. 3 in the main text). Due to the nonlinearity of the equation of motion, the system may show multistability; the obtained solution depends on the initial condition. Here, at each frequency, we sweep from weak to strong driving using the preceding calculation as the initial condition for the next calculation. We confirm the stability of the obtained solutions by adding slight noise to the initial conditions.

The blank area corresponds to the case where the Krylov-Newton method fails to obtain periodic steady solutions. The strong instability appears around $\omega_\text{dr} \simeq \omega_\text{J}$ and $\omega_\text{H}/2$, which agrees with the numerical solutions in the main text. The harmonic balance method overestimates the instability regimes due the difficulty of solving nonlinear algebraic equations accurately. At higher frequencies near ω_H, we find that the multistability is more prominent, and that the instability needs large driving amplitude. This regime corresponds to the heating regime identified via spectral
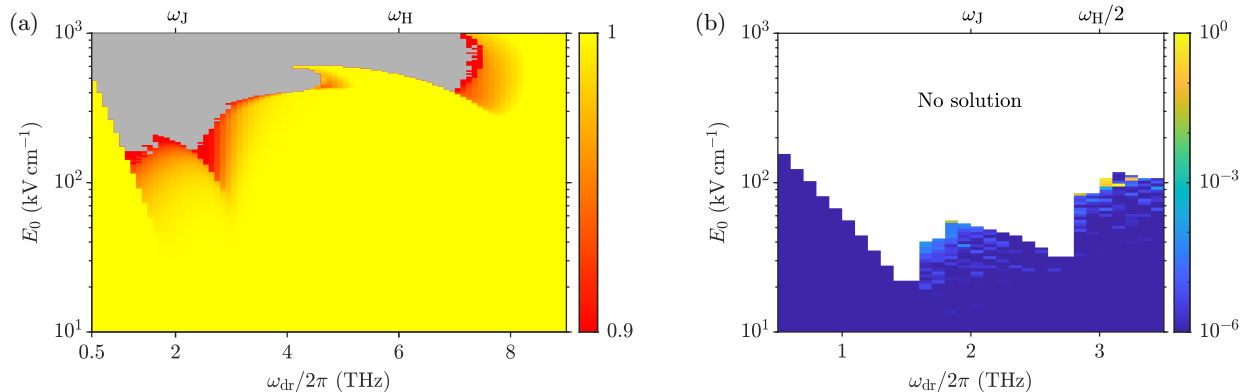
FIG. 3. Depletion of the condensate. (a) Dependence of the time-averaged amplitude of the order parameter $|\psi|/|\psi_0|$ on the driving frequency ω_{dr} and the field strength E_0. (b) Absolute value of the time-averaged Higgs field $h = |\psi|/|\psi_0| - 1$ as a function of driving frequency and field strength, as obtained by the harmonic balance method with ten harmonics.

entropy or depletion. The deviation between the harmonic balance method and the numerical solutions may come from the fact that chaotic solutions cannot be obtained by the harmonic balance method due to its harmonic ansatz.

V. THE ROLE OF THE DAMPING COEFFICIENTS AND THE CAPACITIVE COUPLING CONSTANT

In this section, we investigate how the Higgs mode mediated enhancement of interlayer transport depends on the damping coefficients and the capacitive coupling constant. In analogy to Fig. 3 in the main text, we numerically evaluate the renormalized interlayer coupling for different driving parameters, but we choose larger damping coefficients $\gamma_H/2\pi = \gamma_J/2\pi = 1$ THz. We see in Fig. 4 that the enhancement and reduction regimes are similar as before. The magnitude of the enhancement is generally smaller, but it is still possible to enhance the effective coupling by 50% when using sufficiently strong fields.

To further scrutinize the role of the damping coefficients, we present the effective interlayer coupling for different values of γ_H and γ_J for the the two cases of the ratio ω_J/ω_H that are not shown in the main text. Figure 5 displays the effect of increasing the damping coefficient of the Higgs mode. In both cases, the renormalization of the effective interlayer coupling is visible for higher values of γ_H, but the effect is notably weaker. Higher values of γ_J, on the other hand, do not significantly reduce the enhancement of the effective interlayer coupling for driving frequencies near the Higgs frequency, as shown in Fig. 6. Interestingly, the enhancement near the plasma frequency for $\omega_H < \omega_J < \sqrt{3}\omega_H$ is more severely affected by γ_J than by γ_H.
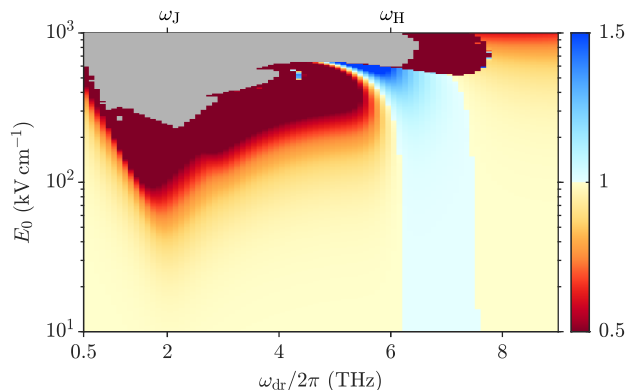

FIG. 4. Dependence of the effective interlayer coupling J_{eff}/J_0 on the driving frequency ω_{dr} and the field strength E_0. The gray area marks the heating regime. The damping coefficients are $\gamma_H/2\pi = \gamma_J/2\pi = 1$ THz.

To modify the capacitive coupling constant α, we vary the interaction strength g and adjust the tunneling coefficient t_z such that the previous values of the plasma frequency ω_J are recovered. It is evidenced by Fig. 7 that the Higgs mode mediated enhancement is qualitatively not affected by the value of α, which is of the order of 1 in the cuprates [2]. As expected, the enhancement is most pronounced for the largest α.
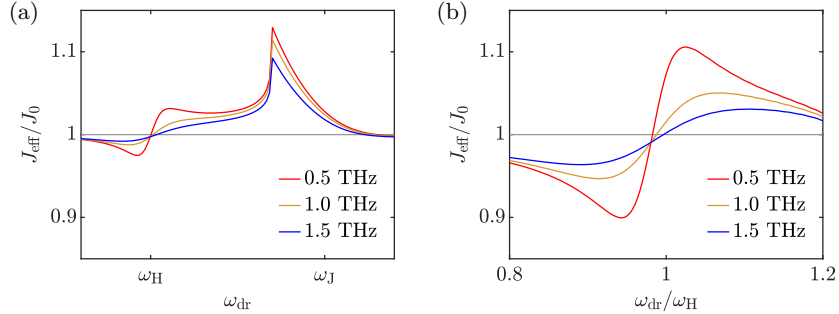
FIG. 5. Effective interlayer coupling for various values of $\gamma_H/2\pi$. The Higgs frequency $\omega_H/2\pi = 6$ THz and $\gamma_J/2\pi = 0.5$ THz are kept fixed. The choice of the driving amplitude depends on the plasma frequency: (a) $E_0 = 20$ kV cm^{-1} for $\omega_J/2\pi = 9$ THz and (b) $E_0 = 100$ kV cm^{-1} for $\omega_J/2\pi = 15$ THz.

FIG. 6. Effective interlayer coupling for various values of $\gamma_J/2\pi$. The Higgs frequency $\omega_H/2\pi = 6$ THz and $\gamma_H/2\pi = 0.5$ THz are kept fixed. The choice of the driving amplitude depends on the plasma frequency: (a) $E_0 = 20$ kV cm^{-1} for $\omega_J/2\pi = 9$ THz and (b) $E_0 = 100$ kV cm^{-1} for $\omega_J/2\pi = 15$ THz.

FIG. 7. Effective interlayer coupling for various values of the capacitive couling constant α. The Higgs frequency is $\omega_H/2\pi = 6$ THz. The choice of the driving amplitude depends on the plasma frequency: (a) $E_0 = 200$ kV cm^{-1} for $\omega_J/2\pi = 2$ 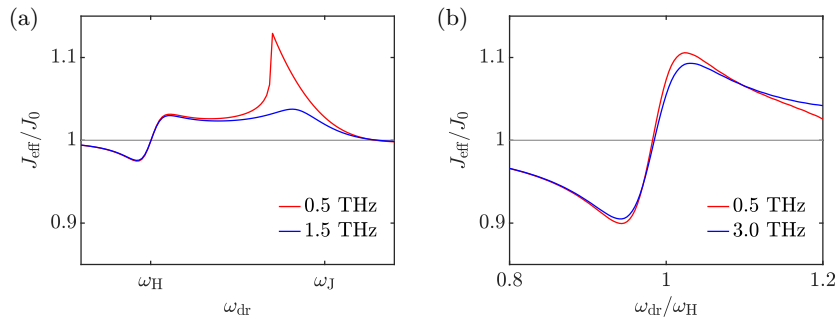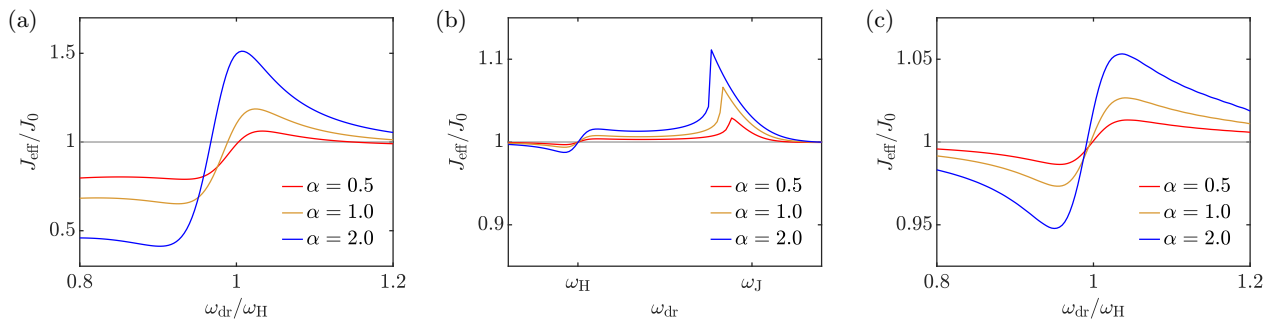THz, (b) $E_0 = 10$ kV cm^{-1} for $\omega_J/2\pi = 9$ THz, and (c) $E_0 = 50$ kV cm^{-1} for $\omega_J/2\pi = 15$ THz.

VI. HIGGS MODE MEDIATED ENHANCEMENT AT NONZERO TEMPERATURE

Here, we consider a monolayer cuprate superconductor at nonzero temperature. For this purpose, we simulate a three-dimensional system of $48 \times 48 \times 4$ sites with the parameters specified in the Appendix of the main text, choosing $t_z = 9.44 \times 10^{-4}$ meV. The equations of motion read

$$\partial_t^2 \psi_{\mathbf{r}} = \frac{1}{K\hbar^2} \frac{\partial \mathcal{L}}{\partial \psi_{\mathbf{r}}^*} - \gamma_{\mathrm{H}} \partial_t \psi_{\mathbf{r}} + \xi_{\mathbf{r}}, \tag{23}$$

$$\partial_t^2 A_{s,\mathbf{r}} = \frac{1}{\epsilon_s \epsilon_0} \frac{\partial \mathcal{L}}{\partial A_{s,\mathbf{r}}} - \gamma_{\mathrm{J}} \partial_t A_{s,\mathbf{r}} + \eta_{s,\mathbf{r}}, \tag{24}$$

where $\xi_{\mathbf{r}}$ and $\eta_{s,\mathbf{r}}$ represent the thermal fluctuations of the superconducting order parameter and the vector potential, respectively. These Langevin noise terms have a white Gaussian distribution with zero mean. To satisfy the fluctuation-dissipation theorem, we take the noise of the order parameter as

$$\langle \mathrm{Re}\{\xi_{\mathbf{r}}(t)\}\mathrm{Re}\{\xi_{\mathbf{r}'}(t')\}\rangle = \frac{\gamma_{\mathrm{H}} k_{\mathrm{B}} T}{K\hbar^2 V_0} \delta_{\mathbf{rr}'}\delta(t-t'), \tag{25}$$

$$\langle \mathrm{Im}\{\xi_{\mathbf{r}}(t)\}\mathrm{Im}\{\xi_{\mathbf{r}'}(t')\}\rangle = \frac{\gamma_{\mathrm{H}} k_{\mathrm{B}} T}{K\hbar^2 V_0} \delta_{\mathbf{rr}'}\delta(t-t'), \tag{26}$$

$$\langle \mathrm{Re}\{\xi_{\mathbf{r}}(t)\}\mathrm{Im}\{\xi_{\mathbf{r}'}(t')\}\rangle = 0. \tag{27}$$

The noise correlations for the vector potential are

$$\langle \eta_{x,\mathbf{r}}(t)\eta_{x,\mathbf{r}'}(t')\rangle = \frac{2\gamma_{\mathrm{J}} k_{\mathrm{B}} T}{\epsilon_x \epsilon_0 V_0} \delta_{\mathbf{rr}'}\delta(t-t'), \tag{28}$$

$$\langle \eta_{y,\mathbf{r}}(t)\eta_{y,\mathbf{r}'}(t')\rangle = \frac{2\gamma_{\mathrm{J}} k_{\mathrm{B}} T}{\epsilon_y \epsilon_0 V_0} \delta_{\mathbf{rr}'}\delta(t-t'), \tag{29}$$

$$\langle \eta_{z,\mathbf{r}}(t)\eta_{z,\mathbf{r}'}(t')\rangle = \frac{2\gamma_{\mathrm{J}} k_{\mathrm{B}} T}{\epsilon_z \epsilon_0 V_0} \delta_{\mathbf{rr}'}\delta(t-t'). \tag{30}$$

The thermal equilibrium at a given temperature is established as follows. We initialize the system in its ground state at $T = 0$ and let the dynamics evolve without external driving, influenced only by thermal fluctuations and dissipation. To characterize the phase transition, we introduce the order parameter

$$O = \frac{\left| \sum_{l,m,n} \psi_{l,m,n+1}^* \psi_{l,m,n} \, \mathrm{e}^{\mathrm{i}a_{l,m,n}^z} \right|}{\sum_{l,m,n} |\psi_{l,m,n}|^2}. \tag{31}$$

The order parameter measures the gauge-invariant phase coherence of the condensate across different layers. In our simulations, this quantity converges to a constant after 10 ps of free time evolution, indicating that thermal equilibrium is reached. For each trajectory, the order parameter is evaluated from the average of 200 measurements within a time interval of 2 ps. Finally, we take the ensemble average of 100 trajectories. As shown in Fig. 8(a), the temperature dependence of the order parameter is reminiscent of a second order phase transition. Due to the finite size of the simulated system, the order parameter converges to a plateau with nonzero value for high temperatures. Instead of a sharp discontinuity, one finds a distinct crossover at $T_c \sim 30$ K.

To obtain the c-axis conductivity at nonzero temperature, we add a probe term to the equations of motion for $A_{z,\mathbf{r}}$. Then, we compute $\sigma(\omega)$ as the ratio of the sample averages of $J_z(\omega)$ and $E_z(\omega)$ before taking the ensemble average of several hundred trajectories. In Fig. 8(b), we present an example of Higgs mode mediated enhancement of interlayer transport at $T = 1.5$ K. Applying an optical drive with the frequency $\omega_{\mathrm{dr}}/2\pi = 7.4$ THz and the field strength $E_0 = 400$ kV cm^{-1}, we find a low-frequency enhancement of σ_2 by $\sim 10\%$. Note that the c-axis plasma frequency and the Higgs frequency are $\omega_{\mathrm{J}}/2\pi \approx 2$ THz and $\omega_{\mathrm{H}}/2\pi \approx 6.7$ THz, respectively, at this temperature.

[1] J. C. Slater, Mousai: An open-source general purpose harmonic balance solver, 13th ASME Dayton Engineering Sciences Symposium (2017).
[2] M. Machida and T. Koyama, Localized rotating-modes in capacitively coupled intrinsic Josephson junctions: Systematic study of branching structure and collective dynamical instability, Phys. Rev. B **70**, 024523 (2004).
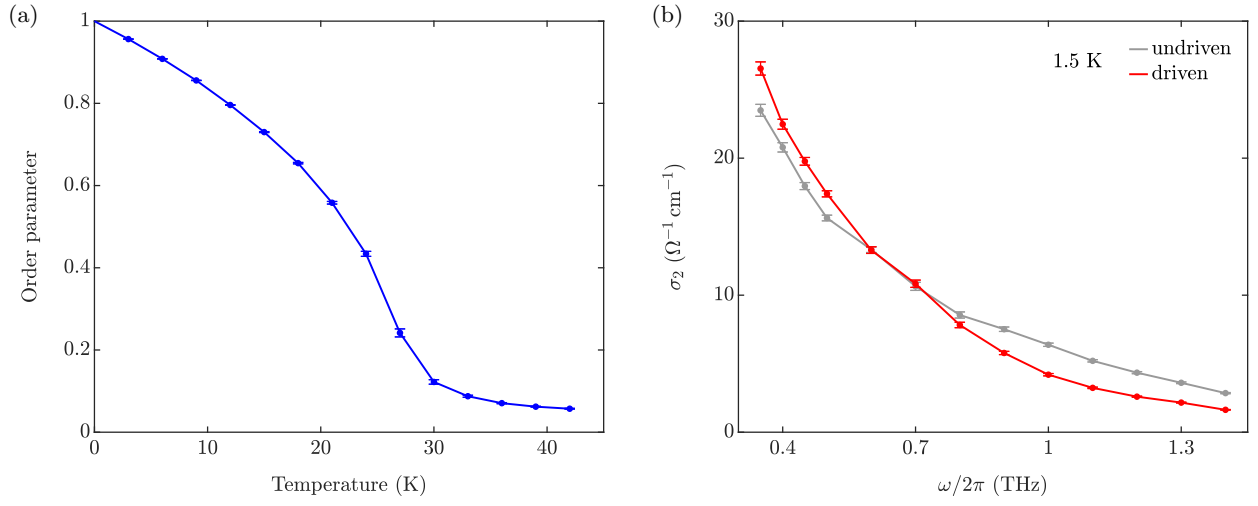
FIG. 8. Finite-temperature results. (a) Phase transition of a system of $48 \times 48 \times 4$ sites. (b) Higgs mode mediated enhancement of the imaginary c-axis conductivity for low frequencies at $T = 1.5$ K. The driving frequency is $\omega_{\mathrm{dr}} \approx 1.1\,\omega_{\mathrm{H}}$. In both panels, the error bars indicate the standard errors of the ensemble averages.

D.3   Terahertz amplifiers based on gain reflectivity in cuprate superconductors

Terahertz amplifiers based on gain reflectivity in cuprate superconductors

Guido Homann [1], Jayson G. Cosme [2], and Ludwig Mathey[1,3]

[1]*Zentrum für Optische Quantentechnologien und Institut für Laserphysik, Universität Hamburg, 22761 Hamburg, Germany*
[2]*National Institute of Physics, University of the Philippines, Diliman, Quezon City 1101, Philippines*
[3]*The Hamburg Centre for Ultrafast Imaging, Luruper Chaussee 149, 22761 Hamburg, Germany*

We demonstrate that parametric driving of suitable collective modes in cuprate superconductors results in a reflectivity $R > 1$ for frequencies in the low terahertz regime. We propose to exploit this effect for the amplification of coherent terahertz radiation in a laserlike fashion. As an example, we consider the optical driving of Josephson plasma oscillations in a monolayer cuprate at a frequency that is blue-detuned from the Higgs frequency. Analogously, terahertz radiation can be amplified in a bilayer cuprate by driving a phonon resonance at a frequency slightly higher than the upper Josephson plasma frequency. We show this by simulating a driven-dissipative $U(1)$ lattice gauge theory on a three-dimensional lattice, encoding a bilayer structure in the model parameters. We find a parametric amplification of terahertz radiation at zero and nonzero temperature.

I. INTRODUCTION

Coherent radiation sources in the terahertz regime have applications in spectroscopy and imaging in numerous fields, such as biology and medical diagnostics, nondestructive evaluation, and solid state research [1–5]. While significant progress has been made in the development of powerful terahertz sources [6–14], further development of terahertz technologies is imperative to close the "terahertz gap," particularly in the range between 0.5 and 1.5 THz [11,12]. In this work, we propose the design of an optical parametric oscillator [15–17] in the low-terahertz regime, i.e., $\sim$1 THz, to be utilized as an optical amplifier in a laserlike operation. We base this design on a general strategy to control the reflectivity of solids. The central mechanism is to use a collective mode with a nonlinear coupling to the electromagnetic field for parametric amplification. We apply this mechanism to cuprate superconductors and propose a laserlike setup for the amplification of terahertz radiation. In this setup, a light-driven superconductor with reflectivity $R_2 = R(\omega_{pr}) > 1$ serves as one of three mirrors forming an optical resonator as depicted in Fig. 1. The probe with frequency ω_{pr} enters the resonator through a partially transparent mirror with reflectivity $R_1 < 1$ and transmissivity $T_1 > 0$. The third mirror is assumed to have perfect reflectivity $R_3 = 1$. For $R_1 R_2 < 1$, the intensity ratio of the outgoing and the ingoing signal is given by

$$\frac{I_{out}}{I_{in}} = \frac{R_2 T_1^2}{1 - R_1 R_2} + R_1. \tag{1}$$

The gain condition of this setup, $R_2 > 1/R_1$, is reflected by the divergence of I_{out} for $R_1 R_2 \rightarrow 1$. Above this threshold, the gain saturates once the probe signal enters the nonlinear response regime such that $R(\omega_{pr})$ decreases.

As our proposal requires pump lasers with field strengths of several hundred kV/cm, we suggest the following strategy towards its technical realization. The first step would be to test the proposed amplification mechanism using a pump pulse with a duration of $\sim$1 ps. Following the interpretation of the measurements in Ref. [18], we propose to achieve better overlap of the pump and probe laser fields in the material by varying the incident angle of the probe pulse. We note that observing a net reflectivity gain from a light-driven superconductor would also be interesting from a purely scientific point of view. The next step would be a terahertz amplifier that is operated in pulsed fashion. Extending the duration of the pump pulse to $\sim$1 ns, as in Ref. [19], would allow for several round trips of the probe pulse in an optical resonator with a path length of a few centimeters.

In this paper, we first demonstrate parametric amplification of terahertz radiation in monolayer cuprates using a gauge-invariant two-mode model with a cubic coupling process of the Higgs and plasma modes [20,21]. We find that
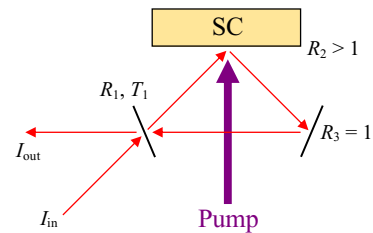
FIG. 1. Setup of an optical parametric oscillator using a superconductor (SC) with reflectivity $R_2 > 1$ as a gain medium.

driving plasmonic excitations blue-detuned from the Higgs mode leads to a reflectivity $R > 1$ for probe frequencies below the Josephson plasma edge. As a second example, we consider a periodic modulation of the interlayer coupling in bilayer cuprates, which models a periodic excitation of a phonon mode. Here, the low-frequency reflectivity is larger than 1 when the frequency of the excited phonon mode is blue-detuned from the upper Josephson plasma frequency. We implement a three-dimensional $U(1)$ lattice gauge theory with anisotropic lattice parameters to simulate this scenario at nonzero temperature. Our calculations show that phonon mediated amplification of terahertz radiation is effective at temperatures up to ∼20% of the critical temperature T_c. Optical amplification in light-driven solids was also discussed in Refs. [18,22–26].

The key requirement for the amplification mechanism presented in this work is a cubic coupling term of the form $\phi\theta^2$ in the Lagrangian, where θ is the plasma mode and ϕ represents another collective mode. Note that the plasma mode directly couples to the electric field E. When one applies pump and probe processes to the system, as sketched in Fig. 2(a), there are two scenarios for a parametric amplification of the probe. In one scenario, the pump directly excites the plasma mode θ at a frequency that is blue-detuned from the eigenfrequency of the mode ϕ, which acts as an idler mode. Alternatively, the pump primarily couples to the collective mode ϕ. An enhanced response is then achieved for a pump frequency ω_{dr} that is blue-detuned with respect to the plasma frequency. Here, the plasma mode serves as the idler mode. In both cases, the probe couples to the plasma mode, and its frequency should be $\omega_{pr} = \omega_{dr} - \omega_r$, where ω_r denotes the eigenfrequency of the idler mode. Thus three-wave mixing of the probe with the pump and resonant excitations of the idler mode induces the amplification of the probe signal. An important signature of this effect is a negative peak in the real part of the optical conductivity σ_1 at $\omega_{pr} = \omega_{dr} - \omega_r$.

II. HIGGS MODE MEDIATED AMPLIFICATION IN LIGHT-DRIVEN MONOLAYER CUPRATES

Josephson plasma oscillations are characteristic excitations of cuprate superconductors [27–31], corresponding to the tunneling of Cooper pairs between copper-oxide layers. The Higgs mode, on the other hand, describes amplitude oscillations of the superconducting order parameter [32–38]. While plasma modes directly couple to the electromagnetic vector potential, the Higgs mode has no linear coupling to electromagnetic fields in a system with approximate particle-hole symmetry [39,40]. A two-mode model of a light-driven monolayer cuprate at zero temperature was derived in Refs. [20,21]. The underlying Lagrangian includes a cubic term $\sim h\theta^2$, coupling the plasma mode θ and the Higgs mode h. The equations of motion read

$$\ddot{\theta} + \gamma_J\dot{\theta} + \omega_J^2 \sin(\theta)(1+h)^2 = j, \tag{2}$$

$$\ddot{h} + \gamma_H\dot{h} + \omega_H^2\left(h + \frac{3}{2}h^2 + \frac{1}{2}h^3\right)$$
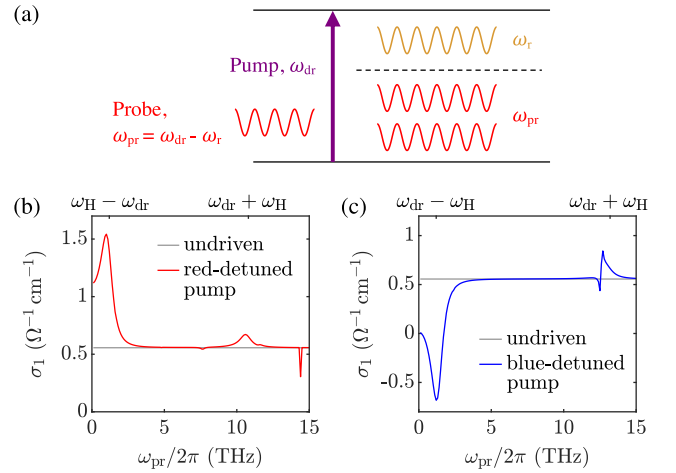$$+ 2\alpha\omega_J^2[1 - \cos(\theta)](1+h) = 0, \tag{3}$$

FIG. 2. Parametric amplification of terahertz radiation in a solid with a plasma mode θ and a collective mode ϕ that are nonlinearly coupled. (a) Schematic illustration of the amplification process. The pump laser excites the plasma mode θ (or the collective mode ϕ) with frequency ω_{dr}. The pump signal is down-converted to the lower frequency $\omega_{pr} = \omega_{dr} - \omega_r$ of the probe by simultaneous excitation of the collective mode ϕ (or the plasma mode θ) at its eigenfrequency ω_r. The numerical results in (b) and (c) are obtained for a monolayer cuprate, in which Josephson plasma oscillations are driven by the pump laser and the Higgs mode is the idler mode. (b) When the pump frequency is red-detuned from the Higgs frequency $\omega_r \equiv \omega_H$, a probe with $\omega_{pr} \approx \omega_H - \omega_{dr}$ is attenuated as indicated by the positive peak in the real part σ_1 of the optical conductivity. The pump frequency is $\omega_{dr}/2\pi = 4.8$ THz and the pump strength is $E_0 = 150$ kV/cm. (c) A blue-detuned pump frequency leads to an amplification of the probe for $\omega_{pr} \approx \omega_{dr} - \omega_H$, corresponding to a negative peak in σ_1. In this case, the pump frequency is $\omega_{dr}/2\pi = 7.2$ THz and the pump strength is $E_0 = 300$ kV/cm. The probe strength is $E_{pr} = 1$ kV/cm in both cases. The Josephson plasma frequency is $\omega_J/2\pi = 2$ THz and the Higgs frequency is $\omega_H/2\pi = 6$ THz. The remaining parameters are $\gamma_J/2\pi = 0.25$ THz, $\gamma_H/2\pi = 1$ THz, $\alpha = 1$, $\epsilon_\infty = 4$, and $d = 10$ Å.

where ω_H is the Higgs frequency, ω_J is the plasma frequency, and γ_H and γ_J are damping coefficients. The capacitive coupling constant α is of the order of 1 in cuprate superconductors [41]. The interlayer current $j(t) = j_{dr}(t) + j_{pr}(t)$ is induced by an external electric field polarized along the c axis of the crystal and describes the pump and probe processes. A monochromatic pump with field strength E_0 gives rise to $j_{dr}(t) = (-2ed\omega_{dr}E_0/\hbar\epsilon_\infty)\sin(\omega_{dr}t)$, where $-2e$ is the Cooper pair charge, d is the interlayer spacing, and ϵ_∞ is the background dielectric constant of the material. To calculate the optical conductivity, we include a weak probe current $j_{pr}(t)$ and evaluate the Fourier components $j(\omega_{pr})$ and $\theta(\omega_{pr})$ in the steady state. The conductivity is given by $\sigma(\omega_{pr}) = i\epsilon_\infty\epsilon_0 j(\omega_{pr})/\omega_{pr}\theta(\omega_{pr})$, as follows from the Josephson relation $\dot{\theta} = 2edE/\hbar$ [42].

In Figs. 2(b) and 2(c), we present numerical results for the real part of the optical conductivity of a monolayer cuprate with Josephson plasma frequency $\omega_J/2\pi = 2$ THz and Higgs frequency $\omega_H/2\pi = 6$ THz. For a pump frequency that is red-detuned with respect to the Higgs frequency, σ_1 exhibits a
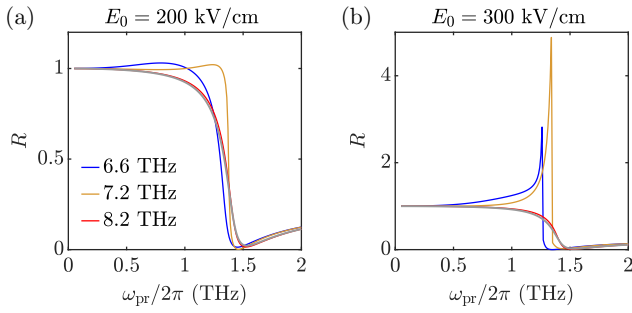
FIG. 3. Higgs mode mediated amplification of terahertz radiation in a monolayer cuprate. The reflectivity at normal incidence is shown for two choices of the pump strength: (a) $E_0 = 200$ kV/cm and (b) 300 kV/cm. The pump frequencies for the higher pump strength in (b) are the same as indicated for the lower pump strength in (a). Gray lines correspond to the undriven case. The probe strength is $E_{pr} = 1$ kV/cm. The model parameters are the same as in Fig. 2.

pronounced absolute maximum at $\omega_{pr} \approx \omega_H - \omega_{dr}$ and a local maximum at $\omega_{pr} \approx \omega_H + \omega_{dr}$. The peak at $\omega_{pr} \approx \omega_H - \omega_{dr}$ corresponds to an excitation of the Higgs mode via resonant two-photon processes, whereas a probe with $\omega_{pr} \approx \omega_H + \omega_{dr}$ amplifies the pump signal and simultaneously excites the Higgs mode. The minimum slightly below 15 THz results from the coupling of the probe to the third-harmonic of the pump.

For a blue-detuned pump frequency, we find $\sigma_1 < 0$ for low probe frequencies. The minimum at $\omega_{pr} \approx \omega_{dr} - \omega_H$ indicates a resonant amplification of the probe due to a down-conversion of the pump by simultaneous excitation of the Higgs mode. The conductivity displays a maximum at $\omega_{pr} \approx \omega_{dr} + \omega_H$, similarly to the case of a red-detuned pump frequency, while the third-harmonic of the pump is outside the plotted frequency range. In Appendix A, we provide an analytical estimate of $\sigma(\omega_{pr} = \omega_{dr} - \omega_H)$ based on a perturbative expansion for weak pump-probe strengths. Our analytical estimate is in qualitative agreement with the numerical results.

In the following, we focus on pump frequencies that are blue-detuned from the Higgs frequency. As we shall see below, a negative conductivity σ_1 implies a reflectivity $R > 1$ at low frequencies. The reflectivity at normal incidence is obtained from the optical conductivity via the Fresnel equation

$$R(\omega) = \left| \frac{1 - n(\omega)}{1 + n(\omega)} \right|^2. \tag{4}$$

The refractive index $n(\omega) = \pm\sqrt{\epsilon(\omega)}$ is a function of the dielectric permittivity $\epsilon(\omega) = \epsilon_\infty + i\sigma(\omega)/\epsilon_0\omega$. The sign of the refractive index for a given frequency is fixed by causality [43,44]. We choose the positive sign unless both the real part and the imaginary part of $\epsilon(\omega)$ are negative. Thus the electric field penetrates the bulk for frequencies above the plasma edge around $\omega_J/\sqrt{2}$, while it is screened for lower frequencies. This is the characteristic response of a Josephson plasma, also in the presence of a periodic drive [26].

Figure 3 displays the low-frequency reflectivity for different strengths and frequencies of the optical pump applied to the same monolayer cuprate as before. For pump frequencies

that are slightly blue-detuned from the Higgs frequency, the reflectivity is larger than 1 at probe frequencies below the plasma edge. This is an immediate consequence of the negative σ_1 at low probe frequencies in those cases. As expected, the enhancement of the reflectivity is more pronounced for the stronger pump in Fig. 3(b) than for the weaker pump in Fig. 3(a). The amplification mechanism is particularly effective if the detuning $\omega_{dr} - \omega_H$, and thus the minimum of σ_1, approaches the plasma edge frequency, as is the case for $\omega_{dr}/2\pi = 7.2$ THz. We note that the plasma edge is shifted to a slightly lower frequency by the pump, corresponding to a small reduction of the time-averaged superconducting order parameter. The magnitude of this shift increases with increasing pump strength and decreasing detuning of the pump frequency from the Higgs frequency.

III. PHONON MEDIATED AMPLIFICATION IN BILAYER CUPRATES

We now turn to our second example of parametric amplification of terahertz radiation in cuprate superconductors. While the Higgs mode is strongly damped in the cuprates in general [34,35,45], phononic excitations have picosecond lifetimes, such as vibrations of apical oxygen atoms in YBa$_2$C$_3$O$_{7-\delta}$ (YBCO) [46,47]. In the following, we consider the scenario in which the pump laser periodically modulates the Josephson coupling between the copper-oxide layers as it resonantly couples to a phonon mode. Parametric driving of Josephson plasma oscillations by optically excited phonons was also discussed in Refs. [48–51].

Specifically, we consider bilayer cuprates utilizing a particle-hole symmetric $U(1)$ lattice gauge theory in three dimensions [20,21]. We formulate a Lagrangian with dynamical and static terms on an anisotropic lattice that corresponds to a bilayer structure as illustrated in Fig. 4(a). The static part of the Lagrangian resembles the Ginzburg-Landau free energy [52]. That is, we describe the Cooper pairs as a condensate of interacting bosons with charge $-2e$, represented by the complex field ψ_r. This model is suitable for simulating the coupled dynamics of the order parameter of the superconducting state and the electromagnetic field at temperatures below T_c.

The order parameter $\psi_r(t)$ is located on the lattice sites. According to the Peierls substitution, each component of the electromagnetic vector potential $A_{k,r}(t)$ is defined on the bond between the site $\mathbf{r}$ and its nearest neighbor in the $k \in \{x, y, z\}$ direction. The intra- and interbilayer spacings $d_{s,w}$ are taken as the distances between the CuO$_2$ planes in the crystal, and the in-plane discretization length d_{ab} is introduced as a short-range cutoff of the order of the in-plane coherence length. The bilayer structure results in the appearance of two Josephson plasma modes. The lower Josephson plasma resonance is dominated by interbilayer currents, due to the interbilayer tunneling energy t_w. The upper Josephson plasma resonance, on the other hand, is dominated by intrabilayer currents, due to the intrabilayer tunneling energy t_s. We choose the tunneling coefficients t_s and t_w to yield realistic values for the Josephson plasma frequencies. The in-plane tunneling coefficient t_{ab} does not only define an in-plane plasma frequency but also sets the critical temperature of the system. Note that we suppose the z direction to be aligned with the c axis of the

crystal. The Lagrangian of the lattice gauge model is

$$\mathcal{L} = \mathcal{L}_{sc} + \mathcal{L}_{em} + \mathcal{L}_{kin}. \tag{5}$$

The first term is the $|\psi|^4$ model of the superconducting condensate in the absence of Cooper pair tunneling,

$$\mathcal{L}_{sc} = \sum_{\mathbf{r}} K\hbar^2 |\partial_t \psi_{\mathbf{r}}|^2 + \mu |\psi_{\mathbf{r}}|^2 - \frac{g}{2} |\psi_{\mathbf{r}}|^4, \tag{6}$$

with the fixed Ginzburg-Landau coefficients μ and g. The coefficient K describes the magnitude of the dynamical term [33,40].

The electromagnetic part $\mathcal{L}_{em}$ is the Lagrangian of the free electromagnetic field on a lattice, modified by the screening due to bound charges in the material,

$$\mathcal{L}_{em} = \sum_{k,\mathbf{r}} \frac{\kappa_{k,\mathbf{r}}\epsilon_{k,\mathbf{r}}\epsilon_0}{2} E_{k,\mathbf{r}}^2 - \frac{\kappa_{z,\mathbf{r}}}{\kappa_{k,\mathbf{r}}\beta_{k,\mathbf{r}}^2\mu_0}[1 - \cos(\beta_{k,\mathbf{r}} B_{k,\mathbf{r}})], \tag{7}$$

where $E_{k,\mathbf{r}}$ denotes the k component of the electric field. Note that we choose the temporal gauge for our calculations, i.e., $E_{k,\mathbf{r}} = -\partial_t A_{k,\mathbf{r}}$. The magnetic field components $B_{k,\mathbf{r}} = \epsilon_{klm}\delta_l A_{m,\mathbf{r}}$ are centered on the plaquettes of the lattice. We calculate the spatial derivatives according to $\delta_l A_{m,\mathbf{r}} = (A_{m,\mathbf{r}'(l)} - A_{m,\mathbf{r}})/d_{l,\mathbf{r}}$, where $\mathbf{r}'(l)$ is the neighboring site of $\mathbf{r}$ in the l direction. The discretization lengths are $d_{x,\mathbf{r}} = d_{y,\mathbf{r}} = d_{ab}$ for in-plane junctions, $d_{z,\mathbf{r}} = d_s$ for intrabilayer junctions, and $d_{z,\mathbf{r}} = d_w$ for interbilayer junctions. The background dielectric constants are $\epsilon_{x,\mathbf{r}} = \epsilon_{y,\mathbf{r}} = \epsilon_{ab}$ for in-plane junctions, $\epsilon_{z,\mathbf{r}} = \epsilon_s$ for intrabilayer junctions, and $\epsilon_{z,\mathbf{r}} = \epsilon_w$ for interbilayer junctions. The other prefactors in Eq. (7) account for the anisotropic lattice geometry. Introducing $d_c = (d_s + d_w)/2$, we write $\kappa_{x,\mathbf{r}} = \kappa_{y,\mathbf{r}} = 1$ and $\kappa_{z,\mathbf{r}} = d_{z,\mathbf{r}}/d_c$, while $\beta_{x,\mathbf{r}} = \beta_{y,\mathbf{r}} = 2ed_{ab}d_{z,\mathbf{r}}/\hbar$ and $\beta_{z,\mathbf{r}} = 2ed_{ab}^2/\hbar$.

The kinetic part of the Lagrangian is given by

$$\mathcal{L}_{kin} = -\sum_{k,\mathbf{r}} t_{k,\mathbf{r}} |\psi_{\mathbf{r}'(k)} - \psi_{\mathbf{r}} e^{ia_{k,\mathbf{r}}}|^2. \tag{8}$$

The unitless vector potential $a_{k,\mathbf{r}} = -2ed_{k,\mathbf{r}}A_{k,\mathbf{r}}/\hbar$ directly couples to the phase of the order parameter. Thus it does not only ensure the local gauge invariance of $\mathcal{L}_{kin}$, but it also gives rise to a nonlinear coupling between the order parameter and the electromagnetic field. This coupling accounts for the Coulomb interaction between the Cooper pairs. The Lagrangian (5) is particle-hole symmetric due to its invariance under $\psi_{\mathbf{r}} \to \psi_{\mathbf{r}}^*$.

We add damping terms and Langevin noise to the equations of motion, which are given by the Euler-Lagrange equations. This enables us to numerically determine the time evolution of the order parameter and the vector potential at zero and nonzero temperature. We employ periodic boundary conditions and integrate the stochastic differential equations using Heun's method with a step size of $\Delta t = 1.6$ as. To mimic the effect of a driven phonon mode, we make the interlayer tunneling coefficients time-dependent [49,50], i.e.,

$$t_{s,w} \to t_{s,w}[1 \pm \Lambda_{s,w}\cos(\omega_{dr}t)]. \tag{9}$$

This captures a phononic excitation with a wavelength that is large compared to the system size of the simulation. As before, the reflectivity is calculated numerically by adding a
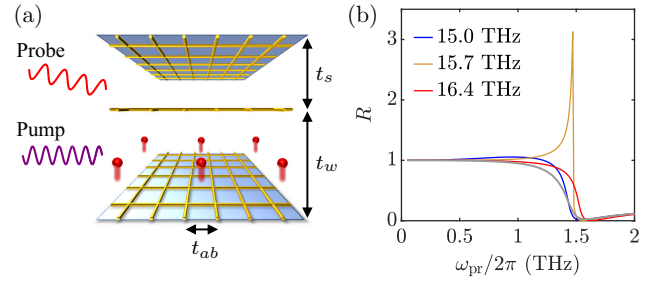

FIG. 4. Phonon mediated amplification of terahertz radiation in a bilayer cuprate. (a) Schematic illustration of the pump-probe dynamics in a bilayer cuprate. The superconducting order parameter is discretized on a layered lattice. The pump excites a phonon mode, represented by the red atoms moving along the c axis. Thus the interlayer tunneling coefficients $t_{s,w}$ become time-dependent, which modifies the plasmonic response to the c-axis polarized probe. (b) Reflectivity at normal incidence for different pump frequencies at $T = 0$. The modulation amplitudes are $\Lambda_s = 0.2$ and $\Lambda_w = 0.8$. The gray line corresponds to the undriven case. The probe strength is $E_{pr} = 1$ kV/cm. The lower and upper Josephson plasma frequencies are $\omega_{J1}/2\pi = 2$ THz and $\omega_{J2}/2\pi = 14.3$ THz, respectively. The full parameter set is specified in Table I.

probe to the equations of motion for the z component of the electromagnetic vector potential. We assume the existence of a suitable phonon resonance such that ω_{dr} is blue-detuned from the upper Josephson plasma frequency ω_{J2}.

In Fig. 4(b), we show that the phonon mediated pump has a similar effect as the plasmonic excitations discussed before. This analogy derives from tunneling terms of the form $\sim t_{k,\mathbf{r}} A_{k,\mathbf{r}}^2$ in the Lagrangian. That is, the parametric amplification of the terahertz probe is enabled by the cubic coupling of the tunneling coefficients and the vector potential. In contrast to the case of Higgs mode mediated amplification, the pump does not primarily couple to the vector potential but to the tunneling coefficients, which models the excited phonon mode. Here, the maximum gain is realized when the detuning $\omega_{dr} - \omega_{J2}$ approaches the frequency of the lower reflectivity edge at $\omega_{J1}/\sqrt{2}$. The amplification of terahertz radiation is feasible up to probe strengths of ~ 100 kV/cm; see Appendix E. Note that the amplification mechanism also works if the frequency of the excited phonon mode is slightly blue-detuned from the lower Josephson plasma frequency. However, this requires a pump frequency of the order of 1 THz [53], which is in the frequency range that lacks suitable radiation sources.

Finally, we investigate the phonon mediated amplification of terahertz signals at nonzero temperature T by simulating an ensemble of several hundred trajectories for a bilayer system of $40 \times 40 \times 4$ sites. To obtain the c-axis conductivity $\sigma(\omega_{pr})$ for a single trajectory, we evaluate the sample averages of the c-axis current $J_z(\omega_{pr})$ and the c-axis electric field $E_z(\omega_{pr})$. We then take the ensemble average of $\sigma(\omega_{pr})$ and calculate the reflectivity $R(\omega_{pr})$ using Eq. (4). As shown in Figs. 5(a) and 5(c), the phonon mediated amplification of terahertz radiation is effective at $\sim 20\%$ of T_c despite the thermal broadening of the parametric resonance expected at $\omega_{pr}/2\pi \approx 1$ THz. Importantly, the real part of the conductivity is negative at frequencies around 1 THz and below, leading to a reflectivity
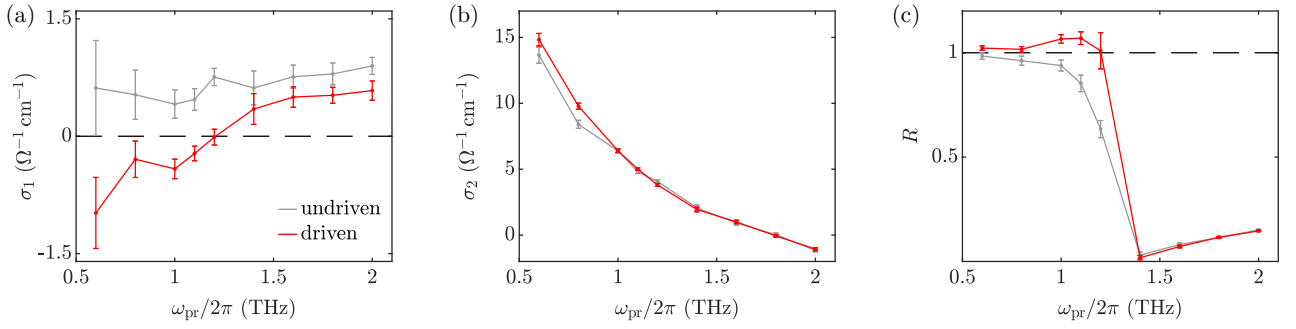
FIG. 5. Phonon mediated amplification of terahertz radiation in a bilayer cuprate at $T = 5$ K $\sim 0.2T_c$. (a) Real part of the optical conductivity. (b) Imaginary part of the optical conductivity. (c) Reflectivity at normal incidence. The pump frequency is $\omega_{dr}/2\pi = 14.8$ THz, and the modulation amplitudes are $\Lambda_s = 0.2$ and $\Lambda_w = 0.8$. The error bars indicate the standard errors of the ensemble averages. The probe strength is $E_{pr} = 30$ kV/cm. The bilayer system is the same as in Fig. 4. The upper Josephson plasma frequency is shifted to $\omega_{J2} \approx 13.8$ THz due to thermal fluctuations.

$R > 1$ in this regime. Additionally, we observe a parametric enhancement of the imaginary part of the low-frequency conductivity in Fig. 5(b); see also Refs. [21,48–50].

IV. DISCUSSION AND OUTLOOK

In conclusion, we propose a terahertz amplification technology based on parametric amplification in high-T_c superconductors, utilizing an optical pump mechanism. A key feature of the amplifier and its underlying mechanism is that the enhancement of the reflectivity is controlled via the pump frequency and the pump strength. Superconductors are promising candidates to induce a reflectivity $R > 1$ because their low-frequency reflectivity is close to 1 in equilibrium. We emphasize, however, that the mechanism we put forth can not only be realized in cuprate superconductors but also in other materials with collective modes that couple nonlinearly to light. The parametric amplification of terahertz signals is limited by the finite penetration depth of the pump, which is smaller than the penetration depth of the probe in many cases [18,54,55]. To reduce the mismatch of the penetration depths of the pump and the probe, we propose to choose a large incident angle for the probe beam while orienting the pump beam parallel to the surface normal; see Fig. 1. As mentioned in the introduction, we recommend to implement an amplifier in pulsed operation once net optical gain from a light-driven solid is achieved. This would also be advantageous with regards to heating effects, which are further discussed in Appendix F.

Our proposed terahertz amplifier advances pump-probe experiments on high-T_c superconductors towards a potential application. It motivates a demonstration of a stable and sufficiently strong enhancement of the reflectivity above 1 and the design of an optical cavity as shown in Fig. 1, with the purpose of developing coherent radiation sources in the terahertz regime.

APPENDIX A: ANALYTICAL ESTIMATE OF HIGGS MODE MEDIATED AMPLIFICATION IN MONOLAYER CUPRATES

Neglecting all nonlinear terms except for the quadratic coupling between the Higgs mode h and the plasma mode θ in Eqs. (2) and (3), we find

$$\ddot{\theta} + \gamma_J \dot{\theta} + \omega_J^2 \theta + 2\omega_J^2 \theta h = j, \tag{A1}$$

$$\ddot{h} + \gamma_H \dot{h} + \omega_H^2 h + \alpha \omega_J^2 \theta^2 = 0, \tag{A2}$$

as in Refs. [20,21]. Now, we expand j, θ, and h in the form

$$f = f^{(0)} + \lambda f^{(1)} + \lambda^2 f^{(2)} + \lambda^3 f^{(3)} + \mathcal{O}(\lambda^4), \tag{A3}$$

where $\lambda \ll 1$ is a small expansion parameter. We take the current j induced by the pump and the probe as

$$j^{(1)} = j_{dr,1} e^{-i\omega_{dr}t} + j_{pr,1} e^{-i\omega_{pr}t} + \text{c.c.} \tag{A4}$$

Hence, there are no zeroth order contributions and we obtain

$$\theta^{(1)} = \theta_{dr,1} e^{-i\omega_{dr}t} + \theta_{pr,1} e^{-i\omega_{pr}t} + \text{c.c.}, \tag{A5}$$

$$h^{(1)} = 0 \tag{A6}$$

in first order, where

$$\theta_{dr,1} = \frac{j_{dr,1}}{\omega_J^2 - \omega_{dr}^2 - i\gamma_J \omega_{dr}}, \tag{A7}$$

$$\theta_{pr,1} = \frac{j_{pr,1}}{\omega_J^2 - \omega_{pr}^2 - i\gamma_J \omega_{pr}}. \tag{A8}$$

In second order, we have

$$\theta^{(2)} = 0, \tag{A9}$$

$$h^{(2)} = h_0 + h_1 e^{-2i\omega_{dr}t} + h_2 e^{-2i\omega_{pr}t} + h_3 e^{-i(\omega_{dr}-\omega_{pr})t} + h_4 e^{-i(\omega_{dr}+\omega_{pr})t} + \text{c.c.}, \tag{A10}$$

where

$$h_0 = -\frac{2\alpha\omega_J^2}{\omega_H^2}\left(|\theta_{dr,1}|^2 + |\theta_{pr,1}|^2\right), \tag{A11}$$

$$h_1 = \frac{\alpha\omega_J^2\theta_{dr,1}^2}{4\omega_{dr}^2 - \omega_H^2 + 2i\gamma_H\omega_{dr}}, \tag{A12}$$

$$h_2 = \frac{\alpha\omega_J^2\theta_{pr,1}^2}{4\omega_{pr}^2 - \omega_H^2 + 2i\gamma_H\omega_{pr}}, \tag{A13}$$

$$h_3 = \frac{2\alpha\omega_J^2\theta_{dr,1}\theta_{pr,1}^*}{(\omega_{dr}-\omega_{pr})^2 - \omega_H^2 + i\gamma_H(\omega_{dr}-\omega_{pr})}, \tag{A14}$$

$$h_4 = \frac{2\alpha\omega_J^2\theta_{dr,1}\theta_{pr,1}}{(\omega_{dr}+\omega_{pr})^2 - \omega_H^2 + i\gamma_H(\omega_{dr}+\omega_{pr})}. \tag{A15}$$

In third order, we find the following correction for the vector potential at the probe frequency:

$$\theta_{pr,3} = \frac{2\omega_J^2\left(h_0\theta_{pr,1} + h_2\theta_{pr,1}^* + h_3^*\theta_{dr,1} + h_4\theta_{dr,1}^*\right)}{\omega_{pr}^2 - \omega_J^2 + i\gamma_J\omega_{pr}}. \tag{A16}$$

We consider a probe with $|j_{pr,1}| \ll |j_{dr,1}|$ and $\omega_{pr} = \omega_{dr} - \omega_H$ such that we can neglect the h_2 term. Moreover, we assume near-resonant driving, i.e., $\omega_{dr} \simeq \omega_H$, to simplify the denominators in Eqs. (A14) and (A15),

$$\theta_{pr,3} \approx \frac{-4\alpha\omega_J^4|\theta_{dr,1}|^2\theta_{pr,1}}{\omega_{pr}^2 - \omega_J^2 + i\gamma_J\omega_{pr}}\left(\frac{1}{\omega_H^2} + \frac{2}{i\gamma_H\omega_H}\right)$$

$$\approx \frac{4\alpha\omega_J^4|j_{pr,1}|^2 j_{pr,1}(\gamma_H - 2i\omega_H)}{\gamma_H\omega_H^2\left[(\omega_{dr}-\omega_H)^2 - \omega_J^2 + i\gamma_J(\omega_{dr}-\omega_H)\right]^2\left[\left(\omega_{dr}^2 - \omega_J^2\right)^2 + \gamma_J^2\omega_{dr}^2\right]}. \tag{A17}$$

As $\dot{\theta} = 2edE/\hbar$ [42], the optical conductivity is given by

$$\sigma(\omega_{pr}) = \frac{i\epsilon_\infty\epsilon_0 j(\omega_{pr})}{\omega_{pr}\theta(\omega_{pr})} = \frac{i\epsilon_\infty\epsilon_0\lambda j_{pr,1}}{\omega_{pr}(\lambda\theta_{pr,1} + \lambda^3\theta_{pr,3})}, \tag{A18}$$

and we obtain

$$\sigma(\omega_{pr} = \omega_{dr} - \omega_H)$$

$$\approx \frac{-i\epsilon_\infty\epsilon_0\gamma_H\omega_H^2\left[(\omega_{dr}-\omega_H)^2 - \omega_J^2 + i\gamma_J(\omega_{dr}-\omega_H)\right]^2\left[(\omega_{dr}^2 - \omega_J^2)^2 + \gamma_J^2\omega_{dr}^2\right](\omega_{dr}-\omega_H)^{-1}}{\gamma_H\omega_H^2\left[(\omega_{dr}-\omega_H)^2 - \omega_J^2 + i\gamma_J(\omega_{dr}-\omega_H)\right]\left[(\omega_{dr}^2 - \omega_J^2) + \gamma_J^2\omega_{dr}^2\right] - 4\alpha\omega_J^4|j_{dr}|^2(\gamma_H - 2i\omega_H)}, \tag{A19}$$

with the original pump amplitude $j_{dr} = \lambda j_{dr,1}$. Taking $j_{dr} = 0$ leads to the equilibrium solution

$$\sigma_1(\omega_{pr} = \omega_{dr} - \omega_H) = \epsilon_\infty\epsilon_0\gamma_J. \tag{A20}$$

for the real part of the conductivity. In the above calculation, ω_{pr} is formally negative for $\omega_{dr} < \omega_H$. However, our analytical prediction has the property that $\sigma_1(\omega_{pr}) = \sigma_1(-\omega_{pr})$, as characteristic for Fourier transforms of real quantities. In Fig. 6, the real part of the conductivity at $\omega_{pr} = \omega_{dr} - \omega_H$ is displayed as a function of the pump frequency according to our analytical estimate in Eq. (A19). The field strength E_0 of the applied electric field gives rise to the pump amplitude $|j_{dr}| = ed\omega_{dr}E_0/\hbar\epsilon_\infty$. Consistent with the numerical results, we find a negative conductivity when the pump frequency is slightly blue-detuned from the Higgs frequency. On the other hand, the conductivity is positive for red-detuned pump frequencies. A quantitative comparison to the numerical results reveals notable deviations, which are due to the approximations made in the derivation of Eq. (A19).

APPENDIX B: EQUATIONS OF MOTION FOR THE THREE-DIMENSIONAL LATTICE GAUGE MODEL

Including damping terms and thermal fluctuations, the equations of motion read

$$\partial_t^2\psi_\mathbf{r} = \frac{1}{K\hbar^2}\frac{\partial\mathcal{L}}{\partial\psi_\mathbf{r}^*} - \gamma_H\partial_t\psi_\mathbf{r} + \xi_\mathbf{r}, \tag{B1}$$

$$\partial_t^2 A_{x,\mathbf{r}} = \frac{1}{\epsilon_{ab}\epsilon_0}\frac{\partial\mathcal{L}}{\partial A_{x,\mathbf{r}}} - \gamma_{ab}\partial_t A_{x,\mathbf{r}} + \eta_{x,\mathbf{r}}, \tag{B2}$$
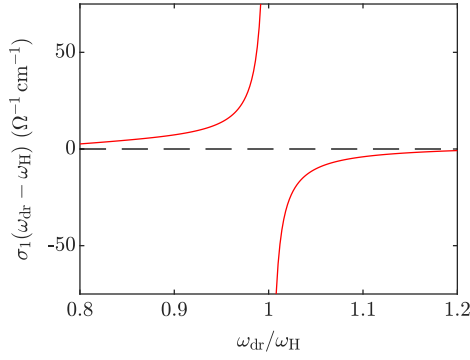
FIG. 6. Analytical estimate of the optical conductivity of a monolayer cuprate, in which Josephson plasma oscillations are optically driven. The negative conductivity for $\omega_{dr} \gtrsim \omega_H$ indicates the Higgs mode mediated amplification of terahertz radiation. As in Fig. 2, the Josephson plasma frequency is $\omega_J/2\pi = 2$ THz and the Higgs frequency is $\omega_H/2\pi = 6$ THz. The remaining parameters are $E_0 = 300$ kV/cm, $\gamma_J/2\pi = 0.25$ THz, $\gamma_H/2\pi = 1$ THz, $\alpha = 1$, $\epsilon_\infty = 4$, and $d = 10$ Å.

$$\partial_t^2 A_{y,\mathbf{r}} = \frac{1}{\epsilon_{ab}\epsilon_0} \frac{\partial \mathcal{L}}{\partial A_{y,\mathbf{r}}} - \gamma_{ab} \partial_t A_{y,\mathbf{r}} + \eta_{y,\mathbf{r}}, \quad \text{(B3)}$$

$$\partial_t^2 A_{z,\mathbf{r}} = \frac{1}{\kappa_{z,\mathbf{r}}\epsilon_{z,\mathbf{r}}\epsilon_0} \frac{\partial \mathcal{L}}{\partial A_{z,\mathbf{r}}} - \gamma_{z,\mathbf{r}} \partial_t A_{z,\mathbf{r}} + \eta_{z,\mathbf{r}}, \quad \text{(B4)}$$

where $\xi_{\mathbf{r}}$ and $\boldsymbol{\eta}_{\mathbf{r}}$ represent the thermal fluctuations of the superconducting order parameter and the vector potential, respectively. These Langevin noise terms have a white Gaussian

distribution with zero mean. The damping coefficients of the intra- and interbilayer electric fields are γ_s and γ_w, respectively. To satisfy the fluctuation-dissipation theorem, we take the noise of the order parameter as

$$\langle \text{Re}\{\xi_{\mathbf{r}}(t)\} \text{Re}\{\xi_{\mathbf{r}'}(t')\} \rangle = \frac{\gamma_H k_B T}{K \hbar^2 V_0} \delta_{\mathbf{rr}'} \delta(t - t'), \quad \text{(B5)}$$

$$\langle \text{Im}\{\xi_{\mathbf{r}}(t)\} \text{Im}\{\xi_{\mathbf{r}'}(t')\} \rangle = \frac{\gamma_H k_B T}{K \hbar^2 V_0} \delta_{\mathbf{rr}'} \delta(t - t'), \quad \text{(B6)}$$

$$\langle \text{Re}\{\xi_{\mathbf{r}}(t)\} \text{Im}\{\xi_{\mathbf{r}'}(t')\} \rangle = 0, \quad \text{(B7)}$$

where $V_0 = d_{ab}^2 d_c$. The noise correlations for the vector potential are

$$\langle \eta_{x,\mathbf{r}}(t) \eta_{x,\mathbf{r}'}(t') \rangle = \frac{2\gamma_{ab} k_B T}{\epsilon_{ab}\epsilon_0 V_0} \delta_{\mathbf{rr}'} \delta(t - t'), \quad \text{(B8)}$$

$$\langle \eta_{y,\mathbf{r}}(t) \eta_{y,\mathbf{r}'}(t') \rangle = \frac{2\gamma_{ab} k_B T}{\epsilon_{ab}\epsilon_0 V_0} \delta_{\mathbf{rr}'} \delta(t - t'), \quad \text{(B9)}$$

$$\langle \eta_{z,\mathbf{r}}(t) \eta_{z,\mathbf{r}'}(t') \rangle = \frac{2\gamma_{z,\mathbf{r}} k_B T}{\kappa_{z,\mathbf{r}}\epsilon_{z,\mathbf{r}}\epsilon_0 V_0} \delta_{\mathbf{rr}'} \delta(t - t'). \quad \text{(B10)}$$

APPENDIX C: SIMULATION PARAMETERS OF THE BILAYER CUPRATE

In this work, we simulate a bilayer cuprate with $40 \times 40 \times 4$ sites, choosing the parameters summarized in Table I. Our choice of μ and g implies an equilibrium condensate density $n_0 = \mu/g = 2 \times 10^{21}$ cm^{-3} at $T = 0$. The bilayer system has two longitudinal c-axis plasma modes. Their eigenfrequencies are

$$\omega_{J1,J2}^2 = \left(\frac{1}{2} + \alpha_s\right)\Omega_s^2 + \left(\frac{1}{2} + \alpha_w\right)\Omega_w^2 \mp \sqrt{\left[\left(\frac{1}{2} + \alpha_s\right)\Omega_s^2 - \left(\frac{1}{2} + \alpha_w\right)\Omega_w^2\right]^2 + 4\alpha_s\alpha_w\Omega_s^2\Omega_w^2}, \quad \text{(C1)}$$

as follows from a sine-Gordon analysis [28,29]. Here we introduced the bare plasma frequencies of the strong and weak junctions

$$\Omega_{s,w} = \sqrt{\frac{8t_{s,w} n_0 e^2 d_c d_{s,w}}{\epsilon_{s,w}\epsilon_0 \hbar^2}}, \quad \text{(C2)}$$

where $d_c = (d_s + d_w)/2$. The capacitive coupling constants are given by

$$\alpha_{s,w} = \frac{\epsilon_{s,w}\epsilon_0}{8K n_0 e^2 d_c d_{s,w}}. \quad \text{(C3)}$$

Besides, there is a transverse c-axis plasma mode with the eigenfrequency

$$\omega_T^2 = \frac{1 + 2\alpha_s + 2\alpha_w}{\alpha_s + \alpha_w}\left(\alpha_s\Omega_s^2 + \alpha_w\Omega_w^2\right). \quad \text{(C4)}$$

We have $\alpha_s \approx 1.5$, $\alpha_w \approx 3.0$, $\omega_{J1}/2\pi \approx 2.0$ THz, $\omega_{J2}/2\pi \approx 14.3$ THz, and $\omega_T/2\pi \approx 13.2$ THz for the parameters specified in Table I.

The in-plane plasma frequency is

$$\omega_{ab} = \sqrt{\frac{8t_{ab} n_0 e^2 d_{ab}^2}{\epsilon_{ab}\epsilon_0 \hbar^2}} \approx 2\pi \times 70 \text{ THz}, \quad \text{(C5)}$$

and the Higgs frequency is

$$\omega_H = \sqrt{\frac{2\mu}{K\hbar^2}} \approx 2\pi \times 6.1 \text{ THz}. \quad \text{(C6)}$$

TABLE I. Model parameters of the simulated bilayer cuprate.

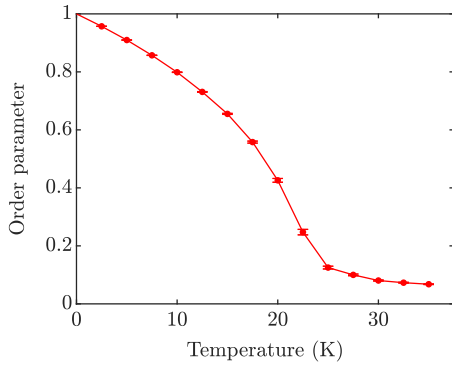|	
K (meV^{-1})	1.9×10^{-5}
μ (meV)	6.0×10^{-3}
g (meV Å^3)	3.0
$\gamma_H/2\pi$ (THz)	1.0
$\gamma_{ab}/2\pi$ (THz)	7.0
$\gamma_s/2\pi$ (THz)	1.5
$\gamma_w/2\pi$ (THz)	0.25
ϵ_{ab}	4
ϵ_s	2
ϵ_w	8
d_{ab} (Å)	15
d_s (Å)	4
d_w (Å)	8
t_{ab} (meV)	5.2×10^{-1}
t_s (meV)	2.4×10^{-2}
t_w (meV)	1.7×10^{-3}

FIG. 7. Phase transition of a bilayer cuprate with $40 \times 40 \times 4$ sites and the parameters specified in Table I. The error bars indicate the standard errors of the ensemble averages.

The average background dielectric constant along the c axis is

$$\epsilon_\infty = \frac{(d_s + d_w)\epsilon_s \epsilon_w}{d_s \epsilon_w + d_w \epsilon_s} = 4. \tag{C7}$$

APPENDIX D: THERMAL PHASE TRANSITION

The thermal equilibrium at a given temperature is established as follows. We initialize the system in its ground state at $T = 0$ and let the dynamics evolve without external driving, influenced only by thermal fluctuations and dissipation. To characterize the phase transition, we introduce the order parameter

$$O = \frac{2 \left| \sum_{\{\mathbf{r},\mathbf{r}'\} \in \text{inter}} \psi_{\mathbf{r}'}^* \psi_{\mathbf{r}} \, e^{i a_{z,\mathbf{r}}} \right|}{\sum_{\mathbf{r}} |\psi_{\mathbf{r}}|^2}. \tag{D1}$$

The sum in the numerator is taken over all interbilayer bonds, with site $\mathbf{r}$ in the lower layer. Thus the order parameter measures the gauge-invariant phase coherence of the condensate across different bilayers. In our simulations, this quantity converges to a constant after 10 ps of free time evolution, indicating the onset of thermal equilibrium. For each trajectory, the order parameter is evaluated from the average of

200 measurements within a time interval of 2 ps. Finally, we take the ensemble average of 100 trajectories. As depicted in Fig. 7, the temperature dependence of the order parameter is reminiscent of a second order phase transition. Due to the finite size of the simulated system, the order parameter converges to a plateau with nonzero value for high temperatures. At $T_c \sim 25$ K, there is a distinct crossover.

APPENDIX E: DEPENDENCE OF PHONON MEDIATED AMPLIFICATION ON THE PUMP AND PROBE STRENGTHS

Figure 8(a) displays the reflectivity of a bilayer cuprate, corresponding to the examples of phonon mediated amplification of terahertz radiation in Fig. 4(b). While the pump frequencies are the same, the modulation amplitudes of the interlayer tunneling coefficients are larger here.

Next, we investigate the dependence of the reflectivity on the probe strength. As one can see in Fig. 8(b), the results for $E_{\text{pr}} = 1$ kV/cm and $E_{\text{pr}} = 30$ kV/cm are in very good agreement. There is only a small deviation close to the maximum. This demonstrates that these probe strengths correspond to the linear response regime. For higher probe strenths, however, the amplification peak in the reflectivity decreases and the plasma edge is shifted to lower frequencies. Remarkably, the reflectivity still exceeds 1 for probe frequencies slightly above 1 THz when the probe strength reaches 100 kV/cm.

APPENDIX F: SAMPLE HEATING

Here, we estimate an upper limit for the heating of the sample by a pump pulse. We consider a cubic YBCO sample with a volume of 1 mm^3, corresponding to $N \approx 10^{-5}$ mol. The specific heat capacity of YBCO at 20 K is $C \approx 4$ J mol^{-1}K^{-1} [56]. If an entire face of the sample is irradiated by a laser with a fluence of $u = 20$ mJ cm^{-2} [19], the sample can absorb energy up to an amount of $U = 0.2$ mJ. Assuming that all the energy is dissipated and converted into heat, we find a temperature increase of

$$\Delta T = \frac{U}{CN} \approx 5 \text{ K}. \tag{F1}$$
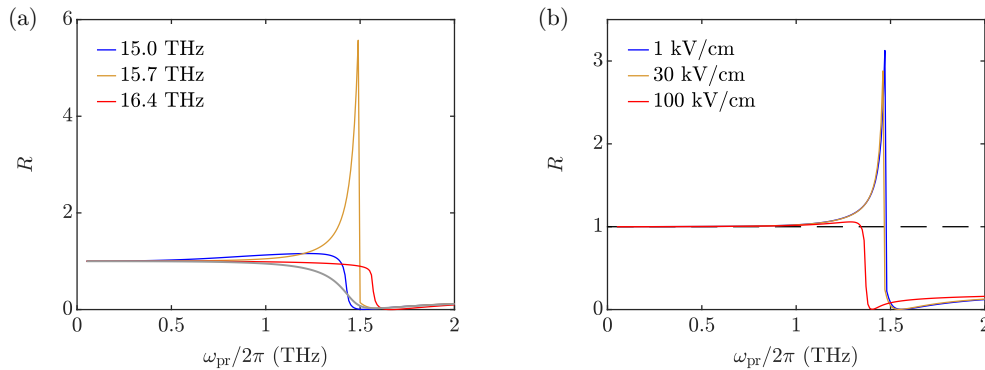
FIG. 8. Reflectivity of a bilayer cuprate in the presence of a phonon mediated pump at $T = 0$. (a) Reflectivity at normal incidence for different pump frequencies. The modulation amplitudes of the interlayer tunneling coefficients are $\Lambda_s = 0.3$ and $\Lambda_w = 1$. The gray line corresponds to the undriven case. (b) Reflectivity at normal incidence for different probe strengths. The pump frequency is $\omega_{\text{dr}}/2\pi = 15.7$ THz, and the modulation amplitudes are $\Lambda_s = 0.2$ and $\Lambda_w = 0.8$. See Sec. C for model parameters.

For a material with $T_c \sim 90$ K, this would be a moderate effect. Due to the finite penetration depth of the pump, the surface of the sample generally heats up disproportionately. Experimental observations on various cuprates indicate robustness against surface heating for pump pulses with a field strength of ~ 1 MV/cm and a duration of a few hundred femtoseconds [54,55,57].

[1] B. Ferguson and X. C. Zhang, Materials for terahertz science and technology, Nat. Mater. **1**, 26 (2002).

[2] M. Tonouchi, Cutting-edge terahertz technology, Nat. Photonics **1**, 97 (2007).

[3] E. Pickwell and V. P. Wallace, Biomedical applications of terahertz technology, J. Phys. D: Appl. Phys. **39**, R301 (2006).

[4] H. Y. Hwang, S. Fleischer, N. C. Brandt, B. G. P., Jr., M. Liu, K. Fan, A. Sternbach, X. Zhang, R. D. Averitt, and K. A. Nelson, A review of non-linear terahertz spectroscopy with ultrashort tabletop-laser pulses, J. Mod. Opt. **62**, 1447 (2015).

[5] D. M. Mittleman, Twenty years of terahertz imaging, Opt. Express **26**, 9417 (2018).

[6] B. S. Williams, Terahertz quantum-cascade lasers, Nat. Photonics **1**, 517 (2007).

[7] S. Kumar, Recent progress in terahertz quantum cascade lasers, IEEE J. Sel. Top. Quantum Electron. **17**, 38 (2011).

[8] M. Asada, S. Suzuki, and N. Kishimoto, Resonant tunneling diodes for sub-terahertz and terahertz oscillators, Jpn. J. Appl. Phys. **47**, 4375 (2008).

[9] M. Feiginov, H. Kanaya, S. Suzuki, and M. Asada, Operation of resonant-tunneling diodes with strong back injection from the collector at frequencies up to 1.46 THz, Appl. Phys. Lett. **104**, 243509 (2014).

[10] L. Ozyuzer, A. E. Koshelev, C. Kurter, N. Gopalsami, Q. Li, M. Tachiki, K. Kadowaki, T. Yamamoto, H. Minami, H. Yamaguchi, T. Tachiki, K. E. Gray, W. K. Kwok, and U. Welp, Emission of coherent THz radiation from superconductors, Science **318**, 1291 (2007).

[11] U. Welp, K. Kadowaki, and R. Kleiner, Superconducting emitters of THz radiation, Nat. Photonics **7**, 702 (2013).

[12] I. Kakeya and H. Wang, Terahertz-wave emission from Bi2212 intrinsic Josephson junctions: A review on recent progress, Supercond. Sci. Technol. **29**, 073001 (2016).

[13] R. Kleiner and H. Wang, Terahertz emission from $Bi_2Sr_2CaCu_2O_{8+x}$ intrinsic Josephson junction stacks, J. Appl. Phys. **126**, 171101 (2019).

[14] R. Cattaneo, E. A. Borodianskyi, A. A. Kalenyuk, and V. M. Krasnov, Superconducting Terahertz Sources with 12% Power Efficiency, Phys. Rev. Applied **16**, L061001 (2021).

[15] J. A. Giordmaine and R. C. Miller, Tunable Coherent Parametric Oscillation in $LiNbO_3$ at Optical Frequencies, Phys. Rev. Lett. **14**, 973 (1965).

[16] S. A. Akhmanov, A. I. Kovrigin, A. S. Piskarskas, V. V. Fadeev, and R. V. Khokhlov, Observation of parametric amplification in the optical range, JETP Lett. **2**, 191 (1965).

[17] F. Duarte, *Tunable Laser Applications*, 3rd ed. (CRC Press, Boca Raton, 2016).

[18] M. Buzzi, G. Jotzu, A. Cavalleri, J. I. Cirac, E. A. Demler, B. I. Halperin, M. D. Lukin, T. Shi, Y. Wang, and D. Podolsky, Higgs-Mediated Optical Amplification in a Nonequilibrium Superconductor, Phys. Rev. X **11**, 011055 (2021).

[19] M. Budden, T. Gebert, M. Buzzi, G. Jotzu, E. Wang, T. Matsuyama, G. Meier, Y. Laplace, D. Pontiroli, M. Riccò, F. Schlawin, D. Jaksch, and A. Cavalleri, Evidence for metastable photo-induced superconductivity in K_3C_{60}, Nat. Phys. **17**, 611 (2021).

[20] G. Homann, J. G. Cosme, and L. Mathey, Higgs time crystal in a high-T_c superconductor, Phys. Rev. Research **2**, 043214 (2020).

[21] G. Homann, J. G. Cosme, J. Okamoto, and L. Mathey, Higgs mode mediated enhancement of interlayer transport in high-T_c cuprate superconductors, Phys. Rev. B **103**, 224503 (2021).

[22] G. Chiriacò, A. J. Millis, and I. L. Aleiner, Transient superconductivity without superconductivity, Phys. Rev. B **98**, 220510(R) (2018).

[23] A. Cartella, T. F. Nova, M. Fechner, R. Merlin, and A. Cavalleri, Parametric amplification of optical phonons, Proc. Natl. Acad. Sci. USA **115**, 12148 (2018).

[24] S. Sugiura, E. A. Demler, M. Lukin, and D. Podolsky, Resonantly enhanced polariton wave mixing and Floquet parametric instability, arXiv:1910.03582 [physics.optics].

[25] L. Broers and L. Mathey, Observing light-induced Floquet band gaps in the longitudinal conductivity of graphene, Commun. Phys. **4**, 248 (2021).

[26] M. H. Michael, M. Först, D. Nicoletti, S. R. U. Haque, A. Cavalleri, R. D. Averitt, D. Podolsky, and E. Demler, Generalized Fresnel-Floquet equations for driven quantum materials, arXiv:2110.03704 [cond-mat.str-el].

[27] T. Koyama and M. Tachiki, *I-V* characteristics of Josephson-coupled layered superconductors with longitudinal plasma excitations, Phys. Rev. B **54**, 16183 (1996).

[28] D. van der Marel and A. A. Tsvetkov, Transverse-optical Josephson plasmons: Equations of motion, Phys. Rev. B **64**, 024530 (2001).

[29] T. Koyama, Josephson plasma resonances and optical properties in high-T_c superconductors with alternating junction parameters, J. Phys. Soc. Jpn. **71**, 2986 (2002).

[30] D. Dulić, A. Pimenov, D. van der Marel, D. M. Broun, S. Kamal, W. N. Hardy, A. A. Tsvetkov, I. M. Sutjaha, R. Liang, A. A. Menovsky, A. Loidl, and S. S. Saxena, Observation of the Transverse Optical Plasmon in $SmLa_{0.8}Sr_{0.2}CuO_{4-\delta}$, Phys. Rev. Lett. **86**, 4144 (2001).

[31] H. Shibata and T. Yamada, Double Josephson Plasma Resonance in T^* Phase $SmLa_{1-x}Sr_xCuO_{4-\delta}$, Phys. Rev. Lett. **81**, 3519 (1998).

[32] R. Matsunaga, N. Tsuji, H. Fujita, A. Sugioka, K. Makise, Y. Uzawa, H. Terai, Z. Wang, H. Aoki, and R. Shimano, Light-induced collective pseudospin precession resonating with Higgs mode in a superconductor, Science **345**, 1145 (2014).

[33] N. Tsuji and H. Aoki, Theory of Anderson pseudospin resonance with Higgs mode in superconductors, Phys. Rev. B **92**, 064508 (2015).

[34] K. Katsumi, N. Tsuji, Y. I. Hamada, R. Matsunaga, J. Schneeloch, R. D. Zhong, G. D. Gu, H. Aoki, Y. Gallais,

and R. Shimano, Higgs Mode in the d-Wave Superconductor Bi$_2$Sr$_2$CaCu$_2$O$_{8+x}$ Driven by an Intense Terahertz Pulse, Phys. Rev. Lett. **120**, 117001 (2018).

[35] H. Chu, M.-J. Kim, K. Katsumi, S. Kovalev, R. D. Dawson, L. Schwarz, N. Yoshikawa, G. Kim, D. Putzky, Z. Z. Li, H. Raffy, S. Germanskiy, J.-C. Deinert, N. Awari, I. Ilyakov, B. Green, M. Chen, M. Bawatna, G. Christiani, G. Logvenov *et al.*, Phase-resolved Higgs response in superconducting cuprates, Nat. Commun. **11**, 1793 (2020).

[36] R. Shimano and N. Tsuji, Higgs mode in superconductors, Annu. Rev. Condens. Matter Phys. **11**, 103 (2020).

[37] L. Schwarz and D. Manske, Theory of driven Higgs oscillations and third-harmonic generation in unconventional superconductors, Phys. Rev. B **101**, 184519 (2020).

[38] G. Seibold, M. Udina, C. Castellani, and L. Benfatto, Third harmonic generation from collective modes in disordered superconductors, Phys. Rev. B **103**, 014512 (2021).

[39] C. M. Varma, Higgs boson in superconductors, J. Low Temp. Phys. **126**, 901 (2002).

[40] D. Pekker and C. Varma, Amplitude/Higgs modes in condensed matter physics, Annu. Rev. Condens. Matter Phys. **6**, 269 (2015).

[41] M. Machida and T. Koyama, Localized rotating-modes in capacitively coupled intrinsic Josephson junctions: Systematic study of branching structure and collective dynamical instability, Phys. Rev. B **70**, 024523 (2004).

[42] B. Josephson, Possible new effects in superconductive tunnelling, Phys. Lett. **1**, 251 (1962).

[43] J. Skaar, Fresnel equations and the refractive index of active media, Phys. Rev. E **73**, 026605 (2006).

[44] B. Nistad and J. Skaar, Causality and electromagnetic properties of active media, Phys. Rev. E **78**, 036603 (2008).

[45] F. Peronaci, M. Schiró, and M. Capone, Transient Dynamics of d-Wave Superconductors after a Sudden Excitation, Phys. Rev. Lett. **115**, 257001 (2015).

[46] R. Mankowsky, A. Subedi, M. Först, S. O. Mariager, M. Chollet, H. T. Lemke, J. S. Robinson, J. M. Glownia, M. P. Minitti, A. Frano, M. Fechner, N. A. Spaldin, T. Loew, B. Keimer, A. Georges, and A. Cavalleri, Nonlinear lattice dynamics as a basis for enhanced superconductivity in YBa$_2$Cu$_3$O$_{6.5}$, Nature (London) **516**, 71 (2014).

[47] R. Mankowsky, M. Först, T. Loew, J. Porras, B. Keimer, and A. Cavalleri, Coherent modulation of the YBa$_2$Cu$_3$o$_{6+x}$ atomic structure by displacive stimulated ionic raman scattering, Phys. Rev. B **91**, 094308 (2015).

[48] S. J. Denny, S. R. Clark, Y. Laplace, A. Cavalleri, and D. Jaksch, Proposed Parametric Cooling of Bilayer Cuprate Superconductors by Terahertz Excitation, Phys. Rev. Lett. **114**, 137001 (2015).

[49] J.-i. Okamoto, A. Cavalleri, and L. Mathey, Theory of Enhanced Interlayer Tunneling in Optically Driven High-T_c Superconductors, Phys. Rev. Lett. **117**, 227001 (2016).

[50] J.-i. Okamoto, W. Hu, A. Cavalleri, and L. Mathey, Transiently enhanced interlayer tunneling in optically driven high-T_c superconductors, Phys. Rev. B **96**, 144505 (2017).

[51] M. H. Michael, A. von Hoegen, M. Fechner, M. Först, A. Cavalleri, and E. Demler, Parametric resonance of Josephson plasma waves: A theory for optically amplified interlayer superconductivity in YBa$_2$Cu$_3$O$_{6+x}$, Phys. Rev. B **102**, 174505 (2020).

[52] V. L. Ginzburg and L. D. Landau, On the theory of superconductivity, Zh. Eksp. Teor. Fiz. **20**, 1064 (1950).

[53] D. N. Basov and T. Timusk, Electrodynamics of high-T_c superconductors, Rev. Mod. Phys. **77**, 721 (2005).

[54] W. Hu, S. Kaiser, D. Nicoletti, C. R. Hunt, I. Gierz, M. C. Hoffmann, M. Le Tacon, T. Loew, B. Keimer, and A. Cavalleri, Optically enhanced coherent transport in YBa$_2$Cu$_3$O$_{6.5}$ by ultrafast redistribution of interlayer coupling, Nat. Mater. **13**, 705 (2014).

[55] S. Kaiser, C. R. Hunt, D. Nicoletti, W. Hu, I. Gierz, H. Y. Liu, M. Le Tacon, T. Loew, D. Haug, B. Keimer, and A. Cavalleri, Optically induced coherent transport far above T_c in underdoped YBa$_2$Cu$_3$O$_{6+\delta}$, Phys. Rev. B **89**, 184516 (2014).

[56] J. W. Loram, K. A. Mirza, J. R. Cooper, and W. Y. Liang, Electronic Specific Heat of YBa$_2$Cu$_3$O$_{6+x}$ from 1.8 to 300 K, Phys. Rev. Lett. **71**, 1740 (1993).

[57] K. A. Cremin, J. Zhang, C. C. Homes, G. D. Gu, Z. Sun, M. M. Fogler, A. J. Millis, D. N. Basov, and R. D. Averitt, Photoenhanced metastable c-axis electrodynamics in stripe-ordered cuprate La$_{1.885}$Ba$_{0.115}$CuO$_4$, Proc. Natl. Acad. Sci. USA **116**, 19875 (2019).

D.4 Parametric control of Meissner screening in light-driven superconductors

New Journal of Physics

The open access journal at the forefront of physics

PAPER

Parametric control of Meissner screening in light-driven superconductors

Guido Homann[1,*] ⓘ **, Jayson G Cosme**[2] ⓘ **and Ludwig Mathey**[1,3]

1 Zentrum für Optische Quantentechnologien und Institut für Laserphysik, Universität Hamburg, 22761 Hamburg, Germany
2 National Institute of Physics, University of the Philippines, Diliman, Quezon City 1101, The Philippines
3 The Hamburg Centre for Ultrafast Imaging, Luruper Chaussee 149, 22761 Hamburg, Germany
* Author to whom any correspondence should be addressed.

E-mail: ghomann@physnet.uni-hamburg.de

Abstract

We investigate the Meissner effect in a parametrically driven superconductor using a semiclassical $U(1)$ lattice gauge theory. Specifically, we periodically drive the z-axis tunneling, which leads to an enhancement of the imaginary part of the z-axis conductivity at low frequencies if the driving frequency is blue-detuned from the plasma frequency. This has been proposed as a possible mechanism for light-enhanced interlayer transport in $YBa_2C_3O_{7-\delta}$ (YBCO). In contrast to this enhancement of the conductivity, we find that the screening of magnetic fields is less effective than in equilibrium for blue-detuned driving, while it displays a tendency to be enhanced for red-detuned driving.

1. Introduction

Optical driving of solids opens up the possibility to induce superconducting-like features in their response to electric fields. This was first achieved in several cuprates by the excitation of specific phonon modes [1, 2] or near-infrared excitation [3, 4]. Later, signatures of a superconducting state were induced in fullerides and organic salts by exciting molecular vibrations [5–7]. In all these experiments, the imaginary part $\sigma_2(\omega)$ of the optical conductivity exhibited a $1/\omega$ divergence at low frequencies following optical excitation at temperatures above the equilibrium critical temperature T_c. In the case of YBCO, an enhancement of the low-frequency conductivity $\sigma_2(\omega)$ along the c axis was also observed below T_c [2, 8]. Several mechanisms have been proposed to explain the enhancement of interlayer transport, including nonlinear lattice dynamics [9], parametric driving [10–13], and suppression of competing orders [14, 15]. While the transient optical response of the light-driven cuprates and organic materials is consistent with enhanced or induced superconducting states, their response to magnetic fields has remained largely unexplored. That is due to the limited lifetimes of the excited states, which make experimental measurements of the magnetic response challenging [16]. Therefore, it is an open question whether the experimental observations of the light-induced transport properties indeed correspond to light-enhanced or light-induced superconductivity in the sense of an enhanced Meissner effect [17–21].

In this paper, we theoretically study the Meissner effect in a parametrically driven superconductor (SC). We consider a specific mechanism of parametric driving, where the Cooper pair tunneling along the z axis is periodically modulated in time [12, 22]. This type of driving enhances the imaginary part of the optical conductivity along the z axis at low frequencies. Based on analytical and numerical calculations, we find that the screening of DC magnetic fields is less effective than in equilibrium for slightly blue-detuned driving. This is due to the generation of electromagnetic waves by the parametric driving. For red-detuned parametric driving, there is no transmission of electromagnetic waves into the bulk and the Meissner screening is enhanced on a length scale that depends on the driving strength and the driving frequency at the order of our analytical investigation. The enhancement of the Meissner screening is particularly effective

Figure 1. Magnetic and optical probing of a SC. (a) Setup of the lattice gauge simulation with a fixed magnetic field at the surface. The order parameter is located on the lattice sites, while the vector potential is defined on the bonds. (b) The *z*-axis optical conductivity is measured by applying a spatially uniform probe current and setting $B_{\mathrm{ext}} = 0$.
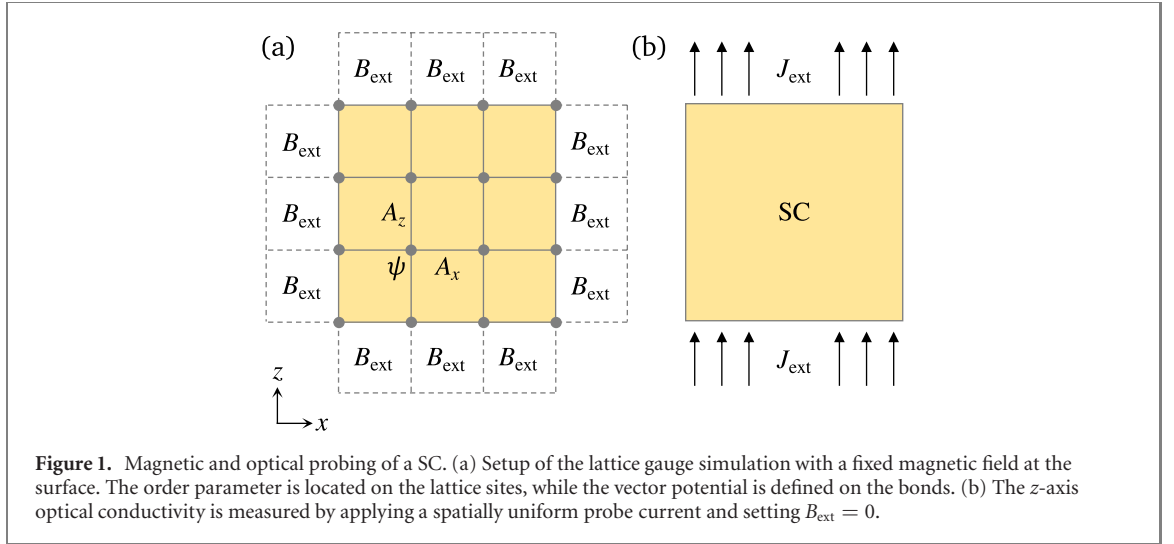
when the driving frequency is close to the plasma frequency. Notably, the imaginary part of the optical conductivity is reduced in this regime of driving frequencies.

This paper is organized as follows. After introducing our semiclassical method in section 2, we discuss the optical conductivity of a parametrically driven SC in section 3. In section 4, we first investigate the Meissner effect in a parametrically driven SC from an analytical perspective. Furthermore, we present numerical results for parametrically driven SCs with isotropic and anisotropic lattice parameters. We conclude this work in section 5.

2. Method

Here, we give an overview of the semiclassical $U(1)$ lattice gauge theory that we utilize to simulate the dynamics of a parametrically driven SC [23–25]. The static part of the Lagrangian is the Ginzburg–Landau free energy [26] on a three-dimensional lattice. As depicted in figure 1(a), the superconducting order parameter $\psi_{\mathbf{r}}(t)$ is located on the sites of a cubic lattice with lattice constant d, where $\mathbf{r} = (x, y, z)$ is the lattice site. The components of the electromagnetic vector potential $A_{j,\mathbf{r}}(t)$ are defined on the lattice bonds, which connect each site $\mathbf{r}$ with its nearest neighbor in the $j \in \{x, y, z\}$ direction. We employ the temporal gauge such that the electric field components are calculated according to $E_{j,\mathbf{r}} = -\partial_t A_{j,\mathbf{r}}$. The magnetic field components $B_{j,\mathbf{r}} = \epsilon_{jkl}(A_{l,\mathbf{r}'(k)} - A_{l,\mathbf{r}})/d$ are found on the lattice plaquettes, with $\mathbf{r}'(k)$ as the neighboring site of $\mathbf{r}$ in the k direction.

The Lagrangian of the lattice gauge model is

$$\mathcal{L} = \sum_{\mathbf{r}} K\hbar^2 |\partial_t \psi_{\mathbf{r}}|^2 + \mu|\psi_{\mathbf{r}}|^2 - \frac{g}{2}|\psi_{\mathbf{r}}|^4 - \sum_{j,\mathbf{r}} t_j |\psi_{\mathbf{r}'(j)} - \psi_{\mathbf{r}}\, \mathrm{e}^{i a_{j,\mathbf{r}}}|^2$$

$$+ \sum_{j,\mathbf{r}} \frac{\epsilon_0}{2} E_{j,\mathbf{r}}^2 - \frac{\hbar^2}{4\mu_0 e^2 d^4}\left[1 - \cos\left(\frac{2e d^2}{\hbar} B_{j,\mathbf{r}}\right)\right], \tag{1}$$

where μ and g are the Ginzburg–Landau coefficients and the coefficient K describes the magnitude of the dynamical term [27, 28]. The dynamical term is of the form $|\partial_t \psi_{\mathbf{r}}|^2$, which supports the particle-hole symmetry of the Lagrangian, i.e. $\mathcal{L}$ is invariant under $\psi_{\mathbf{r}} \to \psi_{\mathbf{r}}^*$ and $e \to -e$. The coupling of the unitless vector potential $a_{j,\mathbf{r}} = -2ed A_{j,\mathbf{r}}/\hbar$ to the phase of the order parameter ensures the local gauge-invariance of the Lagrangian. Note that the charge of a Cooper pair is $-2e$. The tunneling coefficients $t_x = t_y = t_{xy}$ and t_z determine the plasma frequencies of the SC,

$$\omega_j = \sqrt{\frac{8 t_j n_0 e^2 d^2}{\epsilon_0 \hbar^2}}, \tag{2}$$

with the equilibrium Cooper pair density $n_0 = \mu/g$. The SC is isotropic for $t_{xy} = t_z$ and anisotropic for $t_{xy} \neq t_z$.

We derive the Euler–Lagrange equations from equation (1) and include damping terms,

$$\partial_t^2 \psi_{\mathbf{r}} = \frac{1}{K\hbar^2}\frac{\partial \mathcal{L}}{\partial \psi_{\mathbf{r}}^*} - \gamma_{\mathrm{sc}}\partial_t \psi_{\mathbf{r}}, \tag{3}$$

$$\partial_t^2 A_{j,\mathbf{r}} = \frac{1}{\epsilon_0}\frac{\partial \mathcal{L}}{\partial A_{j,\mathbf{r}}} - \gamma_{\mathrm{el},j}\partial_t A_{j,\mathbf{r}}, \tag{4}$$

where γ_{sc} and $\gamma_{\mathrm{el},j}$ are phenomenological damping coefficients of the order parameter and the electric field, respectively. We note that these equations are the zero-temperature limit of the Langevin equations used in reference [25].

We numerically solve the equations of motion employing periodic boundary conditions along the y axis. With this boundary condition, we take the superconducting sample to be spatially homogeneous along the y axis, rather than having open boundary conditions. We assume open boundary conditions in the x and z direction and impose a spatially uniform magnetic field $\mathbf{B} = B_{\mathrm{ext}}\hat{\mathbf{y}}$ at the surfaces in x and z direction. For this purpose, we add one numerical layer outside the sample; see figure 1(a). On the external plaquettes, we fix the magnetic field to zero, ramp it up to a non-zero constant or specify a temporally oscillating value in the following. Thus, we model different physical scenarios. To simulate the vacuum, we set the order parameter and the tunneling coefficients to zero outside the sample. Inside the sample, we initialize the order parameter and the vector potential in the ground state, where $\psi_{\mathbf{r}} \equiv \sqrt{\mu/g}$ and $\mathbf{A}_{\mathbf{r}} \equiv 0$, and integrate the differential equations using Heun's method with a step size of $\Delta t = 2.5$ ns.

3. Conductivity of parametrically driven superconductors

We measure the optical conductivity by adding a weak probe current $J_{\mathrm{ext}}(t) = J_0 \cos(\omega_{\mathrm{pr}}t)$ to the equations of motion for the z component of the electric field,

$$\partial_t^2 A_{z,\mathbf{r}} = \frac{1}{\epsilon_0}\frac{\partial \mathcal{L}}{\partial A_{z,\mathbf{r}}} - \gamma_{\mathrm{el},z}\partial_t A_{z,\mathbf{r}} - \frac{J_{\mathrm{ext}}}{\epsilon_0}, \tag{5}$$

as depicted in figure 1(b). For this measurement, we fix the surface magnetic field to $B_{\mathrm{ext}} = 0$, neglecting radiation from the sample due to the probe current. Thus, the dynamics is spatially homogeneous along the x axis and independent of the sample width. The optical conductivity is $\sigma(\omega_{\mathrm{pr}}) = J_{\mathrm{ext}}(\omega_{\mathrm{pr}})/E(\omega_{\mathrm{pr}})$, where $E(\omega_{\mathrm{pr}})$ is the Fourier transform of the spatial average of the electric field in the steady state. Additionally, we drive the sample by periodically modulating the tunneling coefficients of all z-axis junctions,

$$t_z \to t_z[1 + M\cos(\omega_{\mathrm{dr}}t)]. \tag{6}$$

Experimentally, this could be achieved by resonantly exciting an infrared-active phonon mode; see references [2, 12, 22, 29].

The effect of this parametric driving on the imaginary part $\sigma_2(\omega_{\mathrm{pr}})$ of the z-axis conductivity is displayed in figure 2(a). While σ_2 is reduced for $\omega_{\mathrm{dr}} < \omega_{\mathrm{pl}}$ at probe frequencies $\omega_{\mathrm{pr}} \lesssim |\omega_{\mathrm{pl}} - \omega_{\mathrm{dr}}|$, it is enhanced for $\omega_{\mathrm{dr}} > \omega_{\mathrm{pl}}$. Figure 2(b) reveals that σ_2 approaches a $1/\omega_{\mathrm{pr}}$ behavior at low probe frequencies, regardless of whether the SC is driven or not. These results are consistent with the findings of references [12, 22]. To quantify the superconducting character of the optical response, we use the superconducting weight

$$D = \pi\big[\omega_{\mathrm{pr}}\sigma_2(\omega_{\mathrm{pr}})\big]_{\omega_{\mathrm{pr}}\to 0}, \tag{7}$$

following the definition given in reference [30]. For an infinitely large sample, the analytical expression for the superconducting weight is $D_0 = \pi\epsilon_0\omega_{\mathrm{pl}}^2$. An analytical prediction for the parametrically driven case was derived in reference [12],

$$D = D_0\left(1 - \frac{M^2\omega_{\mathrm{pl}}^2(\omega_{\mathrm{pl}}^2 - \omega_{\mathrm{dr}}^2)}{2(\omega_{\mathrm{pl}}^2 - \omega_{\mathrm{dr}}^2)^2 + 2\gamma_{\mathrm{el},z}^2\omega_{\mathrm{dr}}^2}\right). \tag{8}$$

As one can see in figure 2(b), our numerical results for $M = 0.3$ are in good agreement with this prediction. In the blue-detuned case of $\omega_{\mathrm{dr}} = 1.1\omega_{\mathrm{pl}}$, the superconducting weight is enhanced by approximately 17%. In the red-detuned case of $\omega_{\mathrm{dr}} = 0.9\omega_{\mathrm{pl}}$, the superconducting weight is reduced by approximately 19%. We note that the numerically-obtained conductivity σ_2 does not strictly follow the predicted $1/\omega_{\mathrm{pr}}$ behavior due to the insufficiently small probe frequencies and the finite sample size. The effect of parametric driving on the real part of the optical conductivity and the redistribution of spectral weight are discussed in the supplementary material.

Figure 2. Optical conductivity of a parametrically driven SC. (a) Imaginary part σ_2 of the optical conductivity. (b) σ_2 multiplied by the probe frequency. The dashed lines indicate the analytical prediction for the superconducting weight, which corresponds to the zero-frequency limit of $\pi\omega_{\mathrm{pr}}\sigma_2(\omega_{\mathrm{pr}})$. The z-axis tunneling coefficient is driven with the frequency $\omega_{\mathrm{dr}} = 0.9\omega_{\mathrm{pl}}$ in the red-detuned case and with the frequency $\omega_{\mathrm{dr}} = 1.1\omega_{\mathrm{pl}}$ in the blue-detuned case. The driving strength is $M = 0.3$ in both cases. The plasma frequency is $\omega_{\mathrm{pl}}/2\pi = 100$ THz and the sample height is 100 μm; see supplementary material for the full parameter set (isotropic sample).

4. Meissner screening in parametrically driven superconductors

4.1. Analytical results

The magnetic response of the parametrically driven SC can be understood from an analytical perspective. We suppose that the bottom left corner of the SC has the coordinates $x = 0$ and $z = 0$. First, we derive an approximate equation for the dynamics of the magnetic field close to the center of the left surface, i.e. for $x \ll L_x$ and $z = L_z/2$, where L_x and L_z are the edge lengths of the SC in x and z direction, respectively. According to our semiclassical $U(1)$ gauge theory, the supercurrent density along the z axis is given by

$$J_{z,\mathbf{r}}^{(\mathrm{sup})} = \frac{2t_z e d}{i\hbar} \left(\psi_{\mathbf{r}'(z)}^* \psi_{\mathbf{r}} \, \mathrm{e}^{i a_{z,\mathbf{r}}} - \mathrm{c.c.} \right)[1 + M \cos(\omega_{\mathrm{dr}}t)]. \tag{9}$$

Neglecting fluctuations of the superconducting order parameter, this can be simplified to

$$J_{z,\mathbf{r}}^{(\mathrm{sup})} \approx \frac{4t_z n_0 e d}{\hbar} \sin(a_{z,\mathbf{r}})[1 + M \cos(\omega_{\mathrm{dr}}t)]. \tag{10}$$

In the previous step, we fixed the gauge such that $\arg(\psi_{\mathbf{r}}) \equiv 0$, which complies with the temporal gauge in a charge neutral system. For weak fields, we linearize the above expression and rewrite it using the expression for the plasma frequency ω_{pl} from equation (2),

$$J_{z,\mathbf{r}}^{(\mathrm{sup})} \approx -\epsilon_0 \omega_{\mathrm{pl}}^2 A_{z,\mathbf{r}}[1 + M \cos(\omega_{\mathrm{dr}}t)]. \tag{11}$$

In the following, we treat **A** and **J** as continuous fields and drop the subscript **r**. As $A_x \sim J_x = 0$ for $z = L_z/2$, the magnetic field is given by $B_y = -\partial_x A_z$. Neglecting the current contribution from the damping term, we obtain

$$\nabla \times \mathbf{J} \approx -\epsilon_0 \omega_{\mathrm{pl}}^2[1 + M \cos(\omega_{\mathrm{dr}}t)]B_y\hat{\mathbf{y}} \tag{12}$$

for the curl of the free current density. On the other hand, Maxwell's equations imply

$$\frac{1}{\mu_0}\left(\frac{1}{c^2}\partial_t^2 - \nabla^2\right)\mathbf{B} = \nabla \times \mathbf{J}. \tag{13}$$

Combining equations (12) and (13) yields the minimal model

$$\partial_t^2 B_y + \omega_{\mathrm{pl}}^2[1 + M \cos(\omega_{\mathrm{dr}}t)]B_y \approx c^2 \partial_x^2 B_y, \tag{14}$$

as $\partial_z^2 B_y \ll \partial_x^2 B_y$ for $x \ll L_x$ and $z = L_z/2$. For $M \ll 1$, we use the ansatz

$$B_y(x,t) = B_0(x) + B_1(x)\cos(\omega_{\mathrm{dr}}t) + B_2(x)\sin(\omega_{\mathrm{dr}}t). \tag{15}$$

This leads to

$$\partial_x^2 B_0 = \frac{1}{\lambda^2}\left(B_0 + \frac{M}{2}B_1\right),\tag{16}$$

$$\partial_x^2 B_1 = \frac{1}{\lambda^2}\left(1 - \frac{\omega_{\mathrm{dr}}^2}{\omega_{\mathrm{pl}}^2}\right)B_1 + \frac{M}{\lambda^2}B_0,\tag{17}$$

$$\partial_x^2 B_2 = \frac{1}{\lambda^2}\left(1 - \frac{\omega_{\mathrm{dr}}^2}{\omega_{\mathrm{pl}}^2}\right)B_2,\tag{18}$$

where $\lambda = c/\omega_{\mathrm{pl}}$ is the London penetration depth of the undriven SC. To determine $B_0(x)$ and $B_1(x)$, we use the ansatz

$$B_0 = b_0\, \mathrm{e}^{-x/\ell},\tag{19}$$

$$B_1 = b_1\, \mathrm{e}^{-x/\ell}.\tag{20}$$

The solutions for B_0 and B_1 are superpositions of four exponentials with

$$\ell_{1,2} = \lambda\left(1 - \frac{\omega_{\mathrm{dr}}^2}{2\omega_{\mathrm{pl}}^2} \pm \sqrt{\frac{\omega_{\mathrm{dr}}^4}{4\omega_{\mathrm{pl}}^4} + \frac{M^2}{2}}\right)^{-1/2},\quad \ell_{3,4} = -\ell_{1,2}.\tag{21}$$

While ℓ_1 is generally real-valued and smaller than λ, ℓ_2 is real-valued only for $\omega_{\mathrm{dr}} \lesssim \omega_{\mathrm{pl}}$ and imaginary for $\omega_{\mathrm{dr}} > \omega_{\mathrm{pl}}$. The absolute value of ℓ_2 is larger than λ for $\omega_{\mathrm{dr}} \sim \omega_{\mathrm{pl}}$. The solution for $B_2(x)$ is of the form

$$B_2 = b_2\, \mathrm{e}^{-x/\ell_0},\tag{22}$$

where

$$\ell_0 = \pm\frac{\lambda}{\sqrt{1 - \omega_{\mathrm{dr}}^2/\omega_{\mathrm{pl}}^2}}\tag{23}$$

is real-valued for $\omega_{\mathrm{dr}} < \omega_{\mathrm{pl}}$ and imaginary for $\omega_{\mathrm{dr}} > \omega_{\mathrm{pl}}$.

In the red-detuned case of $\omega_{\mathrm{dr}} < \omega_{\mathrm{pl}}$, we exclude exponentially growing solutions and write the magnetic field inside the SC as

$$B_y^{(\mathrm{in})} = \beta_1\, \mathrm{e}^{-x/\ell_1} + \beta_2\, \mathrm{e}^{-x/\ell_2} + \frac{M\beta_1\, \mathrm{e}^{-x/\ell_1}\, \cos(\omega_{\mathrm{dr}}t)}{\omega_{\mathrm{dr}}^2/2\omega_{\mathrm{pl}}^2 + \sqrt{\omega_{\mathrm{dr}}^4/4\omega_{\mathrm{pl}}^4 + M^2/2}}$$

$$+ \frac{M\beta_2\, \mathrm{e}^{-x/\ell_2}\, \cos(\omega_{\mathrm{dr}}t)}{\omega_{\mathrm{dr}}^2/2\omega_{\mathrm{pl}}^2 - \sqrt{\omega_{\mathrm{dr}}^4/4\omega_{\mathrm{pl}}^4 + M^2/2}} + \beta_3\, \mathrm{e}^{-x/\ell_0}\, \sin(\omega_{\mathrm{dr}}t).\tag{24}$$

The corresponding electric field is

$$E_z^{(\mathrm{in})} = \int \partial_t B_y^{(\mathrm{in})}\mathrm{d}x$$

$$= \frac{\ell_1\omega_{\mathrm{dr}}M\beta_1\, \mathrm{e}^{-x/\ell_1}\, \sin(\omega_{\mathrm{dr}}t)}{\omega_{\mathrm{dr}}^2/2\omega_{\mathrm{pl}}^2 + \sqrt{\omega_{\mathrm{dr}}^4/4\omega_{\mathrm{pl}}^4 + M^2/2}} + \frac{\ell_2\omega_{\mathrm{dr}}M\beta_2\, \mathrm{e}^{-x/\ell_2}\, \sin(\omega_{\mathrm{dr}}t)}{\omega_{\mathrm{dr}}^2/2\omega_{\mathrm{pl}}^2 - \sqrt{\omega_{\mathrm{dr}}^4/4\omega_{\mathrm{pl}}^4 + M^2/2}} - \ell_0\omega_{\mathrm{dr}}\beta_3\, \mathrm{e}^{-x/\ell_0}\, \cos(\omega_{\mathrm{dr}}t).$$

$$\tag{25}$$

We note that red-detuned parametric driving induces an AC contribution to the magnetic field, which is less effectively screened than the DC magnetic field. For blue-detuned parametric driving, the induced AC part of the magnetic field leads to the formation of two standing waves. As these standing waves are induced at the surface, we use the ansatz

$$B_y^{(\mathrm{in})} = \beta_1\, \mathrm{e}^{-x/\ell_1} + \beta_2\, \cos(x/|\ell_2|) + \frac{M\beta_1\, \mathrm{e}^{-x/\ell_1}\, \cos(\omega_{\mathrm{dr}}t)}{\omega_{\mathrm{dr}}^2/2\omega_{\mathrm{pl}}^2 + \sqrt{\omega_{\mathrm{dr}}^4/4\omega_{\mathrm{pl}}^4 + M^2/2}}$$

$$+ \frac{M\beta_2\, \cos(x/|\ell_2|)\, \cos(\omega_{\mathrm{dr}}t)}{\omega_{\mathrm{dr}}^2/2\omega_{\mathrm{pl}}^2 - \sqrt{\omega_{\mathrm{dr}}^4/4\omega_{\mathrm{pl}}^4 + M^2/2}} + \beta_3\, \cos(x/|\ell_0|)\sin(\omega_{\mathrm{dr}}t)\tag{26}$$

for $\omega_{dr} > \omega_{pl}$. The electric field has the form

$$E_z^{(in)} = \int \partial_t B_y^{(in)} dx$$

$$= \frac{\ell_1 \omega_{dr} M \beta_1 \, e^{-x/\ell_1} \, \sin(\omega_{dr} t)}{\omega_{dr}^2 / 2\omega_{pl}^2 + \sqrt{\omega_{dr}^4 / 4\omega_{pl}^4 + M^2/2}} - \frac{|\ell_2| \omega_{dr} M \beta_2 \, \sin(x/|\ell_2|) \, \sin(\omega_{dr} t)}{\omega_{dr}^2 / 2\omega_{pl}^2 - \sqrt{\omega_{dr}^4 / 4\omega_{pl}^4 + M^2/2}}$$

$$+ |\ell_0| \omega_{dr} \beta_3 \, \sin(x/|\ell_0|) \cos(\omega_{dr} t). \tag{27}$$

In general, parametric driving of a SC in the presence of a magnetic field causes emission of electromagnetic waves. Here, we consider the emission of electromagnetic waves from the left edge of the sample,

$$B_y^{(out)} = B_{ext} + \alpha_1 \, \cos(\omega_{dr}(t + x/c)) + \alpha_2 \, \sin(\omega_{dr}(t + x/c)), \tag{28}$$

$$E_z^{(out)} = c\alpha_1 \, \cos(\omega_{dr}(t + x/c)) + c\alpha_2 \, \sin(\omega_{dr}(t + x/c)). \tag{29}$$

Using the continuity of $B_y(x, t)$ and $E_z(x, t)$ at the surface of the sample, we determine the coefficients β_1, β_2 and β_3; see supplementary material for details of the calculation. In the red-detuned case, we obtain

$$\beta_1 = \frac{B_{ext}}{\zeta} \left(1 + \frac{\ell_2 \ell_0 \omega_{dr}^2}{c^2}\right) \left(\frac{\omega_{dr}^2}{2\omega_{pl}^2} + \sqrt{\frac{\omega_{dr}^4}{4\omega_{pl}^4} + \frac{M^2}{2}}\right), \tag{30}$$

$$\beta_2 = -\frac{B_{ext}}{\zeta} \left(1 + \frac{\ell_1 \ell_0 \omega_{dr}^2}{c^2}\right) \left(\frac{\omega_{dr}^2}{2\omega_{pl}^2} - \sqrt{\frac{\omega_{dr}^4}{4\omega_{pl}^4} + \frac{M^2}{2}}\right), \tag{31}$$

$$\beta_3 = \frac{\omega_{dr} M B_{ext}}{\zeta c}(\ell_1 - \ell_2), \tag{32}$$

where

$$\zeta = \left(1 + \frac{\ell_2 \ell_0 \omega_{dr}^2}{c^2}\right) \left(\frac{\omega_{dr}^2}{2\omega_{pl}^2} + \sqrt{\frac{\omega_{dr}^4}{4\omega_{pl}^4} + \frac{M^2}{2}}\right) - \left(1 + \frac{\ell_1 \ell_0 \omega_{dr}^2}{c^2}\right) \left(\frac{\omega_{dr}^2}{2\omega_{pl}^2} - \sqrt{\frac{\omega_{dr}^4}{4\omega_{pl}^4} + \frac{M^2}{2}}\right). \tag{33}$$

In the blue-detuned case, we find

$$\beta_1 = \frac{B_{ext}}{2} \left(1 + \frac{\omega_{dr}^2 / 2\omega_{pl}^2}{\sqrt{\omega_{dr}^4 / 4\omega_{pl}^4 + M^2/2}}\right), \tag{34}$$

$$\beta_2 = \frac{B_{ext}}{2} \left(1 - \frac{\omega_{dr}^2 / 2\omega_{pl}^2}{\sqrt{\omega_{dr}^4 / 4\omega_{pl}^4 + M^2/2}}\right), \tag{35}$$

$$\beta_3 = \frac{B_{ext}}{2c} \frac{\ell_1 \omega_{dr} M}{\sqrt{\omega_{dr}^4 / 4\omega_{pl}^4 + M^2/2}}. \tag{36}$$

In figures 3(a) and (b), we show how red- and blue-detuned driving modifies the spatial dependence of the DC magnetic field inside the SC. In the red-detuned case, the DC part of the magnetic field is the sum of two exponentially decaying contributions. As the driving frequency approaches the plasma frequency, the length scale of the first decay converges to a value below the equilibrium penetration depth,

$$\ell_1 \to \frac{\lambda}{\sqrt{1 + M^2/2}}. \tag{37}$$

This feature of the response by itself indicates a parametric enhancement of the Meissner screening. However, the length scale ℓ_2 of the second exponential decay is generally larger than the equilibrium penetration depth. Thus, the enhancement of the Meissner screening is lessened or reverted. While ℓ_2 diverges for $\omega_{dr} \to \omega_{pl}$, the prefactor of the second exponential decay vanishes in this limit. Taking both into account, the Meissner screening is enhanced as the driving frequency is slightly below the plasma frequency. For larger detuning, the enhanced screening is effective only on a short length scale. Further away from the surface, the slower decaying contribution dominates such that the DC magnetic field is larger than in the absence of driving. This is visible in figure 3(a).

Figure 3. Analytical results for the Meissner screening in a parametrically driven SC. (a) Spatial dependence of the DC magnetic field for $M = 0.3$ and two different red-detuned driving frequencies. (b) Spatial dependence of the DC magnetic field for $M = 0.3$ and two different blue-detuned driving frequencies. (c) Attenuation length R_x of the DC magnetic field as a function of the driving frequency for two different driving strengths. In panels (a) and (b), the equilibrium magnetic field $B_{eq} = B_{ext} \exp(-x/\lambda)$ is subtracted, where λ is the London penetration depth.

For blue-detuned driving, the DC part of the magnetic field is the sum of a contribution that decays exponentially on the length scale $\ell_1 < \lambda$ and a spatially oscillating contribution. As evidenced by figure 3(b), the spatially oscillating contribution reduces the Meissner screening such that the DC magnetic field is larger than in the absence of driving. In the supplementary material, we present the spatial dependence of the DC magnetic field explicitly, using a higher driving amplitude of $M = 0.6$.

Figure 3(c) displays the attenuation length of the magnetic field as a function of the driving frequency for blue-detuned driving. The attenuation length is defined by the condition $B_y(x = R_x) = B_{ext} \exp(-1)$. While the attenuation length equals the London penetration depth in equilibrium, it is increased by slightly blue-detuned driving. The attenuation length grows as the detuning of the driving frequency from the plasma frequency is decreased and the driving strength is increased.
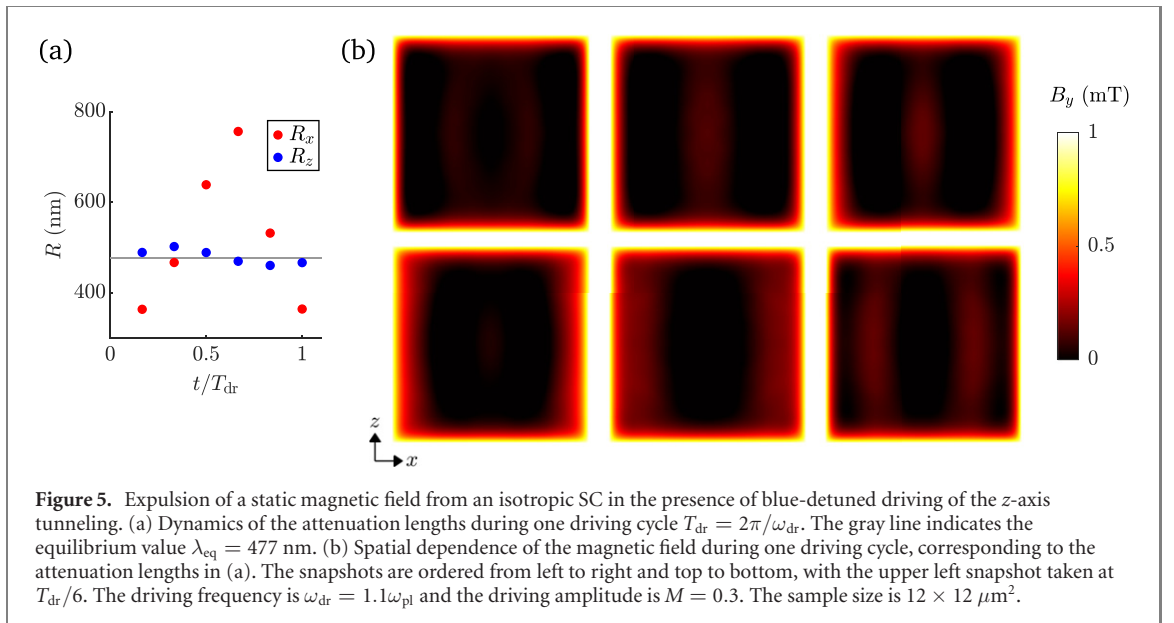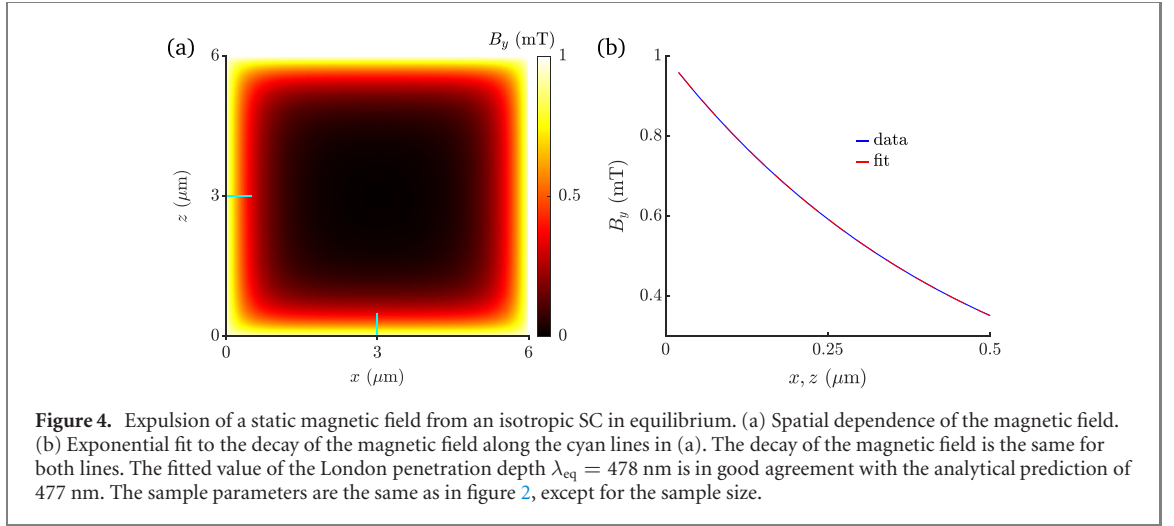
In our simulations, we apply a static magnetic field at the surface of the SC. The analytical solution for this boundary condition is provided in the supplementary material. We find that the solution for the DC magnetic field inside the SC is not affected in the case of blue-detuned driving. However, the modified boundary condition suppresses the enhancement regime for red-detuned driving.

4.2. Numerical results for an isotropic superconductor

To simulate the Meissner effect, we apply a small surface magnetic field along the y axis, i.e. $\mathbf{B} = B_{ext}\hat{\mathbf{y}}$. Throughout this paper, we use $B_{ext} = 1$ mT. Note that we obtain consistent results for $B_{ext} = 0.1$ mT, which confirms that the linear response is measured. In figure 4, we present equilibrium results for an isotropic SC with the same parameters as in section 3, except for the sample size. The plasma frequency is $\omega_{pl}/2\pi = 100$ THz and the edge length is $L = 6\ \mu$m along both axes. We see in figure 4(a) that the magnetic field $B_y(x, z)$ is screened away from the surface, which is the characteristic response of a SC to a magnetic field. As shown in figure 4(b), the decay of the magnetic field from the sample surfaces is well captured by the exponential fit functions $B_y(x, 0) = B_{ext} \exp(-x/\lambda_{eq})$ and $B_y(0, z) = B_{ext} \exp(-z/\lambda_{eq})$, with λ_{eq} being the only free parameter. The fitted value $\lambda_{eq} = 478$ nm of the London penetration depth is in excellent agreement with the analytical prediction $\lambda = c/\omega_{pl} = 477$ nm. In fact, the numerical value converges to the analytical prediction for larger sample size; see supplementary material.

In the remainder of this section, we investigate the response of an isotropic SC to an external magnetic field in the presence of parametric driving as defined in equation (6). We characterize the Meissner screening in the driven state by the attenuation lengths R_x and R_z. The attenuation length R_x quantifies the Meissner screening at the center of the left sample surface, i.e. for $x \ll L_x$ and $z = L_z/2$. To resolve changes of R_x below the discretization length d, we interpolate the magnetic field linearly between the plaquettes left and right of $x = R_x$. The attenuation length along the z axis, R_z, is determined analogously. In equilibrium, the attenuation lengths equal the London penetration depth, i.e. $R_x = R_z = \lambda_{eq}$.

We consider a superconducting sample with the same parameters as before but with a sample size of $12 \times 12\ \mu$m^2 to ensure the convergence of our results. First, we choose the driving frequency $\omega_{dr}/2\pi = 110$ THz and the driving amplitude $M = 0.3$, consistent with the conductivity measurements shown in figure 2. Once a steady state is reached, the magnetic field inside the SC oscillates with the driving frequency. Snapshots of the time evolution of the magnetic field during one driving cycle are displayed in figure 5(b). The parametric driving with $\omega_{dr} > \omega_{pl}$ has two main effects. Firstly, electromagnetic waves generated at the left and right surfaces are transmitted into the bulk of the sample. However, the magnitude

Figure 4. Expulsion of a static magnetic field from an isotropic SC in equilibrium. (a) Spatial dependence of the magnetic field. (b) Exponential fit to the decay of the magnetic field along the cyan lines in (a). The decay of the magnetic field is the same for both lines. The fitted value of the London penetration depth $\lambda_{eq} = 478$ nm is in good agreement with the analytical prediction of 477 nm. The sample parameters are the same as in figure 2, except for the sample size.

Figure 5. Expulsion of a static magnetic field from an isotropic SC in the presence of blue-detuned driving of the z-axis tunneling. (a) Dynamics of the attenuation lengths during one driving cycle $T_{dr} = 2\pi/\omega_{dr}$. The gray line indicates the equilibrium value $\lambda_{eq} = 477$ nm. (b) Spatial dependence of the magnetic field during one driving cycle, corresponding to the attenuation lengths in (a). The snapshots are ordered from left to right and top to bottom, with the upper left snapshot taken at $T_{dr}/6$. The driving frequency is $\omega_{dr} = 1.1\omega_{pl}$ and the driving amplitude is $M = 0.3$. The sample size is $12 \times 12\ \mu m^2$.

of the magnetic field inside the SC is strongly suppressed compared to the surface field B_{ext}. Secondly, the attenuation lengths are no longer isotropic and exhibit an oscillatory behavior in time. As evidenced by figure 5(a), R_x exhibits a pronounced oscillation, while R_z has a small oscillation amplitude. Remarkably, we find that there is no generation of electromagnetic waves for driving frequencies red-detuned from the plasma frequency. The time evolution of the magnetic field for one example of red-detuned driving is shown in the supplementary material.

Next, we average the magnetic field over 1 ps with a detection rate of 5 PHz and evaluate the attenuation lengths $R_x = 488$ nm and $R_z = 479$ nm of the time-averaged magnetic field. The attenuation lengths in the driven state are both larger than the equilibrium value $\lambda_{eq} = 477$ nm of this sample. So, while the parametric driving leads to a significant enhancement of z-axis transport, the time-averaged screening of magnetic fields is slightly reduced. This result also holds for larger sample size and AC magnetic fields with small frequencies $\sim$1 THz; see supplementary material. We note that the relative phase between the oscillation of R_x and the oscillation of R_z depends on the lateral sample size. This suggests that the modulation of R_z is due to the transmission of electromagnetic waves from the left and right surfaces.

We proceed by varying the driving strength and the driving frequency. Figure 6(a) demonstrates that the attenuation length R_x grows monotonically with increasing driving amplitude. The data points in figure 6(b) indicate a divergence of R_x as the driving frequency approaches the plasma frequency. We compare our numerical results to the analytical solution from section 4.1, applying the boundary condition of a static magnetic field at the sample surface. The numerical results show good agreement with the analytical solution, except for the data point at $\omega_{dr} = 1.3\omega_{pl}$. This discrepancy is due to the approximations that we used in the derivation of the analytical solution. For example, we neglected the spatial dependence

Figure 6. Attenuation length R_x of the time-averaged magnetic field for different driving strengths and frequencies. (a) R_x for $\omega_{dr} = 1.1\omega_{pl}$ and different driving strengths. (b) R_x for $M = 0.3$ and different driving frequencies. The gray line indicates the equilibrium value $\lambda_{eq} = 477$ nm. In both panels, the dashed red line indicates the analytical solution for R_x. The sample size is $12 \times 12\ \mu m^2$, except for the two largest driving frequencies in (b), where converged results are obtained for a sample size of $16 \times 16\ \mu m^2$.

Figure 7. Expulsion of a static magnetic field from an anisotropic SC in the presence of blue-detuned driving of the z-axis tunneling. (a) Attenuation lengths as a function of time during one driving cycle $T_{dr} = 2\pi/\omega_{dr}$. The gray lines indicate the equilibrium values λ_z and λ_x, and the dashed lines indicate the attenuation lengths of the time-averaged magnetic field in the driven state. (b) Spatial dependence of the magnetic field during one driving cycle, corresponding to the attenuation lengths in (a). The snapshots are ordered from left to right and top to bottom, with the upper left snapshot taken at $T_{dr}/6$. The driving frequency is $\omega_{dr} = 1.1\omega_z$ and the driving amplitude is $M = 0.3$. The sample size is $24 \times 6\ \mu m^2$.

of the magnetic field along the z axis and temporal oscillations at higher harmonics of the driving frequency. Thus, the analytical solution is valid only close to the sample surface and does not capture the propagation of electromagnetic waves in the case of blue-detuned driving.

4.3. Numerical results for an anisotropic superconductor

In this section, we study the effect of parametric driving on the magnetic response of an anisotropic SC. Since our analytical arguments in section 4.1 are not limited to an isotropic SC, we expect a similar reduction of the Meissner screening for an anisotropic SC. In cuprate SCs, the ratio between the in-plane plasma frequency and the (lower) c-axis plasma frequency is of the order of 100. Due to numerical constraints, we choose plasma frequencies with a smaller ratio. In the following, we consider a SC with the plasma frequencies $\omega_x/2\pi = 300$ THz and $\omega_z/2\pi = 50$ THz along the x axis and the z axis, respectively. Consistent with the relations $\lambda_x = c/\omega_x$ and $\lambda_z = c/\omega_z$, we find the attenuation lengths $R_x = \lambda_z = 954$ nm and $R_z = \lambda_x = 159$ nm in equilibrium. The sample size is $24 \times 6\ \mu m^2$.

We then add parametric driving with frequency $\omega_{dr}/2\pi = 55$ THz and amplitude $M = 0.3$. We show in figure 7(b) that the time evolution of the magnetic field during one driving cycle is comparable to the isotropic case. However, the spatial patterns are sharper and more pronounced, especially towards the top and bottom of the sample. While the oscillation amplitude of R_x compared to its temporal average is similar to the isotropic case, the oscillation amplitude of R_z is significantly larger as shown in figure 7(a). This

further indicates that the modulation of R_z is a consequence of electromagnetic waves transmitted into the bulk. Here, the attenuation lengths of the time-averaged magnetic field are $R_x = 977$ nm and $R_z = 161$ nm in the driven state. The increase of R_x by approximately 2% is in good agreement with our observation for an isotropic SC, where we also used $\omega_{dr} = 1.1\omega_z$ and $M = 0.3$. The increase of R_z by more than 1% is considerably larger than in the isotropic case.

5. Conclusion

In conclusion, we have presented the response of light-driven SCs to magnetic fields for the scenario of parametrically driven z-axis tunneling. For driving with a frequency blue-detuned from the plasma frequency, we find an enhancement of z-axis transport and a reduction of the Meissner screening along the x axis, the direction perpendicular to the parametric drive and the applied magnetic field. This key result is in contrast to the equilibrium behavior of SCs. In the absence of driving, both London theory [31] and our model in equation (1) predict that an enhancement of the low-frequency $\sigma_2(\omega)$ along the z axis implies an enhancement of the Meissner screening along the x axis. Our simulations demonstrate the breakdown of this general relation in a driven SC. In fact, the screening of DC magnetic fields is reduced for slightly blue-detuned driving, which can be understood analytically based on a minimal model that we derived in this work. According to our analytical calculations, the screening of DC magnetic fields shows a tendency to be enhanced for slightly red-detuned driving. This enhanced screening is enabled by emission of electromagnetic waves from the SC. If the emission of electromagnetic waves is suppressed, as in our simulations, the Meissner screening for red-detuned driving is generally less effective than in the absence of driving. We emphasize that we observe similar behavior for isotropic and anisotropic SCs.

Our findings suggest that the enhancement of the low-frequency conductivity is naturally accompanied by a suppression of the Meissner effect in the parametrically driven scenario that we consider. The parametric driving mixes the Josephson plasmon into the low-frequency response. While this admixture provides an enhanced conductivity, it results in a suppressed Meissner screening due to the transmission of unscreened plasma excitations into the SC. More generally, our results suggest that the light-induced state is a genuinely non-equilibrium state, rather than a renormalized equilibrium state, in which some of the reasoning derived from equilibrium SCs does not apply.

Our work is relevant for the interpretation of pump–probe experiments on light-driven SCs, particularly cuprates. An improved understanding of these experiments might eventually provide new insights into the nature of the superconducting state in unconventional SCs.

Acknowledgments

Data availability statement

The data that support the findings of this study are available upon reasonable request from the authors.

ORCID iDs

Guido Homann ⬤ https://orcid.org/0000-0002-3678-309X
Jayson G Cosme ⬤ https://orcid.org/0000-0001-9943-4711

References

[1] Fausti D *et al* 2011 Light-induced superconductivity in a stripe-ordered cuprate *Science* **331** 189
[2] Hu W *et al* 2014 Optically enhanced coherent transport in YBa$_2$Cu$_3$O$_{6.5}$ by ultrafast redistribution of interlayer coupling *Nat. Mater.* **13** 705–11
[3] Nicoletti D *et al* 2014 Optically induced superconductivity in striped La$_{2-x}$Ba$_x$CuO$_4$ by polarization-selective excitation in the near infrared *Phys. Rev.* B **90** 100503
[4] Cremin K A, Zhang J, Homes C C, Gu G D, Sun Z, Fogler M M, Millis A J, Basov D N and Averitt R D 2019 Photoenhanced metastable *c*-axis electrodynamics in stripe-ordered cuprate La$_{1.885}$Ba$_{0.115}$CuO$_4$ *Proc. Natl Acad. Sci. USA* **116** 19875–9
[5] Mitrano M *et al* 2016 Possible light-induced superconductivity in K$_3$C$_{60}$ at high temperature *Nature* **530** 461–4
[6] Budden M *et al* 2021 Evidence for metastable photo-induced superconductivity in K$_3$C$_{60}$ *Nat. Phys.* **17** 611–8

[7] Buzzi M *et al* 2020 Photomolecular high-temperature superconductivity *Phys. Rev. X* **10** 031028

[8] Kaiser S *et al* 2014 Optically induced coherent transport far above T_c in underdoped YBa$_2$Cu$_3$O$_{6+\delta}$ *Phys. Rev. B* **89** 184516

[9] Mankowsky R *et al* 2014 Nonlinear lattice dynamics as a basis for enhanced superconductivity in YBa$_2$Cu$_3$O$_{6.5}$ *Nature* **516** 71–3

[10] Denny S J, Clark S R, Laplace Y, Cavalleri A and Jaksch D 2015 Proposed parametric cooling of bilayer cuprate superconductors by terahertz excitation *Phys. Rev. Lett.* **114** 137001

[11] Höppner R, Zhu B, Rexin T, Cavalleri A and Mathey L 2015 Redistribution of phase fluctuations in a periodically driven cuprate superconductor *Phys. Rev. B* **91** 104507

[12] Okamoto J-i, Cavalleri A and Mathey L 2016 Theory of enhanced interlayer tunneling in optically driven high-T_c superconductors *Phys. Rev. Lett.* **117** 227001

[13] Michael M H, von Hoegen A, Fechner M, Först M, Cavalleri A and Demler E 2020 Parametric resonance of Josephson plasma waves: a theory for optically amplified interlayer superconductivity in YBa$_2$Cu$_3$O$_{6+x}$ *Phys. Rev. B* **102** 174505

[14] Raines Z M, Stanev V and Galitski V M 2015 Enhancement of superconductivity via periodic modulation in a three-dimensional model of cuprates *Phys. Rev. B* **91** 184506

[15] Patel A A and Eberlein A 2016 Light-induced enhancement of superconductivity via melting of competing bond-density wave order in underdoped cuprates *Phys. Rev. B* **93** 195139

[16] Paone D *et al* 2021 All-optical and microwave-free detection of Meissner screening using nitrogen-vacancy centers in diamond *J. Appl. Phys.* **129** 024306

[17] Chiriacò G, Millis A J and Aleiner I L 2018 Transient superconductivity without superconductivity *Phys. Rev. B* **98** 220510

[18] Bittner N, Tohyama T, Kaiser S and Manske D 2019 Possible light-induced superconductivity in a strongly correlated electron system *J. Phys. Soc. Japan* **88** 044704

[19] Paeckel S, Fauseweh B, Osterkorn A, Köhler T, Manske D and Manmana S R 2020 Detecting superconductivity out of equilibrium *Phys. Rev. B* **101** 180507

[20] Dai Z and Lee P A 2021 Superconductinglike response in a driven gapped bosonic system *Phys. Rev. B* **104** 054512

[21] Dai Z and Lee P A 2021 Superconducting-like response in driven systems near the Mott transition *Phys. Rev. B* **104** L241112

[22] Okamoto J-ichi, Hu W, Cavalleri A and Mathey L 2017 Transiently enhanced interlayer tunneling in optically driven high-T_c superconductors *Phys. Rev. B* **96** 144505

[23] Homann G, Cosme J G and Mathey L 2020 Higgs time crystal in a high-T_c superconductor *Phys. Rev. Res.* **2** 043214

[24] Homann G, Cosme J G, Okamoto J and Mathey L 2021 Higgs mode mediated enhancement of interlayer transport in high-T_c cuprate superconductors *Phys. Rev. B* **103** 224503

[25] Homann G, Cosme J G and Mathey L 2022 Terahertz amplifiers based on gain reflectivity in cuprate superconductors *Phys. Rev. Res.* **4** 013181

[26] Ginzburg V L and Landau L D 1950 On the theory of superconductivity *Zh. Eksp. Teor. Fiz.* **20** 1064

[27] Pekker D and Varma C M 2015 Amplitude/Higgs modes in condensed matter physics *Annu. Rev. Condens. Matter Phys.* **6** 269–97

[28] Shimano R and Tsuji N 2020 Higgs mode in superconductors *Annu. Rev. Condens. Matter Phys.* **11** 103–24

[29] Liu B, Först M, Fechner M, Nicoletti D, Porras J, Loew T, Keimer B and Cavalleri A 2020 Pump frequency resonances for light-induced incipient superconductivity in YBa$_2$Cu$_3$O$_{6.5}$ *Phys. Rev. X* **10** 011053

[30] Resta R 2018 Drude weight and superconducting weight *J. Phys.: Condens. Matter* **30** 414001

[31] London F and London H 1935 The electromagnetic equations of the supraconductor *Proc. R. Soc.* A **149** 71

Supplementary material for
Parametric control of Meissner screening in light-driven superconductors

Guido Homann,[1] Jayson G. Cosme,[2] and Ludwig Mathey[1,3]

[1]*Zentrum für Optische Quantentechnologien and Institut für Laserphysik,*
Universität Hamburg, 22761 Hamburg, Germany
[2]*National Institute of Physics, University of the Philippines,*
Diliman, Quezon City 1101, Philippines
[3]*The Hamburg Centre for Ultrafast Imaging,*
Luruper Chaussee 149, 22761 Hamburg, Germany

CONTENTS

I. REDISTRIBUTION OF SPECTRAL WEIGHT

As shown in Fig. 1, the real part σ_1 of the optical conductivity exhibits a maximum around $\omega^* = |\omega_{\mathrm{pl}} - \omega_{\mathrm{dr}}|$ for red-detuned driving, while it exhibits a minimum around ω^* for blue-detuned driving. These extrema of σ_1 correspond to parametric attenuation/amplification as discussed in Ref. [1]. Following the notation in Ref. [2], we write the optical conductivity as

$$\sigma(\omega) = D\left(\delta(\omega) + \frac{i}{\pi\omega}\right) + \sigma^{\mathrm{regular}}(\omega). \tag{1}$$

The total spectral weight is then given by

$$S = \int_0^\infty d\omega\, \sigma_1(\omega) = \frac{D}{2} + \int_0^\infty d\omega\, \sigma_1^{\mathrm{regular}}(\omega). \tag{2}$$

Here, we evaluate the spectral weight difference

$$\Delta W = \int_{\omega_a}^{\omega_b} d\omega\, \left(\sigma_1^{\mathrm{driven}}(\omega) - \sigma_1^{\mathrm{undriven}}(\omega)\right) \tag{3}$$

with $\omega_a/2\pi = 2$ THz and $\omega_b/2\pi = 100$ THz. For red-detuned driving, we find $\Delta W_{\mathrm{red}} \approx -0.84 \cdot (D_{\mathrm{red}} - D_0)/2$, while we obtain $\Delta W_{\mathrm{blue}} \approx -0.94 \cdot (D_{\mathrm{blue}} - D_0)/2$ for blue-detuned driving. Note that the absolute value of ΔW is underestimated in both cases due to the lower cutoff at ω_a. These results indicate that the parametric driving redistributes spectral weight, while the total spectral weight is conserved.
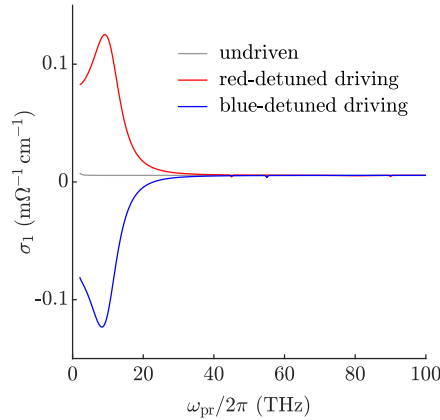

FIG. 1. Real part of the optical conductivity of a parametrically driven superconductor. The driving amplitude is $M = 0.3$. The driving frequencies are $\omega_{\mathrm{dr}} = 0.9\omega_{\mathrm{pl}}$ and $\omega_{\mathrm{dr}} = 1.1\omega_{\mathrm{pl}}$, consistent with Fig. 2 in the main text.

II. DETAILS ON THE ANALYTICAL SOLUTION

A. Emitting boundary condition

As mentioned in Section 4.1 of the main text, the electromagnetic waves emitted by the parametrically driven superconductor have the form

$$B_y^{(\text{out})} = B_{\text{ext}} + \alpha_1 \cos\big(\omega_{\text{dr}}(t + x/c)\big) + \alpha_2 \sin\big(\omega_{\text{dr}}(t + x/c)\big), \tag{4}$$

$$E_z^{(\text{out})} = c\alpha_1 \cos\big(\omega_{\text{dr}}(t + x/c)\big) + c\alpha_2 \sin\big(\omega_{\text{dr}}(t + x/c)\big). \tag{5}$$

For the magnetic and the electric field inside the superconductor, we use the general ansatz from Section 4.1 of the main text. In the red-detuned case, the continuity of $B_y(x,t)$ at $x = 0$ implies

$$B_{\text{ext}} = \beta_1 + \beta_2, \tag{6}$$

$$\alpha_1 = \frac{M\beta_1}{\omega_{\text{dr}}^2/2\omega_{\text{pl}}^2 + \sqrt{\omega_{\text{dr}}^4/4\omega_{\text{pl}}^4 + M^2/2}} + \frac{M\beta_2}{\omega_{\text{dr}}^2/2\omega_{\text{pl}}^2 - \sqrt{\omega_{\text{dr}}^4/4\omega_{\text{pl}}^4 + M^2/2}}, \tag{7}$$

$$\alpha_2 = \beta_3. \tag{8}$$

The continuity of $E_z(x,t)$ at $x = 0$ implies

$$c\alpha_1 = -\ell_0\omega_{\text{dr}}\beta_3, \tag{9}$$

$$c\alpha_2 = \frac{\ell_1\omega_{\text{dr}}M\beta_1}{\omega_{\text{dr}}^2/2\omega_{\text{pl}}^2 + \sqrt{\omega_{\text{dr}}^4/4\omega_{\text{pl}}^4 + M^2/2}} + \frac{\ell_2\omega_{\text{dr}}M\beta_2}{\omega_{\text{dr}}^2/2\omega_{\text{pl}}^2 - \sqrt{\omega_{\text{dr}}^4/4\omega_{\text{pl}}^4 + M^2/2}}. \tag{10}$$

Thus, we obtain

$$\beta_1 = \frac{B_{\text{ext}}}{\zeta}\left(1 + \frac{\ell_2\ell_0\omega_{\text{dr}}^2}{c^2}\right)\left(\frac{\omega_{\text{dr}}^2}{2\omega_{\text{pl}}^2} + \sqrt{\frac{\omega_{\text{dr}}^4}{4\omega_{\text{pl}}^4} + \frac{M^2}{2}}\right), \tag{11}$$

$$\beta_2 = -\frac{B_{\text{ext}}}{\zeta}\left(1 + \frac{\ell_1\ell_0\omega_{\text{dr}}^2}{c^2}\right)\left(\frac{\omega_{\text{dr}}^2}{2\omega_{\text{pl}}^2} - \sqrt{\frac{\omega_{\text{dr}}^4}{4\omega_{\text{pl}}^4} + \frac{M^2}{2}}\right), \tag{12}$$

$$\beta_3 = \frac{\omega_{\text{dr}}MB_{\text{ext}}}{\zeta c}\left(\ell_1 - \ell_2\right), \tag{13}$$

where

$$\zeta = \left(1 + \frac{\ell_2\ell_0\omega_{\text{dr}}^2}{c^2}\right)\left(\frac{\omega_{\text{dr}}^2}{2\omega_{\text{pl}}^2} + \sqrt{\frac{\omega_{\text{dr}}^4}{4\omega_{\text{pl}}^4} + \frac{M^2}{2}}\right) - \left(1 + \frac{\ell_1\ell_0\omega_{\text{dr}}^2}{c^2}\right)\left(\frac{\omega_{\text{dr}}^2}{2\omega_{\text{pl}}^2} - \sqrt{\frac{\omega_{\text{dr}}^4}{4\omega_{\text{pl}}^4} + \frac{M^2}{2}}\right). \tag{14}$$

3

In the blue-detuned case, the continuity of $B_y(x,t)$ at $x = 0$ implies

$$B_{\text{ext}} = \beta_1 + \beta_2, \tag{15}$$

$$\alpha_1 = \frac{M\beta_1}{\omega_{\text{dr}}^2/2\omega_{\text{pl}}^2 + \sqrt{\omega_{\text{dr}}^4/4\omega_{\text{pl}}^4 + M^2/2}} + \frac{M\beta_2}{\omega_{\text{dr}}^2/2\omega_{\text{pl}}^2 - \sqrt{\omega_{\text{dr}}^4/4\omega_{\text{pl}}^4 + M^2/2}}, \tag{16}$$

$$\alpha_2 = \beta_3. \tag{17}$$

The continuity of E_z at $x = 0$ implies

$$c\alpha_1 = 0, \tag{18}$$

$$c\alpha_2 = \frac{\ell_1 \omega_{\text{dr}} M \beta_1}{\omega_{\text{dr}}^2/2\omega_{\text{pl}}^2 + \sqrt{\omega_{\text{dr}}^4/4\omega_{\text{pl}}^4 + M^2/2}}. \tag{19}$$

We find

$$\beta_1 = \frac{B_{\text{ext}}}{2}\left(1 + \frac{\omega_{\text{dr}}^2/2\omega_{\text{pl}}^2}{\sqrt{\omega_{\text{dr}}^4/4\omega_{\text{pl}}^4 + M^2/2}}\right), \tag{20}$$

$$\beta_2 = \frac{B_{\text{ext}}}{2}\left(1 - \frac{\omega_{\text{dr}}^2/2\omega_{\text{pl}}^2}{\sqrt{\omega_{\text{dr}}^4/4\omega_{\text{pl}}^4 + M^2/2}}\right), \tag{21}$$

$$\beta_3 = \frac{\ell_1 \omega_{\text{dr}} M B_{\text{ext}}/c}{2\sqrt{\omega_{\text{dr}}^4/4\omega_{\text{pl}}^4 + M^2/2}}. \tag{22}$$

Figure 2 displays the analytical solution for the spatial dependence of the DC magnetic field explicitly. Here, the driving amplitude is chosen relatively high such that the effect of the parametric driving is visible.
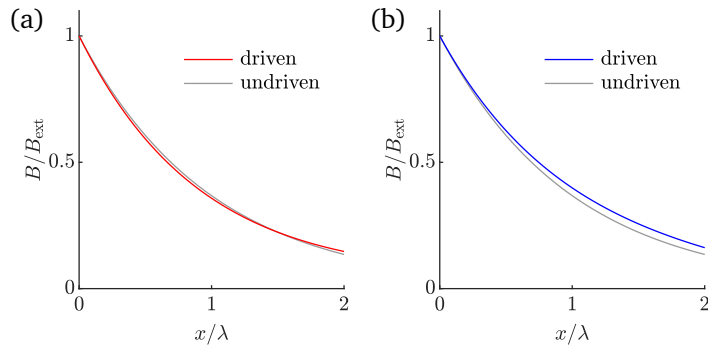

FIG. 2. Spatial dependence of the DC magnetic field for M = 0.6. (a) Red-detuned driving, $\omega_{\text{dr}} = 0.95\omega_{\text{pl}}$. (b) Blue-detuned driving, $\omega_{\text{dr}} = 1.05\omega_{\text{pl}}$.

4

B. Static boundary condition

For comparison with the numerical simulations, we apply the boundary condition $B_y(x = 0, t) = B_\text{ext}$. With the general ansatz for the magnetic field inside the superconductor from Section 4.1 of the main text, we then obtain

$$\beta_1 = \frac{B_\text{ext}}{2}\left(1 + \frac{\omega_\text{dr}^2/2\omega_\text{pl}^2}{\sqrt{\omega_\text{dr}^4/4\omega_\text{pl}^4 + M^2/2}}\right), \tag{23}$$

$$\beta_2 = \frac{B_\text{ext}}{2}\left(1 - \frac{\omega_\text{dr}^2/2\omega_\text{pl}^2}{\sqrt{\omega_\text{dr}^4/4\omega_\text{pl}^4 + M^2/2}}\right), \tag{24}$$

$$\beta_3 = 0 \tag{25}$$

for both red- and blue-detuned driving. In the case of blue-detuned driving, the DC part of the magnetic field is the same as for the emitting boundary condition considered in the previous section. For red-detuned driving, however, the modified boundary condition qualitatively changes the solution. In contrast to the emitting case, β_2 does not vanish in the limit of $\omega_\text{dr} \to \omega_\text{pl}$ such that the divergence of ℓ_2 implies a less effective Meissner screening than in the absence of driving; see Fig. 3. Our analytical results are in good agreement with the numerical simulations as evidenced by Fig. 6 in the main text.
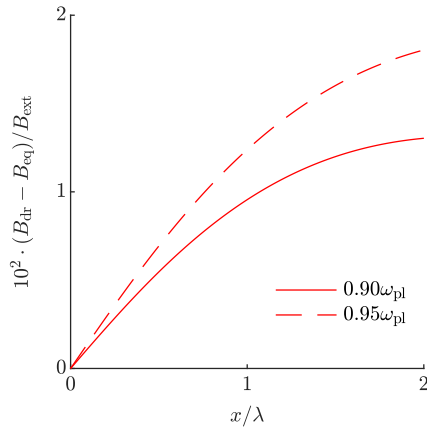

FIG. 3. Spatial dependence of the DC magnetic field for $M = 0.3$ and two different red-detuned driving frequencies, applying the boundary condition $B_y(x = 0, t) = B_\text{ext}$ to the analytical solution. The equilibrium magnetic field $B_\text{eq} = B_\text{ext}\exp(-x/\lambda)$ is subtracted, where λ is the London penetration depth.

TABLE I. Model parameters of the simulated superconductors. If a second value is provided, it refers to the anisotropic sample.

K (meV^{-1})	4.7×10^{-5}
μ (meV)	1.0×10^{-3}
g (meV Å^3)	0.5
d (Å)	200
$\gamma_{\mathrm{sc}}/2\pi$ (THz)	1
$\gamma_{\mathrm{el},xy}/2\pi$ (THz)	10, 30
$\gamma_{\mathrm{el},z}/2\pi$ (THz)	10, 5
t_{xy} (meV)	$1.48 \times 10^{-3}, 1.33 \times 10^{-2}$
t_z (meV)	$1.48 \times 10^{-3}, 3.7 \times 10^{-4}$

III. SIMULATION PARAMETERS

The parameters of the simulated superconductors are summarized in Table I. Our choice of μ and g implies a Cooper pair density of $n_0 = \mu/g = 2 \times 10^{21}$ cm^{-3} in equilibrium. The discretization length d is of the order of the Ginzburg-Landau estimate for the coherence length,

$$\xi = \sqrt{\frac{t_{xy}d^2}{\mu}} = \sqrt{\frac{t_z d^2}{\mu}} = 243 \text{ Å} \tag{26}$$

for the isotropic sample. The Higgs frequency is

$$\omega_{\mathrm{H}} = \sqrt{\frac{2\mu}{K\hbar^2}} = 2\pi \times 5 \text{ THz.} \tag{27}$$

IV. FINITE SIZE ANALYSIS

In the main text, we present results for a parametrically driven superconductor with a sample size of 12×12 μm^2. Here, we investigate the magnetic response of isotropic
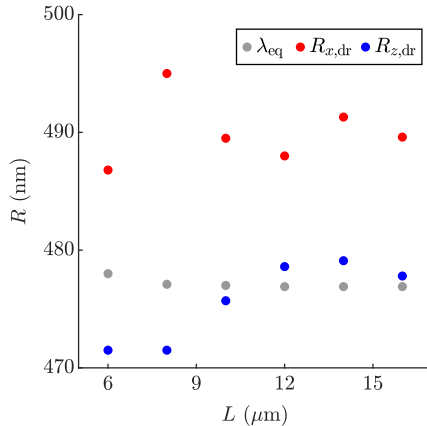
6

FIG. 4. Attenuation lengths of the time-averaged magnetic field in an isotropic superconductor for different sample sizes. In equilibrium, the attenuation length equals the London penetration depth λ_{eq}. The driving frequency is $\omega_{\mathrm{dr}} = 1.1\omega_{\mathrm{pl}}$ and the driving amplitude is $M = 0.3$.

superconductors with different sample sizes $L \times L$. As visible in Fig. 4, the value of the equilibrium penetration depth is fully converged for samples with a size of 12×12 $\mu\mathrm{m}^2$ or larger. In fact, the numerical result agrees with the analytical prediction of $\lambda = 477$ nm.

In the driven state, the values of the attenuation length R_x exhibit no systematic drift for large samples, varying between 488 and 491 nm for $L \geq 12$ μm. The values of the attenuation length R_z vary between 478 and 479 nm for $L \geq 12$ μm. We conclude that a sample with a size of 12×12 $\mu\mathrm{m}^2$ accurately reflects the magnetic response of large samples, both in equilibrium and in the presence of parametric driving.

V. TIME EVOLUTION OF THE MAGNETIC FIELD FOR RED-DETUNED DRIVING

In Fig. 5, we show the time evolution of the magnetic field for one example of parametric driving, in which the driving frequency is red-detuned from the plasma frequency. In stark contrast to the blue-detuned case shown in Fig. 5 in the main text, there is no visible transmission of electromagnetic waves from the left and right surfaces into the bulk of the sample. Thus, the modulation of R_z is negligible, while the oscillation of R_x is similar to the blue-detuned case.
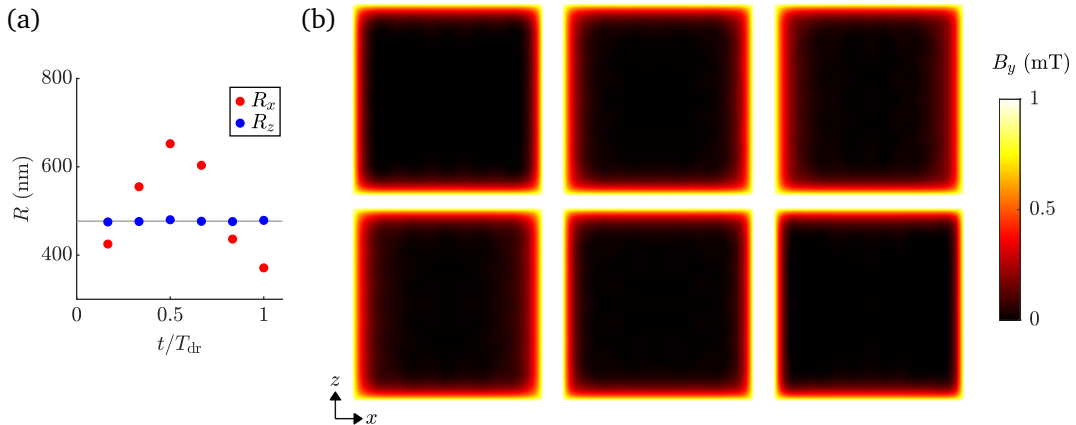
FIG. 5. Expulsion of a static magnetic field from an isotropic superconductor in the presence of red-detuned driving of the z-axis tunneling. (a) Attenuation lengths as a function of time during one driving cycle $T_{\mathrm{dr}} = 2\pi/\omega_{\mathrm{dr}}$. The gray line indicates the equilibrium value $\lambda_{\mathrm{eq}} = 477$ nm. (b) Spatial dependence of the magnetic field during one driving cycle, corresponding to the attenuation lengths in (a). The snapshots are ordered from left to right and top to bottom, with the upper left snapshot taken at $T_{\mathrm{dr}}/6$. The driving frequency is $\omega_{\mathrm{dr}} = 0.9\omega_{\mathrm{pl}}$ and the driving amplitude is $M = 0.3$. The sample size is $12 \times 12~\mu\mathrm{m}^2$.

VI. AC MEISSNER EFFECT IN A PARAMETRICALLY DRIVEN SUPERCONDUCTOR

Finally, we briefly discuss the response of a parametrically driven isotropic superconductor to AC magnetic fields, i.e., $B_{\mathrm{ext}} \to B_{\mathrm{ext}} \cos(\omega_{\mathrm{pr}}t)$. Once a steady state is reached, we record the time evolution of the magnetic field for 10 ps with a detection rate of 5 PHz. We then compute the Fourier transform of the magnetic field to evaluate the component of $B_y(x,z)$ that oscillates with the probe frequency ω_{pr}. Eventually, we determine the attenuation lengths R_x and R_z as in the case of a static magnetic field.

Figure 6 displays the attenuation lengths as a function of the probe frequency. Importantly, the attenuation lengths of an AC magnetic field with $\omega_{\mathrm{pr}}/2\pi = 1$ THz approach the attenuation lengths of a static magnetic field. Therefore, it is sufficient to probe the sample with a static magnetic field in order to obtain the low-frequency limit of its magnetic response. This is particularly relevant when comparing the magnetic response to the optical response in Section 3 of the main text. For increasing probe frequency, the equilibrium
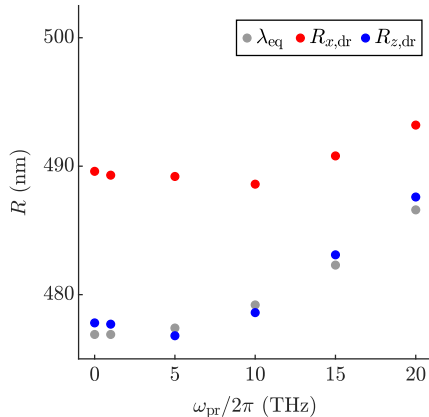
8

FIG. 6. Attenuation lengths of the time-averaged magnetic field for different probe frequencies. In equilibrium, the attenuation length equals the London penetration depth λ_{eq}. The driving frequency is $\omega_{\mathrm{dr}} = 1.1\omega_{\mathrm{pl}}$ and the driving amplitude is $M = 0.3$. The sample size is 16×16 $\mu\mathrm{m}^2$.

penetration depth also increases, which can be understood from an analytical perspective. As mentioned in Section 4.1 of the main text, Maxwell's equations imply

$$\frac{1}{\mu_0}\left(\frac{1}{c^2}\partial_t^2 - \nabla^2\right)\mathbf{B} = \nabla \times \mathbf{J}. \tag{28}$$

We insert the London equation $\nabla \times \mathbf{J} = -\mathbf{B}/(\mu_0\lambda^2)$ into Eq. (28), where λ is the London penetration depth of a static magnetic field. This leads to

$$-\left(\frac{1}{c^2}\partial_t^2 - \nabla^2\right)\mathbf{B} = \frac{1}{\lambda^2}\mathbf{B}, \tag{29}$$

implying

$$\lambda(\omega_{\mathrm{pr}}) = \frac{\lambda}{\sqrt{1 - \omega_{\mathrm{pr}}^2/\omega_{\mathrm{pl}}^2}}. \tag{30}$$

For example, the numerical value of $\lambda_{\mathrm{eq}} = 487$ nm for $\omega_{\mathrm{pr}}/2\pi = 20$ THz agrees with the analytical prediction based on Eq. (30). In the presence of parametric driving, the attenuation lengths follow a qualitatively similar dependence on the probe frequency as in equilibrium.

_____

[1] G. Homann, J. G. Cosme, and L. Mathey, Terahertz amplifiers based on gain reflectivity in cuprate superconductors, Phys. Rev. Research **4**, 013181 (2022).

[2] R. Resta, Drude weight and superconducting weight, J. Phys. Condens. Matter **30**, 414001 (2018).

Bibliography

[1] V. V. Schmidt, *The Physics of Superconductors*, Springer, Berlin (1997).

[2] M. Tinkham, *Introduction to Superconductivity*, Dover Publ., Mineola, NY, 2nd edn. (2004).

[3] K. Fossheim and A. Sudbø, *Superconductivity: Physics and Applications*, Wiley, Chichester (2004).

[4] C. Enss and S. Hunklinger, *Low-Temperature Physics*, Springer, Berlin (2005).

[5] A. J. Leggett, *Quantum Liquids: Bose condensation and Cooper pairing in condensed-matter systems*, Oxford Univ. Press, Oxford (2006).

[6] A. K. Saxena, *High-Temperature Superconductors*, Springer, Berlin, 2nd edn. (2012).

[7] H. K. Onnes, *The resistance of pure mercury at helium temperatures*, Commun. Phys. Lab. Univ. Leiden **12**, 120 (1911).

[8] P. Drude, *Zur Elektronentheorie der Metalle*, Ann. Phys. (Berl.) **306**, 566 (1900).

[9] P. Drude, *Zur Ionentheorie der Metalle*, Phys. Z. **1**, 161 (1900).

[10] F. London and H. London, *The electromagnetic equations of the supraconductor*, Proc. R. Soc. Lond. A **149**, 71 (1935).

[11] W. Meissner and R. Ochsenfeld, *Ein neuer Effekt bei Eintritt der Supraleitfähigkeit*, Naturwissenschaften **21**, 787 (1933).

[12] J. C. Maxwell, *A treatise on electricity and magnetism*, Clarendon Press, Oxford (1873).

[13] A. A. Abrikosov, *On the magnetic properties of superconductors of the second group*, Sov. Phys. JETP **5**, 1174 (1957).

[14] U. Essmann and H. Träuble, *The direct observation of individual flux lines in type II superconductors*, Phys. Lett. A **24**, 526 (1967), doi:10.1016/0375-9601(67)90819-5.

[15] H. F. Hess, R. B. Robinson, R. C. Dynes, J. M. Valles and J. V. Waszczak, *Scanning-tunneling-microscope observation of the Abrikosov flux lattice and the density of states near and inside a fluxoid*, Phys. Rev. Lett. **62**, 214 (1989), doi:10.1103/PhysRevLett. 62.214.

[16] L. N. Cooper, *Bound electron pairs in a degenerate Fermi gas*, Phys. Rev. **104**, 1189 (1956), doi:10.1103/PhysRev.104.1189.

[17] J. Bardeen, L. N. Cooper and J. R. Schrieffer, *Microscopic theory of superconductivity*, Phys. Rev. **106**, 162 (1957), doi:10.1103/PhysRev.106.162.

[18] J. Bardeen, L. N. Cooper and J. R. Schrieffer, *Theory of superconductivity*, Phys. Rev. **108**, 1175 (1957), doi:10.1103/PhysRev.108.1175.

[19] H. Fröhlich, *Theory of the superconducting state. I. The ground state at the absolute zero of temperature*, Phys. Rev. **79**, 845 (1950), doi:10.1103/PhysRev.79.845.

[20] J. Bardeen, *Wave functions for superconducting electrons*, Phys. Rev. **80**, 567 (1950), doi:10.1103/PhysRev.80.567.

[21] B. S. Deaver and W. M. Fairbank, *Experimental evidence for quantized flux in superconducting cylinders*, Phys. Rev. Lett. **7**, 43 (1961), doi:10.1103/PhysRevLett.7.43.

[22] R. Doll and M. Näbauer, *Experimental proof of magnetic flux quantization in a superconducting ring*, Phys. Rev. Lett. **7**, 51 (1961), doi:10.1103/PhysRevLett.7.51.

[23] E. Maxwell, *Isotope effect in the superconductivity of mercury*, Phys. Rev. **78**, 477 (1950), doi:10.1103/PhysRev.78.477.

[24] C. A. Reynolds, B. Serin, W. H. Wright and L. B. Nesbitt, *Superconductivity of isotopes of mercury*, Phys. Rev. **78**, 487 (1950), doi:10.1103/PhysRev.78.487.

[25] R. E. Glover and M. Tinkham, *Transmission of superconducting films at millimeter-microwave and far infrared frequencies*, Phys. Rev. **104**, 844 (1956), doi:10.1103/PhysRev.104.844.

[26] D. M. Ginsberg and M. Tinkham, *Far infrared transmission through superconducting films*, Phys. Rev. **118**, 990 (1960), doi:10.1103/PhysRev.118.990.

[27] I. Giaever, *Energy gap in superconductors measured by electron tunneling*, Phys. Rev. Lett. **5**, 147 (1960), doi:10.1103/PhysRevLett.5.147.

[28] I. Giaever, *Electron tunneling between two superconductors*, Phys. Rev. Lett. **5**, 464 (1960), doi:10.1103/PhysRevLett.5.464.

[29] I. Giaever and K. Megerle, *Study of superconductors by electron tunneling*, Phys. Rev. **122**, 1101 (1961), doi:10.1103/PhysRev.122.1101.

[30] I. Giaever, H. R. Hart and K. Megerle, *Tunneling into superconductors at temperatures below $1°K$*, Phys. Rev. **126**, 941 (1962), doi:10.1103/PhysRev.126.941.

[31] G. Eliashberg, *Interactions between electrons and lattice vibrations in a superconductor*, Sov. Phys. JETP **11**, 696 (1960).

[32] V. L. Ginzburg and L. D. Landau, *On the theory of superconductivity*, Zh. Eksp. Teor. Fiz. **20**, 1064 (1950).

[33] L. D. Landau and E. M. Lifšic, *Statistical Physics*, Pergamon Press, Oxford, 3rd edn., part 1 (1980).

[34] L. P. Gor'kov, *Microscopic derivation of the Ginzburg-Landau equations in the theory of superconductivity*, Sov. Phys. JETP **36**, 1364 (1959).

[35] B. D. Josephson, *Possible new effects in superconductive tunnelling*, Phys. Lett. **1**, 251 (1962).

[36] P. W. Anderson and J. M. Rowell, *Probable observation of the Josephson superconducting tunneling effect*, Phys. Rev. Lett. **10**, 230 (1963), doi:10.1103/PhysRevLett.10.230.

[37] B. D. Josephson, *Coupled superconductors*, Rev. Mod. Phys. **36**, 216 (1964), doi:10.1103/RevModPhys.36.216.

[38] W. C. Stewart, *Current-voltage characteristics of Josephson junctions*, Appl. Phys. Lett. **12**, 277 (1968).

[39] D. E. McCumber, *Effect of ac impedance on dc voltage-current characteristics of superconductor weak-link junctions*, J. Appl. Phys. **39**, 3113 (1968).

[40] A. Schilling, M. Cantoni, J. D. Guo and H. R. Ott, *Superconductivity above 130 K in the Hg-Ba-Ca-Cu-O system*, Nature **363**, 56 (1993), doi:10.1038/363056a0.

[41] G. F. Sun, K. W. Wong, B. R. Xu, Y. Xin and D. F. Lu, T_c *enhancement of* $HgBa_2Ca_2Cu_3O_{8+\delta}$ *by Tl substitution*, Phys. Lett. A **192**, 122 (1994).

[42] J. G. Bednorz and K. A. Müller, *Possible high* T_c *superconductivity in the Ba-La-Cu-O system*, Z. Phys. B **64**, 189 (1986), doi:10.1007/BF01303701.

[43] M. K. Wu, J. R. Ashburn, C. J. Torng, P. H. Hor, R. L. Meng, L. Gao, Z. J. Huang, Y. Q. Wang and C. W. Chu, *Superconductivity at 93 K in a new mixed-phase Y-Ba-Cu-O compound system at ambient pressure*, Phys. Rev. Lett. **58**, 908 (1987), doi:10.1103/PhysRevLett.58.908.

[44] K. Zhang, D. A. Bonn, S. Kamal, R. Liang, D. J. Baar, W. N. Hardy, D. Basov and T. Timusk, *Measurement of the* ab *plane anisotropy of microwave surface impedance of untwinned* $YBa_2Cu_3O_{6.95}$ *single crystals*, Phys. Rev. Lett. **73**, 2484 (1994), doi:10.1103/PhysRevLett.73.2484.

[45] D. N. Basov, R. Liang, D. A. Bonn, W. N. Hardy, B. Dabrowski, M. Quijada, D. B. Tanner, J. P. Rice, D. M. Ginsberg and T. Timusk, *In-plane anisotropy of the penetration depth in* $YBa_2Cu_3O_{7-x}$ *and* $YBa_2Cu_4O_8$ *superconductors*, Phys. Rev. Lett. **74**, 598 (1995), doi:10.1103/PhysRevLett.74.598.

[46] A. A. R. Fernandes, J. Santamaria, S. L. Bud'ko, O. Nakamura, J. Guimpel and I. K. Schuller, *Effect of physical and chemical pressure on the superconductivity of high-temperature oxide superconductors*, Phys. Rev. B **44**, 7601 (1991), doi:10.1103/PhysRevB.44.7601.

[47] B. Keimer, S. A. Kivelson, M. R. Norman, S. Uchida and J. Zaanen, *From quantum matter to high-temperature superconductivity in copper oxides*, Nature **518**, 179 (2015), doi:10.1038/nature14165.

[48] C. E. Gough, M. S. Colclough, E. M. Forgan, R. G. Jordan, M. Keene, C. M. Muirhead, A. I. M. Rae, N. Thomas, J. S. Abell and S. Sutton, *Flux quantization in a high-T_c superconductor*, Nature **326**, 855 (1987).

[49] D. A. Wollman, D. J. Van Harlingen, W. C. Lee, D. M. Ginsberg and A. J. Leggett, *Experimental determination of the superconducting pairing state in ybco from the phase coherence of YBCO-Pb dc SQUIDs*, Phys. Rev. Lett. **71**, 2134 (1993), doi:10.1103/PhysRevLett.71.2134.

[50] D. J. Van Harlingen, *Phase-sensitive tests of the symmetry of the pairing state in the high-temperature superconductors—evidence for $d_{x^2-y^2}$ symmetry*, Rev. Mod. Phys. **67**, 515 (1995), doi:10.1103/RevModPhys.67.515.

[51] C. C. Tsuei, J. R. Kirtley, C. C. Chi, L. S. Yu-Jahnes, A. Gupta, T. Shaw, J. Z. Sun and M. B. Ketchen, *Pairing symmetry and flux quantization in a tricrystal superconducting ring of $YBa_2Cu_3O_{7-\delta}$*, Phys. Rev. Lett. **73**, 593 (1994), doi:10.1103/PhysRevLett.73.593.

[52] H. Ding, M. R. Norman, J. C. Campuzano, M. Randeria, A. F. Bellman, T. Yokoya, T. Takahashi, T. Mochiku and K. Kadowaki, *Angle-resolved photoemission spectroscopy study of the superconducting gap anisotropy in $Bi_2Sr_2CaCu_2O_{8+x}$*, Phys. Rev. B **54**, R9678 (1996), doi:10.1103/PhysRevB.54.R9678.

[53] A. Damascelli, Z. Hussain and Z.-X. Shen, *Angle-resolved photoemission studies of the cuprate superconductors*, Rev. Mod. Phys. **75**, 473 (2003), doi:10.1103/RevModPhys.75.473.

[54] M. Hashimoto, I. M. Vishik, R.-H. He, T. P. Devereaux and Z.-X. Shen, *Energy gaps in high-transition-temperature cuprate superconductors*, Nat. Phys. **10**, 483 (2014), doi:10.1038/nphys3009.

[55] C. C. Tsuei and J. R. Kirtley, *Pairing symmetry in cuprate superconductors*, Rev. Mod. Phys. **72**, 969 (2000), doi:10.1103/RevModPhys.72.969.

[56] J. F. Annett, *Superconductivity, Superfluids, and Condensates*, Oxford Univ. Press, Oxford (2004).

[57] S. E. Barrett, D. J. Durand, C. H. Pennington, C. P. Slichter, T. A. Friedmann, J. P. Rice and D. M. Ginsberg, *[63]Cu Knight shifts in the superconducting state of $YBa_2Cu_3O_{7-\delta}$ (T_c=90 K)*, Phys. Rev. B **41**, 6283 (1990), doi:10.1103/PhysRevB.41.6283.

[58] P. Monthoux, A. V. Balatsky and D. Pines, *Toward a theory of high-temperature superconductivity in the antiferromagnetically correlated cuprate oxides*, Phys. Rev. Lett. **67**, 3448 (1991), doi:10.1103/PhysRevLett.67.3448.

[59] T. Dahm, V. Hinkov, S. V. Borisenko, A. A. Kordyuk, V. B. Zabolotnyy, J. Fink, B. Büchner, D. J. Scalapino, W. Hanke and B. Keimer, *Strength of the spin-fluctuation-mediated pairing interaction in a high-temperature superconductor*, Nat. Phys. **5**, 217 (2009), doi:10.1038/nphys1180.

[60] J. P. Carbotte, T. Timusk and J. Hwang, *Bosons in high-temperature superconductors: an experimental survey*, Rep. Prog. Phys. **74**, 066501 (2011), doi:10.1088/0034-4885/74/6/066501.

[61] D. J. Scalapino, *A common thread: The pairing interaction for unconventional superconductors*, Rev. Mod. Phys. **84**, 1383 (2012), doi:10.1103/RevModPhys.84.1383.

[62] A. J. Millis, S. Sachdev and C. M. Varma, *Inelastic scattering and pair breaking in anisotropic and isotropic superconductors*, Phys. Rev. B **37**, 4975 (1988), doi:10.1103/PhysRevB.37.4975.

[63] A. Lanzara, P. V. Bogdanov, X. J. Zhou, S. A. Kellar, D. L. Feng, E. D. Lu, T. Yoshida, H. Eisaki, A. Fujimori, K. Kishio, J. I. Shimoyama, T. Noda *et al.*, *Evidence for ubiquitous strong electron-phonon coupling in high-temperature superconductors*, Nature **412**, 510 (2001), doi:10.1038/35087518.

[64] D. Reznik, L. Pintschovius, M. Ito, S. Iikubo, M. Sato, H. Goka, M. Fujita, K. Yamada, G. D. Gu and J. M. Tranquada, *Electron-phonon coupling reflecting dynamic charge inhomogeneity in copper oxide superconductors*, Nature **440**, 1170 (2006), doi:10.1038/nature04704.

[65] D. N. Basov and T. Timusk, *Electrodynamics of high-T_c superconductors*, Rev. Mod. Phys. **77**, 721 (2005), doi:10.1103/RevModPhys.77.721.

[66] J. R. Schrieffer, ed., *Handbook of High-Temperature Superconductivity*, Springer, New York (2007).

[67] G. Grissonnanche, O. Cyr-Choinière, F. Laliberté, S. René de Cotret, A. Juneau-Fecteau, S. Dufour-Beauséjour, M. È. Delage, D. Leboeuf, J. Chang, B. J. Ramshaw, D. A. Bonn, W. N. Hardy *et al.*, *Direct measurement of the upper critical field in cuprate superconductors*, Nat. Commun. **5**, 3280 (2014), doi:10.1038/ncomms4280.

[68] Y. J. Uemura, G. M. Luke, B. J. Sternlieb, J. H. Brewer, J. F. Carolan, W. N. Hardy, R. Kadono, J. R. Kempton, R. F. Kiefl, S. R. Kreitzman, P. Mulhern, T. M. Riseman *et al.*, *Universal correlations between T_c and $\frac{n_s}{m^*}$ (carrier density over effective mass) in high-T_c cuprate superconductors*, Phys. Rev. Lett. **62**, 2317 (1989), doi:10.1103/PhysRevLett.62.2317.

[69] Y. J. Uemura, L. P. Le, G. M. Luke, B. J. Sternlieb, W. D. Wu, J. H. Brewer, T. M. Riseman, C. L. Seaman, M. B. Maple, M. Ishikawa, D. G. Hinks, J. D. Jorgensen *et al.*, *Basic similarities among cuprate, bismuthate, organic, Chevrel-phase, and heavy-fermion superconductors shown by penetration-depth measurements*, Phys. Rev. Lett. **66**, 2665 (1991), doi:10.1103/PhysRevLett.66.2665.

[70] N. E. Hussey, K. Takenaka and H. Takagi, *Universality of the Mott–Ioffe–Regel limit in metals*, Phil. Mag. **84**, 2847 (2004), doi:10.1080/14786430410001716944.

[71] C. M. Varma, P. B. Littlewood, S. Schmitt-Rink, E. Abrahams and A. E. Ruckenstein, *Phenomenology of the normal state of Cu-O high-temperature superconductors*, Phys. Rev. Lett. **63**, 1996 (1989), doi:10.1103/PhysRevLett.63.1996.

[72] C. Renner, B. Revaz, J.-Y. Genoud, K. Kadowaki and O. Fischer, *Pseudogap precursor of the superconducting gap in under- and overdoped $Bi_2Sr_2CaCu_2O_{8+\delta}$*, Phys. Rev. Lett. **80**, 149 (1998), doi:10.1103/PhysRevLett.80.149.

[73] A. Matsuda, S. Sugita and T. Watanabe, *Temperature and doping dependence of the $Bi_{2.1}Sr_{1.9}CaCu_2O_{8+\delta}$ pseudogap and superconducting gap*, Phys. Rev. B **60**, 1377 (1999), doi:10.1103/PhysRevB.60.1377.

[74] D. S. Marshall, D. S. Dessau, A. G. Loeser, C.-H. Park, A. Y. Matsuura, J. N. Eckstein, I. Bozovic, P. Fournier, A. Kapitulnik, W. E. Spicer and Z.-X. Shen, *Unconventional electronic structure evolution with hole doping in $Bi_2Sr_2CaCu_2O_{8+\delta}$: Angle-resolved photoemission results*, Phys. Rev. Lett. **76**, 4841 (1996), doi:10.1103/PhysRevLett.76.4841.

[75] H. Ding, T. Yokoya, J. C. Campuzano, T. Takahashi, M. Randeria, M. R. Norman, T. Mochiku, K. Kadowaki and J. Giapintzakis, *Spectroscopic evidence for a pseudogap in the normal state of underdoped high-T_c superconductors*, Nature **382**, 51 (1996), doi:10.1038/382051a0.

[76] A. G. Loeser, Z.-X. Shen, D. S. Dessau, D. S. Marshall, C. H. Park, P. Fournier and A. Kapitulnik, *Excitation gap in the normal state of underdoped $Bi_2Sr_2CaCu_2O_{8+\delta}$*, Science **273**, 325 (1996), doi:10.1126/science.273.5273.325.

[77] V. J. Emery and S. A. Kivelson, *Importance of phase fluctuations in superconductors with small superfluid density*, Nature **374**, 434 (1995), doi:10.1038/374434a0.

[78] Y. Uemura, *Bose-Einstein to BCS crossover picture for high-T_c cuprates*, Physica C **282-287**, 194 (1997), doi:https://doi.org/10.1016/S0921-4534(97)00194-9.

[79] L. I. Glazman and A. E. Koshelev, *Critical behavior of layered superconductors*, Sov. Phys. JETP **70**, 774 (1990).

[80] W. Janke and T. Matsui, *Crossover in the XY model from three to two dimensions*, Phys. Rev. B **42**, 10673 (1990), doi:10.1103/PhysRevB.42.10673.

[81] P. Minnhagen and P. Olsson, *Crossover to effectively two-dimensional vortices for high-T_c superconductors*, Phys. Rev. Lett. **67**, 1039 (1991), doi:10.1103/PhysRevLett.67.1039.

[82] P. Minnhagen and P. Olsson, *Monte Carlo calculation of the vortex interaction for high-T_c superconductors*, Phys. Rev. B **44**, 4503 (1991), doi:10.1103/PhysRevB.44.4503.

[83] D. S. Fisher, M. P. A. Fisher and D. A. Huse, *Thermal fluctuations, quenched disorder, phase transitions, and transport in type-II superconductors*, Phys. Rev. B **43**, 130 (1991), doi:10.1103/PhysRevB.43.130.

[84] B. Chattopadhyay and S. R. Shenoy, *Kosterlitz-Thouless signatures from 3D vortex loops in layered superconductors*, Phys. Rev. Lett. **72**, 400 (1994), doi:10.1103/PhysRevLett.72.400.

[85] V. L. Berezinskii, *Destruction of long-range order in one-dimensional and two-dimensional systems having a continuous symmetry group I. Classical systems*, Sov. Phys. JETP **32**, 493 (1971).

[86] V. L. Berezinskii, *Destruction of long-range order in one-dimensional and two-dimensional systems possessing a continuous symmetry group II. Quantum systems*, Sov. Phys. JETP **34**, 610 (1972).

[87] J. M. Kosterlitz and D. J. Thouless, *Ordering, metastability and phase transitions in two-dimensional systems*, J. Phys. C **6**, 1181 (1973), doi:10.1088/0022-3719/6/7/010.

[88] J. M. Kosterlitz, *The critical properties of the two-dimensional xy model*, J. Phys. C **7**(6), 1046 (1974), doi:10.1088/0022-3719/7/6/005.

[89] A. Dubroka, M. Rössle, K. W. Kim, V. K. Malik, D. Munzar, D. N. Basov, A. A. Schafgans, S. J. Moon, C. T. Lin, D. Haug, V. Hinkov, B. Keimer *et al.*, *Evidence of a precursor superconducting phase at temperatures as high as 180 K in $RBa_2Cu_3O_{7-\delta}$ $(R = Y, Gd, Eu)$ superconducting crystals from infrared spectroscopy*, Phys. Rev. Lett. **106**, 047006 (2011), doi:10.1103/PhysRevLett.106.047006.

[90] W. Hu, S. Kaiser, D. Nicoletti, C. R. Hunt, I. Gierz, M. C. Hoffmann, M. Le Tacon, T. Loew, B. Keimer and A. Cavalleri, *Optically enhanced coherent transport in $YBa_2Cu_3O_{6.5}$ by ultrafast redistribution of interlayer coupling*, Nat. Mater. **13**, 705 (2014), doi:10.1038/nmat3963.

[91] S. Kaiser, C. R. Hunt, D. Nicoletti, W. Hu, I. Gierz, H. Y. Liu, M. Le Tacon, T. Loew, D. Haug, B. Keimer and A. Cavalleri, *Optically induced coherent transport far above T_c in underdoped $YBa_2Cu_3O_{6+\delta}$*, Phys. Rev. B **89**, 184516 (2014).

[92] A. von Hoegen, M. Fechner, M. Först, N. Taherian, E. Rowe, A. Ribak, J. Porras, B. Keimer, M. Michael, E. Demler and A. Cavalleri, *Amplification of superconducting fluctuations in driven $YBa_2Cu_3O_{6+x}$*, Phys. Rev. X **12**, 031008 (2022), doi:10.1103/PhysRevX.12.031008.

[93] G. Ghiringhelli, M. L. Tacon, M. Minola, S. Blanco-Canosa, C. Mazzoli, N. B. Brookes, G. M. D. Luca, A. Frano, D. G. Hawthorn, F. He, T. Loew, M. M. Sala *et al.*, *Long-range incommensurate charge fluctuations in $(Y,Nd)Ba_2Cu_3O_{6+x}$*, Science **337**, 821 (2012), doi:10.1126/science.1223532.

[94] J. Chang, E. Blackburn, A. T. Holmes, N. B. Christensen, J. Larsen, J. Mesot, R. Liang, D. A. Bonn, W. N. Hardy, A. Watenphul, M. V. Zimmermann, E. M. Forgan *et al.*, *Direct observation of competition between superconductivity and charge density wave order in $YBa_2Cu_3O_{6.67}$*, Nat. Phys. **8**, 871 (2012), doi:10.1038/nphys2456.

[95] S. Blanco-Canosa, A. Frano, E. Schierle, J. Porras, T. Loew, M. Minola, M. Bluschke, E. Weschke, B. Keimer and M. Le Tacon, *Resonant x-ray scattering study of charge-density wave correlations in* $YBa_2Cu_3O_{6+x}$, Phys. Rev. B **90**, 054513 (2014), doi: 10.1103/PhysRevB.90.054513.

[96] E. Fradkin, S. A. Kivelson and J. M. Tranquada, *Colloquium: Theory of intertwined orders in high temperature superconductors*, Rev. Mod. Phys. **87**, 457 (2015), doi: 10.1103/RevModPhys.87.457.

[97] B. Liu, M. Först, M. Fechner, D. Nicoletti, J. Porras, T. Loew, B. Keimer and A. Cavalleri, *Pump frequency resonances for light-induced incipient superconductivity in* $YBa_2Cu_3O_{6.5}$, Phys. Rev. X **10**, 011053 (2020), doi:10.1103/PhysRevX.10.011053.

[98] R. Mankowsky, A. Subedi, M. Först, S. O. Mariager, M. Chollet, H. T. Lemke, J. S. Robinson, J. M. Glownia, M. P. Minitti, A. Frano, M. Fechner, N. A. Spaldin *et al.*, *Nonlinear lattice dynamics as a basis for enhanced superconductivity in* $YBa_2Cu_3O_{6.5}$, Nature (London) **516**, 71 (2014), doi:10.1038/nature13875.

[99] R. Höppner, B. Zhu, T. Rexin, A. Cavalleri and L. Mathey, *Redistribution of phase fluctuations in a periodically driven cuprate superconductor*, Phys. Rev. B **91**, 104507 (2015), doi:10.1103/PhysRevB.91.104507.

[100] S. J. Denny, S. R. Clark, Y. Laplace, A. Cavalleri and D. Jaksch, *Proposed parametric cooling of bilayer cuprate superconductors by terahertz excitation*, Phys. Rev. Lett. **114**, 137001 (2015), doi:10.1103/PhysRevLett.114.137001.

[101] J.-i. Okamoto, A. Cavalleri and L. Mathey, *Theory of enhanced interlayer tunneling in optically driven high-T_c superconductors*, Phys. Rev. Lett. **117**(22), 227001 (2016), doi:10.1103/PhysRevLett.117.227001.

[102] J.-i. Okamoto, W. Hu, A. Cavalleri and L. Mathey, *Transiently enhanced interlayer tunneling in optically driven high-T_c superconductors*, Phys. Rev. B **96**, 144505 (2017), doi:10.1103/PhysRevB.96.144505.

[103] Z. M. Raines, V. Stanev and V. M. Galitski, *Enhancement of superconductivity via periodic modulation in a three-dimensional model of cuprates*, Phys. Rev. B **91**, 184506 (2015), doi:10.1103/PhysRevB.91.184506.

[104] A. A. Patel and A. Eberlein, *Light-induced enhancement of superconductivity via melting of competing bond-density wave order in underdoped cuprates*, Phys. Rev. B **93**, 195139 (2016), doi:10.1103/PhysRevB.93.195139.

[105] M. H. Michael, A. von Hoegen, M. Fechner, M. Först, A. Cavalleri and E. Demler, *Parametric resonance of Josephson plasma waves: A theory for optically amplified interlayer superconductivity in* $YBa_2Cu_3O_{6+x}$, Phys. Rev. B **102**, 174505 (2020), doi: 10.1103/PhysRevB.102.174505.

[106] D. Fausti, R. I. Tobey, N. Dean, S. Kaiser, A. Dienst, M. C. Hoffmann, S. Pyon, T. Takayama, H. Takagi and A. Cavalleri, *Light-induced superconductivity in a stripe-ordered cuprate*, Science **331**, 189 (2011), doi:10.1126/science.1197294.

[107] D. Nicoletti, E. Casandruc, Y. Laplace, V. Khanna, C. R. Hunt, S. Kaiser, S. S. Dhesi, G. D. Gu, J. P. Hill and A. Cavalleri, *Optically induced superconductivity in striped* $La_{2-x}Ba_xCuO_4$ *by polarization-selective excitation in the near infrared*, Phys. Rev. B **90**, 100503 (2014), doi:10.1103/PhysRevB.90.100503.

[108] K. A. Cremin, J. Zhang, C. C. Homes, G. D. Gu, Z. Sun, M. M. Fogler, A. J. Millis, D. N. Basov and R. D. Averitt, *Photoenhanced metastable c-axis electrodynamics in stripe-ordered cuprate* $La_{1.885}Ba_{0.115}CuO_4$, Proc. Natl. Acad. Sci. USA **116**(40), 19875 (2019), doi:10.1073/pnas.1908368116.

[109] M. Mitrano, A. Cantaluppi, D. Nicoletti, S. Kaiser, A. Perucchi, S. Lupi, P. Di Pietro, D. Pontiroli, M. Riccò, S. R. Clark, D. Jaksch and A. Cavalleri, *Possible light-induced superconductivity in* K_3C_{60} *at high temperature*, Nature **530**, 461 (2016), doi:10.1038/nature16522.

[110] A. Cantaluppi, M. Buzzi, G. Jotzu, D. Nicoletti, M. Mitrano, D. Pontiroli, M. Riccò, A. Perucchi, P. Di Pietro and A. Cavalleri, *Pressure tuning of light-induced superconductivity in* K_3C_{60}, Nat. Phys. **14**, 837 (2018), doi:10.1038/s41567-018-0134-8.

[111] M. Budden, T. Gebert, M. Buzzi, G. Jotzu, E. Wang, T. Matsuyama, G. Meier, Y. Laplace, D. Pontiroli, M. Riccò, F. Schlawin, D. Jaksch *et al.*, *Evidence for metastable photo-induced superconductivity in* K_3C_{60}, Nat. Phys. **17**, 611 (2021), doi:10.1038/s41567-020-01148-1.

[112] M. Buzzi, D. Nicoletti, M. Fechner, N. Tancogne-Dejean, M. A. Sentef, A. Georges, T. Biesner, E. Uykur, M. Dressel, A. Henderson, T. Siegrist, J. A. Schlueter *et al.*, *Photomolecular high-temperature superconductivity*, Phys. Rev. X **10**, 031028 (2020), doi:10.1103/PhysRevX.10.031028.

[113] M. Buzzi, D. Nicoletti, S. Fava, G. Jotzu, K. Miyagawa, K. Kanoda, A. Henderson, T. Siegrist, J. A. Schlueter, M.-S. Nam, A. Ardavan and A. Cavalleri, *Phase diagram for light-induced superconductivity in* $\kappa-(ET)_2-X$, Phys. Rev. Lett. **127**, 197002 (2021), doi:10.1103/PhysRevLett.127.197002.

[114] W. E. Lawrence and S. Doniach, *Proceedings of the 12th International Conference on Low Temperature Physics (Kyoto, 1970)*, p. 361, Academic Press of Japan, Tokyo (1971).

[115] R. Kleiner and P. Müller, *Intrinsic Josephson effects in high-T_c superconductors*, Phys. Rev. B **49**, 1327 (1994), doi:10.1103/PhysRevB.49.1327.

[116] P. W. Anderson, *Interlayer tunneling mechanism for high-T_c superconductivity: Comparison with c axis infrared experiments*, Science **268**, 1154 (1995), doi:10.1126/science.268.5214.1154.

[117] D. van der Marel and A. A. Tsvetkov, *Transverse optical plasmons in layered superconductors*, Czech. J. Phys. **46**, 3165 (1996), doi:10.1007/BF02548125.

[118] H. Shibata and T. Yamada, *Double Josephson plasma resonance in T^* phase* $SmLa_{1-x}Sr_xCuO_{4-\delta}$, Phys. Rev. Lett. **81**, 3519 (1998), doi:10.1103/PhysRevLett.81.3519.

[119] D. Dulić, A. Pimenov, D. van der Marel, D. M. Broun, S. Kamal, W. N. Hardy, A. A. Tsvetkov, I. M. Sutjaha, R. Liang, A. A. Menovsky, A. Loidl and S. S. Saxena, *Observation of the transverse optical plasmon in $SmLa_{0.8}Sr_{0.2}CuO_{4-\delta}$*, Phys. Rev. Lett. **86**, 4144 (2001), doi:10.1103/PhysRevLett.86.4144.

[120] S. Rajasekaran, E. Casandruc, Y. Laplace, D. Nicoletti, G. D. Gu, S. R. Clark, D. Jaksch and A. Cavalleri, *Parametric amplification of a superconducting plasma wave*, Nat. Phys. **12**, 1012 (2016), doi:10.1038/nphys3819.

[121] Y. Laplace and A. Cavalleri, *Josephson plasmonics in layered superconductors*, Adv. Phys. X **1**, 387 (2016), doi:10.1080/23746149.2016.1212671.

[122] S. Rajasekaran, J. Okamoto, L. Mathey, M. Fechner, V. Thampy, G. D. Gu and A. Cavalleri, *Probing optically silent superfluid stripes in cuprates*, Science **359**, 575 (2018), doi:10.1126/science.aan3438.

[123] F. Gabriele, M. Udina and L. Benfatto, *Non-linear terahertz driving of plasma waves in layered cuprates*, Nat. Commun. **12**, 752 (2021), doi:10.1038/s41467-021-21041-6.

[124] T. Koyama and M. Tachiki, *I-V characteristics of Josephson-coupled layered superconductors with longitudinal plasma excitations*, Phys. Rev. B **54**, 16183 (1996), doi:10.1103/PhysRevB.54.16183.

[125] K. Yee, *Numerical solution of initial boundary value problems involving Maxwell's equations in isotropic media*, IEEE Trans. Antennas Propag. **14**, 302 (1966), doi:10.1109/TAP.1966.1138693.

[126] J. B. Kogut, *An introduction to lattice gauge theory and spin systems*, Rev. Mod. Phys. **51**, 659 (1979), doi:10.1103/RevModPhys.51.659.

[127] J. Goldstone, A. Salam and S. Weinberg, *Broken symmetries*, Phys. Rev. **127**, 965 (1962), doi:10.1103/PhysRev.127.965.

[128] P. W. Anderson, *Plasmons, gauge invariance, and mass*, Phys. Rev. **130**, 439 (1963), doi:10.1103/PhysRev.130.439.

[129] P. W. Higgs, *Broken symmetries and the masses of gauge bosons*, Phys. Rev. Lett. **13**, 508 (1964), doi:10.1103/PhysRevLett.13.508.

[130] F. Englert and R. Brout, *Broken symmetry and the mass of gauge vector mesons*, Phys. Rev. Lett. **13**, 321 (1964), doi:10.1103/PhysRevLett.13.321.

[131] F. Yang and M. W. Wu, *Theory of Higgs modes in d-wave superconductors*, Phys. Rev. B **102**, 014511 (2020), doi:10.1103/PhysRevB.102.014511.

[132] R. Matsunaga, N. Tsuji, H. Fujita, A. Sugioka, K. Makise, Y. Uzawa, H. Terai, Z. Wang, H. Aoki and R. Shimano, *Light-induced collective pseudospin precession resonating with Higgs mode in a superconductor*, Science **345**, 1145 (2014), doi:10.1126/science.1254697.

[133] S. Nakamura, Y. Iida, Y. Murotani, R. Matsunaga, H. Terai and R. Shimano, *Infrared activation of the Higgs mode by supercurrent injection in superconducting NbN*, Phys. Rev. Lett. **122**, 257001 (2019), doi:10.1103/PhysRevLett.122.257001.

[134] K. Katsumi, N. Tsuji, Y. I. Hamada, R. Matsunaga, J. Schneeloch, R. D. Zhong, G. D. Gu, H. Aoki, Y. Gallais and R. Shimano, *Higgs mode in the d-wave superconductor $Bi_2Sr_2CaCu_2O_{8+x}$ driven by an intense terahertz pulse*, Phys. Rev. Lett. **120**, 117001 (2018), doi:10.1103/PhysRevLett.120.117001.

[135] H. Chu, M.-J. Kim, K. Katsumi, S. Kovalev, R. D. Dawson, L. Schwarz, N. Yoshikawa, G. Kim, D. Putzky, Z. Z. Li, H. Raffy, S. Germanskiy *et al.*, *Phase-resolved Higgs response in superconducting cuprates*, Nat. Commun. **11**, 1793 (2020), doi:10.1038/s41467-020-15613-1.

[136] L. Schwarz and D. Manske, *Theory of driven Higgs oscillations and third-harmonic generation in unconventional superconductors*, Phys. Rev. B **101**, 184519 (2020), doi:10.1103/PhysRevB.101.184519.

[137] G. Seibold, M. Udina, C. Castellani and L. Benfatto, *Third harmonic generation from collective modes in disordered superconductors*, Phys. Rev. B **103**, 014512 (2021), doi:10.1103/PhysRevB.103.014512.

[138] D. Pekker and C. Varma, *Amplitude/Higgs modes in condensed matter physics*, Annu. Rev. Condens. Matter Phys. **6**, 269 (2015), doi:10.1146/annurev-conmatphys-031214-014350.

[139] R. Shimano and N. Tsuji, *Higgs mode in superconductors*, Annu. Rev. Condens. Matter Phys. **11**, 103 (2020), doi:10.1146/annurev-conmatphys-031119-050813.

[140] M. Machida, T. Koyama and M. Tachiki, *Dynamical breaking of charge neutrality in intrinsic Josephson junctions: Common origin for microwave resonant absorptions and multiple-branch structures in the $I - V$ characteristics*, Phys. Rev. Lett. **83**, 4618 (1999), doi:10.1103/PhysRevLett.83.4618.

[141] M. Machida and T. Koyama, *Localized rotating-modes in capacitively coupled intrinsic Josephson junctions: Systematic study of branching structure and collective dynamical instability*, Phys. Rev. B **70**, 024523 (2004), doi:10.1103/PhysRevB.70.024523.

[142] D. v. d. Marel, H. J. A. Molegraaf, J. Zaanen, Z. Nussinov, F. Carbone, A. Damascelli, H. Eisaki, M. Greven, P. H. Kes and M. Li, *Quantum critical behaviour in a high-T_c superconductor*, Nature **425**, 271 (2003), doi:10.1038/nature01978.

[143] T. Koyama, *Josephson plasma resonances and optical properties in high-T_c superconductors with alternating junction parameters*, J. Phys. Soc. Jpn. **71**, 2986 (2002), doi:10.1143/JPSJ.71.2986.

[144] D. van der Marel and A. A. Tsvetkov, *Transverse-optical Josephson plasmons: Equations of motion*, Phys. Rev. B **64**, 024530 (2001), doi:10.1103/PhysRevB.64.024530.

[145] T. Schneider and E. Stoll, *Molecular-dynamics study of structural-phase transitions. I. One-component displacement models*, Phys. Rev. B **13**, 1216 (1976), doi:10.1103/PhysRevB.13.1216.

[146] S. R. Shenoy and B. Chattopadhyay, *Anisotropic three-dimensional XY model and vortex-loop scaling*, Phys. Rev. B **51**, 9129 (1995), doi:10.1103/PhysRevB.51.9129.

[147] G. Mozurkewich, M. B. Salamon and S. E. Inderhees, *Crossover analysis of the heat capacity of $YBa_2Cu_3O_{7-x}$ near T_c: Evidence for XY-like critical behavior*, Phys. Rev. B **46**, 11914 (1992), doi:10.1103/PhysRevB.46.11914.

[148] S. Kamal, D. A. Bonn, N. Goldenfeld, P. J. Hirschfeld, R. Liang and W. N. Hardy, *Penetration depth measurements of 3D XY critical behavior in $YBa_2Cu_3O_{6.95}$ crystals*, Phys. Rev. Lett. **73**, 1845 (1994), doi:10.1103/PhysRevLett.73.1845.

[149] B. I. Halperin, T. C. Lubensky and S.-k. Ma, *First-order phase transitions in superconductors and smectic-A liquid crystals*, Phys. Rev. Lett. **32**, 292 (1974), doi:10.1103/PhysRevLett.32.292.

[150] C. Dasgupta and B. I. Halperin, *Phase transition in a lattice model of superconductivity*, Phys. Rev. Lett. **47**, 1556 (1981), doi:10.1103/PhysRevLett.47.1556.

[151] J. Pearl, *Current distribution in superconducting films carrying quantized fluxoids*, Appl. Phys. Lett. **5**, 65 (1964), doi:10.1063/1.1754056.

[152] H. Suhl, *Inertial mass of a moving fluxoid*, Phys. Rev. Lett. **14**, 226 (1965), doi:10.1103/PhysRevLett.14.226.

[153] L. N. Bulaevskii, *Interaction of pancake vortices with c-axis plasmon in Josephson-coupled layered superconductors*, Journal de Physique I **6**, 2355 (1996), doi:10.1051/jp1:1996222.

[154] H. B. Callen and T. A. Welton, *Irreversibility and generalized noise*, Phys. Rev. **83**, 34 (1951), doi:10.1103/PhysRev.83.34.

[155] R. Kubo, *Statistical-mechanical theory of irreversible processes. I. General theory and simple applications to magnetic and conduction problems*, J. Phys. Soc. Jpn. **12**, 570 (1957), doi:10.1143/JPSJ.12.570.

[156] S. Savel'ev, V. A. Yampol'skii, A. L. Rakhmanov and F. Nori, *Terahertz Josephson plasma waves in layered superconductors: spectrum, generation, nonlinear and quantum phenomena*, Rep. Prog. Phys. **73**, 026501 (2010), doi:10.1088/0034-4885/73/2/026501.

[157] U. Fano, *Effects of configuration interaction on intensities and phase shifts*, Phys. Rev. **124**, 1866 (1961), doi:10.1103/PhysRev.124.1866.

[158] B. I. Halperin and D. R. Nelson, *Resistive transition in superconducting films*, J. Low Temp. Phys. **36**, 599 (1979), doi:10.1007/BF00116988.

[159] A. Shapere and F. Wilczek, *Classical time crystals*, Phys. Rev. Lett. **109**, 160402 (2012), doi:10.1103/PhysRevLett.109.160402.

[160] F. Wilczek, *Quantum time crystals*, Phys. Rev. Lett. **109**, 160401 (2012), doi: 10.1103/PhysRevLett.109.160401.

[161] P. Bruno, *Comment on "quantum time crystals"*, Phys. Rev. Lett. **110**, 118901 (2013), doi:10.1103/PhysRevLett.110.118901.

[162] H. Watanabe and M. Oshikawa, *Absence of quantum time crystals*, Phys. Rev. Lett. **114**, 251603 (2015), doi:10.1103/PhysRevLett.114.251603.

[163] F. Wilczek, *Superfluidity and space-time translation symmetry breaking*, Phys. Rev. Lett. **111**, 250402 (2013), doi:10.1103/PhysRevLett.111.250402.

[164] S. Choi, J. Choi, R. Landig, G. Kucsko, H. Zhou, J. Isoya, F. Jelezko, S. Onoda, H. Sumiya, V. Khemani, C. von Keyserlingk, N. Y. Yao *et al.*, *Observation of discrete time-crystalline order in a disordered dipolar many-body system*, Nature **543**, 221 (2017), doi:10.1038/nature21426.

[165] J. Zhang, P. W. Hess, A. Kyprianidis, P. Becker, A. Lee, J. Smith, G. Pagano, I.-D. Potirniche, A. C. Potter, A. Vishwanath, N. Y. Yao and C. Monroe, *Observation of a discrete time crystal*, Nature **543**, 217 (2017), doi:10.1038/nature21413.

[166] T. L. Heugel, M. Oscity, A. Eichler, O. Zilberberg and R. Chitra, *Classical many-body time crystals*, Phys. Rev. Lett. **123**, 124301 (2019), doi:10.1103/PhysRevLett. 123.124301.

[167] N. Y. Yao, C. Nayak, L. Balents and M. P. Zaletel, *Classical discrete time crystals*, Nat. Phys. **16**, 438 (2020), doi:10.1038/s41567-019-0782-3.

[168] F. Iemini, A. Russomanno, J. Keeling, M. Schirò, M. Dalmonte and R. Fazio, *Boundary time crystals*, Phys. Rev. Lett. **121**, 035301 (2018), doi:10.1103/PhysRevLett. 121.035301.

[169] B. Buca, J. Tindall and D. Jaksch, *Non-stationary coherent quantum many-body dynamics through dissipation*, Nat. Commun. **10**, 1730 (2019), doi:10.1038/ s41467-019-09757-y.

[170] P. Kongkhambut, J. Skulte, L. Mathey, J. G. Cosme, A. Hemmerich and H. Keßler, *Observation of a continuous time crystal*, Science **377**, 670 (2022), doi:10.1126/ science.abo3382.

[171] K. Sacha and J. Zakrzewski, *Time crystals: a review*, Rep. Prog. Phys. **81**, 016401 (2018), doi:10.1088/1361-6633/aa8b38.

[172] D. V. Else, C. Monroe, C. Nayak and N. Y. Yao, *Discrete time crystals*, Annu. Rev. Condens. Matter Phys. **11**, 467 (2020), doi:10.1146/ annurev-conmatphys-031119-050658.

[173] L. D. Landau and E. M. Lifšic, *Mechanics*, Butterworth-Heinemann, Oxford, 3rd edn. (1976).

[174] S. V. Dordevic, S. Komiya, Y. Ando and D. N. Basov, *Josephson plasmon and inhomogeneous superconducting state in $La_{2-x}Sr_xCuO_4$*, Phys. Rev. Lett. **91**, 167401 (2003), doi:10.1103/PhysRevLett.91.167401.

[175] M. Hashimoto, T. Yoshida, K. Tanaka, A. Fujimori, M. Okusawa, S. Wakimoto, K. Yamada, T. Kakeshita, H. Eisaki and S. Uchida, *Distinct doping dependences of the pseudogap and superconducting gap of $La_{2-x}Sr_xCuO_4$ cuprate superconductors*, Phys. Rev. B **75**, 140503 (2007), doi:10.1103/PhysRevB.75.140503.

[176] F. Peronaci, M. Schiró and M. Capone, *Transient dynamics of d-wave superconductors after a sudden excitation*, Phys. Rev. Lett. **115**, 257001 (2015), doi:10.1103/PhysRevLett.115.257001.

[177] Y. Murakami, P. Werner, N. Tsuji and H. Aoki, *Damping of the collective amplitude mode in superconductors with strong electron-phonon coupling*, Phys. Rev. B **94**, 115126 (2016), doi:10.1103/PhysRevB.94.115126.

[178] J. Skaar, *Fresnel equations and the refractive index of active media*, Phys. Rev. E **73**, 026605 (2006), doi:10.1103/PhysRevE.73.026605.

[179] B. Nistad and J. Skaar, *Causality and electromagnetic properties of active media*, Phys. Rev. E **78**, 036603 (2008), doi:10.1103/PhysRevE.78.036603.

[180] M. H. Michael, M. Först, D. Nicoletti, S. R. U. Haque, Y. Zhang, A. Cavalleri, R. D. Averitt, D. Podolsky and E. Demler, *Generalized Fresnel-Floquet equations for driven quantum materials*, Phys. Rev. B **105**, 174301 (2022), doi:10.1103/PhysRevB.105.174301.

[181] S. Kumar, *Recent progress in terahertz quantum cascade lasers*, IEEE J. Sel. Top. Quantum Electron. **17**, 38 (2011), doi:10.1109/JSTQE.2010.2049735.

[182] M. Feiginov, H. Kanaya, S. Suzuki and M. Asada, *Operation of resonant-tunneling diodes with strong back injection from the collector at frequencies up to 1.46 THz*, Appl. Phys. Lett. **104**, 243509 (2014), doi:10.1063/1.4884602.

[183] U. Welp, K. Kadowaki and R. Kleiner, *Superconducting emitters of THz radiation*, Nat. Photonics **7**, 702 (2013), doi:10.1038/nphoton.2013.216.

[184] I. Kakeya and H. Wang, *Terahertz-wave emission from Bi2212 intrinsic Josephson junctions: a review on recent progress*, Supercond. Sci. Technol. **29**, 073001 (2016), doi:10.1088/0953-2048/29/7/073001.

[185] R. Kleiner and H. Wang, *Terahertz emission from $Bi_2Sr_2CaCu_2O_{8+x}$ intrinsic Josephson junction stacks*, J. Appl. Phys. **126**, 171101 (2019), doi:10.1063/1.5116660.

[186] B. Ferguson and X. C. Zhang, *Materials for terahertz science and technology*, Nat. Mater. **1**, 26 (2002), doi:10.1038/nmat708.

[187] M. Tonouchi, *Cutting-edge terahertz technology*, Nat. Photonics **1**, 97 (2007), doi:10.1038/nphoton.2007.3.

[188] E. Pickwell and V. P. Wallace, *Biomedical applications of terahertz technology*, J. Phys. D: Appl. Phys. **39**, R301 (2006), doi:10.1088/0022-3727/39/17/r01.

[189] H. Y. Hwang, S. Fleischer, N. C. Brandt, B. G. P. Jr., M. Liu, K. Fan, A. Sternbach, X. Zhang, R. D. Averitt and K. A. Nelson, *A review of non-linear terahertz spectroscopy with ultrashort tabletop-laser pulses*, J. Mod. Opt. **62**, 1447 (2015), doi:10.1080/09500340.2014.918200.

[190] D. M. Mittleman, *Twenty years of terahertz imaging*, Opt. Express **26**, 9417 (2018), doi:10.1364/OE.26.009417.

[191] P. Langevin, *Sur la théorie du mouvement brownien*, C. R. Acad. Sci. **146**, 530 (1908).

[192] R. Zwanzig, *Nonequilibrium statistical mechanics*, Oxford Univ. Press, Oxford (2001).

[193] E. Hairer, C. Lubich and G. Wanner, *Geometric numerical integration illustrated by the Störmer–Verlet method*, Acta Numer. **12**, 399 (2003), doi:10.1017/S0962492902000144.

[194] K. Heun, *Neue Methoden zur approximativen Integration der Differentialgleichungen einer unabhängigen Veränderlichen*, Z. Math. Phys. **45**, 23 (1900).

[195] E. Süli and D. F. Mayers, *An Introduction to Numerical Analysis*, Cambridge Univ. Press, Cambridge (2003).

Acknowledgments

First of all, I would like to thank my supervisor Ludwig Mathey for giving me the opportunity to do a PhD in his group and for providing so much valuable guidance. Our countless discussions have certainly improved the outcome of my research and enriched my personal development. The same goes for Jayson Cosme, who was also involved in all of my research projects. Thank you for being such a great colleague and for proofreading this dissertation.

Next, I would like to thank Junichi Okamoto and Marios Michael for the excellent collaboration and many fruitful discussions. In addition, I would like to thank Andrea Cavalleri and his team, particularly Gregor Jotzu, for very helpful explanations regarding their pump-probe experiments and for sharing their view on the field.

Furthermore, I am grateful for the positive atmosphere in my group and at the ZOQ in general. I would also like to thank the Physnet team, particularly Bodo Krause-Kyora and Martin Stieben, for their technical support as well as Anja Cordes and Loreen Tornier for their administrative support.

Special thanks go to Jan, Felix and Elif, who accompanied me as loyal friends throughout the entire duration of my PhD.

Last but not least, I would like to thank my parents for their unconditional and unlimited support.

Eidesstattliche Versicherung / Declaration on oath

Hiermit versichere ich an Eides statt, die vorliegende Dissertationsschrift selbst verfasst und keine anderen als die angegebenen Hilfsmittel und Quellen benutzt zu haben.

Hamburg, den 17.02.2023

_____